

ARTIFICIAL GAUGE FIELDS FOR ULTRACOLD NEUTRAL ATOMS

Karina Jiménez-García



Joint Quantum Institute
National Institute of Standards and Technology, and the University of Maryland
Gaithersburg, Maryland

2012
(September 16, 2012)

© 2012

Karina Jiménez-García

All Rights Reserved

ACKNOWLEDGEMENTS

I would like to express my sincere gratitude to Luis Orozco, Miguel Ángel Pérez Angón and Heriberto Castilla for being the link that allowed a research collaboration between CINVESTAV and the Joint Quantum Institute, where the work reported in this thesis was realized.

Being part of the Laser Cooling and Trapping (LCT) group has been *the* experience of a lifetime; not only did I get to learn great physics but also made excellent friends. I would like to express to them my sincere gratitude, I consider them a second family.

I am deeply grateful to my advisor and mentor, Ian Spielman, for the amazing opportunity to join Rb-II, for his example and for always setting high standards. I value very much the chance to have grown as a scientist under his guidance, as well as every piece of advice he has given me. He is always full with suggestions and has a great intuition and understanding of non-trivial physics. His very optimistic personality combined with his efficient leadership, are an important driving force of our team. I truly admire his dedication and his way to approach not only physics but also everyday life.

I would like to thank Bill Phillips for warmly welcome me in the LCT group. I learned a great amount of physics from the various *paper torture* sessions with him and the Rb-II team; and during group meetings and seminars where Bill would always take the lead in asking interesting questions.

I also thank Kris Helmerson, Paul Lett, Trey Porto and Gretchen Campbell for their friendship and advice when I needed it.

My research stay at NIST developed mostly in the Rb-II lab, where I worked side by side with a wonderful team of physicists. I would like to acknowledge and thank my postdocs and lab-buddies: Rob Compton for showing me the daily operation of the Rb-II BEC machine and for teaching me how to control the experiment. Yu-Ju Lin for her valuable guidance and for patiently sharing her knowledge on artificial gauge field experiments. Ross Williams for his example and his friendship, he is a brilliant physicist and a great experimentalist, I learned a lot from him. I particularly thank him very much for carefully reading this thesis. Lindsay LeBlanc for being an ideal lab-mate, when we worked together we always synchronized. She is a very talented physicist and a great friend; I thank her for her advice in physics and in life, and for thoroughly reading this thesis. Matthew Beeler for his patience and support during the writing of this thesis; not only is he a great lab-buddy, he is also a neat office mate. I admire his skills in the lab, particularly when we installed the 1064 nm

optical lattice, that was heavy-duty! Special thanks for his comments to this thesis. Abby Perry for being a great friend, lab-buddy and most importantly my academic sister; I treasure our time together in the lab. Whether we are studying, soldering, playing with cold atoms or even running 5+ Km races, it is always fun to be by her side.

I thank my fellow graduate students for their friendship and support: Roger Brown, Jeremy Clark, Brooke Cranswick, Aizar Enciso, Fernando Favela, Estela Garcés, Anand Ramanathan and Gilberto Tetlalmatzi. Thanks also to my amigos Francisco Elohim Becerra, Carlos López-Mariscal, Alberto Marino and Adrián Pérez-Galván, for always making me feel close to home.

I would like to express my gratitude to Luis Orozco for his friendship, for sharing life experiences and for various delicious Mexican dinners together with me and Neil Vladimir.

I am thankful to my parents for their example and motivation, they are a strong driving force in my life and I am indebted to them in many ways. I owe special thanks to my mom whom has always supported me with non-trivial logistics in Mexico City. My sister has always been a role model in my life, I deeply admire her and thank her for her love and guidance ever since we were little girls. Mis abuelos, Joel y Juany, have always been there for me; they looked after me during a significant part of my life and I remember them with affection. I deeply thank them for their support.

I would like to express my infinite gratitude to Neil Vladimir Corzo-Trejo, my best friend and favorite physicist. We came together to the US to realize our PhD projects, and have lived an innumerable amount of experiences, new to both of us. He has always supported me, kept me focused and has always looked after me, for which I am specially thankful.

My collaboration here would have been almost impossible without the important participation of the administrative staff both at JQI and at CINVESTAV. I would like to thank Kim Emswiler, Gail Griffin-Ferris, Flor Ibañez and Patricia Villar, not only for their friendship but also for making my life easier.

This work was partially supported by the Office of Naval Research; the Army Research Office with funds from the Defense Advanced Research Projects Agency Optical Lattice Emulator program; the Atomtronics Multidisciplinary University Research Initiative; and the National Science Foundation through the Physics Frontier Center at the Joint Quantum Institute. Finally, I acknowledge the support from Consejo Nacional de Ciencia y Tecnología (CONACYT).

RESUMEN

Los átomos ultrafríos han demostrado ser sistemas versátiles para explorar la física de los sistemas más fascinantes e interesantes en el mundo cuántico. Debido al alto grado de control experimental ofrecido por estos sistemas, es posible diseñar y experimentalmente implementar en ellos Hamiltonianos efectivos. Esta característica única hace que los átomos ultrafríos sean sistemas ideales para la simulación cuántica de fenómenos complejos tan importantes como la superconductividad de alta temperatura crítica, y recientemente de novedosos campos de norma artificiales [1, 2, 3, 4].

Esta tesis presenta una variedad de experimentos de simulación cuántica con sistemas de átomos ultrafríos, incluyendo la primera demostración experimental de campos de norma artificiales inducidos por luz en átomos neutros. Los campos de norma artificiales son un ingrediente necesario para poder simular fenómenos electrónicos tales como el efecto Hall cuántico y el efecto spin-Hall cuántico usando átomos neutros.

Nuestros experimentos utilizan condensados de Bose-Einstein iluminados por un par de láseres “Raman” [5]; en este esquema los eigenestados resultantes son superposiciones de spin y momentum. Al preparar los átomos en el eigenestado de mínima energía éstos adquieren una relación de dispersión efectiva, la cual es experimentalmente controlable vía la intensidad del acoplamiento Raman y el *detuning* con respecto de la resonancia Raman. El resultado es la introducción de un campo de norma artificial en el Hamiltoniano.

Nuestras técnicas experimentales para bosones ultrafríos han superado las aparentes limitaciones impuestas por su neutralidad de carga eléctrica [6, 7, 8], su naturaleza bosónica [9, 10], y su baja energía [11] y han permitido la observación de nuevos e interesantes fenómenos físicos. Las proyecciones de este trabajo incluyen la posible realización del efecto Hall cuántico en bosones, de aislantes topológicos [12] y de sistemas que soporten fermiones de Majorana [13].

Este trabajo fue realizado en colaboración con el Departamento de Física del Centro de Investigación y Estudios Avanzados del Instituto Politécnico Nacional, México DF, 07360, México.

ABSTRACT

Ultracold atoms have proven to be a versatile probe for physics at the core of the most intriguing and fascinating systems in the quantum world. Due to the high degree of experimental control offered by such systems, effective Hamiltonians can be designed and experimentally implemented on them. This unique feature makes ultracold atom systems ideal for quantum simulation of complex phenomena as important as high-temperature superconductivity, and recently of novel artificial gauge fields [1, 2, 3, 4].

This thesis presents a variety of experiments on quantum simulation with ultracold atom systems, including the first experimental demonstration of light induced artificial gauge fields for ultracold neutral atoms. Artificial gauge fields are the required ingredient for ultracold atom systems to simulate electronic phenomena such as the quantum Hall effect and the quantum spin Hall effect.

We optically dress our Bose-Einstein condensates with a pair of far detuned “Raman” lasers [5]; the resulting dressed states are spin and momentum superpositions, and we adiabatically load the atoms into the lowest energy dressed state. The atoms acquire a new effective dispersion relation which is experimentally tunable via the strength of the Raman coupling and the detuning from Raman resonance, thus introducing gauge terms into the Hamiltonian.

Our experimental techniques for ultracold bosons have surpassed the apparent limitations imposed by their neutral charge [6, 7, 8], bosonic nature [9, 10], and ultra-low energy [11] and have allowed the observation of these new and exciting phenomena. Future work might allow the realization of the bosonic quantum Hall effect, of topological insulators [12] and of systems supporting Majorana fermions [13] using cold atoms.

This work was done in collaboration with the Physics Department at Centro de Investigación y Estudios Avanzados del Instituto Politécnico Nacional, México DF, 07360, México.

CONTENTS

| | |
|---|------------|
| Acknowledgements | iii |
| Resumen | v |
| Abstract | vi |
| 1 Introduction | 1 |
| 1.1 Artificial gauge fields for ultracold neutral atoms | 1 |
| 1.2 Thesis overview | 2 |
| 2 Basics of Bose-Einstein condensation theory | 4 |
| 2.1 The Bose-Einstein distribution | 4 |
| 2.2 Ideal Bose gas in a 3D harmonic trapping potential. | 8 |
| 2.3 Bose-Einstein condensation of interacting gases | 11 |
| 2.4 BEC dynamics in a harmonic trap | 16 |
| 2.5 Experimental realization of BEC | 20 |
| 3 Laser cooling and trapping ultracold neutral atoms | 22 |
| 3.1 Alkali atoms and the electronic structure of ^{87}Rb | 22 |
| 3.2 Interaction of electromagnetic radiation and matter | 23 |
| 3.3 Angular momentum selection rules | 26 |
| 3.4 Interaction between atoms and electric fields | 31 |
| 3.5 Optical trapping | 34 |
| 3.6 Laser cooling | 36 |
| 3.7 Resonant Absorption Imaging | 43 |
| 3.8 Interaction between atoms and magnetic fields | 47 |
| 3.9 Magnetic trapping | 47 |
| 4 Experimental Setup | 53 |
| 4.1 Experimental sequence to achieve BEC | 53 |
| 4.2 Computer control and Data acquisition | 57 |

| | | |
|----------|--|------------|
| 4.3 | Vacuum system | 60 |
| 4.4 | Cooling Lasers | 63 |
| 4.5 | Magnetic fields | 73 |
| 4.6 | Optical Dipole Trap | 79 |
| 4.7 | Raman and optical lattice lasers | 80 |
| 4.8 | Imaging systems | 83 |
| 4.9 | Magnetic field cancellation | 86 |
| 5 | Artificial gauge fields for ultracold neutral atoms | 96 |
| 5.1 | Basic review of gauge fields for charged particles | 96 |
| 5.2 | Artificial gauge fields for ultracold neutral atoms | 97 |
| 5.3 | Physical manifestation of an artificial vector potential | 103 |
| 5.4 | Experimental characterization | 104 |
| 5.5 | Conclusions | 110 |
| 6 | Synthetic magnetic fields for ultracold neutral atoms | 112 |
| 6.1 | Signature of a synthetic magnetic field | 112 |
| 6.2 | Experimental characterization | 114 |
| 6.3 | Conclusions | 119 |
| 7 | Ultracold Bose gases in optical lattices | 120 |
| 7.1 | Optical lattice potentials | 120 |
| 7.2 | Single particle in a 1D periodic potential | 121 |
| 7.3 | The Bose-Hubbard Hamiltonian | 124 |
| 7.4 | Universal phase diagram for trapped bosons in a 2D lattice | 127 |
| 7.5 | Experimental characterization | 129 |
| 7.6 | Conclusions | 141 |
| 8 | Uniform artificial gauge field in a 1D lattice potential | 143 |
| 8.1 | rf-Raman lattice potential | 143 |
| 8.2 | The Peierls substitution | 145 |
| 8.3 | Momentum representation of $\hat{H}_{\text{rf+R}}$ | 147 |
| 8.4 | Experimental characterization | 149 |
| 8.5 | Conclusions | 156 |
| 9 | Matrix valued gauge fields: spin-orbit coupling in BECs | 157 |
| 9.1 | Spin-orbit coupling | 158 |

| | | |
|--------------------------------|--|------------|
| 9.2 | The Raman coupling scheme for an effective spin-1/2 system | 159 |
| 9.3 | SOC in an effective two-level system | 160 |
| 9.4 | Tunable Spin-Orbit coupling strength | 163 |
| 9.5 | Experimental characterization | 164 |
| 9.6 | Conclusions | 167 |
| 10 | Control of interactions with artificial gauge fields | 168 |
| 10.1 | A novel tool for tuning spinor interactions with light | 168 |
| 10.2 | Synthetic partial waves in ultracold atomic collisions | 172 |
| 10.3 | Experimental characterization | 174 |
| 10.4 | Conclusions | 178 |
| Conclusions and Outlook | | 179 |
| A | Appendix A | 182 |
| A.1 | Quantum mechanical model of the atomic polarizability | 182 |
| A.2 | Classical model to describe the atomic polarizability | 186 |
| A.3 | Rotation operators | 186 |
| A.4 | Addition of angular momentum | 188 |
| Bibliography | | 189 |

LIST OF FIGURES

| | | |
|------|--|----|
| 2.1 | Bose-Einstein distribution. | 5 |
| 2.2 | Condensate fraction for a non-interacting Bose gas. | 7 |
| 2.3 | Lowest energy wave function of a HO and dimensionality. | 9 |
| 2.4 | Interaction potential between two neutral atoms as a function of their separation. . . | 13 |
| 2.5 | Density profile of interacting and non-interacting Bose gases in a HO trap. | 15 |
| 2.6 | Elementary excitations in a BEC. | 18 |
| 3.1 | Hyperfine structure of ^{87}Rb | 23 |
| 3.2 | The quantization axis and the polarization of the electromagnetic field. | 25 |
| 3.3 | Relative strength of electric dipole D ₂ transitions. | 27 |
| 3.4 | Optical pumping and cooling transitions. | 30 |
| 3.5 | Measured scalar light-shift as a function of wavelength for ^{87}Rb | 33 |
| 3.6 | Gaussian beam characterization. | 35 |
| 3.7 | Recoil energy and recoil velocity vs wavelength. | 37 |
| 3.8 | The Zeeman cooling scheme. | 38 |
| 3.9 | The dissipative force in optical molasses and the magneto optical trap. | 40 |
| 3.10 | Resonant absorption cross-section. | 44 |
| 3.11 | Resonant absorption imaging. | 46 |
| 3.12 | Hyperfine structure of the ground state manifold $5^2S_{1/2}$ of ^{87}Rb vs magnetic field. . | 47 |
| 3.13 | Magnetic quadrupole trap. | 48 |
| 3.14 | rf dressed system. | 50 |
| 4.1 | Schematic of Rb-II BEC machine (BEC level). | 54 |
| 4.2 | Schematic of Rb-II BEC machine (lowest level). | 56 |
| 4.3 | Schematic of Rb-K oven. | 61 |
| 4.4 | Temperature, pressure and time scales for baking. | 62 |
| 4.5 | ^{87}Rb D ₂ -line energy levels with the relative frequencies of the cooling lasers. | 64 |
| 4.6 | Master and repump lasers optical layouts and power map. | 66 |
| 4.7 | Master laser locking scheme. | 68 |

| | | |
|------|--|-----|
| 4.8 | Optical layout for the MOT laser, setup for frequency locking to the master laser and overall power map. | 69 |
| 4.9 | Schematic of rf-amplifier and antennae. | 75 |
| 4.10 | Schematic of current stabilization circuit. | 77 |
| 4.11 | Water cooling system. | 78 |
| 4.12 | Tunable aspect ratio of the optical dipole trap. | 79 |
| 4.13 | Schematic of the optical setup and power map of the Ti:Sapph laser. | 81 |
| 4.14 | AOM driver for Raman beams. | 82 |
| 4.15 | <i>xz</i> Imaging magnification. | 85 |
| 4.16 | Cancelling power-line noise. | 88 |
| 4.17 | Picture of the optical setup for the dipole trap. | 90 |
| 4.18 | Picture of the optical setup for the master laser. | 91 |
| 4.19 | Picture of the optical setup for the repump laser. | 92 |
| 4.20 | Picture of the optical setup for the MOT laser. | 93 |
| 4.21 | Picture of the optical setup for the MOT beat-note lock. | 94 |
| 4.22 | Picture of the optical setup for the Raman lasers. | 95 |
| 5.1 | Standard experimental setup and level diagram for implementing light-induced artificial gauge fields on neutral atoms. | 98 |
| 5.2 | Eigenenergies of the Raman dressed states as a function of quasimomentum k_x | 99 |
| 5.3 | Raman dressed states at $\hbar\Omega_R = 10E_L$ for selected values of the detuning. | 101 |
| 5.4 | Detection of Raman dressed states after TOF. | 104 |
| 5.5 | Calibration of Raman coupling strength by pulsing. | 106 |
| 5.6 | Measured vector light-shift for ^{87}Rb atoms as a function of wavelength. | 107 |
| 5.7 | Testing the Lorentz force from a synthetic electric field E^* acting on neutral atoms. . | 109 |
| 5.8 | Summary of experimental setups for the realization of artificial gauge fields. | 111 |
| 6.1 | Signature of an effective magnetic field B^* acting on neutral atoms. | 113 |
| 6.2 | Geometry for the observation of the classical Hall effect and its analogue using ultracold atoms in synthetic magnetic fields. | 114 |
| 6.3 | Calibration of the bias coils along \mathbf{e}_z via rf-spectroscopy. | 115 |
| 6.4 | Setup and level diagram for pioneering synthetic magnetic field experiments. | 116 |
| 6.5 | Vortices entering the condensate as a function of detuning gradient δ' | 117 |
| 6.6 | Superfluid Hall effect in ultracold atomic systems. | 118 |
| 7.1 | Bandstructure of a 1D lattice vs lattice depth. | 122 |
| 7.2 | Lowest band width vs lattice depth. | 124 |

| | | |
|------|---|-----|
| 7.3 | MF calculation of SF-MI transition. | 125 |
| 7.4 | State diagram for a harmonically trapped 2D Bose gas. | 128 |
| 7.5 | Vertical lattice to create a collection of 2D systems. | 129 |
| 7.6 | Dipole force for alignment of laser beams to atoms. | 131 |
| 7.7 | Lattice depth calibration. | 132 |
| 7.8 | Contribution of lattices to overall trapping potential. | 134 |
| 7.9 | Restoring coherence. | 135 |
| 7.10 | Comparison between a uniform pulse and a Blackman pulse. | 136 |
| 7.11 | Atom number calibration. | 137 |
| 7.12 | Matter wave focusing | 139 |
| 7.13 | Condensate fraction of a 2D $N_{2D} \approx 3500$ atom Bose gas measured through the SF to MI transition. | 140 |
| 8.1 | Setup and level diagram for rf-Raman lattice experiments. | 144 |
| 8.2 | Effective Zeeman lattice potential. | 145 |
| 8.3 | Spatial precession of effective Zeeman field. | 146 |
| 8.4 | The Peierls substitution in a lattice potential. | 147 |
| 8.5 | Effective Zeeman lattice properties. | 148 |
| 8.6 | Effective mass and Peierls phase in the engineered lattice potential. | 149 |
| 8.7 | Measured effective mass at $\Omega_z = 0$ | 150 |
| 8.8 | Measured Peierls tunneling amplitude and phase. | 152 |
| 8.9 | Adiabatic measurement of the Peierls phase. | 153 |
| 8.10 | BEC diffraction from the effective Zeeman lattice. | 154 |
| 8.11 | Generation of the 1/3 flux Hofstadter model. | 155 |
| 9.1 | Spin-orbit coupling pictured as a momentum dependent Zeeman field. | 158 |
| 9.2 | Setup and level diagram for SO coupling experiments. | 159 |
| 9.3 | Dispersion relations in a Raman dressed system. | 161 |
| 9.4 | SOC Dispersion relation. | 162 |
| 9.5 | Tunable spin-orbit coupling. | 166 |
| 10.1 | Calculated spin composition of an effective two-level system under SOC. | 170 |
| 10.2 | Quantum phase transition from mixed to phase separated. | 171 |
| 10.3 | Synthetic higher order partial waves in ultracold atomic collisions. | 173 |
| 10.4 | Metastable detuning width for two component phase. | 174 |
| 10.5 | Measuring the quantum phase transition. | 175 |
| 10.6 | Spatial density profiles across the phase transition. | 176 |

| | |
|---|-----|
| 10.7 Setup and level diagram for collision experiments. | 177 |
|---|-----|

LIST OF TABLES

| | | |
|------|---|-----|
| 2.1 | Relevant values for determining the conditions for BEC in selected systems. | 6 |
| 2.2 | Characteristic widths of trapped non-interacting systems. | 10 |
| 2.3 | Scattering lengths of alkali atoms at zero magnetic field. | 14 |
| 2.4 | Lowest energy collective oscillation modes in a homogeneous HO trap. | 20 |
| 4.1 | Bias fields to cancel stray fields, magnetic trapping and optical pumping. | 55 |
| 4.2 | List of AOs and devices to control the experiment. | 58 |
| 4.3 | List of DOs and devices to control the experiment. | 59 |
| 4.4 | Frequencies of the cooling lasers during MOT capture. | 65 |
| 4.5 | Typical operating values for the cooling lasers. | 70 |
| 4.6 | Measured power in cooling beams at MOT stage. | 71 |
| 4.7 | Calibration of bias coils. | 74 |
| 4.8 | <i>x</i> -antenna calibration. | 76 |
| 4.9 | Dimensions and trapping frequencies along dipole beams. | 80 |
| 4.10 | Typical power at the output of the Raman fibers vs AO command. | 82 |
| 4.11 | Dimensions of Ti:Sapph beams. | 83 |
| 4.12 | Contribution of various instruments to ambient field noise at 60 Hz. | 87 |
| 4.13 | Measured magnetic field noise in different directions. | 89 |
| 5.1 | Physical effects of light-induced artificial gauge fields. | 102 |
| 7.1 | Contribution of optical lattices to overall trap frequency. | 134 |
| 7.2 | Measured and QMC values of $(U/t)_c$ | 141 |

CHAPTER 1

INTRODUCTION

Bose-Einstein condensation (BEC) was first experimentally realized in 1995 using dilute gases of alkali metals: ^{87}Rb was used in the experiments led by Eric Cornell and Carl Wieman at JILA [14]; and ^{23}Na was used in the experiments led by Wolfgang Ketterle at MIT [15]. These achievements were crowned with the Nobel prize in Physics in 2001.

Together with superconductivity [16] and superfluidity [17, 18], BEC is one of the few macroscopic manifestations of quantum phenomena. The study of BEC gives us a major opportunity to discover new quantum phenomena, to probe the laws of quantum mechanics, and to better understand the underlying mechanisms of various physical phenomena.

1.1 ARTIFICIAL GAUGE FIELDS FOR UTLRACOLD NEUTRAL ATOMS

A natural procedure to solve a complex problem is to explore a simplified version of it, which retains its essential characteristics. For numerous applications, such a role is played by ultracold atoms, due to their precise experimental control in real-time and their lack of impurities. Quantum simulation with ultracold atoms allows one to address numerous questions in physics which in principle cannot be treated analytically.

Ultracold atoms have proven to be a versatile probe for physics at the core of the most intriguing and fascinating systems in the quantum world. Their characteristic versatility allows the realization of *tailor-made* Hamiltonians, that reproduce interesting physical phenomena. As an example, ultracold bosonic atoms in optical lattices have succeeded in simulating and revealing the physics of the Bose-Hubbard model [19, 20], the bosonic version of a model which is believed to be important to understand high-temperature superconductivity [21, 22].

However, ultracold atom systems are electrically neutral and in the presence of electromagnetic fields they do not experience a Lorentz force. This restricts their use in the study of interesting phenomena such as the quantum Hall effect [23], the quantum spin Hall effect [12, 24] and exotic phenomena like topological insulators [25, 26]. The research on such phenomena not only has important consequences to quantum mechanics but also to quantum computation and information theory [27].

During the last years our group has succeeded in realizing the dynamical conditions exerted by an electromagnetic field on charged particles, by realizing light-induced artificial gauge fields for neutral atoms [1]. Furthermore due to extreme experimental control on the properties of cold atom systems, artificial gauge fields beyond those appearing in condensed matter systems could in principle be realized [28].

1.2 THESIS OVERVIEW

This thesis describes both the experimental apparatus used to prepare samples of ultracold atoms, and the measurements realized on various engineered Hamiltonians for quantum simulation with artificial gauge fields.

Chapter 2 discusses the theory of Bose-Einstein condensation (BEC) in trapped gases. It focuses both on the equilibrium properties of trapped BECs and on its dynamic behavior. We center the attention on the study of collective modes, due to their relevance on our experiments.

Chapter 3 provides the theory of laser cooling and trapping as well as of the basic techniques used to manipulate and probe ultracold atoms.

Chapter 4 gives a detailed description of the experimental apparatus. Our machine combines the efficient capture of atoms from a magneto optical trap (MOT) into a magnetic trap with the rapid evaporation on optical dipole traps to reliably produce ^{87}Rb BECs in typical cycling times of 20 s.

Chapter 5 focuses on the effects of Raman transitions on ultracold atoms. The effective dispersion relation imposed by the dressing fields on the atoms, gives rise to an experimentally tunable artificial vector potential [5] for ultracold neutral atom systems. The effects of an synthetic electric force acting on neutral atoms [6] are discussed.

Chapter 6 describes experiments with synthetic magnetic fields for ultracold neutral atoms [7]. Our measurements of the transport properties of BECs under the influence of such fields [8] constitute the cold-atom analog to Hall measurements in condensed matter (CM) systems.

Chapter 7 details the physics and experimental realization of ultracold atoms in optical lattices. We focused on the superfluid to Mott insulator (MI) quantum phase transition; and measured the critical lattice depth for the first appearance of MI in a two dimensional (2D) system as a function of system size and trapping parameters [29]. The introduction of a characteristic density revealed the universal behavior of the quantum phase transition and provided a test for the validity of the local density approximation.

Chapter 8 describes a method with which we simultaneously implemented an effective gauge field and a lattice potential. We realized the Peierls substitution in this engineered lattice [30] and demonstrated excellent experimental control over both the Peierls tunneling amplitude and phase.

Chapter 9 introduces matrix valued artificial gauge fields and spin-orbit coupling in a CM system. Using an effective “spin-1/2” system under Raman dressing, we demonstrated spin-orbit coupling in ultracold atoms [9], the strength of which can experimentally be adjusted in real time [31].

Chapter 10 addresses the effect of Raman coupling on the interactions of the dressed systems. Working in different Raman coupling regimes we observed modified interactions between the atoms of Raman dressed BECs. In the low Raman coupling regime we describe a new method to control the strength of interatomic interactions between the dressed spins [9]; this technique is robust against atom loss and could overcome the limitations existing in current techniques based on Feshbach resonances. In the large Raman coupling regime, we detected evidence of modified interactions from the scattering products of the ultra-low energy collisions of Raman dressed BECs [11].

The experimental realization of light-induced artificial gauge fields has opened new avenues for the quantum simulation with ultracold atoms, since it allows the study of physical phenomena previously exclusive to CM systems. Other important applications include the generalization of these methods to realize non-abelian gauge fields and topological insulators, and their application to fermionic systems [32, 33].

CHAPTER 2

BASICS OF BOSE-EINSTEIN CONDENSATION THEORY

Bose-Einstein condensation (BEC) is a quantum state of matter, which was first predicted by Bose for the statistics of photons and later generalized by Einstein to the context of bosons in 1924 [34].

BEC occurs when the temperature T of a sample of bosonic particles of mass m is reduced to the point that their spatial extent, characterized by the thermal de Broglie wavelength $\lambda_{\text{dB}} = \sqrt{2\pi\hbar^2/mk_B T}$, is larger than the interatomic spacing; in this limit, the indistinguishable and the quantum nature of their statistics become most evident. In a BEC, all particles occupy the same quantum state.

Extensive reviews on the theory of BEC in trapped systems and experimental techniques to make and probe BECs in dilute alkali gases are Refs. [35] and [36], respectively. In this chapter I describe the basic properties of Bose-Einstein condensation of dilute atomic gases trapped in a harmonic oscillator potential. Due to their importance to our experiments I will also discuss dynamical properties of BEC, in particular, collective excitations.

2.1 THE BOSE-EINSTEIN DISTRIBUTION

At low temperatures the statistical distribution of quantum particles in thermodynamical equilibrium at temperature T depends on their spin degree of freedom. In the case of non-interacting bosons (integer spin), the mean occupation number of particles occupying the state E_j (where j labels the state's energy) is given by the Bose-Einstein distribution

$$n(E_j) = \frac{1}{\exp[(E_j - \mu)/k_B T] - 1}; \quad (2.1)$$

where μ is the chemical potential (the energy required to add or remove a particle from the system) and k_B is Boltzmann's constant. The chemical potential μ is introduced to establish the condition of conservation of the total number of particles $N = \sum_j n(E_j)$, and it is thus a function of N and T . The energy levels E_j in Eq. (2.1) correspond to the eigenenergies of the particles in a potential U .

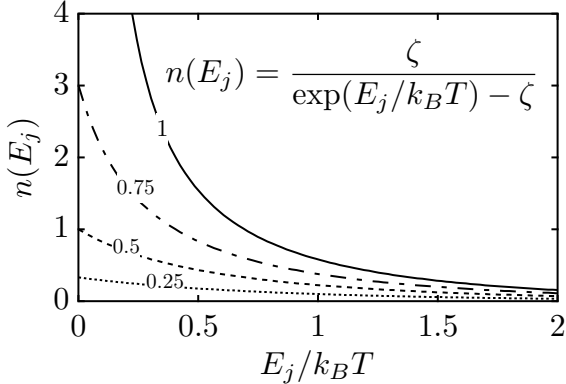


Figure 2.1: Bose-Einstein distribution. Occupation number of bosons as a function of energy at different values of the fugacity: $\zeta = 0.25, 0.5, 0.75$ correspond to chemical potentials $\mu/k_B T \approx -1.39, -0.69, -0.29$, respectively; the condensate state corresponds to $\zeta = 1$.

The Bose-Einstein distribution can also be expressed in terms of the fugacity $\zeta = \exp(\mu/k_B T)$ as

$$n(E_j) = \frac{\zeta}{\exp(E_j/k_B T) - \zeta}. \quad (2.2)$$

At high temperatures, the Bose-Einstein distribution tends to the Boltzmann distribution $n(E_j) \approx \exp[-(E_j - \mu)/k_B T]$, where the mean occupation numbers are $n(E_j) \ll 1$. The condition that $n(E_j) \geq 0 \forall E_j$, in particular for the ground state which we define as E_0 , implies that the chemical potential for a non-interacting Bose gas is $\mu < E_0$ (thus $\zeta < 1$). Fig. 2.1 displays $n(E_j)$ as a function of energy, for different values of the fugacity.

When the temperature goes down, the chemical potential increases but as justified above, it cannot go beyond E_0 ; this imposes a limit on the occupation numbers of the excited states, given by Eq. (2.1) evaluated at $\mu = E_0$. When the excited states have reached their occupation limit, the remaining particles can accumulate in the limitless occupation ground state and Bose-Einstein condensation (BEC) is achieved.

2.1.1 Conditions to reach BEC. There is a critical temperature T_c above which BEC no longer occurs; for temperatures below T_c , the chemical potential is $\mu = E_0$ and the ground state can be macroscopically occupied.

In the following I will assume that the energy $k_B T$ is larger than the energy difference between the energy levels of the system, thus we can express the number of particles in the excited states as an integral of the form

$$N_{\text{ex}} = \sum_{j \neq 0} n(E_j) \rightarrow \int_0^\infty g(E)n(E)dE \quad (2.3)$$

Table 2.1: Relevant values for determining the conditions for BEC in selected systems.

| System and dimensionality | α | $\Gamma(\alpha)$ | $\zeta(\alpha)$ |
|--------------------------------|----------|------------------------------|-------------------------|
| Uniform Bose gas in 1D | 1/2 | $\sqrt{\pi} \approx 1.77$ | -1.46 |
| Uniform Bose gas in 2D | 1 | 1 | ∞ |
| Uniform Bose gas in 3D | 3/2 | $\sqrt{\pi}/2 \approx 0.886$ | 2.612 |
| Bose gas in a harmonic trap 2D | 2 | 1 | $\pi^2/6 \approx 1.645$ |
| Bose gas in a harmonic trap 3D | 3 | 2 | 1.202 |

where $g(E)$ is the density of states¹. The above quantity N_{ex} reaches its maximum value when the chemical potential reaches the energy of the lowest state $\mu = E_0$; we can determine the transition to BEC from the condition that at the critical temperature T_c the total of particles N fully populate the excited states, thus:

$$N = N_{\text{ex}}(T_c, \mu = 0) = \int_0^\infty \frac{g(E)dE}{\exp(E/k_B T_c) - 1}. \quad (2.4)$$

The density of states is given by $g(E) = dG(E)/dE$, where $G(E)$ is the total number of energy states of the system with energy smaller than E ; and in general it can be expressed as $g(E) = C_\alpha E^{\alpha-1}$, where C_α is a constant and relevant values for α are given in Table 2.1. By defining the dimensionless variable $u=E/k_B T_c$, Eq. (2.5) becomes

$$N = C_\alpha (k_B T_c)^\alpha \int_0^\infty \frac{u^{\alpha-1} e^{-u}}{1 - e^{-u}} du.$$

Assuming that e^{-u} is small, we use $(1 - e^{-u})^{-1} \approx \sum_l e^{-lu}$ with $0 \leq l < \infty$ and obtain

$$\begin{aligned} N &= C_\alpha (k_B T_c)^\alpha \int_0^\infty \sum_{l=0}^{\infty} e^{-(l+1)u} u^{\alpha-1} du, \\ &= C_\alpha (k_B T_c)^\alpha \int_0^\infty \sum_{l=1}^{\infty} e^{-u'} \left(\frac{u'}{l}\right)^{\alpha-1} \frac{du'}{l}, \\ &= C_\alpha (k_B T_c)^\alpha \sum_{l=1}^{\infty} l^{-\alpha} \int_0^\infty e^{-u'} u'^{\alpha-1} du', \end{aligned}$$

where $u' = lu$. We identify the Gamma function $\Gamma(\alpha) = \int_0^\infty e^{-u'} u'^{\alpha-1} du'$ and the Riemann zeta

¹The density of states is basically the number of available states of a system at a given energy; it depends on the systems dispersion relation as well as on its dimensionality.

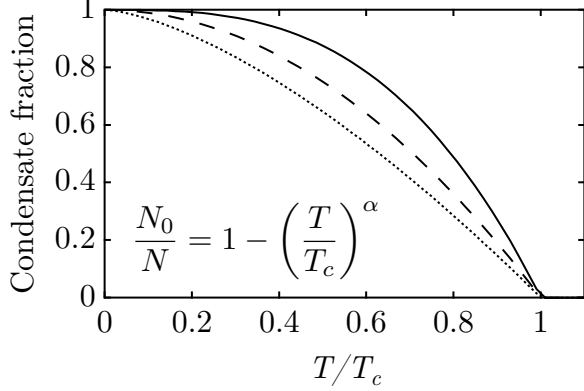


Figure 2.2: Condensate fraction as a function of T/T_c for a non-interacting Bose gas in: a 3D harmonic trap (solid, $\alpha=3$); a 2D harmonic trap (dashed, $\alpha=2$) and in a 3D box (dotted, $\alpha=3/2$).

function $\zeta(\alpha) = \sum_{l=1}^{\infty} l^{-\alpha}$ and rewrite N as

$$N = C_\alpha (k_B T_c)^\alpha \Gamma(\alpha) \zeta(\alpha); \quad (2.5)$$

from which we obtain the critical temperature T_c

$$k_B T_c = \left(\frac{N}{C_\alpha \Gamma(\alpha) \zeta(\alpha)} \right)^{1/\alpha}. \quad (2.6)$$

The critical temperature T_c scales with N but also depends on the values of the special functions $\Gamma(x)$ and $\zeta(x)$ at $x = \alpha$. By calculating the density of states $g(E)$ of a system, the coefficients α and C_α are obtained. Table 2.1 shows relevant values to determine T_c in selected systems, and it is concluded that: (i.) BEC in a 2D system can only occur either at $T_c = 0$ in a box, or at a finite temperature when confined in a harmonic trap; and (ii.) BEC in a 3D system either in a box or in a harmonic trap occurs at finite temperature. BEC cannot occur in 2D and 1D at finite temperature because thermal fluctuations destabilize the condensate [35, 37].

In the following we introduce two quantities which are useful to determine in which limit do the quantum statistics of the system matter. The de Broglie wavelength $\lambda_{dB} = \sqrt{2\pi\hbar^2/mk_B T}$ is a measure of the spatial extent of the wave function of a particle; when λ_{dB} becomes comparable with the interparticle separation quantum effects are relevant; this typically occurs at low temperatures. On the other hand, we define the phase space density $\rho = n\lambda_{dB}^3$ as the number of particles contained in a volume λ_{dB}^3 , where n is the density of particles. The conditions on ρ to observe quantum behavior are better illustrated in the following example.

For a uniform gas of N non-interacting bosons in a 3D box of volume V (with density $n = N/V$) the critical temperature to achieve BEC is obtained from Eq. (2.6) with $\alpha = 3/2$ and the coefficient

$C_{3/2} = Vm^{3/2}/2^{1/2}\pi^2\hbar^3$. The condition to reach BEC reduces to $\rho = \zeta(3/2) \approx 2.612$, thus low temperatures and/or high densities are necessary to observe BEC.

2.1.2 Condensate fraction We now move our attention to compute the fraction of atoms in the BEC state, namely the condensate fraction. The number of particles in the excited states is given by Eq. (2.3); below the transition temperature where $\mu = 0$

$$N_{\text{ex}} = \int_0^\infty \frac{g(E)dE}{\exp(E/k_B T) - 1},$$

which reduces to $N_{\text{ex}} = C_\alpha \Gamma(\alpha) \zeta(\alpha) (k_B T)^{\alpha}$. Using Eq. (2.5) we obtain $N_{\text{ex}}/N = (T/T_c)^\alpha$; thus the fraction of atoms condensed in the lowest energy state is $N_0/N = (1 - N_{\text{ex}}/N)$, namely

$$\frac{N_0}{N} = 1 - \left(\frac{T}{T_c}\right)^\alpha. \quad (2.7)$$

Figure 2.2 displays the condensate fraction as a function of T/T_c for selected systems.

2.2 IDEAL BOSE GAS IN A 3D HARMONIC TRAPPING POTENTIAL.

Due to its relevance in experiments with dilute BECs, this section summarizes the results on BEC for a collection of non-interacting bosons in a 3D harmonic oscillator (HO) potential $U(\mathbf{r})$. Considering

$$U(\mathbf{r}) = -m(\omega_x^2 x^2 + \omega_y^2 y^2 + \omega_z^2 z^2); \quad (2.8)$$

where $\omega_j = 2\pi f_j$ is the angular frequency of the harmonic trap along \mathbf{e}_j ; the transition temperature of an ideal Bose gas in a 3D harmonic potential is obtained from Eq. (2.6) with $\alpha=3$ and $C_3 = (2\hbar^3 \omega_x \omega_y \omega_z)^{-1}$, thus

$$k_B T_c \approx 0.941 \hbar \bar{\omega} N^{1/3}, \quad (2.9)$$

where $\bar{\omega} = (\omega_x \omega_y \omega_z)^{1/3}$ is the geometric mean of the harmonic oscillator frequencies. The condensate fraction is given by

$$\frac{N_0}{N} = 1 - \left(\frac{T}{T_c}\right)^3. \quad (2.10)$$

This result assumes that $k_B T$ is larger than the energy difference between the energy levels of the system. Assuming a $N = 1 \times 10^6$ atom system and using Eq. (2.9), the critical temperature is $k_B T_c \approx 94.1 \hbar \bar{\omega}$; i.e. at the BEC transition there is enough energy to occupy many excited energy levels, but it is the bosonic quantum statistics which favor the population of the lowest energy state. Once a few bosons occupy the ground state, more tend to accumulate in such state in a phenomenon known as Bose stimulation [38].

a. HO potential and ground state wavefunction b. Dimensionality in HO trapped systems

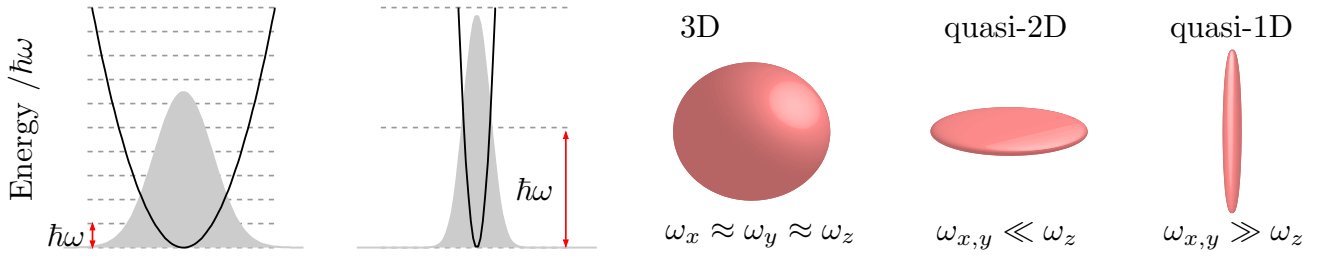


Figure 2.3: Lowest energy wave function of a HO and dimensionality. **a.** The spatial extent of the ground state wave function of a HO is reduced when the trapping frequency increases. The solid curves represent the HO potential and the shaded regions corresponds to the wave function, both as a function of position. **b.** By adjusting the trap parameters, reduced dimensionality can be achieved.

2.2.1 Dimensionality. We have discussed that dimensionality is an important factor to be considered when determining the conditions to reach BEC. In this section I discuss the conventions on reduced dimensionality for trapped systems. In the above treatment for the ideal gas, we assumed that the temperature energy scale was $k_B T \gg \hbar\omega_j$ for $j = x, y, z$. By relaxing these conditions along one or more directions, reduced dimensionality can be achieved.

Trapping potentials for ultracold atoms can be made extremely anisotropic, and this allows experimentalist to work in quasi-2D and quasi-1D regimes. The conditions to reach reduced dimensionality are defined by comparing the thermal and HO energy scales; e.g. to achieve 2D confinement in the xy -plane, it is required that $\hbar\omega_{xy} \ll \omega_z$ as is illustrated in Fig. 2.3, where the spatial extent of the cloud, characterized by $a_j = \sqrt{\hbar/m\omega_j}$ along e_j , is reduced due to the increased trapping frequency to the point that the motion is frozen in that direction. Similarly for sufficiently large trapping frequencies in two directions, the movement of the particles can be restricted to 1D.

2.2.2 Experimental signatures of BEC. Typically experiments probe the atomic distributions either in-situ or after letting the atoms to freely expand in time of flight (TOF) using resonant absorption imaging (see section 3.7). In-situ imaging gives us access to the spatial density profile of the distribution; while imaging after TOF reveals the momentum distribution. In this section I describe an important feature which distinguishes a BEC from a thermal distribution, namely its anisotropic expansion in TOF and its narrow momentum distribution. This behavior provided evidence for the existence of BEC in early experiments [14]. Table 2.2 summarizes this important result. Additionally I briefly discuss on the long-range phase coherence of BECs.

2.2.2.1 Anisotropic expansion in TOF. Let us consider a collection of bosons in an anisotropic HO potential of the form given in Eq. (2.8). The single particle wave function of the lowest energy

Table 2.2: Characteristic widths of trapped non-interacting systems.

| Width of density distribution at | BEC | Thermal |
|----------------------------------|----------------------------|------------------------------|
| $t = 0$ | $(\hbar/m\omega_j)^{1/2}$ | $(2k_B T/m\omega_j^2)^{1/2}$ |
| $t > \omega_j$ | $(\hbar\omega_j/m)^{1/2}t$ | $(2k_B T/m)^{1/2}t$ |

state is given by

$$\psi_0(\mathbf{r}) = \frac{e^{-x^2/2a_x^2} e^{-y^2/2a_y^2} e^{-z^2/2a_z^2}}{\pi^{3/4} \sqrt{a_x a_y a_z}}; \quad (2.11)$$

where $a_j = \sqrt{\hbar/m\omega_j}$ are the characteristic HO lengths along \mathbf{e}_j ; typical trapping frequencies in our experiments range from $2\pi \times 120$ Hz to $2\pi \times 5$ Hz, and correspond to HO lengths from 1 to 5 μm , respectively.

The free expansion of an atomic cloud is largely dictated by its velocity distribution in the trap (although collisions may play an important role in the expansion of the atomic distribution for an interacting system). The velocity distribution is described by the wave-function $\phi(\mathbf{p})$ in momentum space, which in turn is obtained from the Fourier transform of $\psi_0(\mathbf{r})$

$$\phi_0(\mathbf{p}) = \frac{e^{-p_x^2/2b_x^2} e^{-p_y^2/2b_y^2} e^{-p_z^2/2b_z^2}}{\pi^{3/4} \sqrt{b_x b_y b_z}}; \quad (2.12)$$

where $b_i = \hbar/a_i$. The density in momentum space is $n(\mathbf{p}) = N|\phi_0(\mathbf{p})|^2$ and thus is given by

$$n_0(\mathbf{p}) = N \frac{e^{-p_x^2/b_x^2} e^{-p_y^2/b_y^2} e^{-p_z^2/b_z^2}}{\pi^{3/2} b_x b_y b_z}. \quad (2.13)$$

The density distribution has the form of an Maxwell-Boltzmann distribution and it inherits its anisotropy from its spatial counterpart. When the atomic distribution is free to expand in TOF, the single particle wave function follows the time evolution of a free-particle with energy $p^2/2m$, thus the time-dependent wave function in position space is

$$\begin{aligned} \psi_0(\mathbf{r}, t) &= \frac{1}{(2\pi\hbar)^{3/2}} \int e^{i\mathbf{p}\cdot\mathbf{r}/\hbar} \phi_0(\mathbf{p}) e^{-i(p^2/2m)t/\hbar} d\mathbf{p}, \\ &= \frac{1}{\pi^{3/4}(2\pi\hbar)^{3/2}} \prod_{j=\{x,y,z\}} \frac{1}{\sqrt{b_j}} \int \exp \left[-\frac{p_j^2}{2} \left(\frac{it}{\hbar m} + \frac{1}{b_j^2} \right) + \frac{i}{\hbar} p_j j \right]. \end{aligned}$$

Completing a perfect square trinomial in the argument of the exponential by adding and subtracting

the term $-x^2/[2\hbar^2(\frac{1}{b_x^2} + \frac{it}{\hbar m})]$ and using the Gaussian integral $\int_0^\infty e^{-u^2} du = \sqrt{\pi}$, we obtain

$$\psi_0(\mathbf{r}, t) = \frac{1}{\pi^{3/4}} \prod_{j=\{x,y,z\}} \sqrt{\frac{a_j}{1 + ij\omega_j t}} \exp \left[\frac{-j^2}{2a_j(1 + i\omega_j t)} \right]. \quad (2.14)$$

The density distribution $n(\mathbf{r}, t) = N|\psi_0(\mathbf{r}, t)|^2$ becomes

$$n(\mathbf{r}, t) = \frac{N}{\pi^{3/2}} \prod_{j=\{x,y,z\}} \frac{a_j}{1 + ij\omega_j t} \exp \left[\frac{-j^2}{a_j^2(1 + \omega_j^2 t^2)} \right]. \quad (2.15)$$

The above expression demonstrates that at time $t = 0$, the distribution is characterized by a width along \mathbf{e}_j given by $a_j = \sqrt{\hbar/m\omega_j}$; while at time $t > \omega_j^{-1}$ the width is given by $a_j\omega_j t = \sqrt{\hbar\omega_j/m t}$. This means that a BEC in an anisotropic trap dramatically changes its aspect ratio upon expansion. In contrast, the aspect ratio of a thermal cloud, initially confined in an anisotropic trap, tends to 1 for times $t > \omega_j^{-1}$ [39]. The above results are valid when interactions can be neglected compared to the kinetic energy of the system.

2.2.2.2 Long-range phase coherence of a BEC. Long range coherence is an important characteristic of BEC. The well defined phase in a BEC allowed the observation of interference fringes [40] when overlapping with another BEC; this interference constitutes first order coherence of the matter waves. Long-range phase-coherence of a BEC to second and third order has been experimentally demonstrated via measurements of the mean-field energy of a BEC [41] and of three-body recombination rates [42], respectively.

2.3 BOSE-EINSTEIN CONDENSATION OF INTERACTING GASES

Even when the dilute trapped atom systems exhibit densities as low as $10^{13} - 10^{15}$ atoms/cm³ (5 to 6 orders of magnitude less dense than air) they are not ideal gases. Interactions play a crucial role in the experimental realization of BEC, since they are the mechanism for re-thermalization in forced evaporation processes. This section describes BEC in trapped systems in the presence of interactions.

2.3.1 The interaction Hamiltonian. We consider a total of N interacting neutral atoms confined in a trapping potential $V_{\text{ext}}(\mathbf{r})$. In the notation of second quantization, the Hamiltonian describing the interaction of such particles is given by

$$\hat{H} = \int d\mathbf{r} \hat{\Psi}^\dagger(\mathbf{r}) \left[-\frac{\hbar^2}{2m} \nabla^2 + V_{\text{ext}}(\mathbf{r}) \right] \hat{\Psi}(\mathbf{r}) + \frac{1}{2} \int d\mathbf{r} d\mathbf{r}' \hat{\Psi}^\dagger(\mathbf{r}) \hat{\Psi}^\dagger(\mathbf{r}') V(\mathbf{r} - \mathbf{r}') \hat{\Psi}(\mathbf{r}') \hat{\Psi}(\mathbf{r}); \quad (2.16)$$

where $\hat{\Psi}^\dagger(\mathbf{r})$ is the second quantization field operator for the creation of a boson at position \mathbf{r} and $V(\mathbf{r} - \mathbf{r}')$ is the two-particle interaction potential.

The time evolution of the BEC's field operator under the above interaction Hamiltonian is obtained in the Heisenberg picture, where $i\hbar \partial \hat{\Psi}(\mathbf{r}, t) / \partial t = [\hat{\Psi}, \hat{H}]$. This gives

$$i\hbar \frac{\partial \hat{\Psi}(\mathbf{r}, t)}{\partial t} = \left[-\frac{\hbar^2}{2m} \nabla^2 + V_{\text{ext}}(\mathbf{r}) + \int d\mathbf{r}' \hat{\Psi}^\dagger(\mathbf{r}', t) V(\mathbf{r}' - \mathbf{r}) \hat{\Psi}(\mathbf{r}', t) \right] \hat{\Psi}(\mathbf{r}, t). \quad (2.17)$$

To obtain a simpler version of the above equation we will assume in the following sections: (i.) that the number of particles in the condensed state is $N_0 \gg 1$; and (ii.) that the effective interaction potential between a pair of particles is that of hard-spheres, characterized by the *s*-wave scattering length a (assumed to be much smaller than the interparticle separation).

2.3.2 Mean field approximation. In the limit when $N_0 \gg 1$, we propose that the time-dependent BEC field operator has the form

$$\hat{\Psi}(\mathbf{r}, t) = \Phi(\mathbf{r}, t) + \hat{\Psi}'(\mathbf{r}, t); \quad (2.18)$$

where $\Phi(\mathbf{r}, t) \equiv \langle \hat{\Psi}(\mathbf{r}, t) \rangle$ is known as the wave function of the BEC, whose density distribution is given by $n_0(\mathbf{r}, t) = |\Phi(\mathbf{r}, t)|^2$. The term $\hat{\Psi}'(\mathbf{r}, t)$ represents the non-condensed component of the field operator, which can be treated as a small perturbation ($N_0 \gg 1$) to calculate elementary excitations. At zero temperature, where all the particles are in the condensed state, $\hat{\Psi}'(\mathbf{r}, t) = 0$.

The wave function of the BEC $\Phi(\mathbf{r}, t)$ plays the role of the order parameter of the condensate; it is a complex quantity, characterized by an amplitude and a phase:

$$\Phi(\mathbf{r}, t) = \phi(\mathbf{r}) \exp(-i\mu t/\hbar), \quad \int d\mathbf{r} \phi^2(\mathbf{r}) = N_0, \quad (2.19)$$

where μ is the chemical potential and ϕ is a real function, normalized to the total number of particles.

2.3.3 Effective interaction potential. Figure 2.4a shows the molecular potential describing the interaction between two atoms as a function of their separation distance r . This potential features three main regimes of interaction: it has a local minimum at $r = r_{\min}$, where bound states can develop; for separations $r < r_{\min}$ interactions are strong and of repulsive nature; while for $r > r_{\min}$, attractive van der Waals interactions dominate.

Given that the interaction potential $V(\mathbf{r})$ is central, angular momentum is conserved in the collisional processes and the wave functions of the angular part of the Schrödinger equation are the spherical harmonics. Low energy scattering is dominated by the $l=0$ (*s*-wave) term in the partial

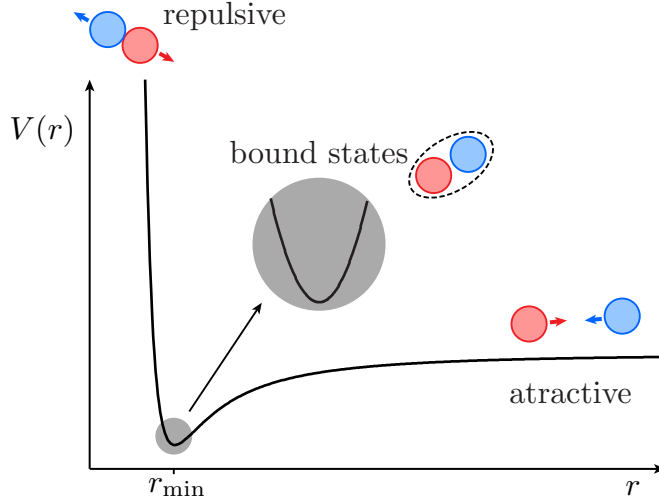


Figure 2.4: Interaction potential $V(r) \propto (1/r^2 - 1/r^6)$ between two neutral atoms as a function of their separation r . The nature of the interaction has three main regimes: for large separations $r > r_{\min}$, van der Waals interactions dominate and the particles attract each other; around the minimum of the potential $r = r_{\min}$ molecular bound states can exist; for small separations $r < r_{\min}$ the electrostatic interaction between electronic distribution of the atoms dominates, and the nature of the potential is repulsive.

wave decomposition of the scattered wave function, and its angular dependence is proportional to the lowest order spherical harmonic $Y_{00} = (4\pi)^{-1/2}$, s -wave scattering is isotropic.

A simplified model of the interaction potential, namely a hybridization between an asymptotic van der Waals potential and that of hard-core spheres, is given by

$$V(\mathbf{r}) = \begin{cases} -C_6/r^6 & \text{if } r > r_c \\ \infty & \text{if } r \leq r_c, \end{cases} \quad (2.20)$$

where the attractive van der Waals interaction with coefficient C_6 , describes the electric dipole-dipole interactions between the distribution of charge in the atoms and is cut off at a distance r_c which describes the radius of the spheres. By equating the kinetic energy of the relative motion of two atoms of reduced mass M to their interaction energy we obtain the van der Waals length scale $a_c = (2MC_6/\hbar^2)^{1/4}$, which is on the order of some nm in the alkalis. The energy scale associated with a_c is on the order of 1 mK, and it imposes an upper bound below which s -wave scattering dominates. At sub-mK temperatures, the interaction potential can be modeled as the pseudo potential $V(\mathbf{r}' - \mathbf{r}) = g\delta(\mathbf{r}' - \mathbf{r})$, where $g = 4\pi\hbar^2 a/m$ is the coupling constant, a is the s -wave scattering length and m is the mass of the particles. The van der Waals length a_c sets the scale of the scattering length a , the latter can have positive or negative values corresponding to an effective repulsion or attraction between the particles, respectively.

2.3.3.1 Scattering length. The scattering length a is the length scale which characterizes low energy (s -wave) interactions between a pair of particles. In BEC, attractive interactions ($a < 0$) make the condensate unstable if the number of particles exceeds a critical value. In contrast, BECs with repulsive interactions ($a > 0$) are stable and robust to increasing number of particles. The scattering length plays an important role in the achievement of BEC in dilute alkali gases, since it dictates the rate at which thermalization processes occur in evaporative cooling. Typical scattering lengths in the alkalis are larger than the size of the atom by about two orders of magnitude; Table 2.3 indicates approximate values of the scattering length for different alkali atoms.

At typical BEC densities ($10^{13} - 10^{15}$ atoms/cm³), the separation between the atoms is on the order of 100 nm, i.e. it is larger than the scattering length scale. While some atomic species exhibit the favorable conditions for scattering ($^{23}\text{Na}, ^{87}\text{Rb}$), others require their scattering length to be tuned via Feshbach resonances [43] in order to optimally achieve BEC.

2.3.4 The Gross-Pitaevskii equation. Assuming $N_0 \gg 1$ and contact interactions between pairs of particles (section 2.3.3), the time-dependent wave function of the BEC satisfies

$$i\hbar \frac{\partial}{\partial t} \Phi(\mathbf{r}, t) = \left[\frac{-\hbar^2}{2m} \nabla^2 + V_{\text{ext}}(\mathbf{r}) + g|\Phi(\mathbf{r}, t)|^2 \right] \Phi(\mathbf{r}, t), \quad (2.21)$$

where the particles are confined by the external potential $V_{\text{ext}}(\mathbf{r})$, and their interactions are characterized by $g=4\pi\hbar^2 a/m$, where a is the scattering length. This nonlinear differential equation is named after Gross and Pitaevskii, and it was first derived in the context of superfluid hydrodynamics [44], with particular interest on the vorticity [45, 46] of such systems. Under the mean field approximation (section 2.3.2) the Gross-Pitaevskii (GP) equation reduces to

$$\left[-\frac{\hbar^2 \nabla^2}{2m} + V_{\text{ext}}(\mathbf{r}) + g\phi^2(\mathbf{r}) \right] \phi(\mathbf{r}) = \mu\phi(\mathbf{r}). \quad (2.22)$$

There exists a length scale associated with the spatial variation of the solutions to the GP

Table 2.3: Scattering lengths of alkali atoms at zero magnetic field.

| Atom | Scattering length a [nm] |
|-------------------|----------------------------|
| ^7Li | -1.32 |
| ^{23}Na | 3.33 |
| ^{39}K | -1.53 |
| ^{85}Rb | -23.44 |
| ^{87}Rb | 5.29 |
| ^{133}Cs | 72.68 |

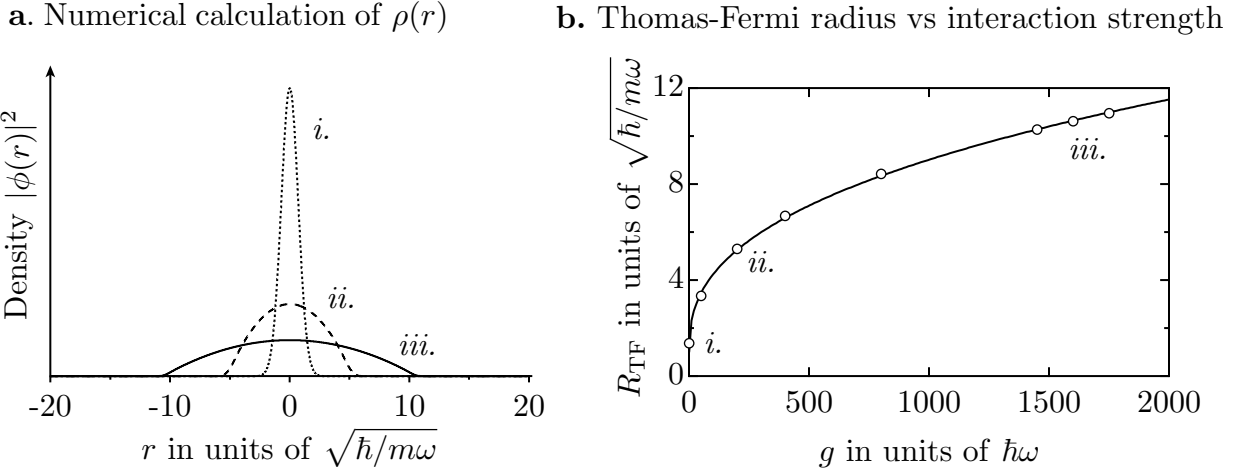


Figure 2.5: **a.** Normalized density distribution $\rho(r) = |\phi(r)|^2$ of a Bose gas in a HO trap, for different effective interaction strengths; $n(r)$ was numerically calculated using a time-splitting spectral method to solve a dimensionless version of the GP equation, as described in [47]. In the absence of interactions, the wave function corresponds to the ground state of the HO Hamiltonian and is Gaussian. As the interactions increase, $\rho(r)$ acquires the functional form of the external potential $V(r) \propto r^2$; **b.** the Thomas-Fermi radius is determined from a fit to the density distributions, and is plotted here as a function of the dimensionless interaction strength.

equation, it is derived from the balance of the interaction and the kinetic energy terms, considering the boundary conditions imposed by the external potential and the continuity of the wave function (or its derivatives). The healing length² is the length within which the wave function rises from zero to its uniform value and is given by $\xi = (8\pi\rho a)^{-1/2}$, where $\rho(\mathbf{r}) = |\phi(\mathbf{r})|^2$ is the density of the system.

2.3.5 The Thomas-Fermi approximation. In the absence of interactions the GP equation becomes the time independent Schrödinger equation; and for a 1D harmonically trapped system the wave function is a Gaussian characterized by the HO width $\sqrt{\hbar/m\omega}$, where ω is the oscillator frequency.

In contrast, when the mean field interaction energy dominates over the kinetic energy, the GP equation (2.22) is further simplified and we enter the regime of the Thomas-Fermi (TF) approximation, where the density distribution $\rho(\mathbf{r})$, reflects the shape of the trapping potential

$$\rho(\mathbf{r}) = g^{-1}[\mu - V_{\text{ext}}(\mathbf{r})], \quad (2.23)$$

when $\mu - V_{\text{ext}}(\mathbf{r}) > 0$, else $\phi^2(\mathbf{r}) = 0$; this is illustrated in Fig. 2.5a for a Bose gas with repulsive interactions, as is the case for ⁸⁷Rb atoms.

²The healing length is crucial in the description of vortices, since it gives the length scale for the size of their cores. Vortices are cylindrically symmetric solutions to the GP equation [44].

The length scale characterizing this distribution is the Thomas-Fermi radius R_{TF} , which is obtained from the condition that the chemical potential μ is equal to the external potential evaluated at R_{TF} . For the 3D harmonic oscillator potential given in Eq. (2.8), the TF radii are given by

$$R_j = \sqrt{\frac{2\mu}{m\omega_j^2}}, \quad j = x, y, z. \quad (2.24)$$

The normalization condition of the density distribution sets the relation between the total number of atoms $N \approx N_0$ and the chemical potential μ

$$\mu = \frac{\hbar\bar{\omega}}{2} \left(\frac{15Na}{\bar{a}} \right)^{2/5}; \quad (2.25)$$

where $\bar{\omega}$ and \bar{a} are the geometrical means of the frequencies of the HO and characteristic lengths. In the case of an isotropic HO trap, the above equations lead to the result that the radius of the condensate increases with the number of atoms N and the scattering length a

$$R = \bar{a} \left(\frac{15Na}{\bar{a}} \right)^{1/5}. \quad (2.26)$$

2.3.6 Dimensionless HO Hamiltonian for numerically solving the GP equation. We numerically solve the dimensionless version of the GP equation for a system in the presence of a HO potential using a time-splitting spectral method as described in [47]. We start with the Hamiltonian for a single particle in an HO potential

$$H = \frac{1}{2}m\omega^2x^2 + \frac{1}{2m}p^2; \quad (2.27)$$

and define the dimensionless variables: $x' = x/x_0$, $p' = p/p_0$, and $t' = t/t_0$; where $x_0 = \sqrt{\hbar/m\omega}$ is the characteristic HO length, $p_0 = \hbar/x_0$ and $t_0 = 2/\omega$. The dimensionless Schrödinger's equation becomes

$$i\frac{d}{dt'}\psi' = (x'^2 + p'^2)\psi'. \quad (2.28)$$

The interaction term $g|\psi|^2$ is included in the calculation by scaling the effective interaction strength g to the energy quantum $\hbar\omega$ of the HO, as shown in Fig. 2.5b.

2.4 BEC DYNAMICS IN A HARMONIC TRAP

The experimental characterization of various phenomena reported in this thesis relies on the dynamics of harmonically trapped BECs, in particular on their collective oscillation modes. In this section I focus on the origin and nature of the lowest energy collective modes of a BEC.

2.4.1 The hydrodynamic equations.

The time-dependent GP equation

$$i\hbar \frac{\partial}{\partial t} \psi = \left[\frac{-\hbar^2}{2m} \nabla^2 + V_{\text{ext}}(\mathbf{r}) + g|\psi|^2 \right] \psi, \quad (2.29)$$

is the basis for the hydrodynamics of a trapped BEC, it leads to a continuity equation for the particle density $\rho = |\psi|^2$

$$\frac{\partial \rho}{\partial t} + \nabla \cdot (\rho \mathbf{v}) = 0, \quad (2.30)$$

where $\mathbf{v} = \mathbf{j}/m\rho$ is the velocity field of the condensate, the momentum density \mathbf{j} is given by

$$\mathbf{j} = \frac{\hbar}{2i} (\psi^* \nabla \psi - \psi \nabla \psi^*). \quad (2.31)$$

If the order parameter is expressed as $\psi = f e^{i\phi}$, then the density becomes $\rho = f^2$ and the velocity field is $\mathbf{v} = \hbar \nabla \phi / m$. The latter is a particularly important result since it implies that the velocity field of a BEC is irrotational, namely

$$\nabla \times \mathbf{v} = \frac{\hbar}{m} \nabla \times \nabla \phi = 0, \quad \text{if } \phi \neq 0. \quad (2.32)$$

This condition imposes constraints on the possible motions that the BEC can develop.

The equations of motion for the amplitude and the phase of the order parameter $\psi = f e^{i\phi}$ are found from the GP equation, by separation of the real and imaginary parts

$$-\hbar \frac{\partial \phi}{\partial t} = -\frac{\hbar^2}{2mf} \nabla^2 f + \frac{1}{2} mv^2 + V_{\text{ext}}(\mathbf{r}) + gf^2, \quad (2.33)$$

$$\frac{\partial f^2}{\partial t} = -\frac{\hbar}{m} \nabla \cdot (f^2 \nabla \phi). \quad (2.34)$$

The latter equation corresponds to Eq. (2.30) expressed in the variables f and ϕ . To find the equation of motion for the velocity field $\mathbf{v} = \nabla \phi$, we take the gradient of Eq. (2.33) and get

$$m \frac{\partial \mathbf{v}}{\partial t} = -\nabla(\tilde{\mu} + \frac{1}{2} mv^2), \quad \text{where} \quad \tilde{\mu} = V_{\text{ext}} + g\rho - \frac{\hbar^2}{2m\sqrt{\rho}} \nabla^2 \sqrt{\rho}. \quad (2.35)$$

At constant temperature we use the Gibbs-Duhem relation $dp = n d\mu$, to associate changes in the chemical potential with changes in the pressure p and obtain from the above equations

$$\frac{\partial \mathbf{v}}{\partial t} = -\frac{1}{mn} \nabla p - \nabla \left(\frac{v^2}{2} \right) + \frac{1}{m} \nabla \left(\frac{\hbar^2}{2m\sqrt{\rho}} \nabla^2 \sqrt{\rho} \right) - \frac{1}{m} \nabla V_{\text{ext}}, \quad (2.36)$$

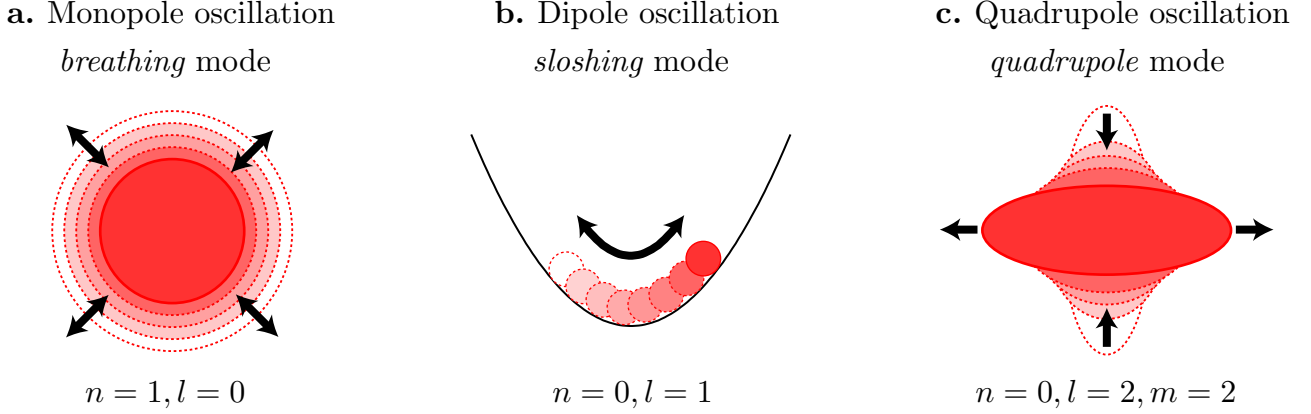


Figure 2.6: Schematic of lowest energy elementary excitations in a BEC. **a.-c.** The *breathing* and *quadrupole* modes correspond to shape oscillations while **b.** the dipole mode corresponds to the center of mass *sloshing* in the trap.

given $\mu = g\rho$ and $p = g\rho^2/2$. If we consider an ideal fluid of density ρ and velocity \mathbf{v} , Eqs. (2.30) and (2.36) almost exactly correspond to its hydrodynamic equations of motion. An ideal fluid is described by the Euler equation

$$\frac{\partial \mathbf{v}}{\partial t} - \mathbf{v} \times (\nabla \times \mathbf{v}) = -\frac{1}{mn} \nabla p - \nabla \left(\frac{v^2}{2} \right) - \frac{1}{m} \nabla V_{\text{ext}}. \quad (2.37)$$

Assuming that the fluid is irrotational, then the difference between the Euler equation and Eq. (2.36) is the term

$$\frac{1}{m} \nabla \left(\frac{\hbar^2}{2m\sqrt{\rho}} \nabla^2 \sqrt{\rho} \right), \quad (2.38)$$

known as the quantum pressure term; this term is associated with spatial variations of the density of the condensate. The origin of the quantum pressure term, as well as of the term $\nabla(v^2/2)$ in Eq. (2.36), is the kinetic energy in the GP equation; while the latter term is related to the actual motion of particles, the quantum pressure does not originate particle currents.

By comparing the pressure terms in Eq. (2.36), assuming that the order parameter varies over a length scale η , we get

$$\frac{1}{mn} \nabla p = \frac{1}{m} \nabla(g\rho) \approx \frac{g\rho}{m\eta} = \frac{\hbar^2}{2m^2\xi^2\eta}, \quad \text{and} \quad \frac{1}{m} \nabla \left(\frac{\hbar^2}{2m\sqrt{\rho}} \nabla^2 \sqrt{\rho} \right) \approx \frac{\hbar^2}{2m^2\eta^3}. \quad (2.39)$$

Thus if η is much greater than the healing length ξ , the quantum pressure term can be neglected; this is the case in ^{87}Rb BECs, whose typical healing lengths are on the order of hundreds of nm, while the spatial extent of their wave functions is a few μm .

2.4.2 Elementary excitations of the BEC. To determine the nature of the elementary excitations of a BEC we will consider small deviations $\delta\rho$ from the equilibrium state of the density ρ_0 , namely $\rho=\rho_0+\delta\rho$, in order to solve Eqs. (2.30) and (2.35).

2.4.2.1 The Thomas-Fermi limit. Whenever interactions dominate over the kinetic energy, the quantum pressure can be neglected. This is associated with the fact that the spatial variation η of the wave function is much greater than the healing length ξ , as we learned above, and thus it is reasonable to look for modes whose spatial variations (wavelength) are actually comparable to η .

Substituting $\rho=\rho_0+\delta\rho$ in Eqs. (2.30) and (2.35), and assuming that the velocity \mathbf{v} and the deviation $\delta\rho$ are small quantities, we obtain

$$m\frac{\partial^2\delta\rho}{\partial t^2}=\nabla\cdot(\rho_0\nabla\delta\tilde{\mu}), \quad (2.40)$$

where $\delta\tilde{\mu}=g\delta\rho$. In the TF approximation, we assume that the equilibrium density is $\rho_0=g^{-1}[\mu-V_{\text{ext}}(\mathbf{r})]$, and assume that the density variations have a time dependence of the form $\delta\rho\propto e^{-i\omega t}$, then Eq. (2.40) becomes

$$\omega^2\delta\rho=\frac{1}{m}\{\nabla V_{\text{ext}}\cdot\nabla\delta\rho-[\mu-V_{\text{ext}}(\mathbf{r})]\nabla^2\delta\rho\}. \quad (2.41)$$

For trapped atoms under isotropic harmonic oscillator confinement $V_{\text{ext}}(\mathbf{r})=m\omega_0^2r^2/2$, with TF radius $R_{\text{TF}}=2\mu/m\omega^2$, Eq. (2.41) reduces to [48]

$$\omega^2\delta\rho=-\frac{\omega_0^2}{2}\nabla(R_{\text{TF}}^2-r^2)\nabla\delta\rho; \quad (2.42)$$

which allows for solutions of the form $\delta\rho=P_l^{2n}(r/R_{\text{TF}})r^lY_{lm}(\theta,\phi)$, defined in the regime $0\leq r\leq R_{\text{TF}}$; where the functions $P_l^{2n}(r/R_{\text{TF}})$ are polynomials of degree $2n$, which contain only even powers of their argument r/R_{TF} . The solutions' angular momentum and their corresponding projection along \mathbf{e}_z are labeled by l and m , respectively; n represents the radial quantum number. In the TF approximation (interaction dominated limit), the natural frequencies for the collective oscillations are given by

$$\omega(n,l)=\omega_0\sqrt{2n^2+2nl+3n+l}. \quad (2.43)$$

The three $n=0, l=1$ dipole modes correspond to *sloshing* in the trap at the trap frequency ω_0 , these modes involve the spatial translation of the cloud, whose structure remains unperturbed in the linear regime. The result can be generalized to an anisotropic trap, thus sloshing in each spatial direction occurs at the corresponding trap frequency. This is the primary mechanism with which we characterize the trapping frequencies of the confining potentials used in our experiments. Most recently we studied a *quadrupole*-like shape-oscillation mode ($n=0, l=2$) to probe the transport

properties of a BEC in an artificial gauge field [8].

It is important to highlight that in contrast with the monopole and quadrupole modes, the dipole mode is independent of interactions [48, 49].

2.4.2.2 Non-interacting limit. The TF approximation breaks down in the limit of large n and l , where the rapid variations of the density ρ can no longer be neglected. In this kinetic-energy dominated limit (collisionless, non-interacting limit) the frequencies of the oscillation modes occur at integer multiples of the trap frequencies [48, 50]. Table 2.4 summarizes basic properties of the lowest energy collective oscillations present in a BEC, both in the interacting and in the non-interacting limits.

2.5 EXPERIMENTAL REALIZATION OF BEC

The experimental realization of BEC in dilute alkali gases is the result of a sequence of stages in which the temperature of an atomic sample is reduced to the point of quantum degeneracy. The process to reach BEC involves the combination of various experimental techniques (see Chapter 3); in this section I give an overview of the process to reach BEC.

As seen at the beginning of this Chapter, I want to emphasize that achieving BEC is not only a matter of decreasing temperature but also of increasing phase space density above a critical value to reach the condition of quantum degeneracy.

Laser cooling allows one to decrease the thermal energy of an atomic sample down to the μK regime, where the atoms move slowly enough to be held by magnetic or electric dipole forces in a trap. Once in the magnetic trap, the atoms are evaporatively cooled via rf-induced transitions, a process which effectively decreases the trap depth and allows the most energetic atoms escape, while the remaining ones are allowed to re-thermalize and reach lower temperatures, about tens of μK .

The atoms are then transferred from the magnetic quadrupole trap into an optical dipole trap, in a process that is optimized to preserve phase space density, and continue the path to quantum degeneracy. Evaporatively cooling is achieved by reducing the power in the optical trap, and temperatures down to tens to hundreds of nK are reached.

Table 2.4: Lowest energy collective oscillation modes in a homogeneous HO trap.

| n | l | ω/ω_0 | Non-Interacting ω/ω_0 | Oscillation mode |
|-----|-----|-------------------|---------------------------------------|-------------------------------|
| 1 | 0 | $\sqrt{5}$ | $\sqrt{5 - E_{\text{kin}}/E_{HO}}$ | Monopole (<i>breathing</i>) |
| 0 | 1 | 1 | 1 | Dipole (<i>sloshing</i>) |
| 0 | 2 | $\sqrt{2}$ | $\sqrt{2(1 + E_{\text{kin}}/E_{HO})}$ | Quadrupole |

In order to achieve ultracold temperatures, the atoms need to be isolated from the environment. Even when magnetic and optical traps already succeed in breaking thermal contact between the atoms and material surfaces, extreme isolation is required to the degree that the atoms are prevented from colliding with surrounding energetic particles, since this might induce losses from the trap.

Ultracold atom experiments require vacuum chambers, operated under ultrahigh vacuum (UHV) to prevent collisions between the BEC and the background gas inside the chamber and to achieve long lifetimes. Typical pressures in ultracold atom experiments are within $10^{-11} - 10^{-12}$ Torr³.

³As a reference for vacuum 1 bar \approx 1 atm and 1 Torr = 1.3 mbar; the UHV required ranges from $10^{-14} - 10^{-15}$ atm.

CHAPTER 3

LASER COOLING AND TRAPPING ULTRACOLD NEUTRAL ATOMS

In this chapter I will focus on the physics of laser cooling, magnetic trapping, optical trapping and evaporative cooling of alkali atomic samples. These fundamental techniques are combined in our experiments to reach the quantum degeneracy of atomic samples of ^{87}Rb .

First I will discuss the particular atomic structure of ^{87}Rb , then I will describe the laser cooling of a thermal atomic beam, followed by the mechanism of magnetic trapping and the collection of atoms in a magneto-optical-trap (MOT); next I will focus on the concepts of optical molasses, optical pumping and on the evaporation schemes in both the magnetic and the optical traps used in our experiments. Finally I will describe the absorption imaging detection scheme.

3.1 ALKALI ATOMS AND THE ELECTRONIC STRUCTURE OF ^{87}Rb

Alkali metals (Li, Na, K, Rb, Cs and Fr) compose Group I of the periodic table of elements. They are characterized by possessing a single valence electron, a feature that simplifies their comprehension and manipulation. The valence electron is described by its orbital angular momentum \mathbf{L} and spin \mathbf{s} ; these vectors couple via the spin-orbit interaction and give rise to the total angular momentum of the electron, $\mathbf{J} = \mathbf{L} + \mathbf{s}$. In the Ls -coupling scheme, the electronic configuration of an atom can be determined as $n^{2s+1}L_J$, where n is the principal quantum number, and s, L, J stand for the electron's spin, orbital and total angular momentum quantum numbers. By convention we label the values of orbital angular momentum with letters: $L = S, P, D, F, \dots$ which stand for $L = 0, 1, 2, 3, \dots$, respectively. In its lowest energy configuration the electron has $L = 0$, its total angular momentum is $J = 1/2$. Due to the hyperfine interaction $H_{\text{hfs}} = A_{\text{hfs}}\mathbf{I} \cdot \mathbf{J}$, the nuclear spin \mathbf{I} and the total angular momentum \mathbf{J} of the electron couple to produce the total angular momentum $\mathbf{F} = \mathbf{I} + \mathbf{J}$. The magnetic dipole constant A_{hfs} corresponds to the ground state manifold.

The experiments described in this thesis were realized with ^{87}Rb , the longest-lived metastable¹ isotope² of rubidium. The coupling between orbital and spin angular momenta is responsible for

¹Given that the half-life of ^{87}Rb is 4.88×10^{10} years, it can be considered stable for practical purposes.

²A total of 50 neutrons and 37 protons live in the nucleus of ^{87}Rb . In combination with its 37 electrons, a total of 124 fermions compose a ^{87}Rb atom.

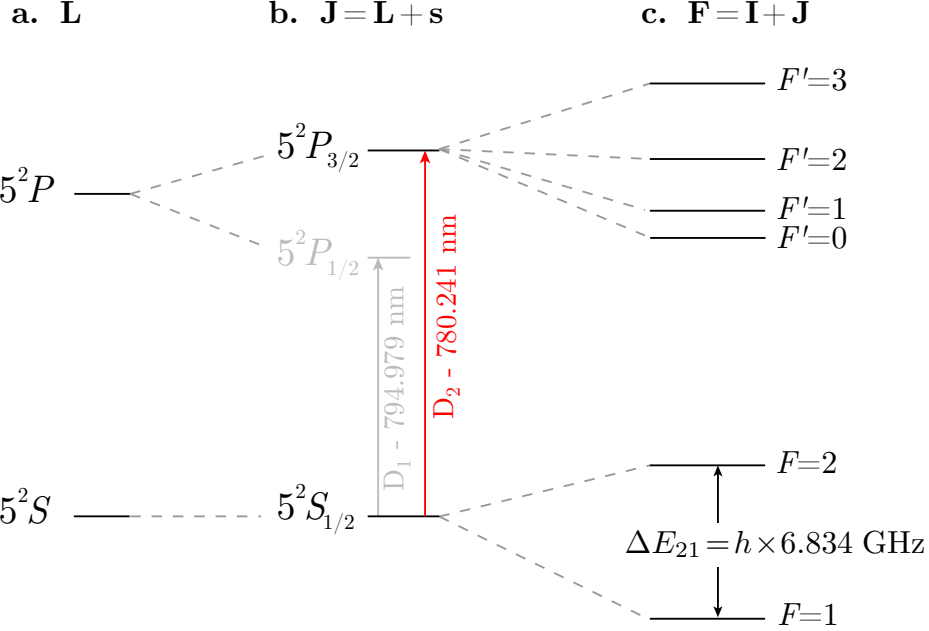


Figure 3.1: Hyperfine structure of ^{87}Rb . **a.** The lowest energy electronic configurations of ^{87}Rb correspond to $L = S, P$. **b.** In the Ls -coupling scheme fine structure emerges, lifting the degeneracy between states with different total angular momentum $\mathbf{J} = \mathbf{L} + \mathbf{s}$. Indicated are the allowed $\Delta L = 1$ electric dipole transitions $D_1: 5^2P_{1/2} \rightarrow 5^2S_{1/2}$ (light arrow) and $D_2: 5^2P_{3/2} \rightarrow 5^2S_{1/2}$ (dark arrow). **c.** The interaction with the nuclear spin further splits the fine levels and gives rise to the hyperfine structure (not shown for $5^2P_{1/2}$). The atom's total angular momentum is $\mathbf{F} = \mathbf{I} + \mathbf{J}$. The magnetic dipole constant associated with the ground state manifold $A_{\text{hfs}} = h \times 3.417 \text{ GHz}$, leads to the ΔE_{21} splitting between $F = 2$ and $F = 1$.

the fine structure, and gives rise to the lowest energy electronic configurations $5^2S_{1/2}$, $5^2P_{1/2}$ and $5^2P_{3/2}$. In turn, the interaction with the nuclear spin $I = 3/2$ further splits the energy levels and reveals the hyperfine structure, as shown in Figure 3.1. Each hyperfine state F contains $2F + 1$ spin energetically degenerate states $m_F = -F, -F + 1, \dots, F$. The Zeeman interaction between an external magnetic field and the magnetic moment of the atom lifts the degeneracy of the hyperfine m_F sub-states as described in Sec. 3.8.

3.2 INTERACTION OF ELECTROMAGNETIC RADIATION AND MATTER

The next section describes the interaction between electromagnetic radiation and matter and the physics of laser cooling and trapping.

In these experiments we deal with the interaction between electromagnetic radiation and atoms. In particular we focus on traveling plane waves of electromagnetic radiation³ whose electric and mag-

³A solution to Maxwell's equations in a medium free of electric charge and current is a traveling plane wave of electromagnetic radiation [51].

netic fields are given by

$$\mathbf{E}(\mathbf{r}) = \epsilon E \exp(i\mathbf{k} \cdot \mathbf{r} - i\omega t) \quad (3.1)$$

$$\mathbf{B}(\mathbf{r}) = \frac{n}{c} \frac{\mathbf{k} \times \mathbf{E}}{k} \quad (3.2)$$

where n is the index of refraction of the medium, c is the speed of light, $k = 2\pi/\lambda$ is the wavenumber, λ is the wavelength, and the wave vector \mathbf{k} defines the direction of propagation. In the laboratory, the sources of such fields are lasers and oscillating electrical currents.

The oscillating electric field of electromagnetic radiation induces an effective dipole moment $\mathbf{d} = -e\mathbf{r}$, where e is the electronic charge and \mathbf{r} its spatial coordinate with respect to the center of mass of the atom, via which the electric field can drive electronic transitions in the atom described by the interaction Hamiltonian $H_E = -\mathbf{d} \cdot \mathbf{E}$. Correspondingly, the oscillating magnetic field interacts with the magnetic moment μ of the atom, a quantity proportional to its total angular momentum \mathbf{F} , and is responsible for driving hyperfine transitions described by the interaction Hamiltonian $H_B = -\mu \cdot \mathbf{B}$. Even when both the electric and the magnetic field coexist together, each can only drive certain transitions in accordance to their angular momentum selection rules; e.g. $\mathbf{E}(\mathbf{r})$ drives parity-changing transitions, while $\mathbf{B}(\mathbf{r})$ can induce transitions between states of the same parity. This will be discussed in more detail in Sec. 3.3.

Optical dipole transitions are of relevance to laser cooling and trapping, while rf-magnetic transitions are useful to perform rf-induced evaporation in a magnetic trap as well as for the manipulation of the hyperfine sub-levels. The electric dipole and the magnetic dipole interactions are described in Sec. 3.4 and Sec. 3.8, respectively.

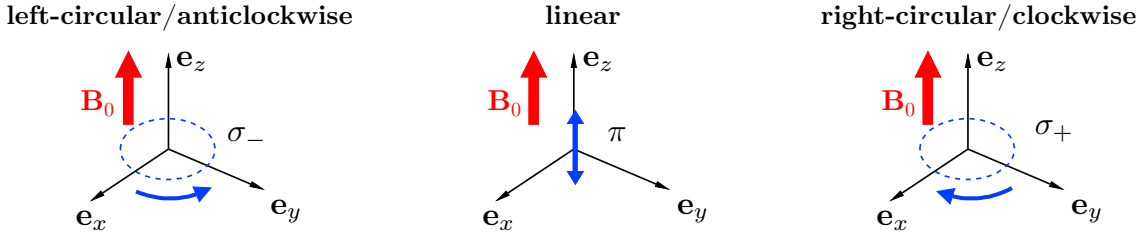
3.2.1 The quantization axis and the polarization of electromagnetic fields. In the presence of a uniform magnetic field, the magnetic moment μ of an atom tends to align with the field. This phenomenon defines an axis along which the projection of the angular momentum is quantized. A uniform magnetic field establishes a quantization axis for the atoms, and the standard choice for the direction of the quantization axis is along \mathbf{e}_z , since the formalism of the quantization of angular momentum is already well established in such notation.

The polarization of an electromagnetic field is defined by the way in which the fields oscillate, and it can be specified in a meaningful way in reference to the quantization axis⁴. A convenient basis of vectors to express the polarization is the one given by the irreducible spherical vectors:

$$\mathbf{e}_{-1} = \frac{\mathbf{e}_x - i\mathbf{e}_y}{\sqrt{2}}, \quad \mathbf{e}_0 = \mathbf{e}_z, \quad \mathbf{e}_{+1} = -\frac{\mathbf{e}_x + i\mathbf{e}_y}{\sqrt{2}}. \quad (3.3)$$

⁴The direction of propagation of the radiation is also to be considered when determining the direction of polarization.

a. Field polarization with respect to the quantization axis



b. Linear polarization as a balanced superposition of σ_+ and σ_-

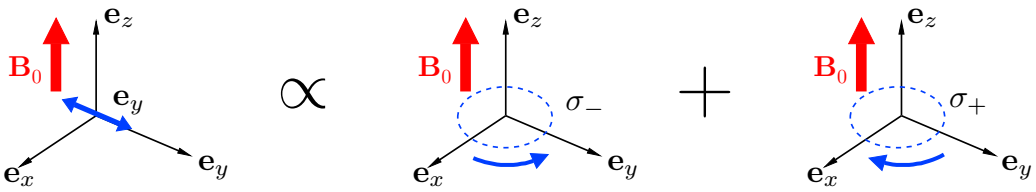


Figure 3.2: The quantization axis and the polarization of the electromagnetic field. **a.** In the presence of a uniform magnetic field \mathbf{B}_0 , the magnetic moment of an atom tends to align with the field and a quantization axis is defined (here along z). In terms of the irreducible spherical vectors, the polarization of light can be decomposed as: left-circularly polarized (σ_-), linearly polarized along the quantization axis (π) and right-circularly polarized (σ_+). **b.** Linearly polarized light orthogonal to the quantization axis can be decomposed as an equal superposition of right- and left-circularly polarized light, e.g. $\mathbf{e}_y = i(\mathbf{e}_{-1} + \mathbf{e}_{+1})/\sqrt{2}$.

In such basis, the radiation can be categorized as: σ_- -polarized, when the field is left-circularly polarized with respect to the quantization axis, π -polarized, when the field is linearly polarized along the quantization axis; and σ_+ -polarized, when the field is right-circularly polarized with respect to the quantization axis, as indicated in Fig. 3.2. Due to the selection rules arising from angular momentum considerations (see Sec. 3.3), it becomes clear that σ_{\pm} -transitions change the magnetic quantum number by $\Delta m = \pm 1$ and that π -transitions imply $\Delta m = 0$. These concepts are useful when designing actual experiments and for the understanding of more complex processes such as two-photon Raman transitions. Finally, denoting the polarization of light by $q = -1, 0, +1$, the following identities are satisfied by the polarization vectors

$$i\mathbf{e}_q^* \times \mathbf{e}_q = -q\mathbf{e}_0, \quad i\mathbf{e}_0^* \times \mathbf{e}_q = q\mathbf{e}_q, \quad i\mathbf{e}_q^* \times \mathbf{e}_0 = -q\mathbf{e}_{-q}. \quad (3.4)$$

3.3 ANGULAR MOMENTUM SELECTION RULES

Angular momentum selection rules can be used to determine whether two states are coupled by the laser light without extensive calculations. In this section we discuss the selection rules for the electric dipole interaction⁵.

Under the central field approximation, the wavefunction of an hydrogen-like (single valence electron) atom can be separated as the product of a radial part and an angular part

$$|nlm\rangle = R_{n,l}(r)Y_{lm}(\theta, \phi), \quad (3.5)$$

where (r, θ, ϕ) are the spherical coordinates and $Y_{lm}(\theta, \phi)$ are the spherical harmonics. In this section we use such hydrogen-like wavefunctions to establish the selection rules for dipole transitions between different electronic states.

As discussed above, the interaction between an atom and an external electric field occurs via the induced electric dipole moment on the atom, and is described by the perturbative Hamiltonian $H' = -\mathbf{d} \cdot \mathbf{E}$, where $\mathbf{d} = -er$ is the induced electric dipole moment. The dipole matrix element between the ground state $|g\rangle = |nlm\rangle$ and an excited state $|e\rangle = |n'l'm'\rangle$ is given by

$$d_{eg} = -e \int R_{n'l'}(r) Y_{l'm'}(\theta, \phi) \mathbf{r} \cdot \hat{\epsilon} R_{nl}(r) Y_{lm}(\theta, \phi) d^3\mathbf{r}. \quad (3.6)$$

In the basis of irreducible spherical vectors defined in Eq. (3.3), the argument of the dipole matrix element reduces to $\mathbf{r} \cdot \hat{\epsilon} = \mathbf{r} \cdot \mathbf{e}_q = r Y_{1,q}(\theta, \phi) \sqrt{4\pi/3}$, where $q = -1, 0, +1$ indicates the polarization of the electric field. The above equation becomes

$$d_{eg} = -e \int R_{n'l'}(r) r R_{nl}(r) r^2 dr \int Y_{l'm'}(\theta, \phi) \sqrt{\frac{4\pi}{3}} Y_{1,q}(\theta, \phi) Y_{lm}(\theta, \phi) \sin \theta d\theta d\phi; \quad (3.7)$$

or in short notation $d_{eg} = \mathcal{R}_{n'l',nl} \mathcal{A}_{l'm',lm}$. In most cases, the radial part $\mathcal{R}_{n'l',nl}$, contributes a numerical factor which determines the coupling strength of a transition. The angular part $\mathcal{A}_{l'm',lm}$ is interesting for it provides the angular momentum selection rules, and has important implications with regards to parity which we shall discuss first.

3.3.1 Parity. The parity operation inverts the spatial coordinates, under the parity operator, $\hat{P}\mathbf{r} = -\mathbf{r}$. If a system is not modified under the parity operation, it is said to be symmetric with respect to parity. The eigenfunctions of the parity operator satisfy $\hat{P}\psi = \lambda_p \psi$, where $\lambda_p = \pm 1$. The spherical harmonics are eigenfunctions of the parity operator satisfying $\hat{P}Y_{lm} = (-1)^l Y_{lm}$; electronic states whose orbital angular momentum quantum number l is even (odd) have even (odd) parity.

⁵The selection rules for magnetic transitions can be determined by a very similar treatment.

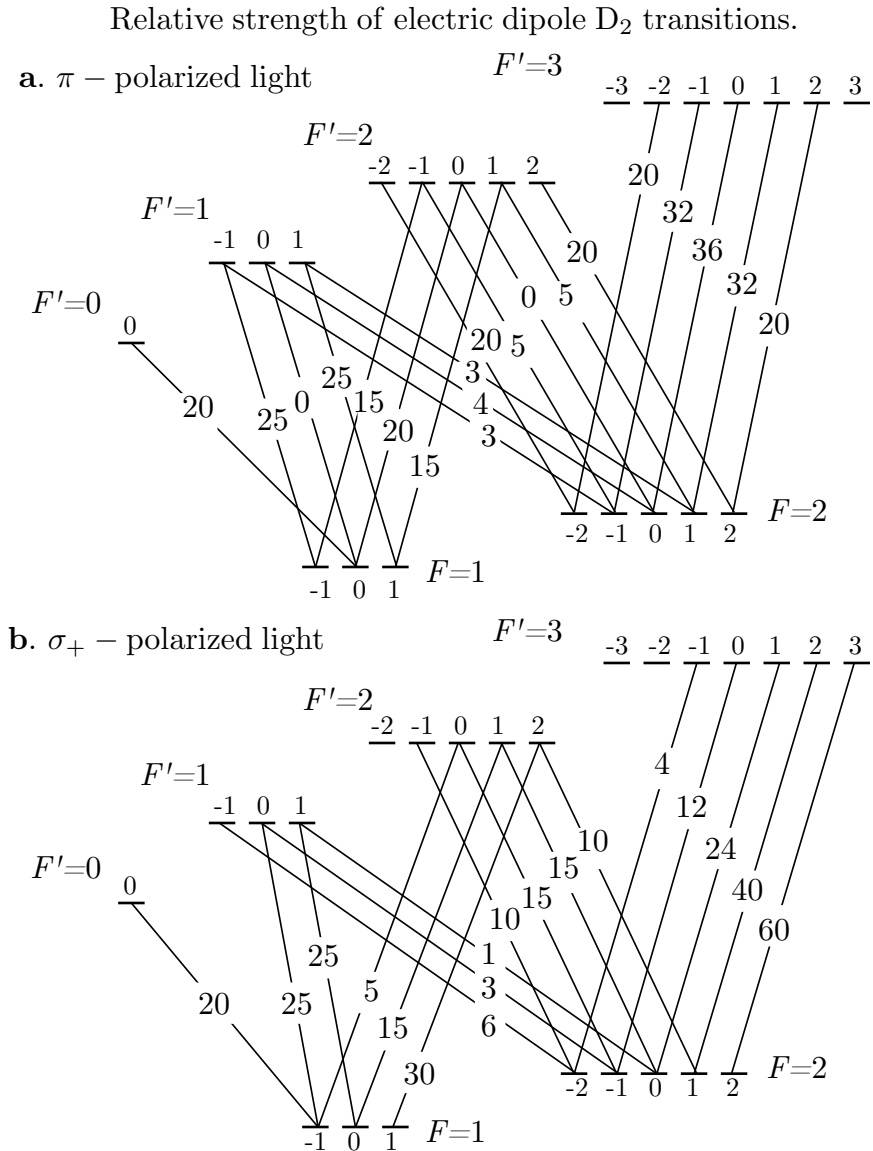


Figure 3.3: Relative strength of electric dipole D₂ transitions. The above relative strengths were calculated from the angular part of Eq. (3.9), considering alkali atoms with nuclear momentum $I = 3/2$ and both **a.** linear ($q = 0$) and **b.** right-circular ($q = +1$) polarized light. From a symmetry argument, the relative strengths for left-circularly polarized light are obtained by replacing m_F by $-m_F$ in **b.** The strengths were normalized with respect to the smallest allowed transition.

Since the angular integral of the dipole matrix element $\mathcal{A}_{l'm',lm}$ is invariant under parity, we obtain $\mathcal{A}_{l'm',lm} = (-1)^{l'+l+1} \mathcal{A}_{l'm',lm}$, meaning that the integral will vanish unless $l' + l + 1$ is even, or equivalently, if the initial and final states have opposite parity. To be concrete, the allowed electric dipole transitions are those for which $\Delta l = \pm 1$, e.g. $5^2S \rightarrow 5^2P$ where $\Delta l = l' - l = 1$.

3.3.2 Angular momentum. The theory of angular momentum has been well developed [52], so that the insights from the angular integral can be explored. The angular integral $\mathcal{A}_{l'm',lm}$ can be reduced to

$$\begin{aligned}\mathcal{A}_{l'm',lm} &= \int Y_{l'm'}(\theta, \phi) \sqrt{\frac{4\pi}{3}} Y_{1,q}(\theta, \phi) Y_{lm}(\theta, \phi) \sin \theta d\theta d\phi, \\ &= \sqrt{(2l'+1)(2l+1)} \begin{pmatrix} l' & 1 & l \\ 0 & 0 & 0 \end{pmatrix} \begin{pmatrix} l' & 1 & l \\ m' & q & m \end{pmatrix},\end{aligned}$$

where both the arrays of quantum numbers displayed in parentheses are known as Wigner's $3j$ -symbols. The first $3j$ -symbol is zero unless $l' + l + 1$ is even, giving the parity selection rule: $\Delta l \neq 0$, as discussed above; specifically, the triangle inequality $|l - 1| \leq l' \leq l + 1$ must be satisfied. Further simplification of the above equation leads to

$$\mathcal{A}_{l'm',lm} = (-1)^{l'-m'} \sqrt{\max(l, l')} \begin{pmatrix} l' & 1 & l \\ -m' & q & m \end{pmatrix}. \quad (3.8)$$

The angular integral vanishes unless $m' = q + m$; this is now related to the polarization of light. Circularly polarized light $q = \pm 1$ is able to drive transitions which change the magnetic quantum number by $\Delta m = m' - m = \pm 1$, while π -polarized light ($q = 0$) leaves it unchanged.

For the laser cooling of alkali atoms, we are interested in the transitions between hyperfine levels $|g\rangle = |F, m_F\rangle$ and $|d\rangle = |F', m'_F\rangle$, where $\mathbf{F} = \mathbf{I} + \mathbf{J}$ is the total angular momentum of the atom and $\mathbf{J} = \mathbf{L} + \mathbf{S}$ is the total angular momentum of the valence electron as discussed in Sec. 3.1. Generalizing the dipole matrix element to consider the hyperfine structure involves the expression of the eigenfunctions in the F -basis in terms of the uncoupled (I, J) -basis, which introduces angular momentum coefficients⁶ involving I, J and F . In turn, when expressing the J -basis in terms of the

⁶When coupling two or more angular momenta, Clebsch-Gordan coefficients and their generalization into $3j$ -symbols and $6j$ -symbols arise.

uncoupled (L, S) -basis, coefficients emerge now related to L, S and J . The final result is

$$\begin{aligned} d_{eg} = & e(-1)^{1+L'+S+J+J'+1-m_F} \langle \alpha' L' || r || \alpha L \rangle \\ & \times \sqrt{(2J+1)(2J'+1)(2F+1)(2F'+1)} \\ & \times \left\{ \begin{array}{ccc} L' & J' & S \\ J & L & 1 \end{array} \right\} \left\{ \begin{array}{ccc} J' & F' & I \\ F & J & 1 \end{array} \right\} \left(\begin{array}{ccc} F & 1 & F' \\ m_F & q & -m_{F'} \end{array} \right); \end{aligned} \quad (3.9)$$

where $\langle \alpha' L' || r || \alpha L \rangle$ is the reduced matrix element that comes from the radial part of the wave function and α represents all other properties of the wave function besides its angular momentum L ; the arrays of quantum numbers in braces are known as $6j$ -symbols, and provide the rules for electric dipole transitions within hyperfine sub-levels. From the $3j$ -symbol we get the triangular condition $|F-1| \leq F' \leq F+1$, indicating $\Delta F = F' - F = 0, \pm 1$; similarly we get the condition for the polarization of light $\Delta m_F = m_{F'} - m_F = q$.

The relative strength of a specific electric dipole transition between the hyperfine levels can be calculated from the magnitude square of the angular part of Eq. (3.9). Figure 3.3 shows the calculated relative strengths of D_2 ($5^2S_{1/2} \rightarrow 5^2P_{3/2}$) dipole transitions between hyperfine sub-levels, for alkali atoms with nuclear momentum $I = 3/2$ (${}^7\text{Li}$, ${}^{23}\text{Na}$, ${}^{39}\text{K}$, ${}^{41}\text{K}$ and ${}^{87}\text{Rb}$).

3.3.3 Angular momentum selection rules and laser cooling. Laser cooling relies on the efficient transfer of momentum from radiation to matter, via the absorption and emission of photons. Given the typical velocities of the atoms at the beginning of the cooling process⁷, and the magnitude of the momentum from a single photon on resonance with the atomic transition ($v_{\text{rec}} \approx 6 \text{ mm/s}$), it requires thousands of such interactions between the laser field and an atom to bring a single ${}^{87}\text{Rb}$ atom to rest.

The selection rules for angular momentum play an important role in laser cooling since they allow the identification of suitable transitions (cooling transitions) to achieve the required large number of scattering events. The strength of the transition has to be sufficiently high, and since the atoms have to undergo a large number of absorption and spontaneous emission cycles, the decay from the excited state to the ground state must be only to the sublevel coupled by the light. This restricts the number of possible cooling transitions.

The selection rule $\Delta F = 0, \pm 1$, when applied to alkali metal atoms, allows the decay of one excited state to any allowed hyperfine ground state, which might not be coupled by the laser light back to an excited state, since the spectral width of the laser is generally much smaller than the

⁷The initial temperature of the atomic vapor of ${}^{87}\text{Rb}$ as it emerges from the oven in our experiment is about $T = 400\text{K}$, which corresponds to a mean velocity $v = \sqrt{2k_B T/m} = 276 \text{ m/s}$; here k_B is Boltzmann constant and m is the atomic mass.

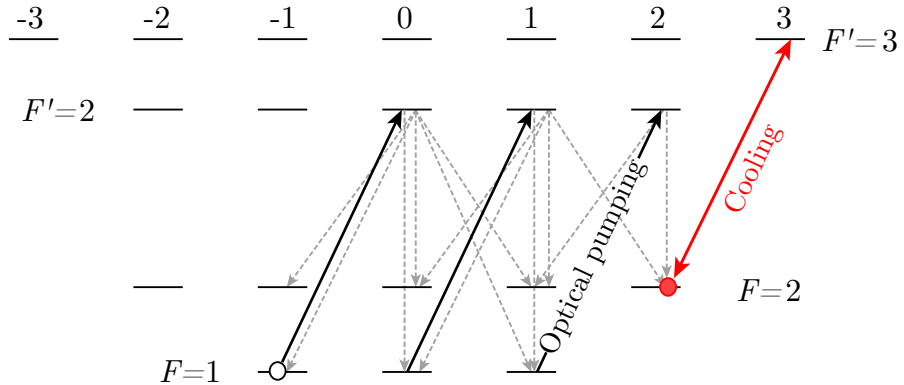


Figure 3.4: Optical pumping and cooling transitions. Standard hyperfine states F , F' and sublevels $m_F, m_{F'}$ relevant for laser cooling. For atoms in the $F = 1$ ground state a σ_+ polarized laser, on resonance with the $F = 1 \rightarrow F' = 2$ transition, is required to pump and maintain the system in the $|F = 2, m_F = 2\rangle$ hyperfine sub-level in preparation for laser cooling. The open symbol represents the initial state, and the closed symbol indicates the final state after optical pumping. The dashed lines indicate all allowed decays.

ground state hyperfine splitting⁸. However, for states with $J=L+1/2$, the decay from the highest F' -state can only occur to the largest F -state, since the other ground state has $F=F'-2$ (i.e. is a forbidden transition). The states of maximum total angular momentum form an effective two level system suitable for laser cooling. Figure 3.3 shows that the dipole transitions between the ground and excited states whose total angular momentum is the highest form an effective two level system (when the polarization is σ_+) and are associated with the largest transition strengths. Laser cooling is typically carried out on the highest F and F' states, in our case this is $F=2 \rightarrow F'=3$.

3.3.4 Optical pumping. Often it is the case that a cooling laser can induce off resonant transitions to the $F' = 2$ state, from which the atoms can decay to either of the two ground states $F=1, 2$. Since the ground state hyperfine splitting is larger than the typical spectral width of a laser (100 kHz to 1 MHz), atoms that decay to the $F = 1$ state are no longer coupled by the laser field; as a consequence all atoms will be out of the cooling transition in the long term. For laser cooling to be successful, the atoms need to be pumped back into $|F = 2, m_F = 2\rangle$; the mechanism to achieve this is known as optical pumping. Optical pumping is the process by which multiple absorption and emission events transfer the atoms into a particular hyperfine sub-level. Figure 3.3.4 illustrates a particular optical pumping scheme of great relevance for our experiments. Atoms in the $|F = 1, m_F = -1\rangle$ hyperfine state are illuminated by a circularly-polarized σ_+ laser field. In accordance with selection rules and the relative strengths of dipole transitions, the atoms undergo a sequence of absorption and spontaneous emission events which favor the population of the

⁸Optical pumping (see Sec. 3.3.4) is a mechanism via which this can be overcome.

$|F=2, m_F=2\rangle$ hyperfine sub-level. Once the atoms are optically pumped into $|F=2, m_F=2\rangle$, a laser in resonance with the $F=2 \rightarrow F'=3$ transition is used to slow down the atoms, or to perform resonant absorption imaging (see Sec. 3.7).

3.4 INTERACTION BETWEEN ATOMS AND ELECTRIC FIELDS

In this section we study the perturbative effect of the interaction between an atom and an external electric field $\mathbf{E} = \mathcal{E}_0 \hat{\epsilon}$. The electric field induces an electric dipole moment $\mathbf{d} = -e\mathbf{r}$ on the atom and leads to the interaction Hamiltonian $H' = -\mathbf{d} \cdot \mathbf{E}$ [53, 39, 54, 55]. This expression relies on the dipole approximation, and it assumes that electric field varies very little within the spatial extent of the atom, i.e. that $\lambda \gg r$, where λ is the wavelength of the electric field.

In the limit of small magnetic field, where the atomic states are described in terms of the total angular momentum $|nFm_F\rangle$, the interaction Hamiltonian H' can be expressed as

$$H_{nF} = -\left(\frac{\mathcal{E}_0}{2}\right)^2 \left[\alpha_{nF}^s + \alpha_{nF}^v (i\hat{\epsilon}^* \times \hat{\epsilon}) \cdot \hat{\mathbf{F}} + \alpha_{nF}^t \left(\frac{3|\hat{\epsilon} \cdot \hat{\mathbf{F}}|^2 - \hat{\mathbf{F}}^2 |\hat{\epsilon}|^2}{F(2F-1)} \right) \right] \quad (3.10)$$

where α_{nF}^s , α_{nF}^v and α_{nF}^t are the scalar, vector and tensor polarizabilities; $\hat{\epsilon}$ represents the polarization of the field; and $\hat{\mathbf{F}}$ is the total angular momentum operator. Equation (3.10) illustrates an important concept for the manipulation of atoms with light, namely that the potential energy of an atom changes in proportion to the intensity of the electric field $I = 2\epsilon_0 c \mathcal{E}_0^2$. We also observe that the vector light-shift vanishes for linearly polarized light, as shown in Eq.(3.4).

Laser cooling and trapping can be explained in terms of the scalar component of the interaction Hamiltonian; however Raman transitions and higher order processes require the vector and tensor components to be properly described.

3.4.1 Frequency dependent scalar polarizability. The interaction between an atom and the oscillating electric field from electromagnetic radiation, e.g. from a laser, is described by means of the electric dipole moment induced on the atom, and can be treated as a perturbation to the bare atomic system $H_0|n\rangle = \hbar\omega_n|n\rangle$. Using second order perturbation theory, we obtain the time-averaged energy shift for a two level atom due to an oscillating electric field $\mathbf{E}(\mathbf{r}, t) = \mathcal{E}_0 \hat{\epsilon} \cos(\omega t)$

$$U = -\alpha(\omega) \langle \mathcal{E}_0^2 \cos^2(\omega t) \rangle_t / 2, \quad (3.11)$$

where $\langle \dots \rangle_t$ indicates the time average, the frequency-dependent atomic polarizability is given by

$$\alpha(\omega) = \frac{1}{\hbar} |\langle e | \mathbf{d} \cdot \hat{\epsilon} | g \rangle|^2 \left(\frac{1}{\omega_{eg} + \omega} + \frac{1}{\omega_{eg} - \omega} \right), \quad (3.12)$$

and $\omega_{eg} = \omega_e - \omega_g$ (see Appendix A). In general $\alpha(\omega)$ is a complex quantity⁹ whose real part accounts for the dispersive properties of the interaction, while its imaginary part is related to absorption (and subsequent spontaneous emission). While the light-shift is associated to the real part of the polarizability $U(\mathbf{r}) = -\text{Re}(\alpha)I(\mathbf{r})/2\epsilon_0c$; absorption is expressed in terms of photon scattering via the scattering rate Γ_{sc} , which is related to the complex part of the polarizability $\Gamma_{sc} = \text{Im}(\alpha)I(\mathbf{r})/\hbar\epsilon_0c$.

The scattering rate or spontaneous decay rate, also referred to as the line width [see Eq. (3.31)], can be calculated from Fermi's golden rule, which states that the transition rate to go from state $|e\rangle$ to state $|g\rangle$ is $\Gamma = 2\pi|\langle e|H'|g\rangle|^2\rho(\omega_{eg})/\hbar$, where $\rho(\omega_{eg})$ is the density of states of the electromagnetic field with frequencies ω_{eg} [56].

By introducing the intensity of the electric field $I(r) = 2\epsilon_0c|\mathcal{E}_0(r)|^2$, the above expressions can be rewritten in terms of the spontaneous decay rate (scattering rate) of the excited level $\Gamma = \omega_{eg}^3|\langle e|\mathbf{d}\cdot\hat{\epsilon}|g\rangle|^2/3\pi\epsilon_0\hbar c^3$ as

$$U(\mathbf{r}) = -\frac{3\pi c^2\Gamma}{2\omega_{eg}^3} \left(\frac{1}{\omega_{eg} + \omega} + \frac{1}{\omega_{eg} - \omega} \right) I(\mathbf{r}), \quad (3.13)$$

$$\Gamma_{sc}(\mathbf{r}) = \frac{3\pi c^2}{2\hbar\omega_{eg}^3} \left(\frac{\omega}{\omega_{eg}} \right)^3 \left(\frac{\Gamma}{\omega_{eg} + \omega} + \frac{\Gamma}{\omega_{eg} - \omega} \right)^2 I(\mathbf{r}). \quad (3.14)$$

Equations (3.13) and (3.14) correspond to the conservative and the dissipative interactions between light and matter [57].

3.4.2 The rotating wave approximation. Typically in experiments the oscillating electric field is that of a laser, and its frequency ω is set very close to the atomic resonance ω_{eg} , such that the detuning $\Delta = \omega - \omega_{eg}$ is small and $\omega/\omega_{eg} \approx 1$. Neglecting the terms rotating at the higher frequency $\omega_{eg} + \omega$ constitutes the rotating wave approximation (RWA), under which equations (3.13) and (3.14) reduce to

$$U(\mathbf{r}) = \frac{3\pi c^2}{2\omega_{eg}^3} \frac{\Gamma}{\Delta} I(\mathbf{r}), \quad (3.15)$$

$$\Gamma_{sc}(\mathbf{r}) = \frac{3\pi c^2}{2\hbar\omega_{eg}^3} \left(\frac{\Gamma}{\Delta} \right)^2 I(\mathbf{r}). \quad (3.16)$$

The dipole trapping potential scales as $I(\mathbf{r})/\Delta$, while the scattering rate scales as $I(\mathbf{r})/\Delta^2$. The spatial dependence of the intensity $I(\mathbf{r})$ adds versatility to the dipole trapping potential $U(\mathbf{r})$; it can be as simple as that of a single Gaussian laser beam, or arise from the interference of two or more lasers, realizing more complicated geometries, such as periodic potentials and beyond (see

⁹A straightforward calculation of the complex polarizability consists of solving the classical equations of motion of an electron in an oscillating electric field under the effects of damping due to energy loss by spontaneous emission of radiation (see Appendix A).

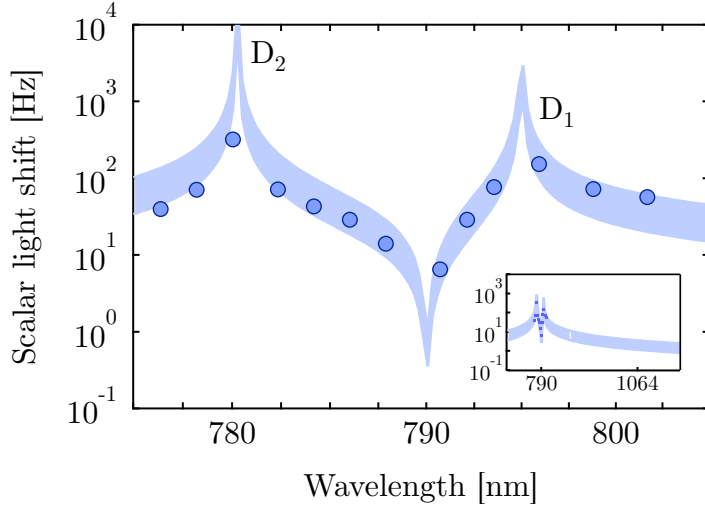


Figure 3.5: Measured scalar light-shift as a function of wavelength for ^{87}Rb . The calculated light-shift (band) considers a Gaussian beam with waist $w_0 = 150 \mu\text{m}$ whose power ranges from 100 mW to 300 mW. The inset displays the light-shift for a larger range of frequencies.

Sec. 3.5). The sign of the detuning Δ determines the attractive or repulsive nature of the trapping potential $U(\mathbf{r})$ with respect to the intensity pattern; if $\Delta < 0$, the atom minimizes its energy by going to the location(s) of maximum intensity, conventionally this is known as a *red* detuned trap; while in the opposite case $\Delta > 0$ (*blue* detuned trap) the atom tends to go away from the intensity maximum (maxima). In addition, the detuning sets the strength of both the trapping potential and the scattering rate; e.g. to minimize dissipation (heating) it is useful to work at large detuning; although it is important to mention that in the large detuning limit, the RWA is no longer a good approximation since both terms in eqns. (3.13) and (3.14) should be considered¹⁰.

3.4.3 Multiple-level atoms. The hyperfine interaction, described in Sec. 3.1, is responsible for the richness in the electronic structure of an atom. We begin this section by introducing the light-shift $U(\mathbf{r})$ of a multiple level atom due to the presence of an oscillating electric field $\mathbf{E}(\mathbf{r}, t) = \mathcal{E}_0 \hat{\epsilon} \cos(\omega t)$

$$U(\mathbf{r}) = -\frac{\mathcal{E}_0^2}{4\hbar} \sum_{n \neq g} |\langle n | \mathbf{d} \cdot \hat{\epsilon} | g \rangle|^2 \left(\frac{1}{\omega_{ng} + \omega} + \frac{1}{\omega_{ng} - \omega} \right). \quad (3.17)$$

Figure 3.5 shows the scalar light-shift for the ground state of ^{87}Rb , as a function of the frequency (wavelength) of the oscillating field, both measured¹¹ and calculated considering the contribution from the hyperfine sub-structure. These data demonstrate the scalar light-shift on ^{87}Rb atoms, which is strongest at the resonance transitions D_1 and D_2 and is minimized at around 790 nm. In

¹⁰For our 1064 nm optical dipole trap for ^{87}Rb atoms, the terms $1/(\omega_{eg} \pm \omega)$ are of comparable magnitude.

¹¹The experimental procedure to perform this measurement is described in Sec. 7.5.3.1.

some of the experiments described in this thesis, some lasers were set near this wavelength to reduce their scalar light-shift on the atoms.

Optical trapping arises from the conservative part of light-matter interactions. It originates in the off-resonant, almost non-dissipative interaction between an oscillating electric field and the corresponding induced electric dipole moment of an atom. In contrast, laser cooling of neutral atoms uses the dissipative interaction of light and matter, and relies on the exchange of momentum between the electromagnetic field and the atoms; by conservation of momentum, an atom that has absorbed radiation has consequently acquired momentum. After a sufficiently large number of such scattering events, the momentum distribution of an atomic sample is modified, in such a way that its energy is reduced, thus the sample is cooled. These phenomena will be discussed in the following sections.

3.5 OPTICAL TRAPPING

The optical trapping potential can be written in a convenient form starting from Eq. (3.17) by expressing the dipole matrix element in terms of its reduced matrix element $\|\mathbf{d} \cdot \hat{\epsilon}\|$ and corresponding Clebsh-Gordan coefficients c_{ng} , i.e. $|\langle n | \mathbf{d} \cdot \hat{\epsilon} | g \rangle| = c_{ng} \|\mathbf{d} \cdot \hat{\epsilon}\|$. The potential is understood as constituted from the contributions of all excited states coupled by the light field, weighted by $c_{ng}^2 / (\omega_{ng} \pm \omega)$.

A description of the weight provided by the Clebsh-Gordan coefficients on the D₂ line is summarized in Fig. 3.3 and a similar analysis can be done for the D₁ line. To determine which terms in the above sum are more relevant, we also consider the weight with respect to the detuning from resonance $\Delta_{ng} = \omega - \omega_{ng}$ and compare it to the fine and hyperfine splittings. The fine splitting between the D₁ and D₂ lines is about 15 nm; while the hyperfine splitting between the 5²S_{1/2} ground states is 6.8 GHz. Our experiments are realized with ⁸⁷Rb atoms, which interact with optical fields with: (a) $780 < \lambda < 820$ nm (laser cooling, optical lattices, Raman transitions) and (b) $\lambda = 1064$ nm (optical dipole trap). While the hyperfine structure is unresolved for those transitions whose detuning Δ_{ng} is larger than the fine splitting (i.e. $\lambda > 795$ nm), the fine structure is still to be considered; these considerations lead to simplified expressions for the light-shift and the scattering rate [57]

$$U(\mathbf{r}) = \frac{\pi c^2 I(\mathbf{r})}{2} \left[\left(\frac{\Gamma_{D2}}{\Delta_{D2}} - \frac{\Gamma_{D2}}{\omega + \omega_{D2}} \right) \frac{2 + qg_F m_F}{\omega_{D2}^3} + \left(\frac{\Gamma_{D1}}{\Delta_{D1}} - \frac{\Gamma_{D1}}{\omega + \omega_{D1}} \right) \frac{1 - qg_F m_F}{\omega_{D1}^3} \right]; \quad (3.18)$$

$$\Gamma_{\text{scatt}}(\mathbf{r}) = \frac{\pi c^2 I(\mathbf{r})}{2} \left[\left(\frac{\Gamma_{D2}}{\Delta_{D2}} - \frac{\Gamma_{D2}}{\omega + \omega_{D2}} \right)^2 \frac{2 + qg_F m_F}{\omega_{D2}^3} + \left(\frac{\Gamma_{D1}}{\Delta_{D1}} - \frac{\Gamma_{D1}}{\omega + \omega_{D1}} \right)^2 \frac{1 - qg_F m_F}{\omega_{D1}^3} \right]; \quad (3.19)$$

where g_F is the Landé g factor and $q = -1, 0, +1$ characterizes the polarization of the light.

The spatial geometry of an optical trap is dictated by the intensity pattern $I(\mathbf{r})$ of the field that creates it. In this thesis we focus on optical dipole traps arising from the superposition of two or

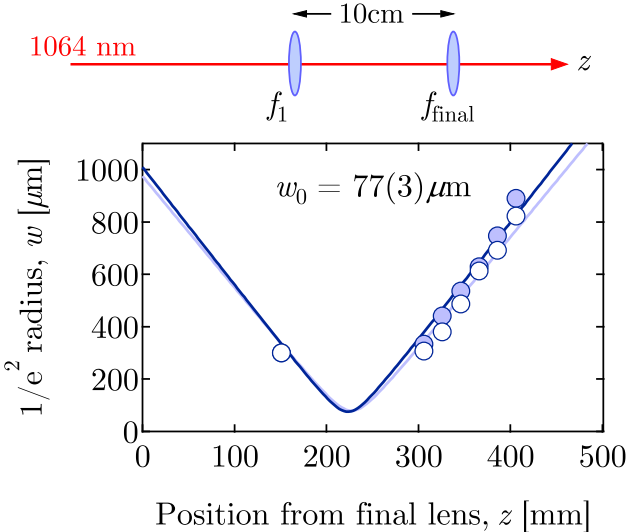
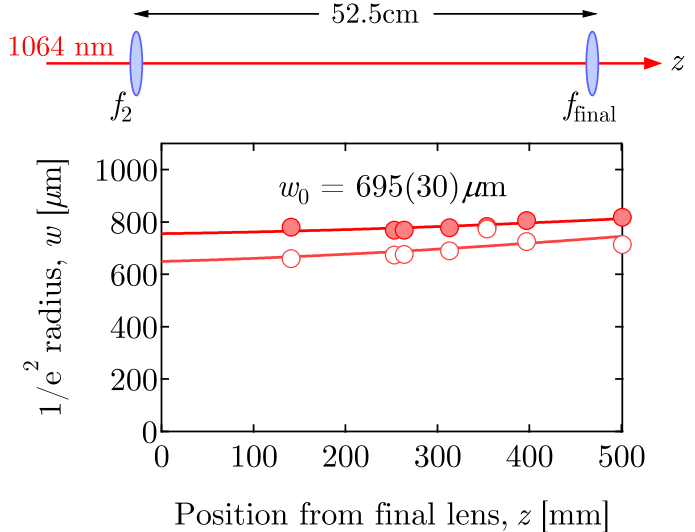
a. Original configuration with $f_1 = 50\text{cm}$ lens**b.** Replacement of f_1 with an $f_2 = 12.5\text{cm}$ lens

Figure 3.6: Gaussian beam characterization. **a.** Here we show the schematic of the lens system to give an average beam waist of $w_0 = 77(4) \mu\text{m}$. **b.** Using the equations for the spatial propagation of a Gaussian beam, we estimated the distance from the final lens at which to install an $f_2 = 12.5\text{ cm}$ lens in order to achieve an enlarged dipole beam. After the $f_1 \rightarrow f_2$ replacement, we measured an average waist of $w_0 = 695(30) \mu\text{m}$. Closed (open) symbols represent the $1/e^2$ radius along x (y).

more Gaussian laser beams.

3.5.1 Gaussian beam propagation and single focussed beam dipole trap. For a Gaussian laser beam propagating along the z direction, the spatial-dependence of the intensity is given by

$$I(\mathbf{r}) = \frac{2P}{\pi w^2(z)} e^{-2(x^2+y^2)/w^2(z)}, \quad (3.20)$$

where P is the total power in the beam; $w(z) = w_0 \sqrt{1 + z^2/z_R^2}$; the minimum radius w_0 is called the beam waist, and $z_R = \pi w_0^2/\lambda$ is the distance over which the beam radius spreads by a factor of $\sqrt{2}$, known as the Raleigh range.

Figure 3.6 shows the measured $1/e^2$ radii of a Gaussian beam, along its direction of propagation z for a 1064 nm laser beam. We use a CCD camera to image the intensity distribution of the beam at normal incidence $I(x, y)$, from which we obtain 1D profiles along x and y . We fit each profile to a 1D Gaussian distribution to obtain the $1/e^2$ radii. The continuous curves fit the data to the spatial propagation of a Gaussian beam with waist w_0 . Figure 3.6a corresponds to a Gaussian beam of waist $w_0 = 77(4) \mu\text{m}$, whose Raleigh range is $z_R = 1.75 \text{ cm}$. The size of the beam can be readily modified by using a lens or an array of lenses as shown in Fig. 3.6b, where $w_0 = 695(30) \mu\text{m}$ and $z_R = 1.28 \text{ m}$. (The typical value for the reduced χ^2 from each fit is about 95).

The trapping potential from a single Gaussian beam can be approximated by a harmonic oscillator potential by means of a Taylor series expansion around $\mathbf{r} = 0$

$$U \approx -U_0 \left[1 - 2 \frac{x^2 + y^2}{w_0^2} - \frac{z^2}{z_R^2} \right], \quad (3.21)$$

where U_0 is the potential depth calculated from Eq. (3.17) or (3.18), and is directly proportional to the intensity of the laser. The oscillator frequencies $f_j = \omega_j/2\pi$, where $j = x, y, z$, are inversely proportional to the dimensions of the beam

$$\omega_j = \sqrt{\frac{4U_0}{m\omega_0^2}}, \quad \text{for } j = x, y \quad \text{and} \quad \omega_z = \sqrt{\frac{2U_0}{mz_R^2}}. \quad (3.22)$$

Since the beams waists w_{0j} are typically larger than λ , the Raleigh range is $z_R \gg w_0$; this means that a single focused laser beam provides a trapping potential mostly in its radial direction, or equivalently it provides quasi-1D confinement. In some applications it is convenient to align the laser beam perpendicular to the gravitational field, to maximally counteract to the effects of gravity.

Designing a harmonic optical dipole trap by focusing a Gaussian beam to a suitable size, can be done with an appropriate choice of lenses. In our experiments we use the combined trapping potential from a pair of laser beams to create our optical dipole trap.

3.5.2 Crossed-beam dipole trap. Our optical dipole trap forms at the intersection of a pair of $\lambda = 1064$ nm laser beams, propagating along $\mathbf{e}_x \pm \mathbf{e}_y$ with orthogonal-linear polarizations. Their overall and relative intensities can be experimentally controlled (see Sec. 4.6). The crossed-beam trapping potential corresponds to the linear superposition of the single beam trapping potentials, given by Eq. (3.21).

3.6 LASER COOLING

Laser cooling is a process where a laser field interacting with an atomic sample, via multiple absorption and spontaneous emission events, imparts momentum to the atoms modifying their initial velocity distribution.

Being almost monochromatic and well collimated, a laser is the ideal candidate to slow down an atomic beam. As discussed in Sec. 3.3, to maximize the number of scattering events, this laser (the MOT laser, see Sec. 4.4.4) has to be frequency locked very close to resonance with respect to cooling transition in ^{87}Rb , this is the D₂ transition from $F = 2 \rightarrow F' = 3$.

I will consider, for simplicity, a two level atom whose energy levels $|g\rangle$ and $|e\rangle$ are separated in energy by $\hbar\omega_0$, and will assume that this system is interacting with the electric field \mathbf{E} from a laser

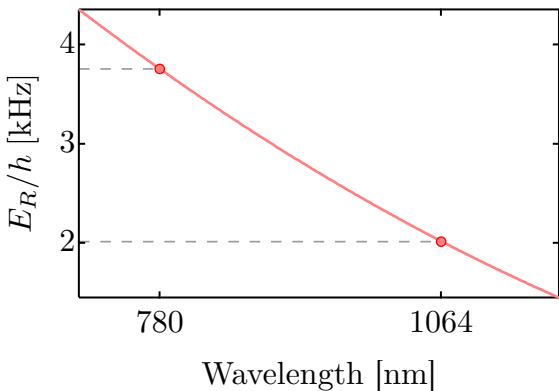
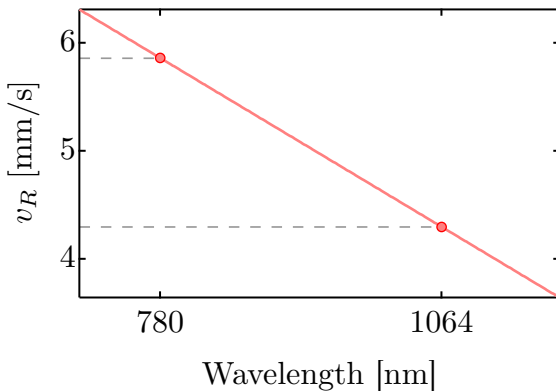
a. Single photon recoil energy**b. Single photon recoil velocity**

Figure 3.7: Single photon recoil energy $E_R = \hbar^2 k_R^2 / 2m$ and recoil velocity $v_R = \hbar k_R / m$ as a function of wavelength for ^{87}Rb atoms.

characterized by the frequency ω . A two level atom scatters photons at a rate

$$\gamma_{\text{scatt}} = \frac{\Gamma}{2} \frac{\Omega^2/2}{\delta^2 + \Omega^2/2 + \Gamma^2/4}, \quad (3.23)$$

where Γ is the spontaneous decay rate, $\delta = \omega - \omega_0$ is the detuning from resonance, and $\Omega = \langle g | \mathbf{e} \cdot \mathbf{E} | e \rangle / \hbar$ is the Rabi frequency associated with the amplitude of the laser field E . The scattering rate on-resonance is optimal for laser cooling; however, the resonance is velocity dependent (due to the Doppler shift) and optimal conditions for scattering are no longer satisfied as atoms slow down (this is discussed in Sec. 3.6.1).

For these processes, the natural units of momentum and energy are the single-photon recoil momentum $\hbar k_R = h/\lambda$ and the single-photon recoil energy $E_R = \hbar^2 k_R^2 / 2m$, which correspond to the amount of momentum transferred to an atom, and to the kinetic energy change in an atom of mass m after the absorption or emission of a single-photon. Figure 3.7 shows typical values of E_R/h for wavelengths relevant to our system.

The scattering force determines the rate at which the photons transfer momentum in units of $\hbar k_R$ to the atoms; in terms of the saturation intensity¹² $I/I_{\text{sat}} = 2\Omega^2/\Gamma^2$ the force is

$$F_{\text{scatt}} = \frac{\hbar k_R \Gamma}{2} \frac{I/I_{\text{sat}}}{1 + I/I_{\text{sat}} + 4\delta^2/\Gamma^2}, \quad (3.24)$$

whose limiting value for increasing intensity $F_{\text{max}} = \hbar k_R \Gamma / 2$, sets the maximum acceleration $a_{\text{max}} = F_{\text{max}}/m = \hbar k_R \Gamma / 2m$. In the case of ^{87}Rb the maximum acceleration is $a_{\text{max}} = 11.16 \text{ cm/ms}^2$, this is

¹²The saturation intensity I_{sat} corresponds to the electric field strength at which a two level system in the presence of radiative damping reaches equilibrium, and both states have balanced populations (see Sec. 3.7.1).

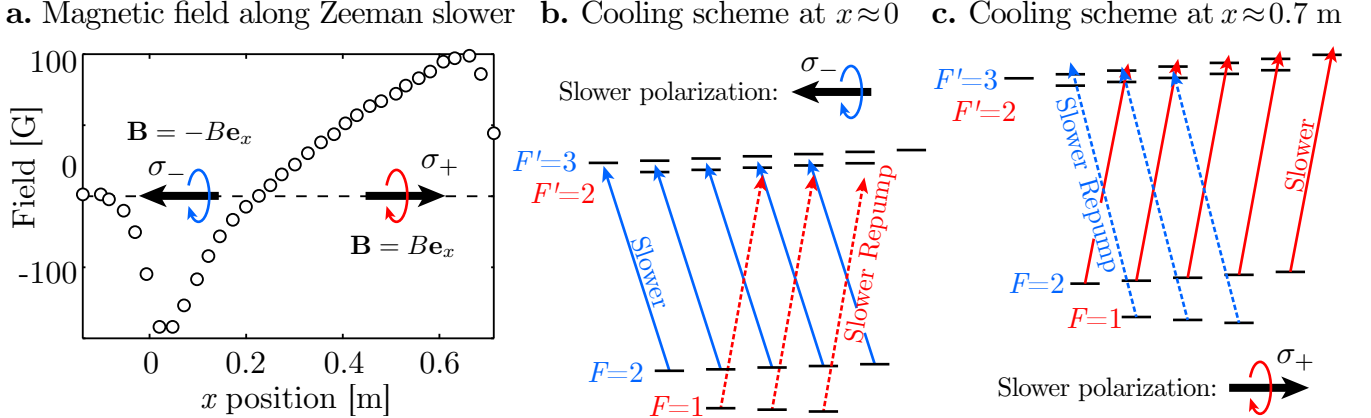


Figure 3.8: The Zeeman cooling scheme. **a.** An inhomogeneous field (circles) Zeeman splits the hyperfine sub-levels to provide a correction to the Doppler effect experienced by the moving atoms as they exit from the $T = 400$ K source and are gradually decelerated by a circularly polarized laser beam (Slower). Optical pumping is performed by a second laser beam (Slower Repump), whose circular polarization is opposite to that of the slower laser. **b-c.** Example cooling schemes along the slower.

$\sim 10^4$ times larger than the standard acceleration of the Earth's gravity $g_n = 9.806 \mu\text{m}/\text{ms}^2$ [58].

The stopping distance Δx of an atom moving under uniform linear acceleration $-a$ along \mathbf{e}_x , is given by $\Delta x = v_0^2/2a$. In our experiments, metallic Rb is vaporized in vacuum by heating it¹³ up to $T = 400$ K. The vapor is then collimated to form an atomic beam with initial speed given by $v_0 = \sqrt{3k_B T/m} \approx 340$ m/s. Decelerating at a_{\max} gives a stopping distance $\Delta x = 0.52$ m. Our slower is 0.69 m in length and runs at approximately $0.7 \times a_{\max}$.

3.6.1 The Doppler effect and the Zeeman slower. Moving atoms experience the Doppler effect, they observe a shift in the frequency of the laser in proportion to their velocity. If an atom has a velocity v , the observed frequency is $\omega' = \omega \pm kv$, where k is the wavenumber and the plus (minus) sign corresponds to an atom traveling toward (away from) the laser source. If the atom is moving in the opposite direction to the propagation of a laser beam, the detuning from resonance can be restated as $\delta = \omega - \omega_0 + kv$.

For atoms emerging from the source, $v_0 = 340$ m/s at the output of the oven, and the Doppler shift on the cooling transition is $kv_0 = 2\pi \times 436.76$ MHz. To efficiently bring the atoms to rest we need to correct for a frequency shift ranging from kv_0 to zero. A technique to account for and exploit the Doppler effect is to apply an inhomogeneous magnetic field \mathbf{B} along the path of the atomic beam to Zeeman split the atomic levels, and continually achieve resonance as the atoms

¹³The vacuum at the oven is on the order of 10^{-11} to 10^{-12} bar, well below the vapor pressure of ⁸⁷Rb at 400 K ($\approx 9 \times 10^{-7}$ bar).

slow down¹⁴. The slowing of an atomic beam of Na atoms was first observed in 1982 by Prodan, et al. [59].

Figure 3.8 shows the field generated by a solenoid with an inhomogeneous linear density of coils; and constitutes the essence of the Zeeman slower. At the entrance of the slower where the Doppler shift is maximum, the density of coils is the largest and the corresponding field is maximum (Fig. 3.8a,c). The combined Doppler and Zeeman effects together with the choice of the slower laser frequency gives a nearly resonant condition for laser cooling. Our Zeeman slower is a zero-crossing field design (see Sec. ??), and close to the exit of the slower solenoid (Fig. 3.8b) the cooling scheme is significantly different. Due to the redefinition of the quantization axis the slower laser is σ_- polarized for $x < 0.2$ m. At $x \approx 0$ the laser cooled atoms have a significantly reduced Doppler shift, and the Zeeman shift is enough for the slower to be on resonance with the cooling transition associated with the lowest angular momentum.

3.6.2 Repumping. In multiple level atoms such as ^{87}Rb , due to the the relatively small hyperfine splitting of the $5P_{3/2}$ ($\Delta < 270$ MHz), the MOT laser (see Sec. ??) might drive off-resonant transitions to other allowed states such as $F = 2 \rightarrow F' = 1, 2, 3$; in turn some atoms could decay into $F = 1$, i.e. the ground state uncoupled by the light, and eventually suppress the cooling mechanism. As discussed in Sec. 3.3.4 a second laser beam (the repump laser, see Sec. 4.4.3) locked to the $F = 1 \rightarrow F' = 2$ transition is useful to optically pump the atoms and reactivate the cooling process. As the speed of the atoms is modified, the repumping mechanism is also affected but corrections can be achieved by means of an inhomogeneous Zeeman as described above.

3.6.3 Cooling and repumping lasers. We use two main lasers as the source of cooling and repumping light. These are frequency locked with respect to a reference laser, the Master, via a beat-note lock mechanism. Both the slower MOT and the slower Repump lasers are significantly below resonance (by ~ 150 MHz) from the cooling ($F = 2 \rightarrow F' = 3$) and repumping ($F = 1 \rightarrow F' = 2$) transitions, respectively; resonance is achieved when the Doppler and Zeeman shifts experienced by the atoms traveling along the Zeeman slower are taken into account (Fig. 3.8).

3.6.4 Optical molasses. Cooled atoms exiting the slower still have three spatial degrees of freedom; thus cooling along the remaining dimensions is needed to further reduce their energy. Optical molasses is an optical mechanism which opposes the motion of the atoms in proportion to their velocity.

¹⁴Figure 3.12 shows the splitting of the hyperfine structure of ^{87}Rb ground states as a function of the magnitude of an external magnetic field \mathbf{B} .

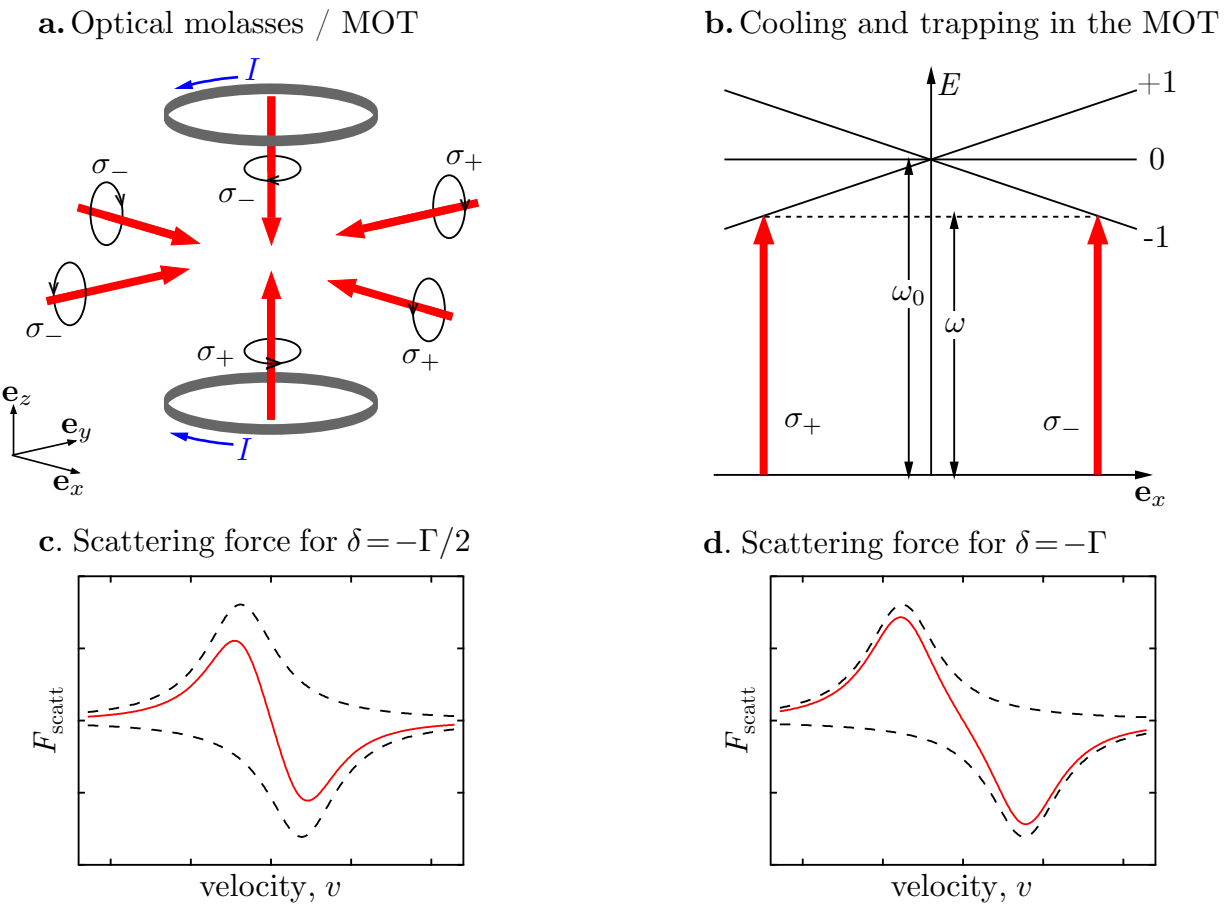


Figure 3.9: The dissipative force in optical molasses and the magneto optical trap.

Optical molasses (OM) uses three orthogonally counter-propagating lasers (all originated from the MOT laser, see Sec. 4.4.4) at about 90 MHz below the cooling transition in our experiment¹⁵ $F = 2 \rightarrow F' = 3$. A simplified scheme for OM is displayed in Fig. 3.9a,b.

For simplicity I will discuss the cooling mechanism from a single pair of counter-propagating beams incident on a two-level atom in the absence of the magnetic field. An atom moving with velocity v is subject to the Doppler effect and observes the laser beams with detunings $\delta_{\text{left/right}} = \delta \mp k_R v$, where $\delta = \omega - \omega_0$. The scattering force from both beams is $F_{\text{scatt}} = F_{\text{left}} - F_{\text{right}}$, and by means of Eq. (3.24) acquires the form $F = -\alpha v$, where

$$\alpha = \frac{2\hbar k_R^2}{\Gamma} \frac{I}{I_{\text{sat}}} \frac{-4\delta}{[1 + (2\delta_{\text{left}}/\Gamma)^2][1 + (2\delta_{\text{right}}/\Gamma)^2]} \quad (3.25)$$

is the damping coefficient and we have assumed laser intensities below saturation $I \ll I_{\text{sat}}$. Since the scattering force $F = -\alpha v$ opposes the motion of the atom in proportion to its velocity (a phenomenon associated with viscous media) the laser medium described above is denominated optical molasses. Figure 3.9c,d shows the scattering force as a function of velocity for $\delta = \Gamma/2$ and Γ . The velocity capture range is on the order of $\Gamma/k_R \approx 4.73$ m/s for the cooling transition of ^{87}Rb ; and the cooling rate Fv at which the kinetic energy of the atoms decreases is associated with the damping time $\tau = m/2\alpha$, which for ^{87}Rb at $\delta = \Gamma/2$ and $v = 0$ this is $\sim 11 \mu\text{s}$.

3.6.5 The Doppler cooling limit. One might think that optical molasses cooling could be applied for a sufficiently long time to arbitrarily decrease the temperature of the atomic sample, but this is not the case since spontaneous emission acts as a heating mechanism which at best only balances the effects of optical molasses.

In each scattering event, the atom absorbs and emits a single photon from each beam and effectively modifies its energy by $2E_R$; this occurs at the scattering rate γ_{scatt} . Assuming that in the steady state the heating rate from both beams ($4E_R\gamma_{\text{scatt}}$) balances the cooling rate (Fv), the equipartition theorem leads to

$$k_B T = -\frac{\hbar\Gamma}{4} \frac{1 + (2\delta/\Gamma)^2}{2\delta/\Gamma}; \quad (3.26)$$

whose minimum value, occurring at $\delta = -\Gamma/2$, gives the minimum temperature $T_D = \hbar\Gamma/2k_B$, which is known as the Doppler cooling limit.

3.6.6 Sub-Doppler polarization gradient cooling. The hyperfine structure of the alkalis not only complicates the cooling mechanism of optical molasses, but also allows cooling below the sub-

¹⁵Optical pumping to maintain the cooling process is implied. In our experimental setup repumping is performed by a single pair of counter-propagating beams originated from the repump laser (see Sec. 4.4.3).

Doppler temperature T_D . This phenomena can be understood by generalizing the simple two-level model illustrated above to a multiple level system interacting with suitable polarized laser fields.

Consider a pair of lasers traveling along $\pm \mathbf{e}_z$ and with opposite circular polarizations¹⁶; the superposition of their electric fields gives $\mathbf{E} = 2E_0 \cos(\omega t) \hat{\epsilon}$, where the polarization vector is

$$\hat{\epsilon} = \cos(kz) \mathbf{e}_x - \sin(kz) \mathbf{e}_y; \quad (3.27)$$

this corresponds to an electric field whose local polarization is linear and which realizes a rotation by 2π around \mathbf{e}_z with spatial periodicity λ . The rotating electric field defines a local quantization axis, the light-shifts are independent of position and only π -transitions are allowed.

Cooling in such scheme relies on the damping forces arising from the population imbalance between Zeeman sub-levels induced by the atomic motion and generated due to the optical pumping processes the atoms undergo as they travel in such a polarization gradient. Under these conditions, the most populated state is the one that absorbs light most efficiently from the σ polarized wave opposing its motion. The unequal absorption of σ_+ and σ_- photons by a moving atom, leads to the disequilibrium between the scattering force arising from each laser and to the subsequent damping of atomic motion [60]. Polarization gradient cooling allows sub-Doppler temperatures [61] down to the recoil limit $T_R \sim E_R/k_B$ to be reached.

3.6.7 The Magneto Optical Trap. The magneto optical trap (MOT) differs from OM, primarily by the addition of a magnetic field gradient (Fig. 3.9a), although detuning and beam intensity also play an important role. In contrast with OM, the MOT is a trapping potential that arises when the scattering force is modified by spatial changes in the detuning using the magnetic field gradient¹⁷. The spatial dependence introduced by the magnetic field gradient is makes the MOT a trap.

A quadrupole magnetic field can be readily implemented as discussed in Sec. 3.9.1; in particular, we align the zero of the field at the intersection of the MOT beams, i.e. at the origin of the coordinate system (Fig. 3.9a). The magnitude of the quadrupole field varies linearly with position and it introduces a uniform detuning gradient on the atomic sample.

To simply understand the way in which the MOT captures the atoms, I will describe the 1D case illustrated in Fig. 3.9b. Assume that two counter-propagating beams, with orthogonal polarizations (σ_\pm propagating along $\mp \mathbf{e}_x$ as shown in Fig. 3.9a), illuminate an atom; and that the frequency of the lasers ω is tuned below atomic resonance ω_0 .

¹⁶In the absence of a magnetic field, here we define the polarization with respect to the propagation axis \mathbf{e}_z , see Sec. 3.2.1. The electric field of a σ_\mp polarized laser traveling along $\pm \mathbf{e}_z$ is: $\mathbf{E}_{\pm z} = E_0 \cos(\omega t \mp kz) \mathbf{e}_x \pm \sin(\omega t \mp kz) \mathbf{e}_y$.

¹⁷The interaction between an atom and an external magnetic field \mathbf{B} is discussed in detail in Sec. 3.8; however, for the present discussion of the MOT it is enough to acknowledge that in the presence of a small external magnetic field, compared to the internal field that gives rise to the hyperfine splitting, they experience the linear Zeeman effect.

Let us assume that the atom has a single ground state and a three-fold degenerate excited state, with sub-levels $m = -1, 0, +1$. The internal sub-levels of a moving atom, are subject both to a spatially dependent Zeeman shift and to the Doppler effect; in particular an atom moving toward $+x$ observes the frequency of the counter-propagating laser closer to resonance with the excited $m = -1$ level. Given our careful choice of polarization (σ_- in this case), optimal conditions for scattering events are achieved and the atom is pushed back to $x = 0$. An equivalent process occurs for an atom traveling toward $-\mathbf{e}_x$, i.e. it is eventually pushed to the trap center $x = 0$ by the σ_+ polarized laser beam.

Decelerated atoms exiting the Zeeman slower are further cooled and collected by a MOT during a total time of ~ 3 s, after which polarization gradient cooling (achieved by turning off the quadrupole magnetic field for the MOT) takes place. In our experiment we prepare optical molasses and let them act for typically 20 ms, with which we achieve cooling down to $T \sim 30 \mu\text{K}$.

3.7 RESONANT ABSORPTION IMAGING

Most probing mechanisms for ultracold atomic samples rely on optical imaging, and they either focus on the amplitude or the phase of the atomic distribution. Resonant absorption imaging is a widely used destructive technique, in which the measurement of the optical density gives the atomic density of the sample. From this image we can obtain all the system parameters including atom number, temperature, condensate fraction, momentum distribution (TOF imaging). It is also possible to extract the equation of state and all the thermodynamical properties of the system [62].

We start by defining the resonant absorption cross-section σ as the effective absorptive area associated with each atom; however, it does not represent the physical size of the atom. Consider a system of atoms with density $n(x, y, z)$, in a volume $A dx$ as shown in Fig. 3.10. A laser beam with initial intensity $I(x, y, z)$ propagating along \mathbf{e}_x , passes thought the atomic media and is absorbed by an amount $IN\sigma dx$. The differential decrease in the intensity is $dI/I = -n(x, y, z)\sigma dx$; the attenuation of the laser is exponential when the cross-section is independent of the intensity and $I \ll I_{\text{sat}}$

$$I(x, y, z) = I(0, y, z)e^{-OD}; \quad (3.28)$$

where $OD = \int n(x, y, z)\sigma dx$ is the optical depth. This result is known as Beer's law, and from it we can infer the density of a medium. This formula works well in the case of low-intensity imaging, where most atoms remain in the ground state.

3.7.1 The saturation intensity and the frequency dependent absorption cross section. In the presence of monochromatic radiation, a two level system undergoes Rabi oscillations between its levels; however in the presence of damping, i.e. when spontaneous emission occurs, the system evolves into a steady state, characterized by the balance of the populations of both energy levels; this

a. Intensity attenuation by absorption b. Frequency dependence of cross-section

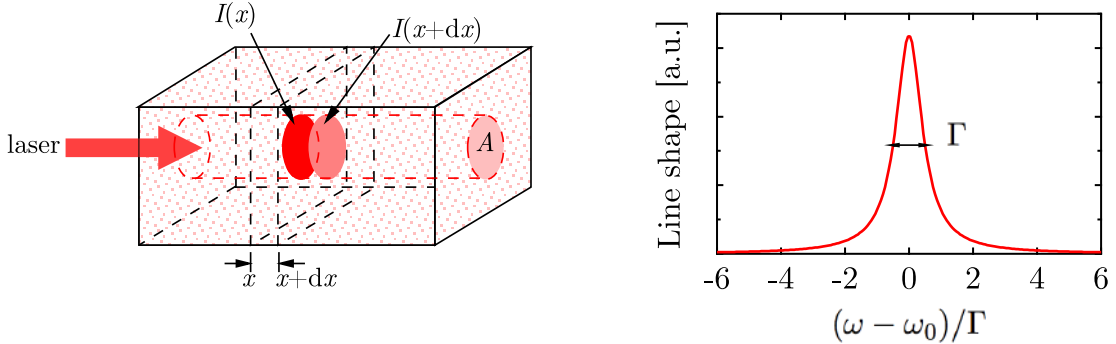


Figure 3.10: Resonant absorption cross-section. The density of a medium can be determined by measuring the intensity attenuation of a laser after passing through it. The resonant absorption cross section has a Lorentzian dependence on the detuning from resonance given by Eq. (3.31), and has a full width at half maximum equal to Γ .

behavior can be described in terms of a saturation effect characterized by the saturation intensity. In this section we discuss the frequency dependence of the absorption cross-section and introduce the saturation intensity.

When the intensity $I(\omega)$ of the laser is large enough such as to induce stimulated emission processes, we need to modify the above model for intensity, to account for this contribution. If N_g and N_e denote the population of atoms in the ground and excited states, respectively we get

$$\frac{dI}{dx} = -(N_g - N_e)\sigma(\omega)I(\omega); \quad (3.29)$$

where we see that the atoms in the ground (excited) state contribute to decrease (increase) the intensity, and $N = N_e + N_g$. Once the light is absorbed, it can either be emitted spontaneously or by a stimulated process; conservation of energy requires that these processes balance

$$(N_g - N_e)\sigma(\omega)I(\omega) = N_e A_{eg} \hbar\omega; \quad (3.30)$$

where A_{eg} is Einstein's coefficient associated with spontaneous emission¹⁸ and $\hbar\omega$ is the energy contained in the emitted photon. For a driven two level system, the fractional population of the excited state is given by¹⁹ $N_e/N = (\Omega^2/4)[\delta^2 + \Omega^2/2 + \Gamma^2/4]^{-1}$; which leads to the frequency dependent

¹⁸Einstein's coefficients B_{ge} , A_{eg} and B_{eg} are properties of the atom and are related to the rate at which absorption, spontaneous emission and stimulated emission occur, respectively. For a two level atom the coefficient A_{eg} describing the decay rate from the excited level $|e\rangle$ to the ground state $|g\rangle$ corresponds to the spontaneous emission rate Γ .

¹⁹This is a consequence of solving the optical Bloch equations, which describe the excitation of a two level atom driven by an almost resonant field and including spontaneous emission [63].

cross-section for absorption

$$\sigma(\omega) = 3 \times \frac{A_{eg}\pi^2 c^2}{\omega_0^2} \frac{\Gamma/2}{\pi[\delta^2 + (\Gamma/2)^2]}. \quad (3.31)$$

The cross-section for absorption has a Lorentzian dependence on the detuning δ (Fig. 3.10), and its full width at half maximum is Γ ; its maximum value, coincides with the cross section of a classical dipole, $\sigma_0 = (3\lambda_0^2/2\pi)$, where $\lambda = 2\pi c/\omega$, occurs on resonance. The pre-factor of 3 can actually be any value in the range 0 to 3, depending on the polarization of the light; to maximize the cross-section, a quantization axis is chosen with respect to which the light is circularly polarized (see Sec. 3.2.1).

The equilibrium condition stated in Eq. (3.30) allows one to express the population difference as

$$N_g - N_e = \frac{N}{1 + I/I_s(\omega)}; \quad (3.32)$$

where the frequency dependent saturation intensity is defined by $I_s = \hbar\omega A_{eg}/2\sigma(\omega)$; its value on resonance $I_{\text{sat}} = \pi hc\Gamma/3\lambda_0^3$ is referred to as the saturation intensity. When the laser intensity reaches I_{sat} , it is expected that the population fractions in the ground and excited levels are equal. An equivalent expression for the saturation intensity²⁰ is $I/I_{\text{sat}} = 2\Omega^2/\Gamma^2$.

For the particular case of ⁸⁷Rb the saturation intensity associated with the $|F = 2, m_F = \pm 2\rangle \rightarrow |F = 3, m_F = \pm 3\rangle$ cooling transition under σ_{\pm} polarized light is $I_{\text{sat}} = 1.662 \text{ mW/cm}^2$; and the resonant absorption cross-section is $\sigma_0 = 2.907 \times 10^{-9} \text{ cm}^2$.

3.7.2 Experimental implementation of absorption imaging The ingredients for optimal resonant absorption imaging are: atoms in $|F = 2, m_F = 2\rangle$, circularly polarized cooling light, and a well defined quantization axis along which the probe beam propagates. As can intuitively be seen from Fig. 3.3b, the pair of states $|F = 2, m_F = 2\rangle$ and $|F' = 3, m_F' = 3\rangle$ form an effective two level system, isolated from the rest of the hyperfine sub-levels given the selection rules for circularly polarized light, so the above treatment for a two level atom is appropriate.

The quantization axis is provided by the direction of an external uniform magnetic field generated by three pairs of Helmholtz coils oriented in mutually orthogonal directions. The field is set along the direction of propagation of the imaging beam to achieve maximum circular-polarization and maximize the cross-section for absorption. Given the saturation intensity for ⁸⁷Rb, it suffices to have a probe beam with very low power. A $w_0 = 400 \mu\text{m}$ Gaussian beam, would need a power $P = 4.2 \mu\text{W}$ to achieve an intensity $I = I_{\text{sat}}$.

²⁰An intensity of I_{sat} corresponds to providing the energy of one photon every two lifetimes over the radiative cross-section σ_0 of the two-level transition [64].

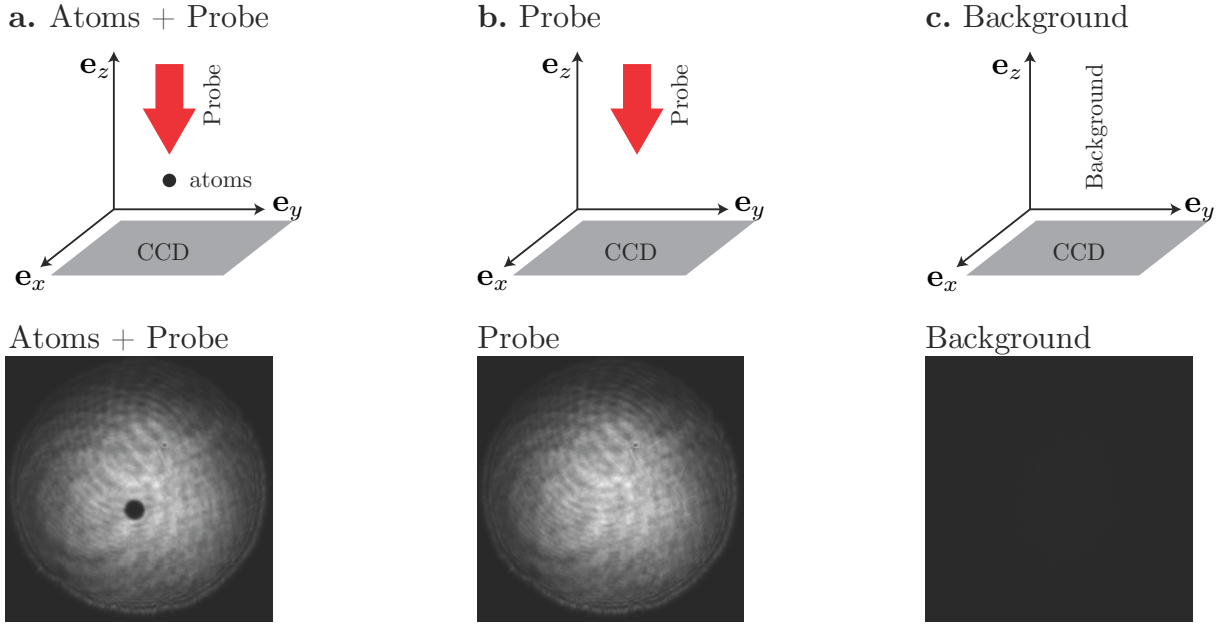


Figure 3.11: Resonant absorption imaging. **a.** An image of the resonantly absorbed probe beam by the atoms is recorded on a CCD chip. The size of the beam is large enough so as to guarantee nearly uniform illumination over the atomic sample. Two reference beams, containing **b.** the unabsorbed probe beam's intensity profile and **c.** the background, are also recorded in order to reconstruct the atomic distribution's optical density.

Our experiments are typically carried out with atoms in the $F = 1$ ground state manifold. Prior to imaging, the atoms are optically pumped into the $F = 2$ ground state. Once there, a pulse of cooling light illuminates the atoms, and they resonantly absorb a fraction of the beam (whose waist is large enough $w_0 \gtrsim 300 \mu\text{m}$ so as to achieve nearly uniform illumination of the atomic sample). Both the light and the shadow of the atoms are recorded on a CCD²¹, from which we obtain an intensity profile I_{atoms} (Fig. 3.11a). Two more images are required to characterize the atomic distribution: an image of the unaltered beam giving the original intensity distribution I_{light} and a background image which provides a zero reference level $I_{\text{background}}$ (Fig. 3.11b,c). Using Eq. (3.28), the measured optical density

$$OD_{\text{exp}} = \ln \left(\frac{I_{\text{light}} - I_{\text{background}}}{I_{\text{atoms}} - I_{\text{background}}} \right), \quad (3.33)$$

gives the integrated density distribution $n(y, z) = \int n(x, y, z)dx$ along the imaging direction \mathbf{e}_x , namely $n(y, z) = OD_{\text{exp}}/\sigma_0$, where we use the on-resonance value of the scattering cross-section $\sigma_0 = 3\lambda_0^2/2\pi$.

²¹A charge-coupled device (CCD), is a high-speed semiconductor device suitable to digitally record images.

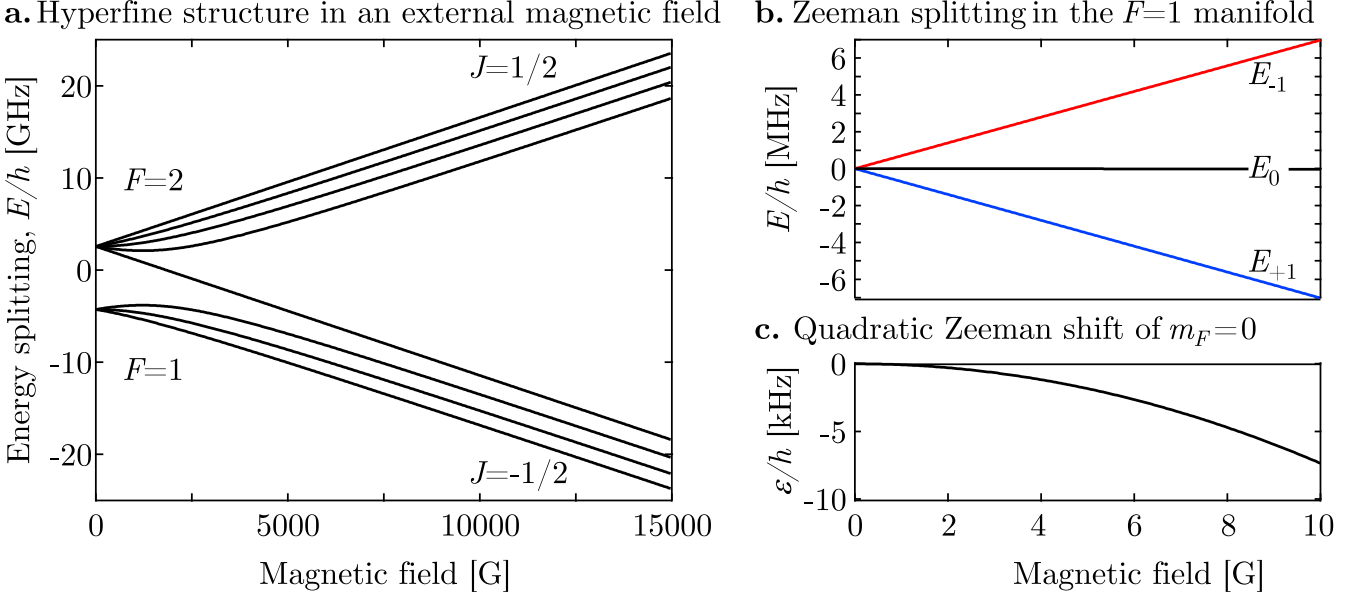


Figure 3.12: Hyperfine structure of the ground state manifold $5^2S_{1/2}$ of ^{87}Rb vs magnetic field. **a.** Calculated hyperfine structure as a function of magnetic field. **b.** Zeeman splitting of the $F = 1$ states for small magnetic fields, these include the typical values used in our experiments. **c.** The relative shift of the $m_F = 0$ state is defined as $\epsilon/h = E_0 - (E_{-1} + E_{+1})/2$; it presents a quadratic dependence on the magnetic field and occurs on a smaller energy scale than the Zeeman splitting of the $m_F = \pm 1$ states.

3.8 INTERACTION BETWEEN ATOMS AND MAGNETIC FIELDS

The Zeeman interaction between an external magnetic field \mathbf{B} and both the magnetic moment $\mu_J = g_J \mu_B \mathbf{J}$ and the nuclear magnetic moment $\mu_N = g_I \mu_N \mathbf{I}$ of the electron, shifts the energy of the total angular momentum states $|F, m_F\rangle$ (Fig. 3.12). In the limit of weak magnetic field, where the Zeeman splitting is small compared to the hyperfine splitting, it is suitable to describe the system in terms of the total angular momentum states. In the limit of strong field, the Zeeman interaction term dominates over the hyperfine interaction, which can be considered as a perturbation to the strong-field eigenstates $|Jm_J Im_I\rangle$.

An alkali atom can effectively be modeled as having a magnetic moment $\mu = \mu_B g_F \mathbf{F}$, where μ_B is the Bohr magneton and g_F is the Landé g -factor of the atomic state. The Zeeman interaction between the atom and an external field is then $U = -\mu \cdot \mathbf{B}$.

3.9 MAGNETIC TRAPPING

Assuming that the atoms are moving slowly enough across the magnetic field, their magnetic moments align with the field. The magnetic trapping potential $U = \mu_B g_F m_F B$, depends on the magnitude of the field B and the atom's hyperfine levels.

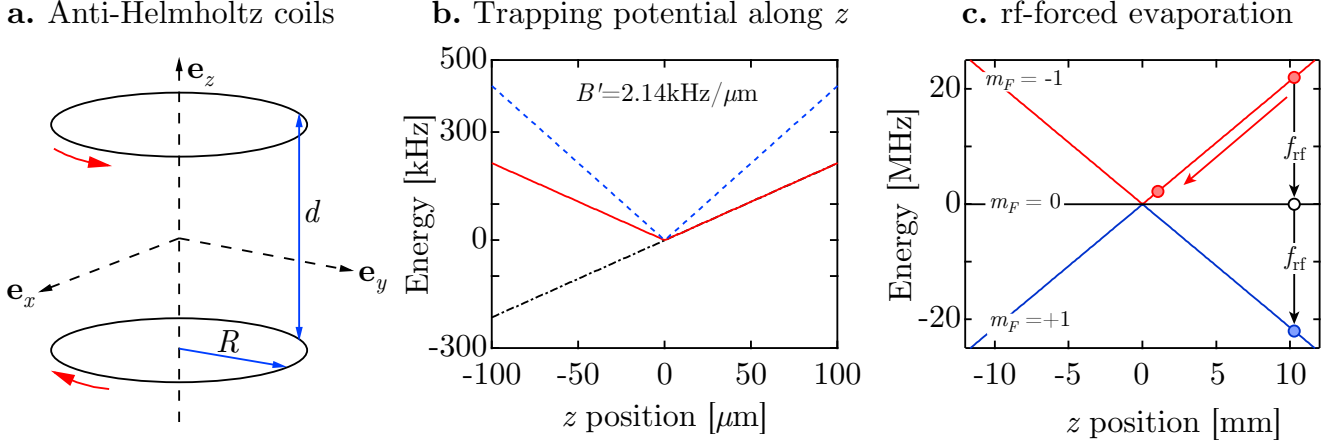


Figure 3.13: Magnetic quadrupole trap. **a.** We generate a magnetic quadrupole field using a pair of parallel coils with electrical currents circulating in opposite directions (anti-Helmholtz coils). **b.** Magnetic trapping potential along e_z for a gradient $B' = 3.06 \text{ mG}/\mu\text{m}$ and for the trappable states of ^{87}Rb : $|F=1, m_F=-1\rangle$, $|F=2, m_F=+1\rangle$ (continuous) $|F=2, m_F=+2\rangle$ (dashed). When $z < 0$, such gradient exactly cancels the gravitational potential experienced by the $m_F = 1$ atoms, corresponding to $B'_g/h = mg/h = 2.14 \text{ kHz}/\mu\text{m}$ (dot-dashed). **c.** Once the atoms are collected in the magnetic trap, an rf-field of variable frequency f_{rf} is applied to selectively transfer the most energetic atoms into untrappable states.

In principle, we would have two choices: (*i*) to locally maximize the magnitude of the field to trap states where $g_F m_F < 0$ or (*ii*) to design a field with a local minimum to trap states where $g_F m_F > 0$. Since it can be proven that in a region free from current and charge distributions, the strength of a quasi static electric or magnetic field can have local minima but not local maxima [65], the scheme proposed in (*i*) is impossible to achieve. The magnetic trappable states are the low-field seeking states, for which $g_F m_F > 0$; in the case of the ground state manifolds of ^{87}Rb the trappable states are: $|F=1, m_F=-1\rangle$ and $|F=2, m_F=1, 2\rangle$.

A magnetic trap consists of a magnetic field which provides a local energy minimum for the atoms to be attracted and collected. One of the simplest magnetic traps is the one arising from a quadrupole magnetic field, such as the one obtained from a pair of anti-Helmholtz coils (Fig. 3.13a). This is the scheme used in our experimental apparatus.

3.9.1 The quadrupole magnetic field. To understand the nature of the quadrupole field generated by a pair of anti-Helmholtz coils, let us focus on its spatial gradients. Given the symmetry of the field $\partial B_x / \partial x = \partial B_y / \partial y$; and from Maxwell's equations we know that $\nabla \cdot \mathbf{B} = 0$,

$$\frac{\partial B_z}{\partial z} = -2 \frac{\partial B_x}{\partial x} = B', \quad (3.34)$$

where B' is the magnetic field gradient along z . The magnetic field near the center has the general form

$$\mathbf{B} = B' \left(-\frac{x}{2} \mathbf{e}_x - \frac{y}{2} \mathbf{e}_y + z \mathbf{e}_z \right) + \mathbf{B}_0, \quad (3.35)$$

where \mathbf{B}_0 is a spatially uniform magnetic field. A uniform magnetic field \mathbf{B}_0 displaces the zero of the magnetic trap such that the field can be expressed as $\mathbf{B} = B'[-(x - x_0)/2, -(y - y_0)/2, z - z_0]$, where $(-x_0/2, -y_0/2, z_0) = -\mathbf{B}_0/B'$. Our experimental apparatus includes three pairs of Helmholtz coils along the orthogonal directions: $\mathbf{e}_x + \mathbf{e}_y$, $\mathbf{e}_x - \mathbf{e}_y$ and \mathbf{e}_z ; to generate uniform magnetic fields in the central region of the magnetic quadrupole trap²². For simplicity I focus on the particular case where $\mathbf{B}_0 = B_0 \mathbf{e}_z$ and the magnetic trapping potential becomes

$$U(\mathbf{r}) = \mu_B g_F m_F B' \sqrt{\frac{x^2}{4} + \frac{y^2}{4} + (z - z_0)^2}, \quad (3.36)$$

where $z_0 = -B_0/B'$. Very close to the center of the trap, where the field is zero, the quadrupole potential is linear along all directions $U(\mathbf{r}) \approx \mu_B g_F m_F B' (\rho/2 + |z - z_0|)$, here ρ is the cylindrical radial coordinate $\rho = \sqrt{x^2 + y^2}$.

Figure 3.13b shows the magnetic trapping potential as a function of position along \mathbf{e}_z . To appreciate the energy scales involved in magnetic trapping, it is useful to compare the magnetic trapping potential to the gravitational potential energy $U_g = mgz$. The gravitational field gradient is $mg/h = 2.14 \text{ kHz}/\mu\text{m}$, where m is the mass of an atom and $g = 9.806 \text{ }\mu\text{m/ms}^2$ is the standard acceleration of gravity [58]. Levitation of magnetically trappable spin states is thus achievable by selecting the appropriate field strength and position with respect to the magnetic trap center. For $|F = 1, m_F = -1\rangle$ ^{87}Rb atoms, a magnetic field gradient of $B' = 3.06 \text{ mG}/\mu\text{m}$ makes it possible to levitate the atoms against gravity for $z < 0$.

In the experimental setup, the strength of the magnetic trapping potential is directly proportional to the current in the anti-Helmholtz coils, the trap can be easily compressed or relaxed. In the experimental sequence to prepare an ultracold gas, the magnetic trap is suddenly turned on after optical pumping and optical molasses, when the atoms have mostly been transferred into $|F = 1, m_F = -1\rangle$.

Once the $F = 1$ atoms are stored in the magnetic trap, we apply a tunable rf-field to remove the most energetic atoms from the trap. High magnetic gradients ($B' \approx 7 \text{ kHz}/\mu\text{m}$) are used at the initial stages of rf-induced evaporation from the magnetic trap, since compression enhances the elastic collisional rate and promotes faster thermalization²³. To understand the mechanism of

²²Atom loss due to non-adiabatic spin-flips at the zero of quadrupole field [66] are overcome in our experiment by this uniform bias field [67].

²³Close to the end of the evaporation process in the magnetic trap, decompression is required to minimize the inelastic collisions that occur at the final high densities.

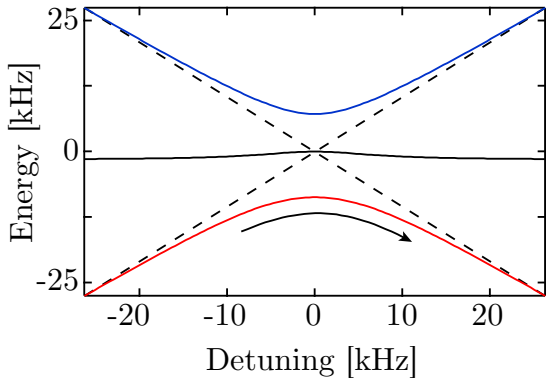
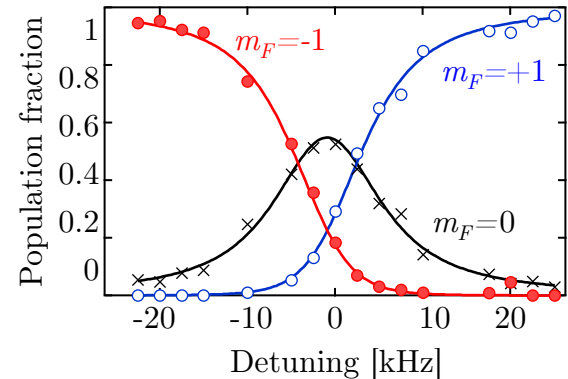
a. Eigenenergies of an $F=1$ rf-dressed system**b.** Spin composition of the lowest energy state

Figure 3.14: rf dressed system. **a.** Calculated eigenenergies of the rf-dressing Hamiltonian H' , with $\Omega_{\text{rf}} = 2\pi \times 11.2$ kHz and $\epsilon = -2\pi \times 1.7$ kHz. **b.** An rf-dressing field in combination with a mechanism to control the detuning constitute a useful technique to manipulate spin states in an optical dipole trap. Shown are measured fractional populations in each spin state from an adiabatic rapid passage sequence (see Sec. 3.9.4): $m_F = -1$ (closed symbols), $m_F = 0$ (crosses), and $m_F = +1$ (open symbols). The continuous curves correspond to the expected behavior for a dressing field using the above parameters.

rf-induced evaporation, it is useful to solve the problem of a multiple level atom in the presence of an oscillating magnetic field. In the following I will focus on the case of the m_F states of the $F = 1$ manifold of ^{87}Rb , interacting with a variable field $\mathbf{B}_{\text{rf}} = B_0 \cos(\omega_{\text{rf}} t) \mathbf{e}_x$.

3.9.2 Three level system in the presence of an oscillating magnetic field. In the presence of a small uniform magnetic field, the $F = 1$ manifold can be considered as a 3-level system with unperturbed eigenenergies E_{-1}, E_0 and E_{+1} , where $E_{-1} - E_{+1} = 2\hbar\omega_Z$.

The interaction with the rf-field is described by the perturbative Hamiltonian $H' = \mu B_0 \cos(\omega t)$, whose matrix representation in the basis of spin states $\{| -1 \rangle, | 0 \rangle, | +1 \rangle\}$ is

$$H' = \hbar \begin{pmatrix} -\delta & \Omega_{\text{rf}} \cos(\omega_{\text{rf}} t) & 0 \\ \Omega_{\text{rf}} \cos(\omega_{\text{rf}} t) & \epsilon & \Omega_{\text{rf}} \cos(\omega_{\text{rf}} t) \\ 0 & \Omega_{\text{rf}} \cos(\omega_{\text{rf}} t) & +\delta \end{pmatrix}, \quad (3.37)$$

where $\hbar\Omega_{\text{rf}} = \langle m_i | \mu B_0 | m_j \rangle$ is the associated Rabi frequency and $m_i \neq m_j$; $\delta = \omega - \omega_Z$ is the detuning from rf resonance; and $\epsilon/\hbar = E_0 - (E_{-1} + E_{+1})/2$ is the quadratic Zeeman shift²⁴. Given that $\cos(\omega_{\text{rf}} t) = (\text{e}^{i\omega_{\text{rf}} t} - \text{e}^{-i\omega_{\text{rf}} t})/2$, a transformation to the frame rotating at ω_Z in combination with

²⁴Given that the wavelength of the rf field ranges from a few cm to tens of km, the single photon recoil momentum is 5 to 11 orders of magnitude smaller than that associated with an optical transition (e.g. 790 nm for ^{87}Rb). An rf transition modifies the spin state of an atom while leaving its momentum unchanged.

the rotating-wave approximation²⁵ gives

$$H' = \hbar \begin{pmatrix} -\delta & \Omega_{\text{rf}}/2 & 0 \\ \Omega_{\text{rf}}/2 & \epsilon & \Omega_{\text{rf}}/2 \\ 0 & \Omega_{\text{rf}}/2 & +\delta \end{pmatrix}. \quad (3.38)$$

The eigenstates of the system are obtained from the diagonalization of H' ; the eigenenergies $E_j = \hbar\omega_j$ ($j = -1, 0, +1$) are the solutions to the characteristic equation

$$\omega_j^3 - \epsilon\omega_j^2 - (\delta^2 + \frac{\Omega_{\text{rf}}^2}{2})\omega_j + \epsilon\delta^2 = 0. \quad (3.39)$$

Figure 3.14 shows the eigenenergies, and the spin composition of the lowest energy eigenstate of H' as a function of δ . Exactly on resonance $\delta = 0$, the normalized lowest energy eigenstate is $|\psi_{\text{rf}}\rangle = (a_{-1}| -1\rangle + a_0| 0\rangle + a_{+1}| +1\rangle)/\sqrt{N}$, with coefficients: $a_{-1} = a_{+1} = \Omega_{\text{rf}}/2E_{-1}$, $a_0 = 1$, where $E_{-1} = -(\epsilon + \sqrt{\epsilon^2 + 2\Omega_{\text{rf}}^2})/2$ is the energy of the lowest rf-dressed state and $N = 1 + (\Omega_{\text{rf}}/E_{-1})^2/2$ is a normalization constant.

3.9.3 rf-induced evaporation in a magnetic trap. rf-induced evaporation uses an rf magnetic field with tunable frequency f_{rf} (Fig. 3.13c.) to selectively transfer the most energetic atoms into untrappable states, forcing evaporation and cooling the system. When the dressed system is close to resonance with the rf-field, an avoided crossing develops, introducing a bend in the potential energy seen by the atoms (Fig. 3.14a.); this is the escape mechanism of the atoms in rf-induced evaporation; at this point, the initial (trappable) spin undergoes transitions to the other (untrappable) spin states (Fig. 3.14b.).

The frequency of the rf-field at the beginning of the evaporation sequence is chosen based upon the initial kinetic energy (temperature) of the atomic sample captured in the magnetic trap. An upper limit to this energy is given by the Doppler cooling limit from the preceding optical molasses stage $k_B T_D = \hbar\Gamma/2$. For ^{87}Rb this is $k_B T_D = h \times 38$ MHz, or equivalently $T_D = 146 \mu\text{K}$. We typically perform forced evaporation in the magnetic trap by scanning the frequency f_{rf} of an external rf-field from 22 MHz down to 2 MHz, corresponding to a final trap depth of $U = k_B 48 \mu\text{K}$.

3.9.4 Adiabatic rapid passage. The manipulation of spin states with rf-fields is efficient and reliable. Adiabatic rapid²⁶ passage (ARP), achieved by sweeping the detuning across resonance to efficiently transfer the system from a spin state to another state, is routinely used in our experiments to prepare spin-superposition states in an optical trap.

²⁵In the rotating-wave approximation we neglect the rapidly variating terms rotating at $\omega + \omega_Z$.

²⁶In case that the transitions are induced by optical fields, “rapid” is relative to the spontaneous emission rate.

We start with a BEC in $m_F = -1$ and ramp a magnetic bias field, which Zeeman splits the spin states in the $F = 1$ ground state manifold of ^{87}Rb by $\hbar\omega_Z$. An rf-dressing field of frequency $\omega_{\text{rf}}/2\pi$ couples these states with strength Ω_{rf} . The amplitude of the bias field sets the detuning from rf-resonance δ . We perform ARP by ramping the bias field adiabatically with respect to the effective change of the dressed state energy, to avoid transitions to higher energy eigenstates. The system follows the lowest dressed energy (Fig. 3.14a, bottom continuous curve) and its spin superposition is modified to the point that it can completely be transferred into $m_F = +1$ for sufficiently large δ . We achieve adiabaticity by ramping the detuning in a time $t > 15$ ms, well above the $\approx 20 \mu\text{s}$ estimated adiabatic time-scale set by the initial detuning $\delta \approx -50$ kHz. The adiabaticity criterion $1/\Delta t \ll \omega_Z$ links the rate $1/\Delta t$ at which the internal energy splittings change as the atom moves, compared with the actual Zeeman splitting ω_Z .

CHAPTER 4

EXPERIMENTAL SETUP

The first part of this chapter describes the experimental sequence to produce ^{87}Rb BECs in our apparatus; succeeding sections detail the main parts of the apparatus and discuss relevant experimental methods.

4.1 EXPERIMENTAL SEQUENCE TO ACHIEVE BEC

Figure 4.1 provides an overview of the experimental setup and sets the laboratory coordinate system. Our experiments start with a sample of natural ^{87}Rb , whose temperature is increased up to 400 K in the Rb-oven to generate a collimated atomic beam propagating along $-\mathbf{e}_x$. When exiting the oven, the atoms interact with a pair of laser beams propagating along $+\mathbf{e}_x$ (the slower and the slower repump) all along the Zeeman slower. The non-homogeneous magnetic field generated by the Zeeman slower compensates for the Doppler shift experienced by the moving atoms and sets the appropriate conditions for laser cooling.

A magneto-optical trap (MOT) collects slowly moving atoms at the center of the main experimental vacuum chamber. Three intersecting and mutually orthogonal pairs of counter-propagating laser beams, and a quadrupolar magnetic field create the MOT. The quadrupolar magnetic field provides a uniform magnetic field gradient $B'_z \approx 12 \text{ G/cm}$ along \mathbf{e}_z , and it is generated by a set of anti-Helmholtz coils running a current of $I_{\text{quad}} = 25 \text{ A}$ (coils not shown in Fig. 4.1). We typically load the MOT from 0.5 to 3 s; we stop loading by closing the oven shutter¹ in 12 ms, and turning off the Zeeman slower fields as well as the slower cooling beams (MOT and repump).

Prior to optical molasses we turn off the quadrupole field from the experiment, and set the laser detuning for the MOT beams 13 MHz above the cooling transition in $10 \mu\text{s}$; additionally the MOT repump laser intensity is decreased. During the 19 ms of optical molasses, we sweep the MOT detuning from 104 to 34.42 MHz below $F = 2 \rightarrow F' = 3$; this allows addressing atoms in a large velocity range.

¹Closing the oven shutter prevents collisions between energetic atoms and the laser cooled atoms.

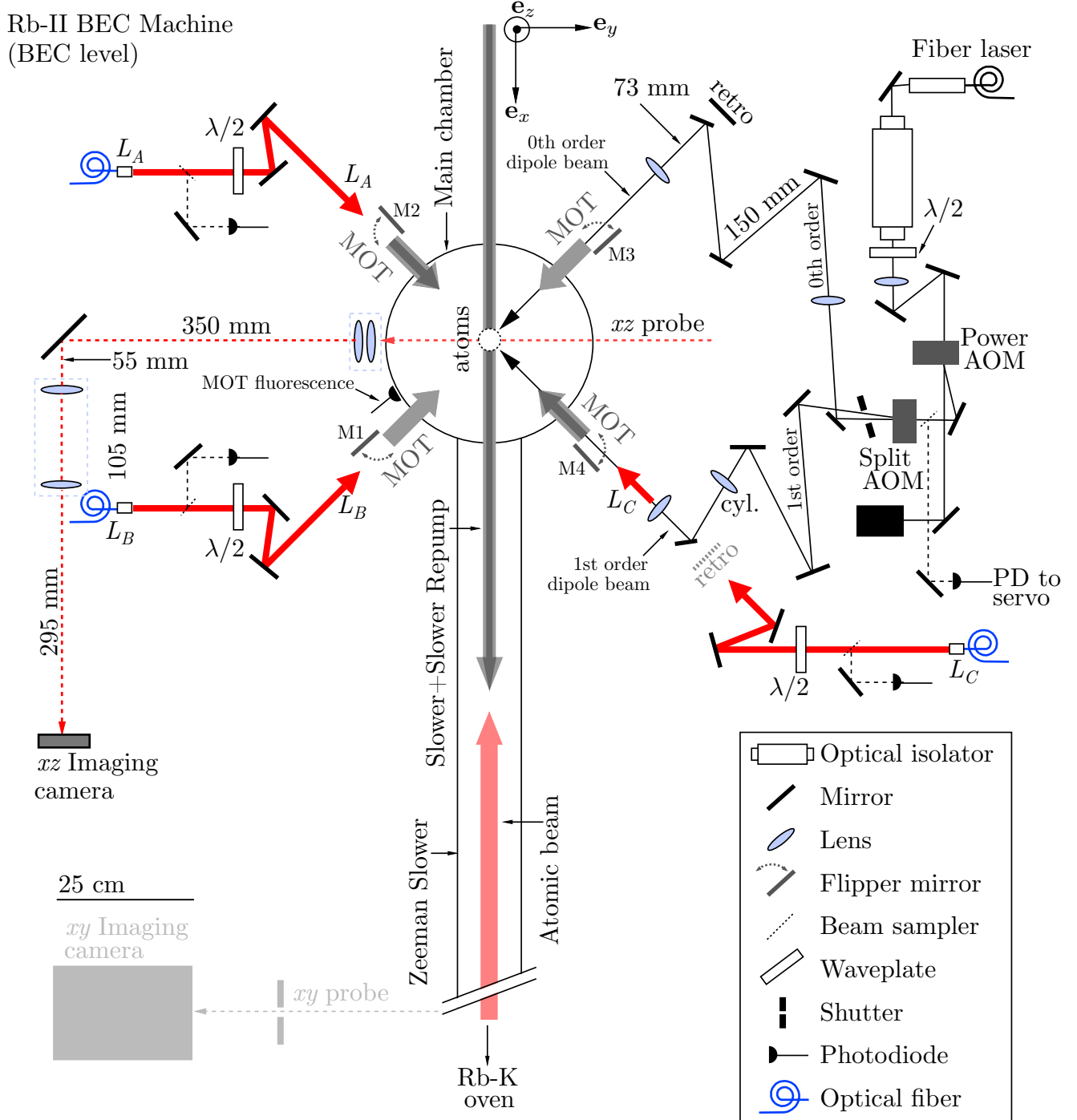


Figure 4.1: Schematic of Rb-II BEC machine (BEC level). An atomic beam emerging from the Rb-K oven is laser cooled along the Zeeman slower and trapped in a MOT at the center of the main experimental chamber. Motorized flipper mirrors (M_1 - M_4 , M_{top} and M_{bottom} not shown) send the 8 mW MOT beams toward the chamber center, and are moved out of the way to allow optical access for dipole trap beams and probing lasers (L_A , L_B , L_C and xy imaging). Indicated are two independent imaging systems whose probe beams propagate along $-e_y$ and $-e_z$. The xy imaging optics and camera are located on a lower level (see Fig. 4.2). This figure is to scale. Also see Fig. 4.17.

With a reduced MOT repump intensity the atoms decay into the $F=1$ ground state. Prior to capturing the atoms into a magnetic trap, we perform optical pumping during 1 ms to increase the population of the magnetically trappable state $|F=1, m_F=-1\rangle$. Optical pumping is performed by illuminating the atoms with the slower repump beam ($F=1 \rightarrow F'=1$). We set up the quantization axis (adjusting the bias fields) such that the atoms see the slower repump as a σ_- -polarized radiation field. We choose the bias fields experimentally, by sending the optical pumping beam to the atoms and scanning the direction of the bias fields to maximize the number of atoms in $|F=1, m_F=-1\rangle$; Table 4.1 shows optimum values.

We proceed to fully turn off the repump and slower repump beams, and to suddenly turn on (in 1 ms) the quadrupole field with current $I_{\text{quad}} \approx 130$ A such that the $|F=1, m_F=-1\rangle$ atoms are trapped. All cooling beams are later turned off and the bias fields are jumped to their optimal values for magnetic trapping (Table 4.1); the result is that the atoms are purely levitated with the quadrupole trap. With a 1 ms pulse of the xz probe beam ($F=2 \rightarrow F'=3$) we blow away the atoms that are not in the $|F=1, m_F=-1\rangle$ state.

After holding the atoms during 20 ms in the magnetic trap, we start the compression process in the magnetic trap, by ramping the quadrupole current to $I_{\text{quad}} = 240$ A, in order to increase the collisional rate for thermalization of the system.

We selectively remove the most energetic atoms from the trap by illuminating the atoms with rf-irradiation to induce transitions into non-trappable states. We sweep the frequency of the rf-field from 22 to 4 MHz in 2 s, using a Novatech 409A programmable frequency synthesizer. In preparation for the final transfer to the 1064 nm optical crossed dipole trap, we send the dipole beams through the chamber at this point; but their optical trapping potential does not overlap with that of the magnetic trap which is displaced vertically with a large bias field along \mathbf{e}_z .

As the atomic sample becomes more dense, we decompress the quadrupole (ramping the current from 300 A to 70 A with a $\tau = 1.5$ s decaying exponential ramp during 3 s) to prevent atom loss due to three body recombination. During the 3 s decompression the 4 MHz rf-knife is still on and we simultaneously load the optical dipole trap from the magnetic quadrupole trap by ramping the bias field along \mathbf{e}_z from 10 A to 5.6 A to move the magnetically trapped atoms to the optical trap location.

Table 4.1: Bias fields to cancel stray fields, magnetic trapping and optical pumping.

| Field direction | Nulling [A] | Magnetic Trapping [A] | Optical Pumping [A] |
|-------------------------------|-------------|-----------------------|---------------------|
| $\mathbf{e}_x - \mathbf{e}_y$ | -1.08 | -6 | 1.368 |
| $\mathbf{e}_x + \mathbf{e}_y$ | 0.03 | 0 | 0.8 |
| \mathbf{e}_z | 3.65 | 10 | 2 |

Rb-II BEC Machine
(lowest level)

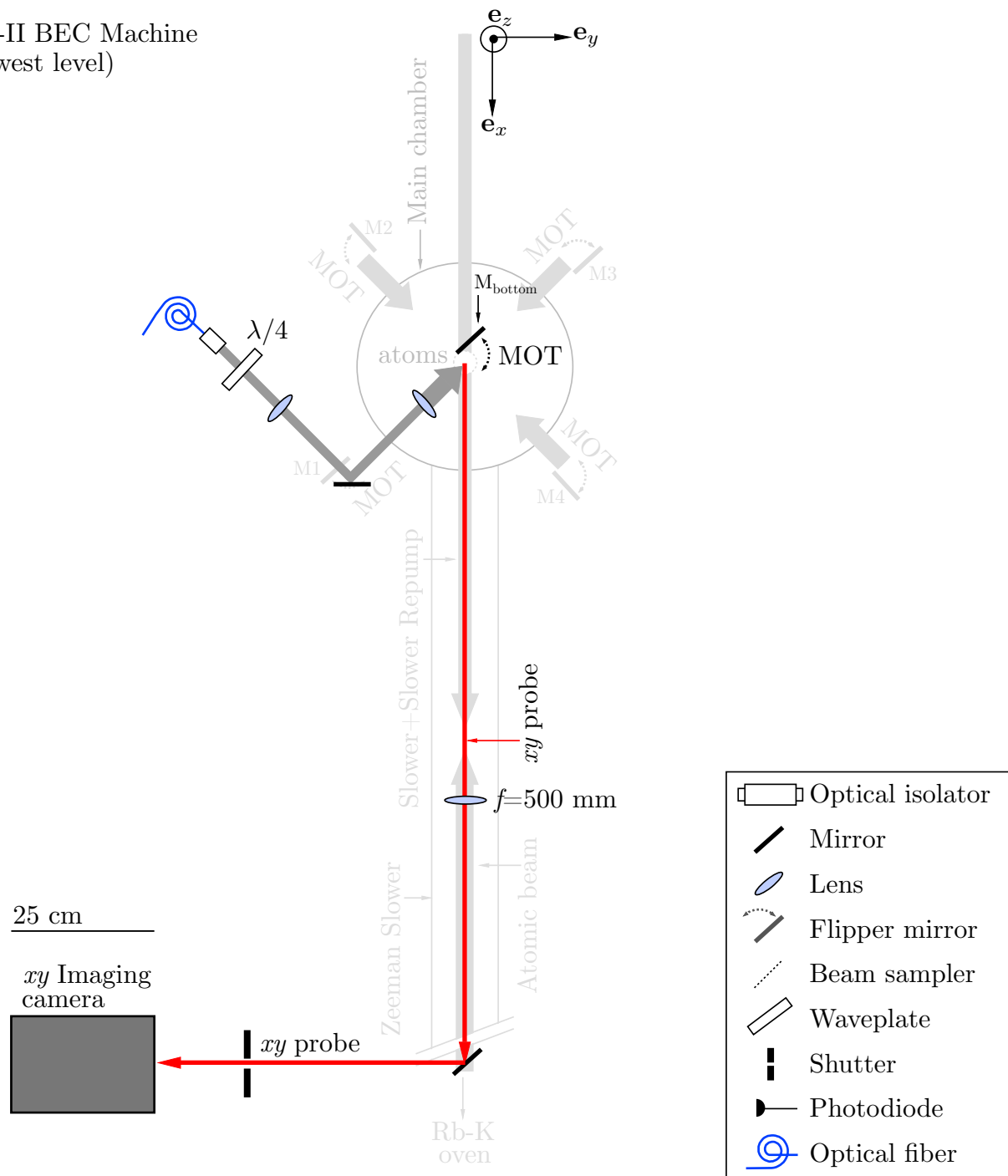


Figure 4.2: Schematic of Rb-II BEC machine (lowest level), continued from Figure 4.1. This figure shows the optical fiber launch of the up-going MOT beam. A tiny right angle prism mirror, sitting at a motorized flipper mount M_{bottom} and located just below the main chamber, sends the MOT beam along e_z . Also shown are some of the optics of the xy imaging system; the xy probe beam originates at the top of the experimental setup and propagates along $-e_z$ across the main chamber and through the atoms to finally reach the camera. This figure is to scale.

After the atoms are in the combined magnetic and optical trapping potential, we modify the optical trapping potentials to allow the most energetic atoms to leave. In our early experiments both beams were similar in size and geometry, and evaporation was performed by keeping their relative powers balanced while reducing their overall power [5]. In our latest experiments, the 1st order beam is significantly smaller than the 0th order beam and evaporation is done by keeping the overall power constant while redistributing the relative power in the beams. Once the final distribution of powers is reached, we decrease the overall power in the dipole beams to reach BEC. At this point the quadrupole field still contributes, with a decreased strength of 10 A, to the trapping potential. Typical time scales for the evaporation in the optical trap range from 1.5 to 3 s.

We finally ramp down the quadrupole current from 10 A to 0 A with a $\tau = 0.5$ s exponential ramp during 3.5 s; the time duration for this step is set by the lowest trapping frequency. Care should be taken to cancel stray magnetic fields since their presence, during the removal of the quadrupole potential, can excite the breathing as well as sloshing modes [39]. We allow the quadrupole field to settle to zero for 100 ms. Our BEC sits now in a purely optical trapping potential.

After preparing a BEC we dedicate the subsequent lines in the program to the system preparation (illuminate with rf-fields, Raman lasers, optical lattices, ...) and the realization of experiments with ultracold atoms; typical time scales for experiments range from 1 μ s to 10 s.

Once the preparation is over we change the system to detection, which can be a combination of: expansion in time of flight (TOF), mapping of the occupied momentum states into free momentum states, spatial separation of spins by a magnetic field gradient (Stern-Gerlach experiment), and others.

Finally we perform resonant absorption imaging in two primary planes xy and xz . First we pump the atoms into the $F=2$ state using the slower repump beam ($F=1 \rightarrow F'=1$), then we pulse the probe beam and image the absorption of this light by the atoms. The imaging pulse typically ranges from 50 to 100 μ s. We also take reference images of the probe beam only, and a background image with no light.

4.2 COMPUTER CONTROL AND DATA ACQUISITION

A fundamental characteristic of ultracold atom experiments is the high degree of control of most experimental variables; this feature relies to a great extent on the computer control of various instruments in the experiment. Additionally, the amount of and rate at which data is collected requires an optimum scheme for data acquisition. We dedicate two separate computers for control (Rubidium-C) and data acquisition (Rubidium-D); both computers use LabVIEW based software. This section describes both, the basic setup for operating our experimental apparatus and the data acquisition scheme.

Table 4.2: List of AOs and devices to control the experiment.

| Channel Name | Analog variable | Min [V] | Max [V] |
|--------------|-------------------|---------|---------|
| Dev1-AO0 | Quadrupole Coil | 0 | 800 |
| Dev1-AO1 | Slower Coil | -10 | 100 |
| Dev1-AO2 | Reverse Coil | -10 | 100 |
| Dev1-AO3 | MOT Detuning | 40 | 250 |
| Dev1-AO4 | Repump Detuning | 0 | 10 |
| Dev1-AO5 | MOT Intensity | 0 | 2 |
| Dev1-AO6 | Slower Intensity | 0 | 2 |
| Dev1-AO7 | Probe Intensity | 0 | 2 |
| Dev2-AO0 | Repump Intensity | -0.5 | 2 |
| Dev2-AO1 | - | - | - |
| Dev2-AO2 | - | - | - |
| Dev2-AO3 | - | - | - |
| Dev2-AO4 | - | - | - |
| Dev2-AO5 | Evaporation Mixer | 0 | 10 |
| Dev2-AO6 | - | - | - |
| Dev2-AO7 | - | - | - |
| Dev3-AO0 | Finebias Z | -20 | 20 |
| Dev3-AO1 | Finebias X-Y | -20 | 20 |
| Dev3-AO2 | Finebias X+Y | -20 | 20 |
| Dev3-AO3 | - | - | - |
| Dev4-AO0 | 1064 Intensity | -1 | 2 |
| Dev4-AO1 | 1064 Split | -0.5 | 2.3 |
| Dev4-AO2 | - | - | - |
| Dev4-AO3 | - | - | - |

4.2.1 Control computer. Rubidium-C is connected to two NI BNC-2110 connector blocks (Dev1 and Dev2) operating as a total of 16 analog out (AO) channels; as well as to two NI USB-6229 data acquisition (DAQ) devices (Dev3 and Dev4) with a total of four AO channels, 32 analog in (AI) channels and 48 (digital out) DO, each. A pair of Icron Ranger 442 high-speed USB extenders is used to independently connect Dev3 and Dev4 to Rubidium-C. Table 4.2 shows all the analog variables controlled in our experiment. Most AOs are sent through a $50\ \Omega$ buffer to amplify the current required to drive various instruments.

We generate digital signals with two SpinCore PB24-512 pulse blasters (PB) with a total of 24 DO channels each, as well as with some DOs of Dev4 as indicated in Table 4.3.

All of these devices are programmed using LabVIEW-based control software. In our control scheme, the PB and other devices are programmed in advance and are triggered from the PB card. A matrix of the experimental hardware timing sequence is stored as a global variable or “hardware

Table 4.3: List of DOs and devices to control the experiment.

| Channel name | Digital variable |
|--------------|------------------------------------|
| PB0-0 | MOT AOM rf-switch |
| PB0-1 | MOT Shutter |
| PB0-2 | MOT Rep./slower Rep. AOM rf-switch |
| PB0-3 | MOT repump Shutter |
| PB0-4 | Slower AOM rf-switch |
| PB0-5 | Slower/slower repump Shutter |
| PB0-6 | - |
| PB0-7 | Oven Shutter |
| PB0-8 | Probe <i>xy/xz</i> AOM rf-switch |
| PB0-9 | <i>xy</i> Probe Shutter |
| PB0-10 | <i>xz</i> Probe Shutter |
| PB0-11 | <i>xy</i> Camera Shutter |
| PB0-12 | Camera Trigger |
| PB0-13 | rf-Evaporation switch |
| PB0-14 to 17 | - |
| PB0-18 | rf-Evaporation Trigger |
| PB0-19 to 20 | - |
| PB0-21 | Oscilloscope Trigger |
| PB0-22 | Raman AOMs rf-switch |
| PB0-23 | AO Staging list “clock in” bit |
| Dev4-DO0 | 1064 AOM rf-switch |
| Dev4-DO1 | 1064 Shutter |
| Dev4-DO2 | - |
| Dev4-DO3 | - |
| Dev4-DO4 | - |
| Dev4-DO5 | MOT Flippers |
| Dev4-DO6 | Raman Shutters |

image”. The basic structure of the control software relies on two programs: `SetList.vi` modifies and generates the hardware configurations/timing of a given “hardware image”, and allows the user to modify the experimental control sequence; while `CycleX.vi` physically programs the hardware reading the “hardware image”.

A synchronization scheme between `SetList.vi` and `CycleX.vi` allows the programming of scans of various experimental parameters. LabVIEW talks to the DAQ computer (Rubidium-D) over the network; both computers can see the “hardware image”. A third control program, namely `ManualControls.vi`, allows to control the experiment in non-cycling mode; e.g. this is ideal to diagnose the MOT.

4.2.2 Data Acquisition computer. Rubidium-D talks to the control computer over the network through **LabVIEW**. It is also connected to the *xy*-imaging camera via an **Icron Ranger 442** high-speed USB extender; and to the *xz*-imaging camera through an **IEEE 1394 FireWire** interface. Both cameras are triggered by the same PB channel.

We use **Wavemetrics Igor Pro** to visualize and analyze data. The software for DAQ is **LabVIEW**-based; it processes the acquired images into an **Igor Pro** binary wave. We exploit the built-in programming environment of **Igor Pro** to automate data processing and analysis.

Finally, the vital signs of our BEC-machine (i.e. MOT fluorescence levels, voltage ramps, rf-fields, intensity in various laser beams, ...) are recorded by two **Tektronix TDS 2014B** oscilloscopes, connected via USB to Rubidium-D.

4.3 VACUUM SYSTEM

Our BEC machine has two independent ultra-high vacuum (UHV) regions corresponding to the Rb-K oven and the main experimental chamber. They join at the input of the Zeeman slower and can be isolated from each other by means of a pneumatic gate valve; this is a nice feature that allows renewal of the alkali sources without the need to vent the main chamber.

4.3.1 Rb-K oven. Figure 4.3 shows the schematic configuration of the oven. The Rb and K reservoirs are independently wrapped with an **Ari Industries BXX06B24-4T** flexible heating rod, and each is connected to an **Omega CN77333-PV** temperature controller. The whole system is covered by heat reflective wrap. The relative temperatures of the reservoirs are modified to control the flux of each atomic species; typical temperatures for experiments with Rb are $T_1 = 125\text{ }^{\circ}\text{C}$ and $T_2 = 100\text{ }^{\circ}\text{C}$.

The oven is pumped by two 55 L s^{-1} **Varian StarCell** ion pumps, and its pressure is maintained around 2×10^{-8} mbar as measured from the current of an ion gauge. The ion pump, installed in the chamber containing the cold cup, is permanently kept at $70\text{ }^{\circ}\text{C}$ to prevent alkali poisoning of the ion pumps.

The cold cup is kept at $-40\text{ }^{\circ}\text{C}$ by a **Custom Thermoelectric 19012-5L31-06CQQ** two stage TEC, whose dissipated power is pumped by a **Swiftech** heat exchanger in combination with a liquid recirculating chiller **ThermoCube 10-400-1C-1-SWVD**. The cold cup is a very important element to keep our vacuum in shape; so we take care that it is always kept below $-30\text{ }^{\circ}\text{C}$. On August 2010, a severe storm triggered the reboot of various instruments in the laboratory as well as a pump failure of the TEC chiller; this in turn caused the melting of the water hoses close to the overheated TEC and the increase of the cold cup temperature to $50\text{ }^{\circ}\text{C}$, which increased the pressure by a factor of 500 from its standard overnight ion current level 10^{-7} A . A one-week bake of the oven region helped to recover the standard operating pressure. To prevent ice formation and the potential failure of the TEC, we let dry nitrogen flow into the TEC region, which is isolated from air by plastic stretch

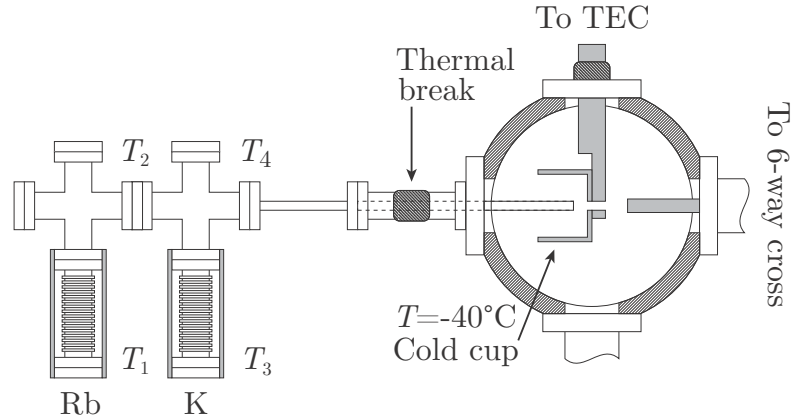


Figure 4.3: Schematic of Rb-K oven. The Rb and K reservoirs are heated up to $T_{1,2} \approx 400$ K to generate an atomic beam of each species. The nozzles are kept at $T_{2,4} \approx 430 - 490$ K to avoid condensation of atoms in the nozzle and subsequent reduction of the atomic flux. The collimation of the atomic beam is achieved as the atoms travel through the pipeline. A copper cold cup, kept at ≈ -40 °C by a water chilled thermoelectric cooler (TEC) collects the excess of atoms that do not reach the 6-way cross region are collected in . A thermal brake isolates the chamber from the hight temperature reservoirs. An in-vacuum shutter prevents the atomic beam to reach the main experimental chamber during and after BEC preparation.

wrapping and thermal insulation tape. We also pay attention to the formation of plugs inside the cooling water system; in particular, the heat exchanger can accumulate an important amount of whitish sediments in its interior, but it is relatively easy to open it and clean it.

4.3.2 Main experimental chamber. The main chamber is made of stainless steel and has a total of 24 viewports: two 14 cm diameter recessed windows located at the top and bottom of the chamber; six viewports with diameter $d = 7$ cm located around the chamber, normal to the xy plane; and 16 mini-conflat windows $d = 3.8$ cm distributed around the chamber. Two of the smallest viewports are dedicated to diagnostics of the MOT. This chamber is pumped by a 55 L s^{-1} Varian StarCell ion pump; its ion gauge reads zero current (μA scale), which corresponds to a significantly reduced pressure from that at the oven.

4.3.3 General advice when working with alkalis and UHV. Metallic K and Rb come in partially full glass ampules. Due to their reactive properties, it is highly recommended to minimize their handling outside their containers. To load the metals in our apparatus, we carefully break one ampule at a time using a pair of pliers; then we get rid of most of the glass and throw the (now open and broken) residual glass with the metal into each reservoir; finally we closed the reservoirs.

It is important to note that K comes embedded in an Ar atmosphere. Ar is a noble gas that can potentially damage an ion pump (it degrades the performance of the pump by erosion of the

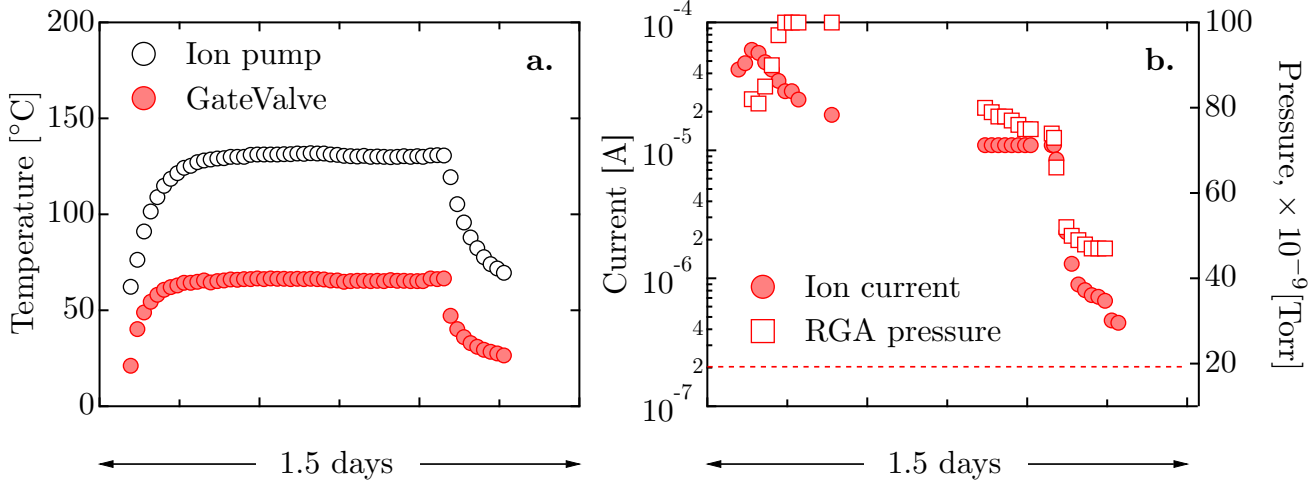


Figure 4.4: Temperature, pressure and time scales for baking. **a.** Temperatures as monitored with a thermocouple reader using K-type thermocouples at the ion pump that is closest to the cold cup and at the gate valve. **b.** The pressures were measured with both an ion gauge and an RGA. The typical ion current when the BEC machine is not cycling (ovens off, oven shutter closed) is $\approx 2 \times 10^{-7}$ A (dashed line) and rises by an order of magnitude when BECs are produced.

chemical layers which cover the cathode) and we want to have as little as possible of it in the system. By opening the glass cell containing K most of the Ar has been released, but it is important not to turn on any ion pumps for a long period of time until high vacuum (where the presence of Ar is minimum and it is safe for the pumps to operate) has been reached.

4.3.4 Baking. Raising the temperature of the whole system (baking) is a standard procedure to allow the release of additional vapors (H, and maybe CO and CO₂) residing on and in its interior walls, i.e. outgassing [68]. Outgassing, and not volume gas removal, determines the final pressure of the high vacuum region.

Prior to and during the bake we pump the system with a Pfeiffer Vacuum HiCube 80 Eco turbo pump (TP). The driving power of the TP typically starts around 20 W, and should decrease to 15 W in the absence of leaks, when high vacuum is reached. The use of a residual gas analyzer (RGA) is recommended to obtain the mass spectrum of the substances pumped out from the system as well as an estimate of the pressure.

4.3.4.1 Standard baking procedure in our apparatus. Below I describe a standard procedure for the baking of the oven region in our apparatus. Depending on the starting pressure (if we are just baking for maintenance or if the system was recently vented), the baking time ranges from a couple of days to several weeks.

1. Prior to baking get: (i.) as many type-K thermocouples² as temperatures you want to monitor;

²Type-K thermocouples (chromel-alumel) are the standard type used in our laboratory.

(ii.) enough heating elements (heat tapes, heat bars, ...); (iii.) enough variacs; (iv.) aluminum foil; (v.) copper wire. It is also important to check the maximum allowable baking temperature of the different parts of the experiment (chamber windows, bellows, magnets of the ion pumps³,...).

2. Install the thermocouples and firmly secure their position with the copper wire if needed.

3. Install the heating elements and fully wrap the system with aluminum foil. Avoid crossing the heat tape on itself, since this would create an extremely hot spot and can cause damage not only to the heat tape but also to other vulnerable parts in the experiment. The hose connected to the TP should also be wrapped in aluminum foil; use the copper wire to secure the wrapping if needed. Connect each heating element to a variac.

4. Gradually heat the system by turning ON the variacs to 20-30%; take care that the ion pumps are heated at a rate less than 40 °C/hr.

5. Remove the TEC from the copper connector to the cold-plate. Install a heating element to the cold-plate connector and wrap it in aluminum foil, then heat the cold-plate. When copper is heated it oxidizes and this affects its thermal conductance later on. Once we are done with baking, we polish the surface of the copper connector to the cold-plate to optimize its performance.

6. Continue increasing the amount of power into the heating elements, using the variacs. In the Oct-2010 Rb-K oven bake, the ion pumps were heated up to 200 °C and the gate valve up to 100 °C.

Due to the increased temperature of the surroundings, the connection from the slower to the oven region reached 35 °C; while the oven shutter almost matched the temperature of the intentionally heated cold cup (115 °C). Even when there is a large temperature gradient across the system during baking, we have not observed any obvious adverse effects.

7. Monitor the pressure using the ion gauges and a RGA as shown in Fig. 4.4b. When the pressure has reached a sufficiently reduced steady value as a result of pumping with the TP, turn on the ion pumps and start the cool-down by turning off the variacs.

4.4 COOLING LASERS

The laser cooling mechanism in our laboratory relies on a pair of laser systems, the MOT laser and the repump laser, beat-note locked to a primary master laser, which in turn is directly locked to a specific frequency in the atomic spectrum of Rb using a lock-in amplifier and Doppler-free saturated absorption spectroscopy [54].

4.4.1 Overview of cooling and repumping frequencies. Figure 4.5 shows the energy levels, including the hyperfine structure for the $5^2S_{1/2} \rightarrow 5^2P_{3/2}$ transition in ^{87}Rb ; the relevant transitions

³The maximum baking temperature for our ion pump is 350 °C with their magnets installed. It is possible to induce the demagnetization of the permanent magnets of the pumps if we exceed their temperature limits.

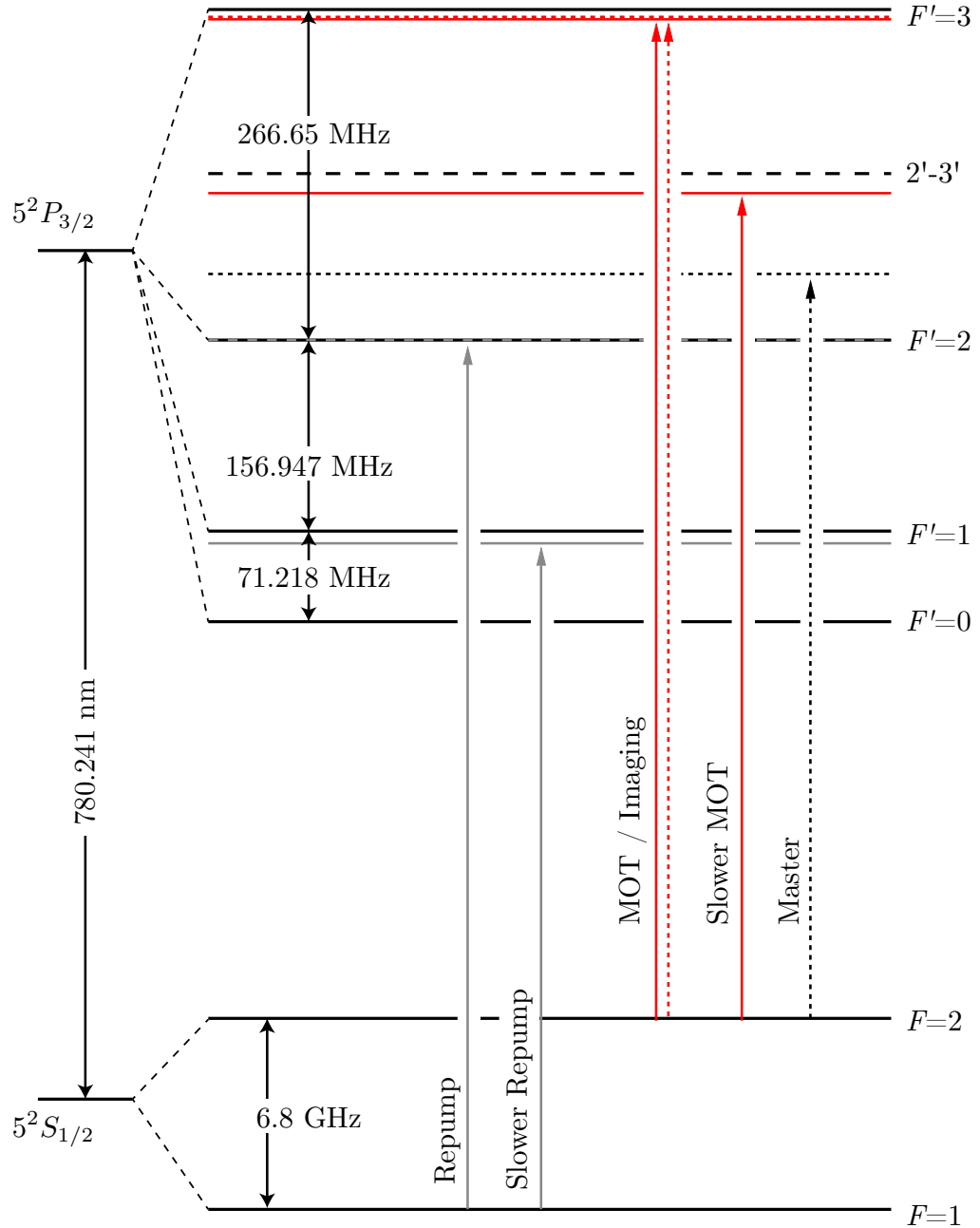
Schematic of cooling and repumping frequencies with respect to the D₂ line

Figure 4.5: ^{87}Rb D₂-line energy levels with the relative frequencies of the cooling lasers. The MOT, the slower and the Imaging lasers come from the same source, a Toptica TA-100; this laser is typically beat-note locked above the master frequency within the interval $50 \text{ MHz} \leq \nu_{\text{MOT beat-note}} \leq 147 \text{ MHz}$. The repump and the slower repump lasers both come from a Toptica DL-100, whose locking frequency is typically $64 \times 102 \text{ MHz} \leq \nu_{\text{repump beat-note}} \leq 64 \times 106 \text{ MHz}$ below the master frequency. This diagram is not to scale.

Table 4.4: Frequencies of the cooling lasers during MOT capture.

| Laser | Frequency shift ν' [MHz] | Reference transition | Detuning [MHz] |
|---------------|------------------------------|------------------------|----------------|
| Master | -80.567 | $F=2 \rightarrow F'=3$ | -213.892 |
| MOT | 59.321 | $F=2 \rightarrow F'=3$ | -7.571 |
| Slower | -81.577 | $F=2 \rightarrow F'=3$ | -148.469 |
| Imaging | 67.568 | $F=2 \rightarrow F'=3$ | 0.676 |
| Repump | 82.361 | $F=1 \rightarrow F'=2$ | -1.321 |
| Slower repump | -81.46 | $F=1 \rightarrow F'=1$ | -8.195 |

for laser cooling are the cooling transition $F = 2 \rightarrow F' = 3$ and the repumping transition $F = 1 \rightarrow F' = 2$.

Most laser beams in our apparatus are frequency shifted by ν' , using acoustic-optic modulators (AOM), with $60 \leq \nu' \leq 110$ MHz. The relative frequencies of the MOT and the repump lasers are given by the linear combination of various frequency shifts, i.e.

$$\nu_{\text{Laser}} = \nu_{\text{master}} + \nu' + \nu_{\text{beat-note}}. \quad (4.1)$$

where ν' is the frequency shift from an AOM; Table 4.4 indicates the cooling and repumping frequencies for typical operating beat-note frequencies:

$$\nu_{\text{MOT beat-note}} = 147 \text{ MHz} \quad \text{and} \quad \nu_{\text{repump beat-note}} = 64 \times 104.66 \text{ MHz} = 6.698 \text{ GHz}. \quad (4.2)$$

Most of the lasers in the laboratory operate free of intensity stabilization; we rely on the stability provided by the AOMs, which are allowed to warm up previous to our experiments, and are kept on during most of the experimental cycle to prevent temperature drifts. We maximize the time the AOMs are on at a constant rf-level with the aid of shutters (see Figs. 4.6, 4.8 and 4.13); we turn off the AOMs for some ms (the time scale is set by the shutter dynamics) while the shutters open to prevent light leaking on the atoms.

4.4.2 The master laser. The master laser beam comes from a **New Focus VORTEX 6013** diode laser (Fig. 4.6a), with tunable wavelength (frequency ν) ranging from 710 to 800 nm. It is frequency locked 80.567 MHz below the $F = 2 \rightarrow F' = 2' - 3'$ crossover of the D₂ line in ⁸⁷Rb by means of saturated absorption spectroscopy. The repump and cooling lasers are frequency locked with respect to the frequency of the master laser, via beat-note lock mechanisms described below.

The main master laser beam is split into two beams, the pump and the probe (Fig. 4.6a). The pump is double passed through an **ISOMET 1205C-2** acousto optic modulator (AOM) driven at

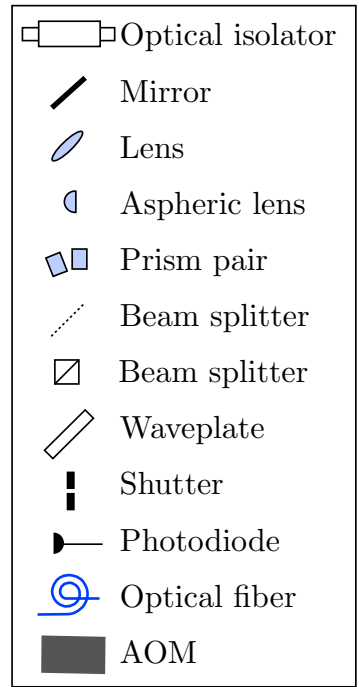
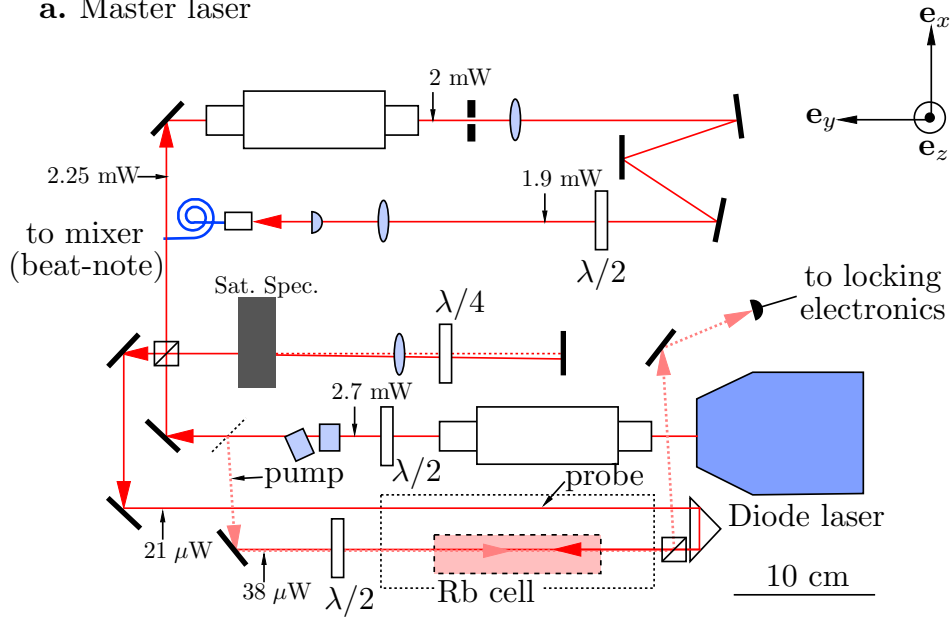
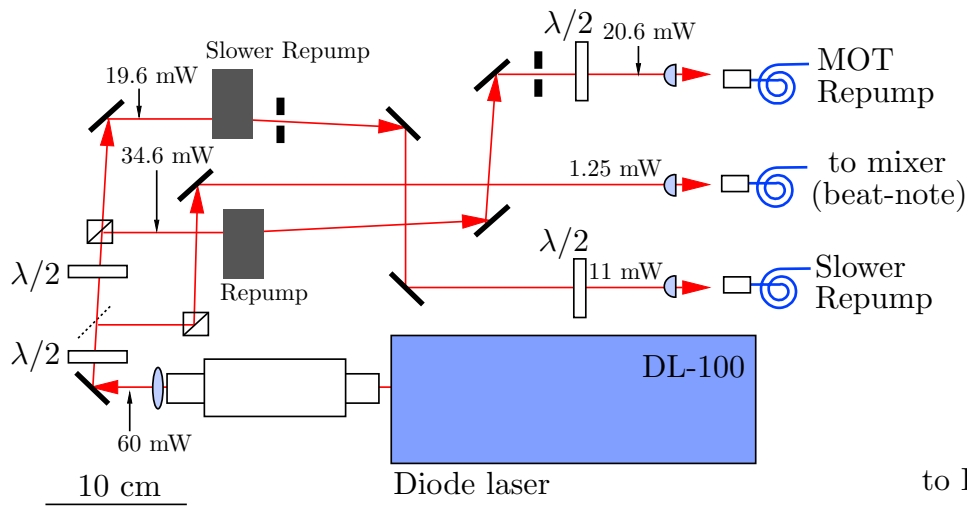
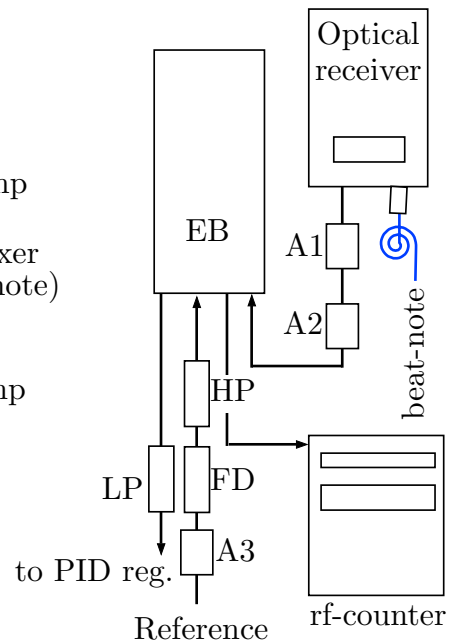
a. Master laser**b. Repump laser****c. Repump locking scheme**

Figure 4.6: Master and repump lasers optical layouts and power map. This figure is to scale. Also see Fig. 4.18 and Fig. 4.19.

$f_0=80.567$ MHz using an IntraAction DE-820MT deflector driver⁴. Both beams counter-propagate along a cell containing Rb vapor, and their frequency difference $\Delta f = 2f_0$ allows velocity-selective two-photon interactions with a group of moving atoms whose Doppler shift corresponds to the AOM driving frequency $\nu_{\text{Doppler}} = f_0$.

4.4.2.1 Frequency locking mechanism for the master laser. Figure 4.7 shows the locking schematic connections of the master laser. We measure the absorption of probe light by Rb atoms using a photodiode (PD). In order to observe the atomic spectrum, we modulate the frequency ν of the master laser in a wide range ($\Delta\lambda \approx 10$ nm) by slowly modulating the voltage of its piezo-actuator with a sawtooth signal ($f_{\text{slow}} = 1$ Hz, $V_{\text{slow}} = 2V_{\text{pp}}$). We also introduce a fast error signal via the modulation of the frequency of the probe beam at a reference rate f_{ref} within the values

$$\nu + 2f_0 - \Delta\nu \leq \nu_{\text{probe}} \leq \nu + 2f_0 + \Delta\nu,$$

where $\Delta\nu < 20$ MHz. We use the built in reference of the lock-in amplifier to generate an $f_{\text{ref}} = 100.63$ kHz signal with amplitude $V_{\text{ref}} = 2$ V. We extract the error by analyzing the probe signal as read from the PD with an SRS SR810-DSP lock-in amplifier. We send the extracted error to our home-built PID controller to get a correction, which is fed-back into the current modulation input of the laser. We focus on the absorption spectrum and the error signal for locking recorded in a Tektronix TDS 220 oscilloscope. The features shown in the error signal correspond to the $F = 2 \rightarrow F'$ set of absorption lines and crossover lines of ^{87}Rb . We lock the master laser at a frequency f_0 above the $F=2 \rightarrow F'=2-3$ crossover of ^{87}Rb (labeled *b.* in Fig. 4.7).

The typical amplitude of the error signal at the line of interest (Fig. 4.7*b.*) is 2 V peak-peak, which can be modified by changing the relative powers in the probe and the pump beams using the $\lambda/2$ wave plate behind the prism pair. The time scale to resolve the absorption features in the oscilloscope (Fig. 4.7) is around 25 ms/div, given the time constants of the system. When locked, the error signal remains close to its zero crossing value (25.8 mV) and the spectrum stays at the value corresponding to the absorption at the locking point 161 mV. A sample of the master laser is sent via optical fiber through a fiber network to be combined with repump and MOT light for frequency locking as described below.

4.4.3 The repump laser. The repump laser is a Toptica DL-100 operated at ~ 780.231 nm whose 60 mW output power is divided, as shown in Figure 4.6*b*, into the slower repump, used both at the initial cooling stage and prior to imaging, and the repump used at the MOT stage. Our MOT

⁴Double passing guarantees preserving the alignment when we modulate the probe frequency, as required in our locking scheme.

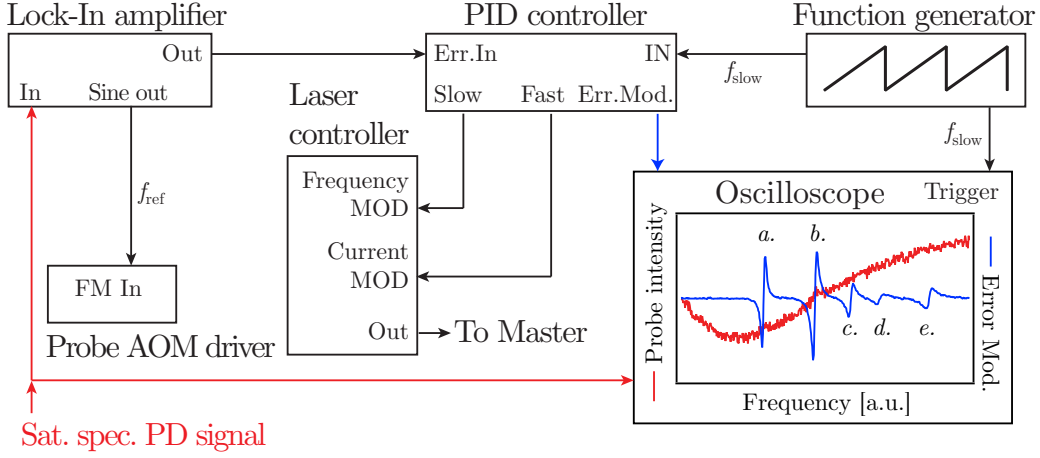


Figure 4.7: Master laser locking scheme. We sample the spectrum of natural Rb by slowly sweeping the piezo-actuator of the master laser at f_{slow} with a saw-tooth signal. A photodiode detects the saturation spectroscopy signal, and sends it to a lock-in amplifier and an oscilloscope. We introduce a fast error signal via the modulation of the frequency of the probe beam at rate f_{ref} . We extract the induced error using the lock-in amplifier and a home-built PID controller, and obtain the correction signal to be fed-back into the laser controller. The features in the error signal, detected in the oscilloscope, correspond to: (a.) $2 \rightarrow 3'$ transition; (b.) $2 \rightarrow 2' - 3'$ crossover; (c.) $2 \rightarrow 1' - 3'$ crossover; (d.) $2 \rightarrow 2'$ transition and (e.) $2 \rightarrow 1' - 2'$ crossover.

is repumped by two beams counter-propagating along $\mathbf{e}_x + \mathbf{e}_y$; they are sent to the atoms by mirrors M2 and M4, and their typical powers are 7-13 mW.

4.4.3.1 Frequency locking mechanism for the repump laser. Figure 4.6c describes the frequency locking scheme for the repump laser. A small sample of light from the master laser is combined in a fiber network with a sample of repump light to create a beat-note⁵. The combined light is sent to the optical input of a Lab-Buddy DSC-R402 optical receiver, whose output rf-signal is amplified by two consecutive MiniCircuits ZJL-7G (A1, A2) and sent to an AD EVAL-ADF4007EBZ1 evaluation board (EB).

The reference signal for the EB comes from a Novatech 409A synthesizer at 104.66 MHz; it is pre-amplified by a MiniCircuits ZX60-4016E-S+ (A3); frequency doubled by MiniCircuits FD-2 (FD); and finally filtered by MiniCircuits BHP-150 (HP). The reference frequency is later multiplied by 64 in the EB, to get the desired ≈ 6.8 GHz; for monitoring purposes, a small sample of the reference signal is probed using a Startek ATH-15 rf-counter. The output of the EB goes through a pair of low pass filters ($RC = 1$ ms) to the PID regulator panel (Toptica PID-110) of the repump laser.

⁵Two beat-notes are actually generated, one at the sum and one at the difference of the optical frequencies of the lasers in question. We focus on the signal at the frequency difference.

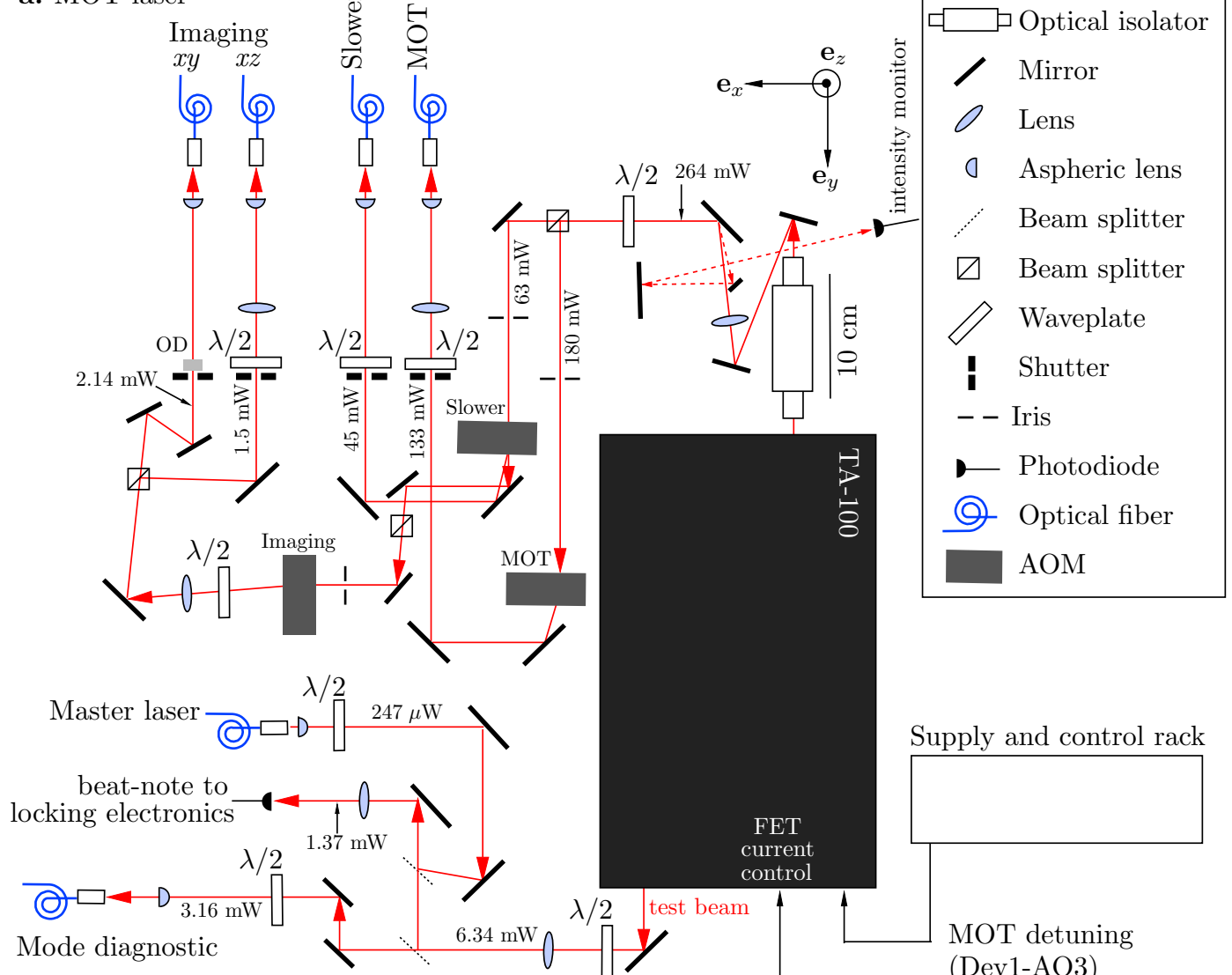
a. MOT laser

Figure 4.8: Optical layout for the MOT laser, setup for frequency locking to the master laser and overall power map. This figure is to scale. Also see Fig. 4.20 and Fig. 4.21.

Table 4.5: Typical operating values for the cooling lasers.

| Characteristic | Master | Repump | MOT |
|-----------------------------|-------------|------------|------------|
| Make | New Focus | Toptica | Toptica |
| Model | Vortex 6013 | DL-100 | TA-100 |
| Wavelength | 780.2 nm | 780.231 nm | 780.245 nm |
| Diode current | 90.2 mA | 123 mA | 79 mA |
| Diode temperature | - | 17.9 °C | 17.9 °C |
| Amplifier current | - | - | 151 mA |
| Amplifier temperature | - | - | 20.1 °C |
| Measured power | 2.7 mW | 60 mW | 264 mW |
| PD signal | 0.412 V | 0.126 V | 0.492 V |
| Amplitude of mode in cavity | 7 mV | 15 mV | 17.6 mV |

4.4.4 The MOT laser. The MOT laser is a Toptica TA-100 operated at ~ 780.245 nm. Major surgery to the MOT laser has involved three replacements of its diode (a Toptica LD-0780-0200-1 has been operating from July 2008); a replacement of the circuit board in the back of the laser control rack and the replacement of its original piezoelectric actuator by a Thorlabs AE0203D08F (both in May 2010). The symptoms for the last failure were the small resistance across the piezo as well as multi-moding and severe noise in the laser; the piezo probably died because we drove it close to its maximum voltage of 140V.

The output of the TA peaks at 500 mW under typical operating conditions, but probably due to age and non-optimum injection of the TA it can be as low as 250 mW and still produce an acceptable MOT. The output of the TA is distributed into four main laser beams (MOT, slower, *xy* Imaging and *xz* Imaging), which are sent to the main experimental apparatus through polarization maintaining optical fibers as shown in Fig. 4.8. In particular, the MOT optical fiber is connected to a Canadian Instrumentation & Research Ltd. fiber splitter, where the beam is divided into ten optical fibers. Six of them are the MOT beams with 10 mW per beam; another is used for intensity monitoring purposes.

To minimize light leakages into the experiment, we use Uniblitz mechanical shutters to block the laser beams; these shutters are mechanically isolated from the MOT laser setup by means of vibration damping mounts.

4.4.4.1 Frequency locking mechanism for the MOT laser. In contrast with the optical-fiber-based locking-scheme for the repump laser; the frequency locking mechanism for the MOT laser is setup in free space. A sample of the master laser is spatially overlapped to the optical path of the test beam coming from the back of the MOT laser. The interference of the linearly polarized laser beams creates a beat-note which is detected by a Thorlabs DET-110 ultrafast photodiode (Fig. 4.8a).

Table 4.6: Measured power in cooling beams at MOT stage.

| Laser beam | Power into fiber [mW] | PD signal [V] |
|-------------------|-----------------------|---------------|
| Master | 1.9 | 0.412 |
| Repump | 20.6 | 0.123 |
| Slower repump | 11 | 0.059 |
| MOT | 133 | 0.403 |
| Slower | 45 | 0.862 |
| <i>xy</i> Imaging | 2.14 | - |
| <i>xz</i> Imaging | 1.5 | - |

An schematic of the frequency locking electronics is shown in Figure 4.8b. The beat-note is filtered by a **MiniCircuits SHP-25** high pass filter, and amplified using a **MiniCircuits ZKL-1R5** coaxial amplifier. For monitoring purposes, a small sample (< 5%) of the signal is probed in a **Startek ATH-15** rf-counter; the signal is further processed into a home-built frequency to voltage converter and sent into a **Precision photonics LB-1005** servo controller. The reference voltage comes from the computer control command MOT detuning (Dev1-AO3). The error signal from the servo controller is fed-back into the FET current control in the back of the MOT laser.

4.4.5 Monitoring the mode of the cooling lasers. We monitor the mode of the cooling lasers with a **Coherent 33-6255-001** Fabry-Perot cavity in combination with a **Leoni M-1100623** eight-channel optical fiber switch, to which optical fibers carrying a sample of the laser of interest are connected. The master and repump combined signal, from the fiber network generating the beat-note for the repump locking, are connected to CH-0 and the MOT diagnostic fiber is connected to CH-7. An advantage of the fiber switch is that it suppresses the fiber plugging/unplugging process associated with monitoring various lasers at the input of our Fabry-Perot setup (which is both time consuming and potentially harmful for the fibers). The output of the cavity is sent into a **Tektronix TDS 220** oscilloscope to visualize the mode of the laser. Table 4.5 indicates typical values for the amplitude of the signal in the cavity when the lasers are single mode.

4.4.6 Warm-up process and daily diagnostics. The warm-up time in our experiment depends largely on the time it takes for the ovens to reach their final temperature (≈ 100 °C from room temperature) and for the cooling lasers to warm up.

Our cooling lasers have been operating without interruption over the course of about 5 years; every night we only turn off the current to the amplifier in the MOT laser. Only on exceptional occasions, e.g. when a power outage or an air conditioning outage is announced, do we fully turn off the diode lasers. The MOT laser takes a considerably amount of time to warm up (≈ 2 hr) and output its highest power. We have observed that the transition from transient to fully warmed up

is sharp, i.e. the laser will output low power (about 50% of the optimum power) and suddenly jump close to its final power after ≈ 1.5 hr from turning on the amplifier current.

We monitor the power of various laser beams using home-built low noise photodetectors (PD) and several readout boxes. A diagnostic to ensure a good performance of the BEC machine consists on preparing a MOT (using `ManualControls.vi` in Rubidium-C) and making sure the PD readouts are similar or better than with those given in Table 4.6.

Another important diagnostic is the MOT fluorescence, we measure it by focusing the MOT fluorescence light on a `Thorlabs SM1PD1A` PD using a 75 mm lens attached to one of the 16 mini-conflat ports of the vacuum chamber. The PD signal is sent to a `SR570` low noise current preamplifier with a sensitivity of $1 \mu\text{A}/\text{V}$. At the settings indicated on Table 4.6, the MOT fluorescence is around 1.7 V. The calibration of our PD gives $\approx 8.9 \times 10^7$ atoms/V.

4.4.7 The MOT and the motorized flipper mirrors. Optical access in our experiment is achieved by having dynamic elements which get out of the way to leave the vacuum chamber viewports unobstructed for the dipole trap and other probe beams to interact with the atoms. This is particularly the case for the six mirror mounts holding the protected gold mirrors that send the MOT beams into the chamber. Five of the six MOT mirrors are `Edmund Optics NT32-086` elliptical mirrors and one is a `Thorlabs MRA05-M01` right angle prism mirror (located below the chamber). All of them are installed on `New Focus 8892-K` motorized flipper mounts as indicated in Fig. 4.1 and Fig. 4.2; and are labeled M1-M4 (*xy* plane mirrors), M_{top} and M_{bottom} .

The MOT flippers realize about 1200 cycles/day for a typical experimental cycle time of about 30 s, and a ≈ 10 hr/day operation of the BEC-machine. When optimally operating, the flipper mirrors offer excellent repeatability of the MOT settings. Stable and precise performance of the flippers means that the MOT alignment, and the MOT fluorescence signal, is preserved after the flippers are periodically operated. A flipper failure is typically diagnosed by looking at the MOT alignment; the beam reflected by a damaged flipper, when inspected at its exiting port deviates with respect to its counter-propagating beam from a few mm up to 1.5 cm. Another diagnostic for a failure is a low MOT fluorescence level; each flipper can individually be tested by looking at the maximum achieved fluorescence value after a single flipper cycle. We have observed an up to 50% loss in MOT fluorescence associated with a single damaged flipper mirror.

The most probable cause of failure of the flippers, and consequent MOT instability, is the wearing-out of their springs; this might be associated to the fact that they carry relatively big optics. We have learned that it is an almost painless experience to replace their springs in-situ vs replacing the whole flipper by a new one and spending more time on aligning the affected MOT beam. In other occasions, we have observed the rupture of the flipping arm, which does require the full flipper mount to be replaced. To be specific: M_{bottom} has not reported any unstable behavior over

2 years; M_{top} holds a MOT mirror from the top, this makes it a potential source of instability to be considered (this was the case a couple of years ago until the flipper was replaced); $M4$ has exhibited unstable behavior within months, a problem that was fixed with minor surgery by replacing its spring in-situ; all other mirrors have rarely failed. An improved approach to having dynamical elements is the use of non-rotating, pneumatic mounts as implemented in the Rb-BEC laboratory of Trey Porto at NIST.

4.4.7.1 MOT alignment. The alignment the MOT beams relies on cage systems built up from the **Thorlabs** 30mm cage system line of products, and anchored to the main experimental chamber. Prior to aligning the beams we install **Thorlabs** CPA1 alignment plates, next to the final lenses along the path of the MOT beams to the chamber, to set the size of the beams across the chamber at 1 mm (the diameter of the MOT beams at the atoms is about 1 cm). MOT alignment is achieved by adjusting the orientation of the flipper mirrors using the set screws located below them; this is a task that requires lots of care and patience in particular when fastening the set screws. Preserving the achieved alignment is easier if the lock nuts of the flipper are first finger-tightened, while monitoring the overlapping beams, and then a nutdriver is used to firmly set them. It is hard but not impossible to reach some setting screws, e.g. in the case of $M1$ they are easily reached if the flipper is in its open position.

4.5 MAGNETIC FIELDS

Static magnetic fields are versatile tools which allow the control not only of the energy splitting of the hyperfine sub-levels of the atom (Zeeman effect), but also of their dynamics (magnetic forces and trapping). On the other hand, time varying fields offer control on the atomic internal degrees of freedom such as spin (rf-induced magnetic transitions).

4.5.1 Zeeman slower. The Zeeman slower [69] uses a single layer, zero-field crossing design [70] where two copper solenoids –with an inhomogeneous linear density of coils– generate the positive and negative contributions to the total magnetic field. We refer to these coils as the slower and the Reverse slower. An extra compensating coil, located in the opposite port of the main vacuum chamber, guarantees that the magnetic field is cancelled at the atoms. The Zeeman solenoids wind around a $d=7.6$ cm aluminum enclosure surrounding the 69 cm conflat vacuum tube of the slower. Its zero-field design helps minimize the dissipation of Joule heating, which is further mitigated by flowing cooled water inside through the coils. Two independent **Kepco ATE 6-100M** unipolar power supplies generate the Zeeman slower currents. During the MOT capture the typical operating currents in the slower and Reverse slower are 72 A and 42 A, respectively.

Two laser beams with mutually orthogonal circular polarization, the slower and the slower repump, propagate along \mathbf{e}_x inside the slower tube. As discussed in section 3.6.1 the Zeeman slower

provides a suitable field amplitude to compensate the Doppler effect experienced by moving atoms traveling toward the main chamber; as well as it defines the quantization axis to achieve laser cooling.

4.5.2 Bias coils. Uniform bias fields are generated with three pairs of mutually orthogonal Helmholtz-coils oriented along $\mathbf{e}_x \pm \mathbf{e}_y$ (see Fig. 4.1 for the orientation of the laboratory coordinate system) and \mathbf{e}_z . All coils are wound from 14 AWG copper wire. The coils in the xy -plane have 30 turns each and a diameter of 7 cm; they surround the Thorlabs 30mm cage system anchored to the main experimental chamber. The z -coils have 2 turns each; they are located on the surface of the top and bottom chamber windows, and their ≈ 14 cm diameter prevents them from blocking the path for the MOT and xy imaging.

Three independent Kepco BOP 20–20M bipolar power supplies provide the currents to generate the bias fields. The currents are stabilized by a PI feedback circuit described below and their time response is about 1 ms; the generated magnetic field is calibrated as a function of current via rf-spectroscopy⁶, see Table 4.7.

4.5.2.1 Feshbach coils. The Feshbach coils have 36 turns each and an inner diameter of ≈ 30 cm. They are located above and below the main experimental chamber. Their current is provided by a Kepco BOP 20–20M bipolar power supply, PI locked as the other bias fields. Their time response is on the order of 200 ms, so we rely on these supplies to set large background fields along \mathbf{e}_z , while we fine control the field with the faster bias coils. Their rf-spectroscopy calibration gives 2.26 MHz/A.

Table 4.7: Calibration of bias coils.

| Field direction | Calibration [MHz/A] |
|-------------------------------|---------------------|
| $\mathbf{e}_x - \mathbf{e}_y$ | 0.179 |
| $\mathbf{e}_x + \mathbf{e}_y$ | 0.189 |
| \mathbf{e}_z | 0.116 |

4.5.3 Quadrupole coils. The quadrupole coils are mounted in the recessed windows of the main chamber, and they have 24 turns each. The current for the quadrupole trap is generated by an Agilent 6690A power supply, which is operated at 25 A when loading the MOT, and up to 320 A at the compression stage in the experimental sequence for BEC production. The magnetic field gradient generated by the quadrupole coils is about $4.8 \text{ mT m}^{-1}\text{A}^{-1}$ along \mathbf{e}_z .

On February 2012 we moved on from a non-feedback/IGBT-switch based control, to a combination of MOSFETs and PI feedback control of the quadrupole current. This improvement has allowed

⁶rf-spectroscopy consists on tracking the resonance condition of an rf-dressed state at various fixed frequencies ν_{rf} with current-controlled adiabatic rapid passage. We explore both the positive and the negative current regimes.

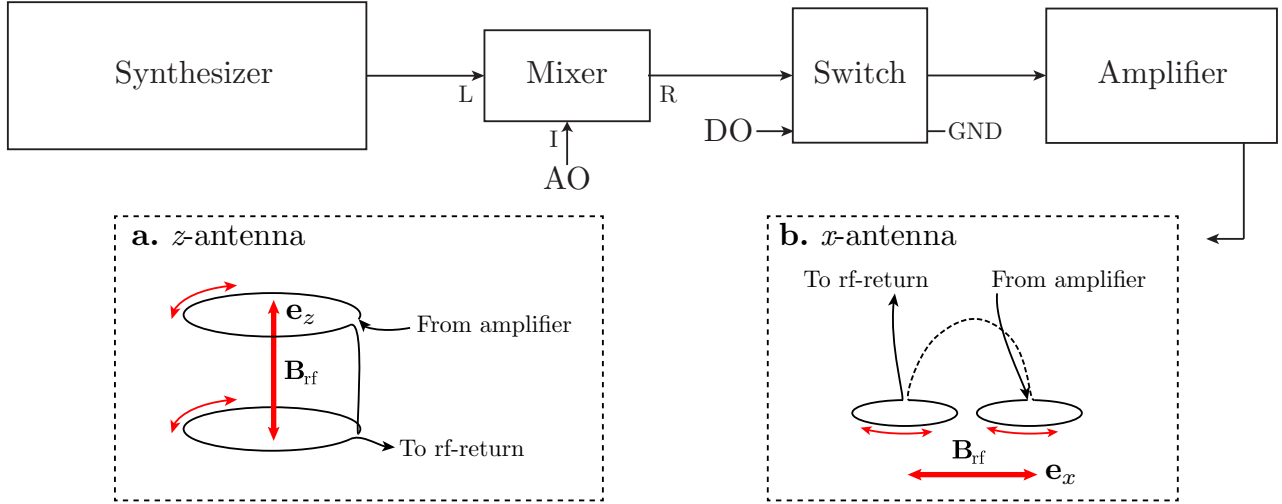


Figure 4.9: Schematic of rf-amplifier and antennae. A programmable synthesizer generates an rf-signal, whose amplitude is further controlled by an AO when both signals are combined in a mixer; a DO channel controls an rf-switch to allow or prevent the signal to pass to the experiment. The signal is amplified and then sent to either of the available antennae (**a-b**).

the faster switching of the fields (from 100 ms to a few μs), which is of particular importance for the recent experiments with K. The PI feedback circuit has some additions to the one used to control the bias fields, described below.

4.5.4 rf-antennae. We broadcast linearly polarized rf-fields along \mathbf{e}_x or \mathbf{e}_z using the antennae depicted in Figure 4.9a,b. A Novatech 409A programmable frequency synthesizer serves as the frequency source, and an AO is used to adjust the amplitude of the rf-field when combined the signal from the synthesizer in a MiniCircuits ZAD-6 mixer. A MiniCircuits ZYSWA-2-50DR coaxial switch controls the flow of rf into the experiment; the switch is driven with a DO from the computer controls. When the switch is closed, the rf-signal passes through a Delta RF 4415 LA10-1-525-40 amplifier⁷. To sample the rf-field we send the returning signal through a total of three high power attenuators (two JFW 50FHC-020-20, and a MiniCircuits BW-S5W5-5W) and monitor the signal in a Tektronix TDS 2014B oscilloscope.

The z -antenna is made of a pair of single-loop coils, located on the top and bottom recessed windows of the main chamber. The x -antenna was installed on February 2009, with the purpose to create a linearly polarized rf-field along \mathbf{e}_x ; it is made of a pair of three-loop 1 inch coils (bypassed with 50 pF capacitors) located on the top window of the chamber and aligned along \mathbf{e}_x with their centers 5 cm apart from each other; the coils were slightly modified from circular to elliptical to prevent them from blocking the MOT and imaging beams. Both antennae are schematically

⁷This amplifier requires a 25 V power supply and a 75 W heat sink. We additionally set up a fan to provide airflow and maintain the amplifier under normal operating conditions.

Table 4.8: *x*-antenna calibration.

| Evaporation Mixer [V] | Coupling strength [kHz] |
|-----------------------|-------------------------|
| 0.6 | 11.4504 |
| 0.105 | 2.0185 |
| 0.055 | 1.08265 |

displayed in Fig. 4.9a,b; and we have successfully performed rf-evaporation in the magnetic trap with similar results using either of them.

We typically characterize the rf-coupling strength by measuring Rabi flopping of the three-level system constituted by the $F=1$ hyperfine sub-states of ^{87}Rb . In such measurements, a uniform bias field is set to define an appropriate quantization axis, as well as to Zeeman split the spin sub-levels. A resonant pulse of rf-radiation illuminates the atoms for variable amounts of time; typically ranging from 1 μs to 2 ms depending on the coupling strength. Due to saturation in the rf-amplifier, the coupling strength has a non-linear behavior as a function of the rf-amplitude (controlled by the Evaporation Mixer channel Dev2-AO5), see Table 4.8.

4.5.5 Stabilization of electrical currents. The bias current and the quadrupole current are stabilized by independent PI feedback circuits, based on the schematic shown on Fig. 4.10. The electrical current is sampled by a FW BELL CLSM-100LA current sensor and sent to the Feedback input, where it is processed. An independent but identical sensor monitors the current in the experiment; this signal is amplified by a BB INA103KP instrumentation amplifier, then sent through a BB BUF634P high speed buffer to finally be detected on one of the Tektronix TDS 2014B oscilloscopes.

The control input corresponds to the AO driving the current (see Table 4.2); this is sent through a resistor chosen to match the maximum output of the Hall sensor. An extra input is dedicated for Fine control (its input resistance sets the resolution), in our experiments this is associated with Dev3-AO3.

All inputs (Feedback, Control and Fine control) are sent to the inverting input of the operational amplifier of the PI. The single diode and the diode bridge are not present in the PI feedback circuits for the bias coils; although they are an important ingredient for the MOSFET-based control of the quadrupole current, since they impose limits on the upper and lower voltages sent into the gates of the MOSFETs. The offset voltage is also only used in the quadrupole current feedback.

The control signal is transferred through a buffer to either the computer control connection on the front panel of the Kepco BOP 20-20M power supplies, or to the gate terminal in the MOSFET bank (a total of 23 MOSFETs connected in parallel are used to control the quadrupole current). The

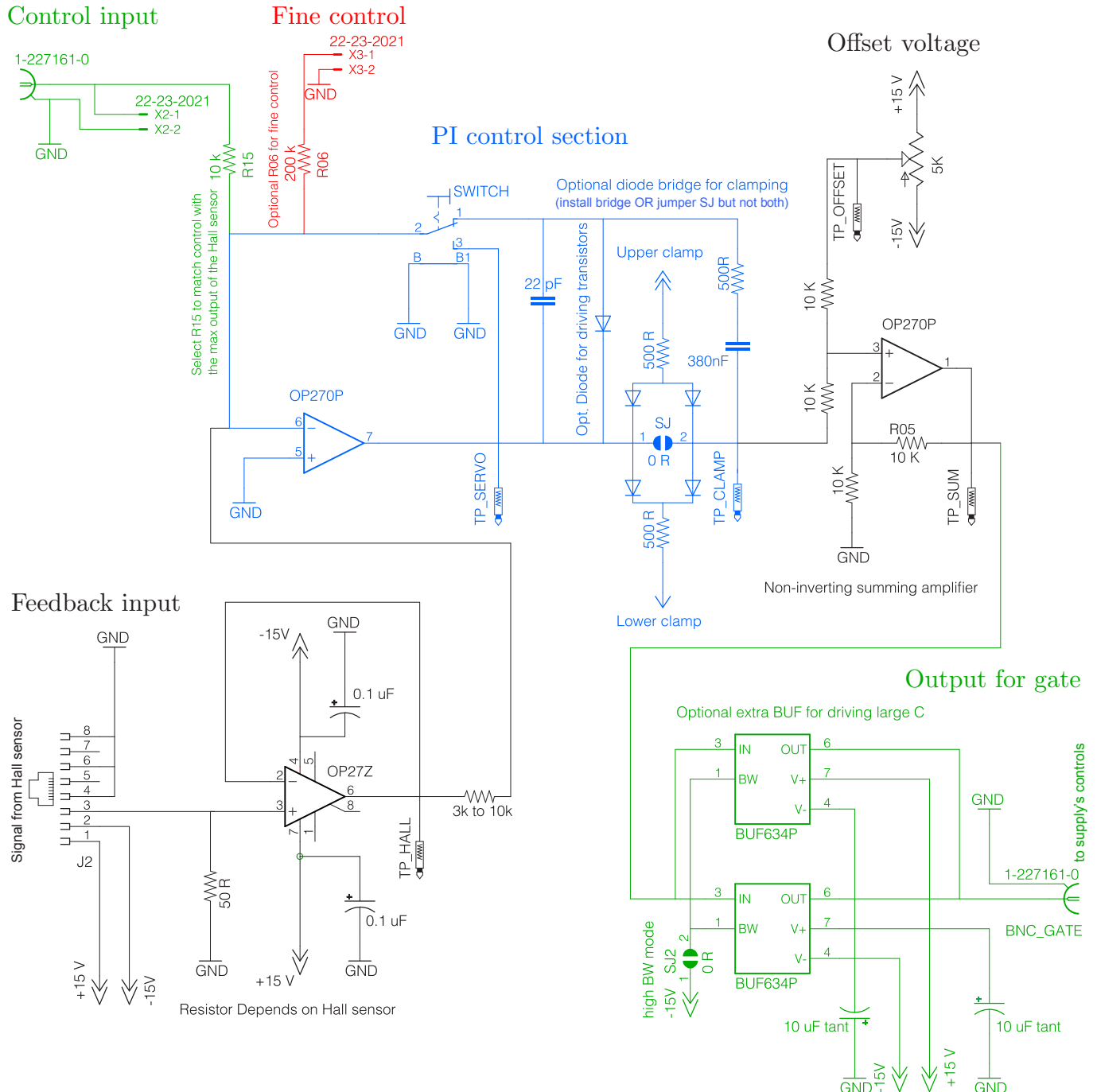


Figure 4.10: Schematic of current stabilization circuit. Shown are the essential ingredients for the PI feedback circuit used to stabilize the currents generating the bias and the quadrupole fields. The single diode, the diode bridge and the offset voltage features are only present in the quadrupole current control.

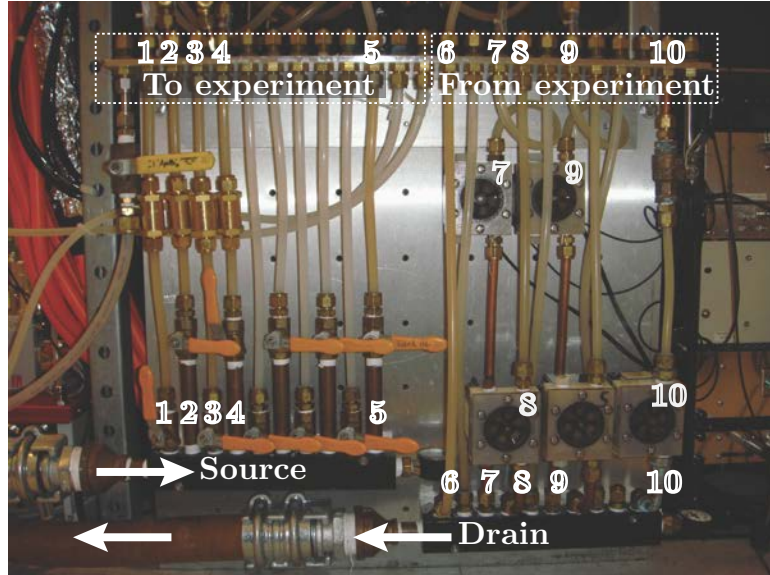


Figure 4.11: Water cooling system. Water is pumped, from the source into the experiment and from the experiment into the drain, by a pair of pumps located in the service corridor. We distribute the cooling water to different sources of Joule heating: **1&7** slower and reverse slower solenoids; **2&8, 3&10** Feshbach coils; **4&9** quadrupole coils; and **5&6** bypass. Flowmeters labeled as **7, 9, 3 &10** form part of a water-flow based interlock which prevents some power supplies from operating, unless a minimum water flow is reached.

drain of the MOSFETs is connected to the quadrupole coils and the other end of the coils is attached to the positive output of the Agilent 6690A power supply; the source is connected to ground.

4.5.6 Water cooling system. All the major electrical components in our experiment (quadrupole coils, slower solenoids and Feshbach coils) are made of insulated hollow copper tube. To dissipate Joule heating we flow water from a circulating chilled water system through these elements; in the case of the MOSFET bank, water cooled plates are in contact with the MOSFETs to dissipate heat. Figure 4.11 shows part of the water cooling system⁸, which consists of a well designed network in which water is distributed into each electrical component. Each branch in the network has an independent valve which simplifies the task of repairing or modifying the system, since just local draining is needed. Water is pumped from the source into the experiment and then back to the drain by a pair of pumps. The differential pressure between the source and the drain is about 14 bar (200 psi) when the bypass valve is closed. A water-flow based interlock for the quadrupole trap and the Zeeman slower current supplies prevents them from operating unless a minimum water flow circulates through the experiment.

⁸The booster and return pumps, as well as the MOSFET bank, are located in the service corridor in the back of the laboratory.

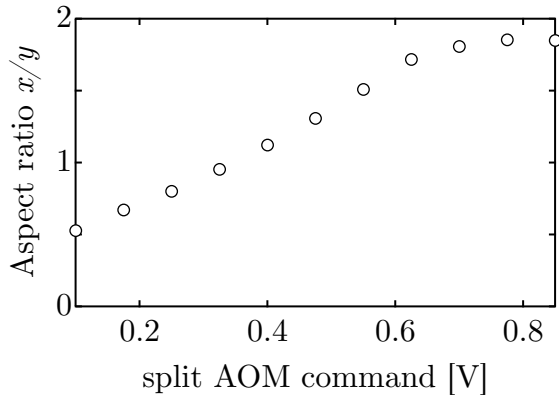


Figure 4.12: Tunable aspect ratio of the optical dipole trap. Our crossed-beam optical dipole trap offers a dynamically tunable variety of geometries, here quantified as the aspect ratio of the trap. The data set was measured from in-situ imaged BECs in the dipole trap described in Table 4.9.

4.6 OPTICAL DIPOLE TRAP

Optical dipole traps for neutral atoms are generated by the dipole interaction between the electromagnetic radiation of a laser and the induced dipole moment in the atom. To minimize scattering and achieve a conservative trapping potential, the laser detuning is maximized, as the scattering losses scale inversely with the square of the detuning. Due to the linear scaling of the trapping potentials with the intensity of the laser and inversely with the detuning from resonance (see Sec. 3.5); far-detuned optical traps required significant power to operate.

The dipole trap is created at the intersection of two 1064 nm laser beams propagating along $\mathbf{e}_x \pm \mathbf{e}_y$ as indicated in Fig. 4.1. The lasers originate from the same IPG YDL-10-LP 10 W, multimode, linearly polarized, fiber laser operated at 8W (typical current 2.3 A and temperature 27 °C).

The output of the fiber laser is passed through a Thorlabs IO-5-1064-VHP optical isolator to prevent back reflections and subsequently through a Crystal Technologies 3080-125 AOM. The non-diffracted order is dumped into a Thorlabs BT600 high power beam trap; while the first diffracted order is sent through a Crystal Technologies 3080-197 AOM. A Thorlabs BSF10-B picks-off a small sample of the diffracted order entering the second AOM; this sample is sent into a PDA10CS detector and subsequently into a Precision photonics LB-1005 servo controller to stabilize the dipole trap overall power; the first AOM is referred to as the “power AOM”. The second AOM splits the input beam to generate the dipole trap beams from its zeroth and first diffracted orders, it is referred to as the “split AOM” and it controls the relative power between the dipole beams. At the stage of capture from the quadrupole trap we command full power to the 0th order beam (≈ 7 W), and later we redistribute the power in both beams when the quadrupole trap is relaxed; at the BEC stage, each beam has about a few tens of mW.

We dedicate two AO channels to control the overall power and split of the dipole trap beams

Table 4.9: Dimensions and trapping frequencies along dipole beams.

| Laser beam | w_{0V} [μm] | w_{0H} [μm] | Trap frequency along beam at split = 0.2 V | Trap frequency along beam at split = 0.4 V |
|------------|----------------------------|----------------------------|--|--|
| 0th order | 98 | 150 | 26 Hz | 37 Hz |
| 1st order | 34 | 118 | 47 Hz | 32 Hz |

(see Table 4.2). One of the AO channels amplitude modulates the split AOM, while the output of the servo controller (referenced to the other AO channel) amplitude modulates the power AOM; both AOMs are driven with 80 MHz **IntraAction** deflector drivers.

Table 4.9 gives the dimensions of the dipole beam at the atoms in the current configuration, where $w_{0V,H}$ is the $1/e^2$ radius along the vertically or horizontally orthogonal direction to that of propagation. As a measure of the versatility of our crossed dipole configuration, Figure 4.12 shows the aspect ratio as a function of the split command; these were measured from in-situ imaged BECs. The dipole beams can readily be resized to achieve a different trap geometry by assuming Gaussian beam propagation and selecting the appropriate lenses.

A small value of the split command means that low power goes into the 1st order dipole beam; thus stronger confinement is realized by the 0th order beam. This behavior is reflected in the measured trapping frequencies indicated in Table 4.9; typical trapping frequencies along \mathbf{e}_z range from 90 Hz to 120 Hz.

Due to its high power the 1064 nm laser is interlocked to the laser safety system in the laboratory; also when the beams are not in use, they are reflected by a **Thorlabs BB05-E03** dielectric mirror attached to the lever arm of a hard-drive shutter; the dipole shutter requires hundreds of ms to open due to the massive mirror it holds.

4.7 RAMAN AND OPTICAL LATTICE LASERS

Once a BEC is prepared, a series of experiments begin. We can probe the properties of the BEC as well as engineer different Hamiltonians for the atoms in a BEC, by illuminating them with lasers. This section describes the experimental setup dedicated to generate the laser beams to be used in Raman processes and optical lattices in our experiments.

We operate a **Coherent Verdi V-10** at 10 W to pump a **Coherent MBR-110** Ti:Sapphire tunable laser. The Ti:Sapph crystal is cooled to 18 °C using a recirculating water chiller, whose coolant is a mixture of 80% distilled water and 20% ethylene glycol (300 mL is enough to fill the chiller reservoir). The output power of the Ti:Sapph peaked at 1.13W, when operating at 810 nm during 2008 and 2009. We have observed decreased power (650 mW at 790 nm) in the past year. Both values are below 50% of **Coherent** specifications for pumping at 10 W. Minimal maintenance based

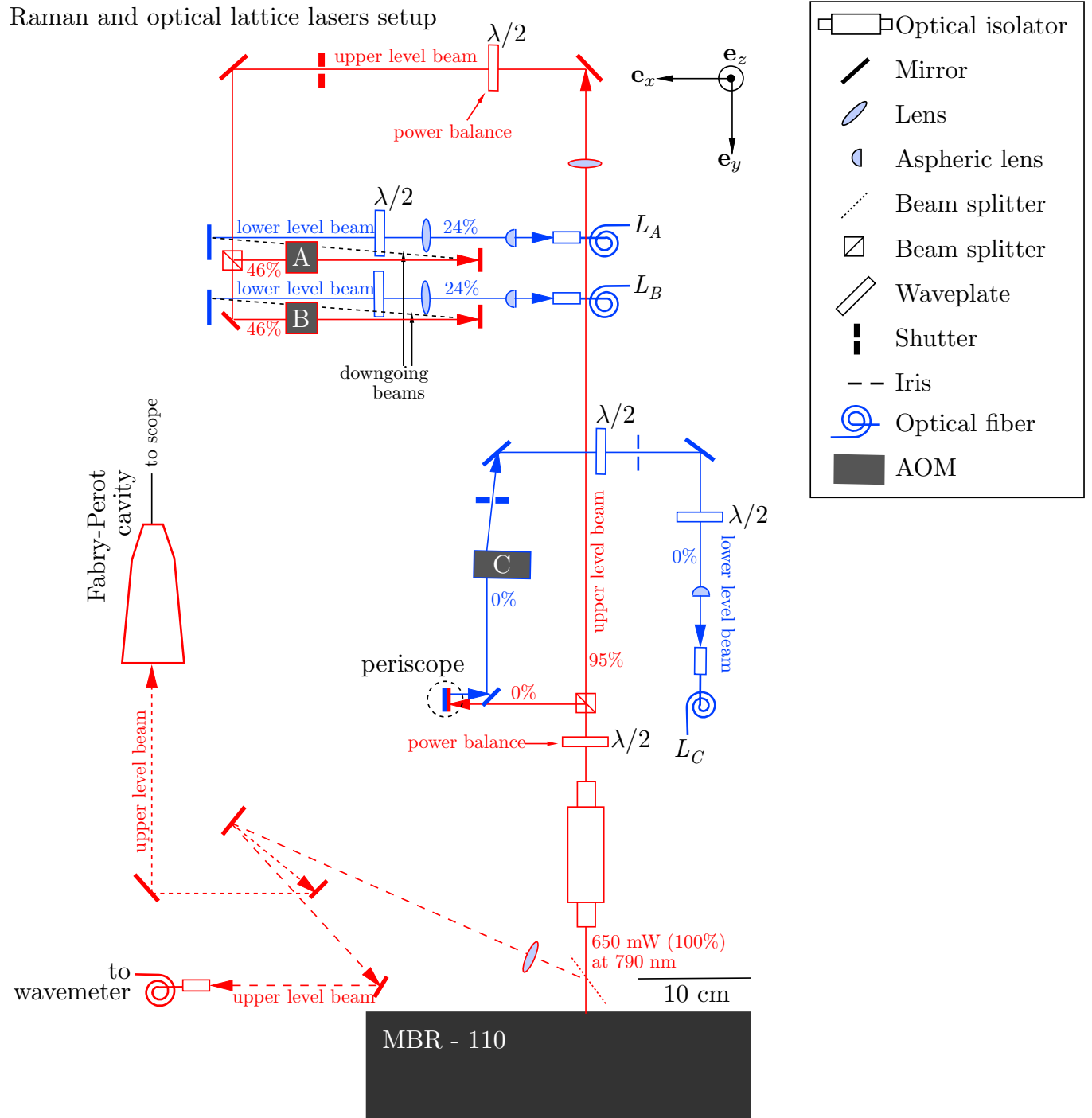


Figure 4.13: Schematic of the optical setup and power map of the Ti:Sapph laser. This configuration corresponds to the optimal operation with L_A and L_B only. The power balance between $L_A + L_B$ and L_C is adjusted using $\lambda/2$ wave plate after the optical isolator. Furthermore, the power balance between the L_A and L_B beams is controlled by the $\lambda/2$ before the AB shutter. Also see Fig. 4.22.

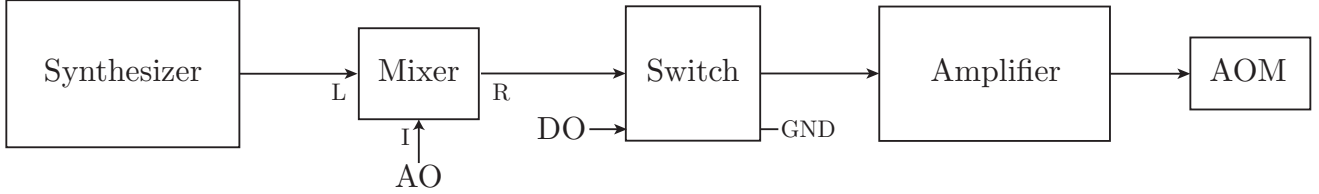


Figure 4.14: AOM driver for Raman beams. A synthesizer sets the frequency to drive the AOM; this signal is mixed with an AO to control its amplitude, and later sent to an rf-switch controlled by a DO. The non-terminated output of the switch is amplified and directly drives the AOM.

on the alignment of the pump and the MBR cavity, as well as the cleaning of the optical elements of the MBR has conserved but not improved the Ti:Sapph output power.

The Ti:Sapph is the source of three laser beams (L_A , L_B and L_C) which are either used in Raman processes or optical lattices. Figure 4.13 shows a schematic of the optical setup and a typical distribution of power for optimal operation with L_A and L_B only. All three AOMs in this setup are **IntraAction ATM-801A2**. In most of our experiments it suffices to use only a pair of beams for which we have two identical rf-amplifiers to drive either pair of AOMs; if required the additional AOM is driven by an 80 MHz **IntraAction** deflector driver.

Table 4.10: Typical power at the output of the Raman fibers vs AO command.

| AOM command [V] | RamanA [mW] | RamanB [mW] | PD _A [mV] | PD _B [mV] |
|-----------------|-------------|-------------|----------------------|----------------------|
| 0 | 0.073 | 0.35 | - | 1.71 |
| 0.02 | 11.5 | 11.5 | 9.4 | 19 |
| 0.03 | 26.7 | 22.5 | 23.5 | 36.9 |
| 0.04 | - | 36.1 | 39.5 | 58.7 |
| 0.05 | 66.3 | 50.4 | 57 | 83.6 |
| 0.06 | 84.6 | 64.2 | 72.7 | 106 |
| 0.07 | 96.6 | 76.4 | 81.7 | 123 |
| 0.08 | 102 | 84 | 83.4 | 133 |
| 0.09 | 103 | 88.3 | 82.5 | 138 |
| 0.1 | 102 | 89.5 | 80.7 | 143 |

Figure 4.14 shows an schematic of the amplifier. We generate an rf-signal in a frequency synthesizer and combine it with DC signal from an AO channel using a **MiniCircuits ZAD-3+** frequency mixer to control its amplitude. The combined signal goes through a **MiniCircuits ZYSWA-200-500R** switch (which is controlled by a DO) and subsequently through a **MiniCircuits ZHL-1-2W** amplifier; the amplified signal directly drives the AOM. An **Agilent 33250A** frequency synthesizer sets the driving frequency of AOM-A, while one of the programmable channels of the rf-evaporation **Novatech 409A** synthesizer sets the driving frequency of AOM-B (both synthesizers are synchro-

Table 4.11: Dimensions of Ti:Sapph beams.

| Laser beam | w_0 [μm] |
|------------|-------------------------|
| L_A | 195 |
| L_B | 180 |
| L_C | 188 |

nized using their 10 MHz external reference input/output ports). It is a standard practice to set the **Agilent 33250A** frequency to 80 MHz, and modify the **Novatech 409A** frequency according to our interests (optical lattice or Raman processes).

Table 4.10 gives a calibration of the power at the output of the fibers (on the experiment side) as a function of the command AO voltage to the AOMs, for driving frequencies $f_A = 72.5$ MHz and $f_B = 87.5$ MHz. Most powers in the experiment are measured using a **Coherent Fieldmaster 33-0506** power-meter and its 1000:1 attenuator. Additionally, the beams are permanently sampled at the output ports (see Fig. 4.1) and monitored with independent photodiodes PD_A and PD_B (a **Thorlabs VT1** variable terminator set at $1 \text{ k}\Omega$ was used at the input of the monitoring oscilloscope).

The first diffracted orders from each AOM are injected into **PMJ-3A3A-850-5/125** polarization maintaining optical fibers with typical fiber coupling efficiency of 64%. The fiber for L_B is slightly different (**PMJ-3A3A-633-4/125-3-6H**) but we have not observed any negative side effects due to it.

At their output port, each laser beam (L_A , L_B and L_C) goes through a **Thorlabs GL10-B** polarizer (not shown in Fig. 4.1) to avoid undesired polarization components; and the polarization can be rotated using a $\lambda/2$ wave plate after the polarizer. Finally, the dimensions of the Ti:Sapph beams at the atoms are indicated in Table 4.11.

4.8 IMAGING SYSTEMS

Resonant absorption imaging is the fundamental method by which we probe the outcome of our experiments on the atoms; it is also our primary source of data and is discussed in detail in section 3.7. In this section I focus on the description of the two imaging systems used in our experiment to probe the atoms in the orthogonal planes are xy and xz ; Fig. 4.1 sets the coordinate system of the laboratory.

The imaging beams originate from the MOT laser and have a $1/e^2$ radius of about 300 μm ; they are sent through polarization maintaining optical fibers to the BEC machine. Both probe beam intensities are controlled by the same AO channel in Rubidium-C (see Table 4.2), switching imaging directions might require an adjustment on the commands, due to effects such as different

fiber coupling efficiency or the use of different CCD sensors; also both cameras are triggered by the same DO channel (see Table 4.3).

4.8.1 *xy* Imaging. The output of the fiber carrying the *xy* imaging beam sits at the top of the main experiment, about 60 cm above the center of the main experimental chamber, and the *xy*-probe beam propagates along $-\mathbf{e}_z$. Various modifications have occurred to the *xy*-imaging system: it evolved from being a simple two-lens telescope, to be an effective telescope composed of a pair of two-lens assemblies, and finally to the current configuration: a combined telescope consisting of a two-lens assembly in combination with a single lens. All these changes have been made in favor of better resolution and increased magnification.

In the current configuration, the two-lens assembly sits immediately below the main experimental chamber and has an effective focal length of $f_{\text{eff}} = 83$ mm. The *xy*-imaging beam passes through the lens-assembly and hits a **Thorlabs PFE20-M01** protected gold mirror at 45° , which reflects it toward \mathbf{e}_x , 8 cm above the optical table. A single lens $f = 500$ mm is located at $f_{\text{eff}} + f$ from the two-lens assembly (see Fig. 4.2, the two-lens system along \mathbf{e}_z is not shown); the calculated magnification of the system is in excellent agreement with the measured value of 6.02.

We image the atoms with a **Princeton Instruments PIXIS 1024** camera operating in **Kinetics** readout mode; this means that only a portion of the CCD is exposed and acquires data while the rest stores it; this way the camera can acquire multiple subframes which are separated by a short amount of time. Ideally we could set up a procedure (probably involving partial repumping) to image the same BEC multiple times, since the time scales associated with the **Kinetics** readout mode are on the order of μs . We use half of the available 1024×1024 camera pixels, preventing the exposure of the other half by covering it with a razor blade; we are restricted to acquire frames separated in time by about 40 ms, in order to avoid an undesired ‘scar-structure’ present in the frames. In addition, we work in the “slow” readout mode (100 kHz) which results in a total readout time of about 10.5 s.

Due to the long time involved in *xy*-imaging, we only acquire a background image at the beginning of the day, and acquire an absorption image and a probe image during each experimental cycle. The **PIXIS** camera is extremely sensitive to background light; we installed an absorptive $OD=1$ filter at the input of the *xy*-imaging fiber in the MOT setup (Fig. 4.8) to minimize leakage from the probe when pre-opening the probe shutter; additionally, the main experimental apparatus is surrounded by black curtains (made of **Thorlabs BK5**) to minimize background leakage.

4.8.2 *xz* Imaging. The *xz*-imaging system consists of a pair of two-lens systems as indicated in Fig. 4.1. The output port of the *xz*-probe beam sends the beam along $-\mathbf{e}_z$ on the dipole trap side, and a dichroic mirror directs it along $-\mathbf{e}_y$ through the center of the chamber. The probe beam goes

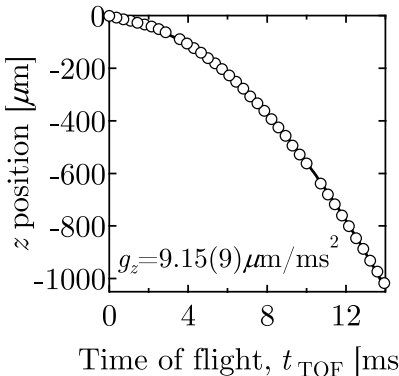
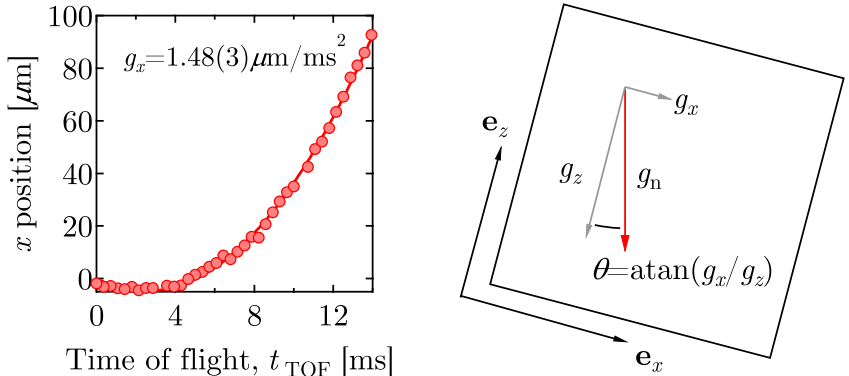
a. Center of mass motion of a BEC under free fall**b.** Projection of g_n on CCD

Figure 4.15: xz Imaging magnification. We measure the magnification of the xz -imaging system by characterizing the center of mass motion of a BEC in free fall.

through a pair of two-lens systems⁹ which give an effective magnification of 1.94, within 5% of its expected value.

The atoms are imaged in the xz plane by a Thorlabs DC210 CCD camera (now discontinued) with a total of 640×480 pixels. In the xz -imaging mode we take a background image in each experimental cycle.

4.8.3 Measuring the magnification of an imaging system. To determine the magnification of an imaging system, it is ideal to focus tiny objects and have a very good measure of their separating distance. Depending on the imaging direction we measure the magnification either by pulsing an optical lattice on a BEC and measuring the diffracted orders, or by characterizing the center of mass motion of a BEC in free fall.

4.8.3.1 Optical lattice pulsing. This method is useful to calibrate the magnification of both the xy and the xz imaging directions. We prepare a dilute BEC, with an optical depth below 1, and set up a pair of lasers from the Ti:Sapph (wavelength λ) to constructively interfere at the atoms and create an optical lattice. By suddenly turning on the lattice on the atoms (in a few μs), we observe matter wave diffraction and measure the location of the diffracted orders after a time of flight t_{TOF} .

Using the orthogonal beams L_A and L_B , the natural units of momentum and energy are $k_L = \sqrt{2\pi/\lambda}$ and $E_L = \hbar^2 k_L^2 / 2m$, where m is the atomic mass. The expected separation between the diffracted orders is $\Delta l = 2\hbar k_L t_{\text{TOF}} / m$.

We pulsed a $57E_L$ -deep lattice for $t_{\text{pulse}} = 15 \mu\text{s}$ and observed the population of up to the 4th order of diffraction. After a $t_{\text{TOF}} = 18.1 \text{ ms}$ TOF and working at $\lambda = 804.1 \text{ nm}$, we expect

⁹The first lens system is composed of an $f_1 = 200 \text{ mm}$ and an $f_2 = 1000 \text{ mm}$ lens, separated by 1.5 cm ($f_{\text{eff}} = 168.776 \text{ mm}$), and has an f -number of 3.32. The second lens system consists of an $f_3 = 750 \text{ mm}$ and an $f_4 = 500 \text{ mm}$ lens, separated by 10.5 cm ($f_{\text{eff}} = 327.511 \text{ mm}$). The probe beam goes from f_1 to f_4 as it exits the chamber.

$\Delta l = 148.48 \mu\text{m}$. By comparing the measured the coordinates of the diffraction orders to their expected locations, we determined a magnification of 4.17; larger than expected by 4%.

4.8.3.2 BEC in free fall. This method is more suitable for characterizing the xz -imaging system. We prepare a BEC and suddenly release it, to take an absorption image after a variable time-of-flight (TOF). From a fit of its coordinates vs TOF, we get the acceleration of the BEC in free fall, and compare it to the standard acceleration of gravity $g_n = 9.806 \text{ m/s}^2$ [58].

Under ideal conditions, when the vertical direction of the CCD is perfectly aligned with the gravitational axis, the magnification is given by $M_{xz} = M'_{xz}(g_z/g_n)$, where $M'_{xz} = 2.05$ is the original estimated magnification of the imaging system. If the camera is at an angle from vertical, the movement is projected along \mathbf{e}_x , and the components of the acceleration are given by $g_x = g_n \sin \theta$ and $g_z = g_n \cos \theta$ as seen in Fig. 4.15. From our measurements: $g_x = 1.48(3) \mu\text{m/ms}^2$ and $g_z = 9.15(9) \mu\text{m/ms}^2$, we obtain $\theta = 9.19^\circ$ to be the angle from vertical; the magnification is $M_{xz} = M'_{xz}(g_z/g_n \cos \theta) = 1.94$.

4.9 MAGNETIC FIELD CANCELLATION

Due to the spinor nature of most of our experiments, magnetic field noise is an issue. In particular, the 60 Hz oscillating field from the laboratory power-line represents the primary source of magnetic field noise. This section describes standard techniques to diagnose and minimize 60 Hz magnetic field noise in the laboratory, as well as to eliminate stray magnetic field gradients [stray uniform magnetic fields can readily be cancelled by the bias coils (see section 4.5)].

4.9.1 Characterization of ambient noise. As a first approximation we characterize the ambient noise using a single axis **MagneticSciences MC910** magnetic field sensor with peak sensitivity of about 90 mV/mG at 60 Hz. The case of the sensor is a small cylindrical enclosure whose flat base is normal to the sensor axis.

We install the detector as close as possible to the atoms. In particular, for measuring the field noise along the vertical direction, we locate the sensor very close to the surface of the top window of the vacuum chamber. A standard procedure is to turn off most of the equipment in the laboratory and gradually turn items on, while monitoring the measured signal. Typical measurements are summarized in Table 4.12; the 6 mV level corresponds to 0.067 mG or to a Zeeman shift of about 47 Hz for ^{87}Rb in $F=1$.

We have found that not only do the spatial location but also the spatial orientation matters for noisy instruments; we optimize their orientation to minimize noise and keep them as far away as possible from the main experiment.

Table 4.12: Contribution of various instruments to ambient field noise at 60 Hz.

| Instrument | Signal [mV] | Instrument | Signal [mV] |
|-------------------------------|-------------|------------------------------|-------------|
| Background | 8.4 | 1064 AOM drivers | |
| Ovens OFF | 8.4 | Verdi AOM driver | 6 |
| Room lights OFF | 7.04 | MOT drivers | 6 |
| Room lights back ON (central) | 7.68 | Supplies above experiment ON | 6.48 |
| Room lights back ON (all lab) | 7.92 | Hallway instruments: | |
| Verdi Chiller OFF | 7.92 | KEPCOs OFF | 7.92 |
| IPG-1064 OFF | 7.6 | KEPCOs ON | 6.5 |
| ThermoCube (90 deg rotation) | 6.16 | Slower OFF (bias ON) | 6.88 |
| Computer monitors OFF | 6 | Booster pump OFF | 6.88 |
| CRT Monitors | 6 | Return pump OFF | 4.4 |
| PIXIS camera OFF | 6 | Bias OFF | 5.28 |
| Ti:Sapph OFF | 6 | Thermocouple reader OFF | 5.28 |
| Oscilloscopes OFF | 6 | rf-amplifier | 5.28 |

4.9.2 Field noise cancellation. A second order approximation to tackle the issue of 60 Hz noise is to measure the effects on the atoms by monitoring the variations in the spin populations of rf-dressed BECs, prepared nominally on resonance (to create a magnetic field dependent superposition state of the three m_F sublevels). We start with an $m_F = -1$ BEC in the presence of a uniform magnetic bias field providing a Zeeman splitting ν_Z . We set an rf-dressing field with strength $\hbar\Omega_{\text{rf}} \approx 2\pi \times 11$ kHz and frequency $\nu_{\text{rf}} = 1.92$ MHz; and define the detuning from rf-resonance as $\hbar\delta = \hbar(\nu_{\text{rf}} - \nu_Z)$. We perform adiabatic rapid passage to resonance, by ramping the bias field in 15 ms, subsequently trigger the remaining lines in the program in phase with the power-line signal, and ramp the coupling strength to $\hbar\Omega_{\text{rf}} \approx 0.5E_L$ in order to increase the sensitivity of the measurement. Figure 4.16a illustrates that in the strong coupling regime (top), the spin populations are less sensitive to changes in the magnetic field near resonance than they are in the weak coupling limit (bottom).

We suddenly switch off the rf-field and release the atoms from the optical trap. The atomic distribution expands in TOF, during which a Stern-Gerlach field is briefly turned on to spatially separate the spin components. Finally we absorption image the resulting spin distributions to measure the fraction of atoms in $m_F = \pm 1$. We repeat this process for various hold times in the rf-dressed state and obtain a measure of the noise signal (Fig. 4.16c.1). To correct for the power-line noise, we used a function generator to synthesize a correction signal at the measured frequency $f_{\text{line}} = 57.953$ Hz, which we introduced in a feed-forward configuration to the power supply generating the bias field.

The magnetic field noise is calculated as a detuning from the population imbalance between the spin states $| -1 \rangle$ and $| +1 \rangle$. From the statistics we find a standard deviation on the detuning ranging

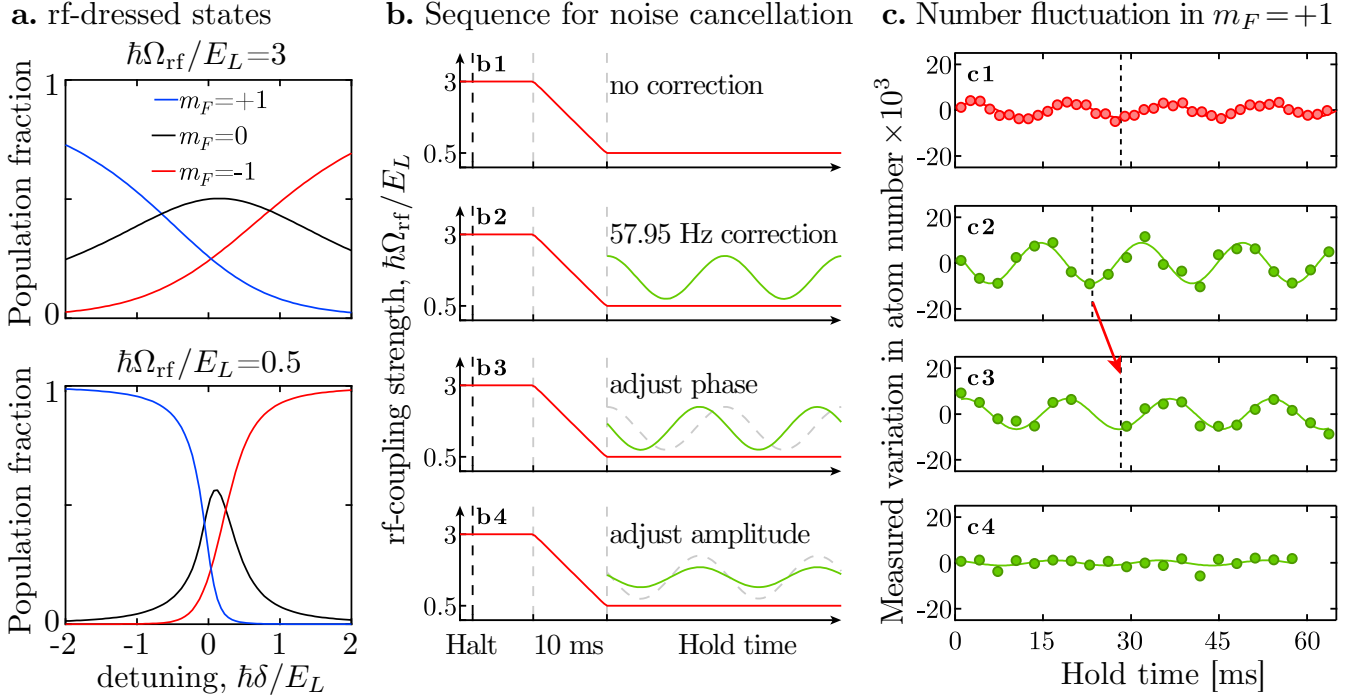


Figure 4.16: **a.** Spin populations in an rf-dressed state as a function of detuning. **b.** Experimental sequence. **c.** Number of atoms in $m_F=+1$ as a function of time: **b1-c1**. noise signal; **b2-c2**. trial correction. We adjust the phase (**b3-c3**) and amplitude (**b4-c4**) of the correction to minimize noise.

from 110 to 590 Hz, depending on the direction of the magnetic field, as shown in Table 4.13.

The noise levels decrease for reduced coupling strengths Ω_{rf} , as expected since we prevent saturation of the rf-amplifier. Under similar experimental conditions and similar background fields, The field noise along $\mathbf{e}_x - \mathbf{e}_y$ is smaller by a factor of ≈ 5 than that along \mathbf{e}_z . The major difference between these configurations are the coils used to generate the magnetic fields.

Finally, we observe abrupt changes in the ambient fields any time the door leading to the service corridor is open. This is due to the architecture of the laboratory: the two walls separating the laboratory from its nearest neighboring laboratories consists of prefabricated gypsum core steel wall panels; while the walls separating the laboratory from the service¹⁰ and pedestrian corridors are made of gypsum wallboard and a special panel for rf-electromagnetic interference shielding [71].

4.9.3 Cancellation of stray gradients. In the absence of magnetic field gradients, a mixture of $F=1$ spin states of ^{87}Rb is spatially miscible [72], with spin mixing time is below 600 ms [73].

We prepared a balanced superposition of the spin states $|m_F=-1\rangle$ in the large quadratic Zeeman regime, using an rf-field as described in section 9.5.1 (no Raman). We characterized the spinor dynamics by removing the rf and holding the atoms in our optical trap for a variable delay of up

¹⁰The equipment that generates most of acoustic and electric noise, such as power supplies and water pumps, locates at the service corridor in the back of the laboratory.

Table 4.13: Measured magnetic field noise in different directions.

| Field direction | $\hbar\Omega_{\text{rf}} [E_L]$ | $\Delta\delta [\text{Hz}]$ | $V_{\text{pp}} [\text{mV}]$ |
|-----------------|---------------------------------|----------------------------|-----------------------------|
| z | 2.49 | 590 | < 3 |
| z | 1.56 | 150 | < 3 |
| y | 2.46 | 120 | 5 |
| $x - y$ | 1.76 | 110 | - |

to 600 ms. After a 30.1 ms TOF, during part of which a gradient along \mathbf{e}_x was applied, we imaged the atoms and determined that the system is phase separated along the \mathbf{e}_y direction. We quantify phase separation as the difference between the spatial density distributions of each spin state [if the spins were spatially mixed, their distributions would be identical (see Sec. 10.3.1)].

We use two pairs of “shim coils” located around an xy MOT viewport (identified by M1 to M4 in Fig. 4.1) and wrapped around the main experimental chamber to set up the canceling gradient. The pairs of coils M1-M3 and M2-M4 are set up in the anti-Helmholtz configuration to generate a quadrupole magnetic fields of the form

$$\mathbf{B}_{13} = B'_{13}(-x_{\text{rot}}\hat{x}_{\text{rot}} + 2y_{\text{rot}}\hat{y}_{\text{rot}}), \quad (4.3)$$

and

$$\mathbf{B}_{24} = B'_{24}(-2x_{\text{rot}}\hat{x}_{\text{rot}} + y_{\text{rot}}\hat{y}_{\text{rot}}), \quad (4.4)$$

in the rotated system defined by $\hat{x}_{\text{rot}} = (\mathbf{e}_x - \mathbf{e}_y)/\sqrt{2}$ and $\hat{y}_{\text{rot}} = (\mathbf{e}_x + \mathbf{e}_y)/\sqrt{2}$. We use two **Agilent E3611A** power supplies to adjust the magnetic field gradients B'_{13} and B'_{24} to cancel the stray gradients along \mathbf{e}_y , by looking at the shape of the density distributions of each spin state and minimizing their differences. Typical currents were set to $I_{13} = -0.28$ A and $I_{24} = 0.35$ A in each supply.

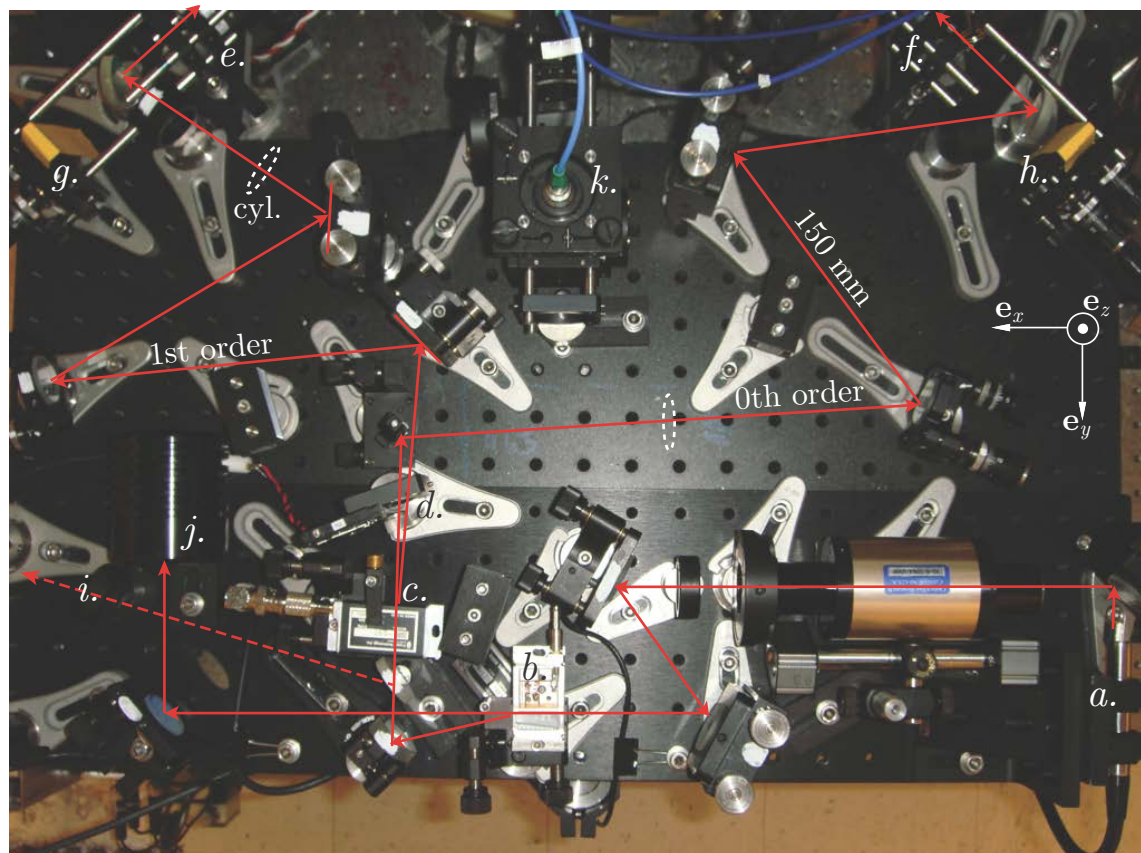


Figure 4.17: Picture of the optical setup for the dipole trap. *a.* Fiber laser; *b.* power AOM; *c.* split AOM; *d.* dipole shutter; *e-f.* final lenses prior to vacuum chamber; *g-h.* retro-reflecting mirrors; *i.* sample beam for intensity locking; *j.* beam dump; *k.* fiber launch for *xz* imaging. Also see Fig. 4.1.

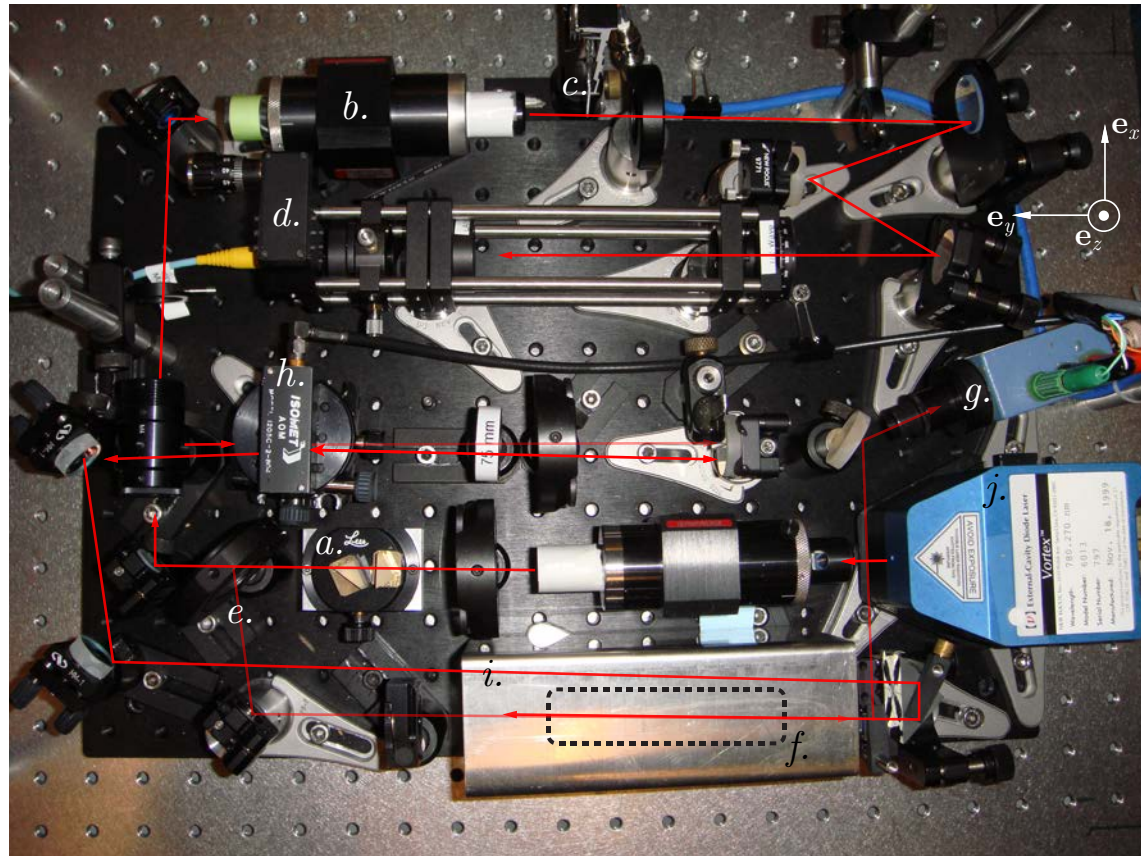


Figure 4.18: Picture of the optical setup for the master laser. *a.* Anamorphic prism pair; *b.* optical isolator; *c.* master shutter; *d.* beam sample for beat-note lock; *e.* pump beam; *f.* rubidium cell; *g.* saturation spectroscopy photodiode; *h.* double passing AOM; *i.* probe beam; *j.* master laser. Also see Fig. 4.6a.

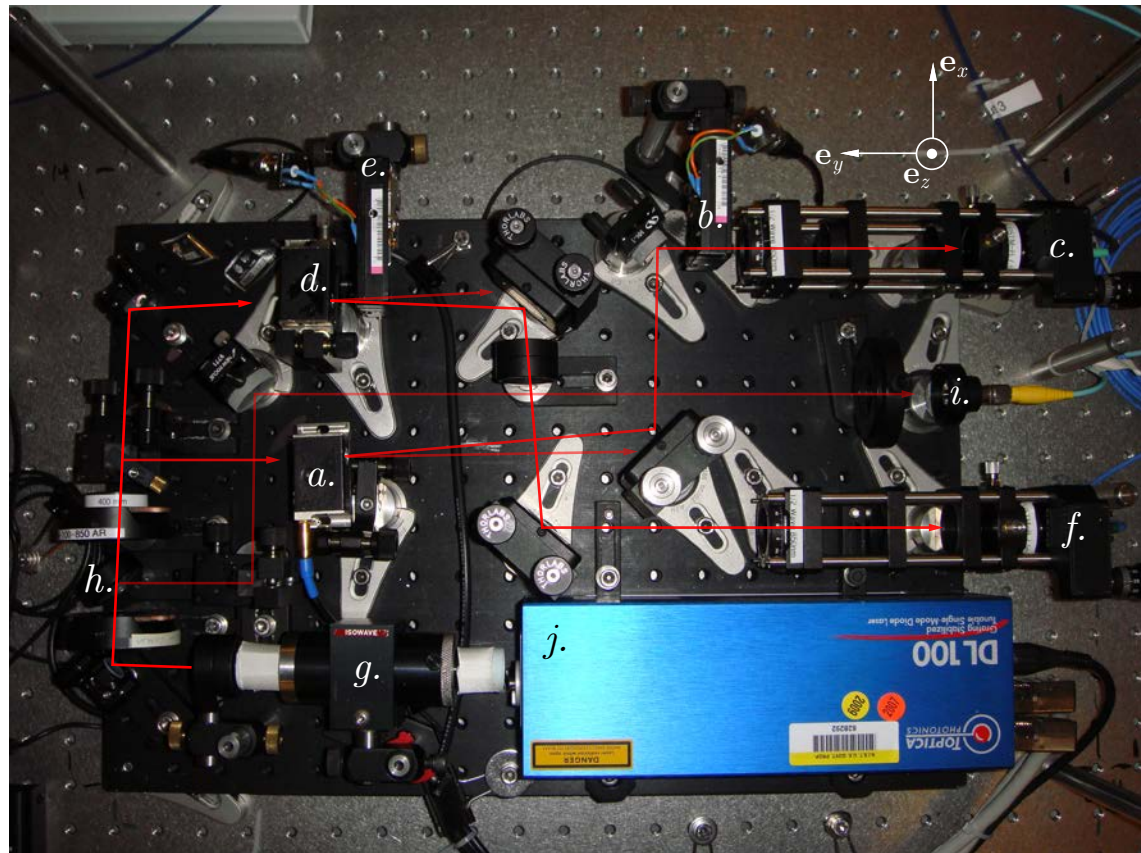


Figure 4.19: Picture of the optical setup for the repump laser. *a-c.* Repump AOM, shutter and optical fiber; *d-f.* slower repump AOM, shutter and optical fiber; *h.* beam splitter; *i.* beam sample for beat-note lock; *j.* repump laser. Also see Fig. 4.6b.

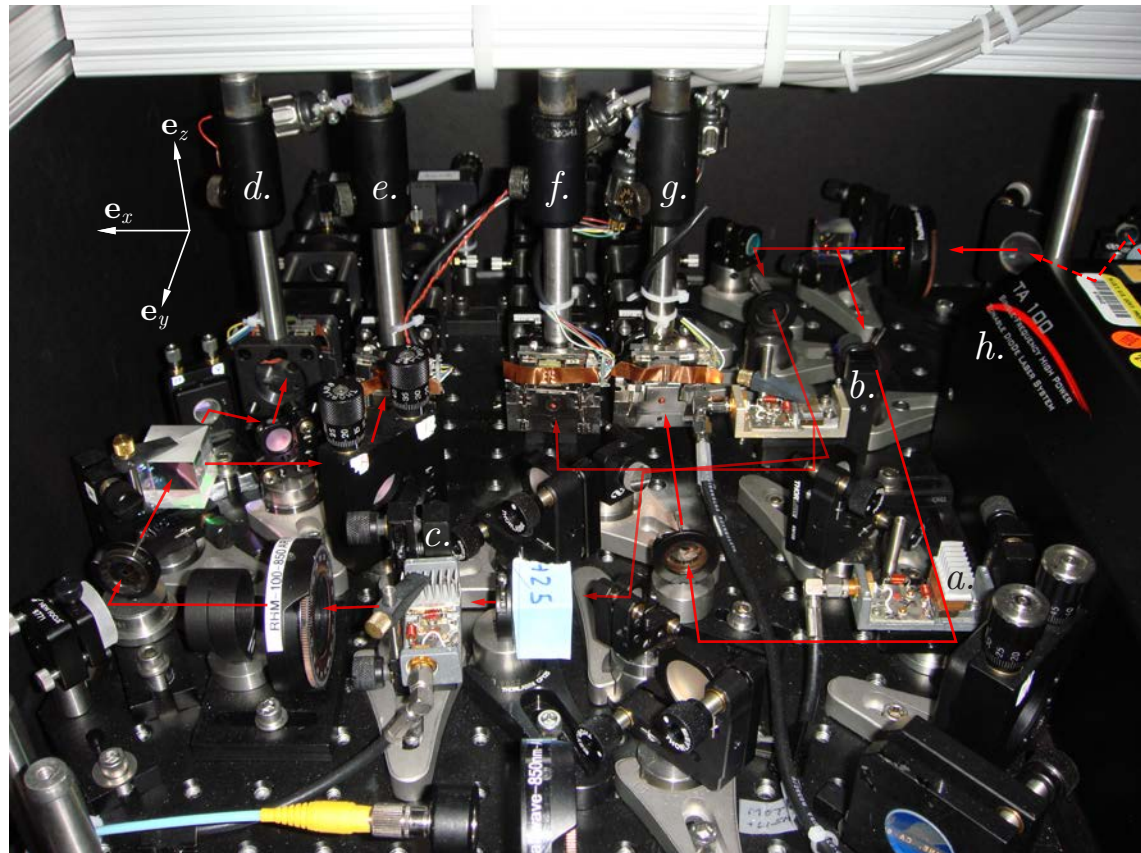


Figure 4.20: Picture of the optical setup for the MOT laser. *a.* MOT AOM; *b.* slower AOM; *c.* imaging AOM; *d-e.* *xy* and *xz* imaging shutters; *f-g.* slower and MOT shutters; *h.* MOT laser. Also see Fig. 4.8.

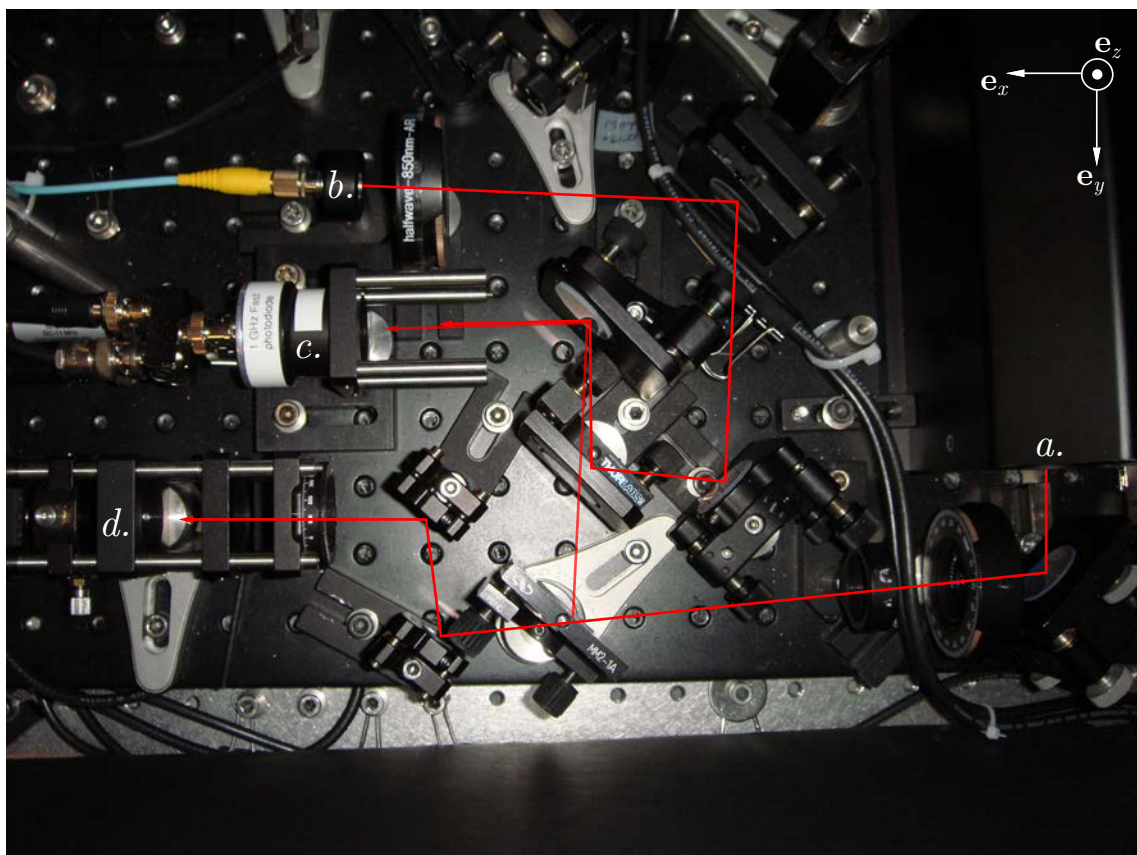


Figure 4.21: Picture of the optical setup for the MOT beat-note lock. *a.* Test beam; *b.* master beam for locking; *c.* photodiode for beat-note locking; *d.* sample beam for mode diagnostic. Also see Fig. 4.8.

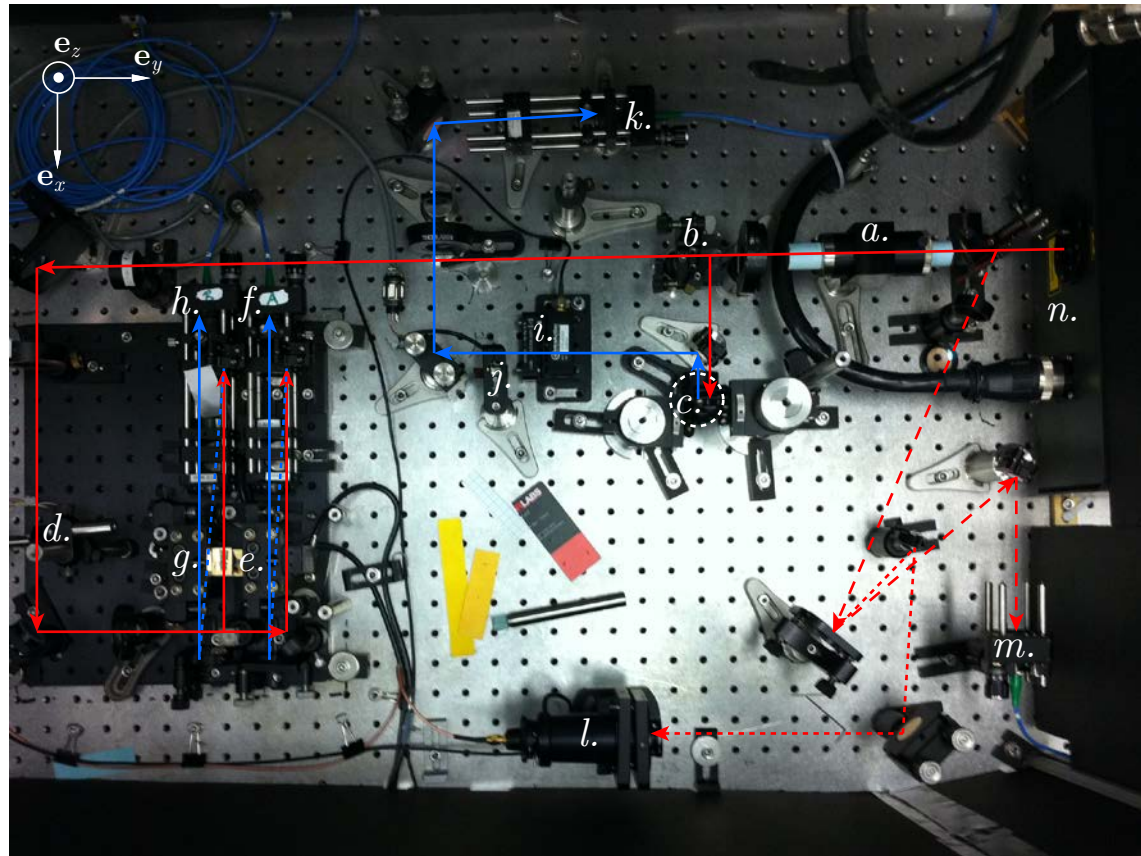


Figure 4.22: Picture of the optical setup for the Raman lasers. *a.* Optical isolator; *b.* beams splitter; *c.* periscope; *d.* Raman A and B shutter; *e-f.* Raman A AOM and optical fiber; *g-h.* Raman B AOM and optical fiber; *i-k.* Raman C AOM, shutter and optical fiber; *l.* Fabry-Perot cavity; *m.* sample beam to wavemeter; *n.* Ti:Sapph laser. Also see Fig. 4.13.

CHAPTER 5

ARTIFICIAL GAUGE FIELDS FOR ULTRACOLD NEUTRAL ATOMS

Given the high degree of experimental control on ultracold atom systems, which makes them ideal to realize quantum simulation of more complex systems, why do we need artificial gauge fields for ultracold neutral atoms?

Current interesting research topics include: quantum Hall systems [23], the spin-Hall effect [74, 75], topological insulators [12], p -wave superconductors [76] and Majorana fermions [13]. One apparent limitation associated with atomic systems is its electrical-charge neutrality; the lack of a Lorentz force prevents the observation of important quantum effects. Phenomena such as the quantum Hall effect, the spin Hall effect and exotic phenomena like topological insulators, would in principle be inaccessible to cold atoms.

There are two ways to overcome this limitation: (a.) by inducing rotation of the cold gases [77] and exploiting the mechanical equivalence between the Coriolis force and the Lorentz force; or (b.) by designing suitable laser fields to induced artificial gauge potentials for cold atom systems [1].

There are distinct approximations to create light-induced artificial gauge fields, namely: (i.) by designing suitable optical fields in which the center of mass motion of and slowly moving atom reproduces that of a charged particle in an electromagnetic field [1]; (ii.) by directly imprinting a Peierls phase on the atoms moving in a lattice potential, using laser assisted tunneling [78, 79]; and (iii.) by modifying the bandstructure of atoms in driven optical potentials [80, 81].

This chapter gives an overview of the pioneering experiments with light-induced artificial gauge fields realized at our group at NIST; with particular emphasis on the experimental techniques not highlighted in the original publications (Table 5.1).

5.1 BASIC REVIEW OF GAUGE FIELDS FOR CHARGED PARTICLES

The goal of our experiments with neutral atoms is to engineer the Hamiltonian of a charged particle in an electromagnetic field. We briefly review classical electrodynamics to establish the form of the Hamiltonian to be implemented on neutral atoms.

Electromagnetism (EM) is a gauge theory where the electromagnetic field can be described by vector and scalar potentials, \mathbf{A} and ϕ , which are defined only up to a gauge choice. Spatial

variations of the scalar potential contribute to the electric field; while the vector potential generates both electric and magnetic fields varying in time and space, respectively

$$\mathbf{E} = -\nabla\phi - \frac{\partial\mathbf{A}}{\partial t}, \quad \mathbf{B} = -\nabla \times \mathbf{A}. \quad (5.1)$$

The Hamiltonian for an electrically charged particle, of charge q and mass m , under the influence of an electromagnetic field can be expressed in terms of the gauge potentials ϕ and \mathbf{A} as [51]

$$H = \frac{1}{2m}(\mathbf{p}_{\text{can}} - \frac{q\mathbf{A}}{c})^2 + q\phi, \quad (5.2)$$

where c is the speed of light in vacuum; and Hamilton's equations lead to the equation of motion of the charged particle, namely to the expression for the Lorentz force $\mathbf{F} = q(\mathbf{E} + \mathbf{v} \times \mathbf{B})$.

The Hamiltonian from Eq. (5.2) is that of a free particle under the substitution $\mathbf{p}_{\text{can}} \rightarrow \mathbf{p}_{\text{can}} - q\mathbf{A}$, where it is important to emphasize that in this replacement \mathbf{p}_{can} is the canonical momentum, i.e. the variable that is canonically conjugated to the position; in the presence of a vector potential, the dispersion relation of a free particle changes from $\mathbf{p}_{\text{can}}^2/2m$ to $(\mathbf{p}_{\text{can}} - q\mathbf{A})^2/2m$; this is the basic idea to introduce the effects of an electromagnetic field in the motion of a charge particle.

5.2 ARTIFICIAL GAUGE FIELDS FOR ULTRACOLD NEUTRAL ATOMS

I describe next the experimental method to implement a gauge term in the Hamiltonian of trapped ultracold neutral atoms, which gives rise to effective electric and magnetic fields. Our approach is based on optically dressing an atomic sample with a pair of Raman beams to induce an experimentally tunable dispersion relation of the form $(\mathbf{p}_{\text{can}} - \mathcal{A})^2/2m^*$, where \mathcal{A} represents an artificial gauge field for ultracold neutral atoms and m^* is an effective mass.

The induced potential $\mathcal{A} = (\mathcal{A}_x, \mathcal{A}_y, \mathcal{A}_z)$ is a vectorial quantity whose components, can be scalar or even have a matrix form. In particular, the commutation relations between the components \mathcal{A}_j , $j \in \{x, y, z\}$ determine if the gauge field is Abelian or not, opening the possibility to other realizations beyond EM.

We work with ^{87}Rb BECs typically in the $F=1$ ground state manifold. The atoms are confined in a spin-independent optical trap potential $V(\mathbf{r})$, such that their Hamiltonian is given by $\hat{H} = [\hbar^2\mathbf{k}^2/2m + V(\mathbf{r})] \otimes \hat{1}$, where $\mathbf{p} = \hbar\mathbf{k}$ is the momentum of the atoms, and $\hat{1}$ is the 3×3 unit matrix acting on the $F=1$ spin space. It is clear that in order to implement an artificial gauge potential, we have to modify the kinetic energy term in this Hamiltonian, and that this must be through a process by which we exchange momentum with the atoms such as to induce a shift of their momentum dispersion relation. Raman transitions within the $F=1$ manifold are suitable to achieve such Hamiltonian [4].

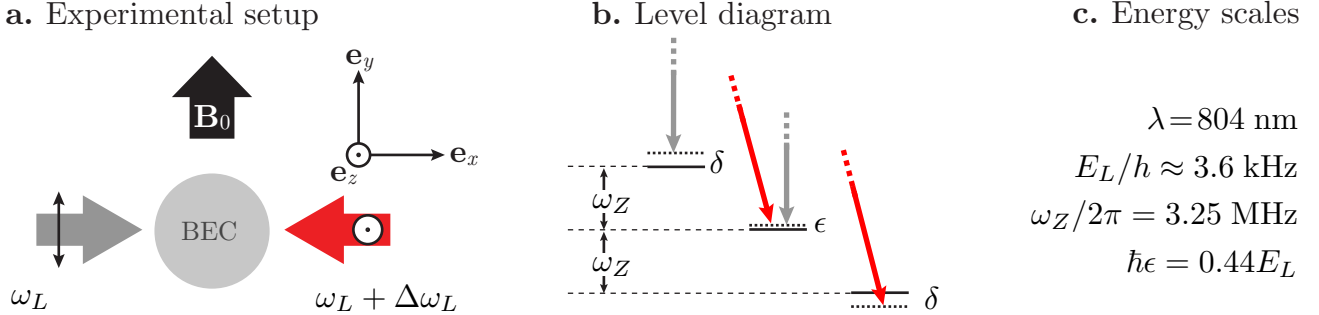


Figure 5.1: Standard experimental setup and level diagram setup for implementing light-induced artificial gauge fields on neutral atoms. **a.** A uniform bias field $B_0\mathbf{e}_y$ Zeeman splits the energy levels in ^{87}Rb 's $F=1$ manifold, while a pair of counter propagating Raman beams illuminates an $m_F=-1$ BEC. **c.** The natural units for momentum and energy are set by the single photon recoil momentum $\hbar k_L = h/\lambda$ and the associated energy $E_L = \hbar^2 k_L^2 / 2m$, acquired by a single atom due to its interaction with a Raman laser.

5.2.1 Raman coupling scheme for an $F=1$ BEC. I now describe the Raman coupling scheme used in our experiments to create artificial gauge fields for ultracold neutral atoms. I focus on the origin of the coupling Hamiltonian both in real and in momentum space, relevant energy scales, and the emergence of an artificial vector potential \mathcal{A} .

5.2.1.1 The experimental setup, Zeeman energies and natural units. Figure 5.1 illustrates the basic ingredients for the realization light-induced artificial gauge fields in our lab. An $F=1$ ^{87}Rb BEC is prepared in an optical trap, and a uniform magnetic field $B_0\mathbf{e}_y$ breaks the degeneracy of the hyperfine magnetic sublevels $|m_F=0, \pm 1\rangle$. The energy splittings between these levels correspond to the linear and quadratic Zeeman shifts¹

$$\hbar\omega_Z = g_F\mu_B B_0 \approx \pm E_{\mp 1}, \quad \text{and} \quad \hbar|\epsilon| = E_0 - (E_{-1} - E_{+1})/2; \quad (5.3)$$

where $g_F\mu_B = 0.7 \text{ MHz/G}$ for ^{87}Rb in $F=1$, and typically $|E_{-1}| \approx |E_{+1}| \gg |E_0|$. A pair of Raman lasers with wavelength λ illuminates the BEC, and couples the m_F states with strength Ω_R . These Raman lasers differ in frequency by $\Delta\omega_L \approx \omega_Z$ and we define the detuning from Raman resonance as $\delta = \omega_L - \omega_Z$.

A Raman transition involves a two-photon process where the atoms and the light exchange momentum and energy, and is governed by energy-, momentum-, and angular-momentum- conservation laws. The natural units to quantize momentum and energy are the ones associated with the

¹The quadratic Zeeman shift is negative and, when expressed as a frequency in kHz, its amplitude for ^{87}Rb in the $F=1$ manifold is given by $\epsilon/h = \epsilon_B B^2$, where: $\epsilon_B \approx 7.1772 \times 10^{-2} \text{ kHz/G}^2$; $B = \omega_Z/(2\pi \times 0.7)$ is the magnetic field in G; and ω_Z is expressed in MHz (see Sec. 3.8). In Chapters 5, 9 and 8 we adopt the convention to express the quadratic as explicitly negative, i.e. as $-\hbar\epsilon$.

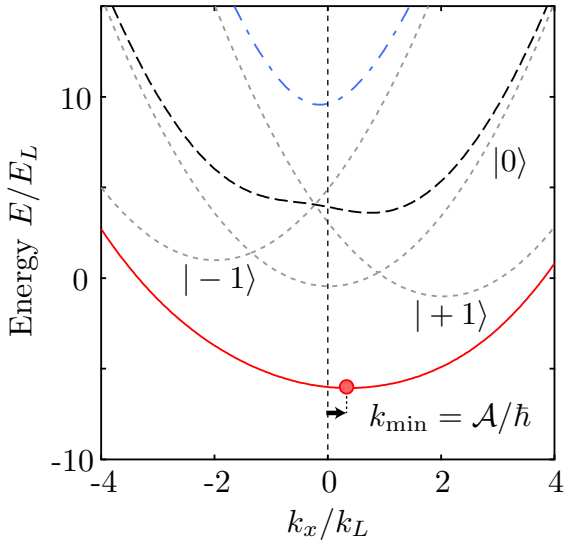
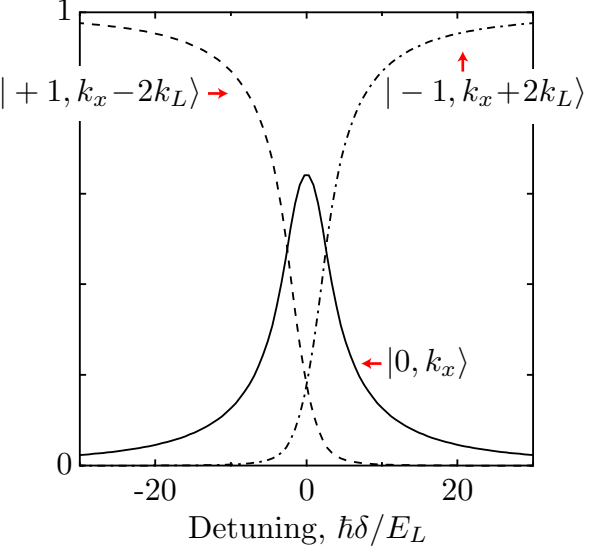
a. Raman dressed dispersion relations**b.** Fractional population of the lowest dressed state

Figure 5.2: Eigenenergies of the Raman dressed states as a function of quasimomentum k_x . **a.** The dotted curves correspond to free-particle dispersion relations of the bare spin-momentum states. The solid, dashed and dot-dashed curves represent the eigenenergies of \hat{H}_x at $\hbar\Omega_R=10.5E_L$, $\hbar\epsilon=0.44E_L$ and $\hbar\delta=-1E_L$. The arrow represents the canonical momentum $\hbar k_{\min}=\mathcal{A}/\hbar$ of the dressed BEC, where \mathcal{A} is the vector potential. **b.** The spin-momentum composition of the lowest dressed state, at $\hbar\Omega_R=10.5E_L$ and $\hbar\epsilon=0.44E_L$, is shown as a function of detuning δ .

effective amount of momentum $\hbar k_L$ acquired by an atom in a single photon absorption process, these are determined as follows. Assume that the Raman beams propagate in arbitrary directions defined by the unit vectors \mathbf{e}_A and \mathbf{e}_B ; an atom that absorbs a photon from the beam A at ω_L acquires momentum k_L along its \mathbf{e}_A , and emits a photon into beam B at $\omega_L+\Delta\omega_L$ thus recoiling toward \mathbf{e}_B with momentum k_L , the direction of momentum transfer is along² $\mathbf{e}_A-\mathbf{e}_B$. The effective momentum transferred to the atom by a single beam, is its projection along the $\mathbf{e}_A-\mathbf{e}_B$ direction. For Raman lasers intersecting at an angle $\theta=\arccos(\mathbf{e}_A \cdot \mathbf{e}_B)$, the effective recoil momentum from a single-photon is $k_L=\pi[\lambda \cos(\theta/2)]^{-1}$; and the corresponding scaled recoil energy acquired by the atom of mass m in the absorption process is $E_L=\hbar^2 k_L^2/2m$. Both quantities, k_L and E_L , set the natural momentum and energy scales in the problem.

5.2.1.2 The Raman coupling Hamiltonian. Without loss of generality we establish our coordinate system to make the direction of the Raman momentum transfer $\mathbf{e}_A-\mathbf{e}_B$ to coincide with the \mathbf{e}_x

²The reverse process is also true, i.e. an atom that absorbs a photon from the beam B emits a photon in beam A and recoils in direction of $-(\mathbf{e}_A-\mathbf{e}_B)$. In Fig. 5.1a the total momentum transfer is $\pm 2k_L \mathbf{e}_x$.

axis, this way the Hamiltonian of the system can be written in the form:

$$\hat{H} = [\hbar^2(k_y^2 + k_z^2)/2m + V(\mathbf{r})] \otimes \hat{1} + \hat{H}_x, \quad (5.4)$$

where \hat{H}_x is a 3×3 matrix that contains the kinetic energy term associated with the x -component of the momentum $k_x = \mathbf{k} \cdot \mathbf{e}_x$, the interaction with the Raman field and the Zeeman energies defined in Eq. (5.3). The origin of the Raman coupling Hamiltonian relies on the vector light-shift introduced by the Raman beams. The electric field from each beam in Fig. 5.1a is

$$\mathbf{E}_A(\mathbf{r}, t) = E_A \exp[ik_L x - i\omega_L t] \mathbf{e}_y, \quad \text{and} \quad \mathbf{E}_B(\mathbf{r}, t) = E_B \exp[-ik_L x - i(\omega_L + \Delta\omega_L)t] \mathbf{e}_z; \quad (5.5)$$

and the total field at the atoms is

$$\mathbf{E}(x, t) = E_0 \{ \exp[i(k_L x - \omega_L t - \Delta\omega_L t)] \mathbf{e}_z + \exp[i(-k_L x - \omega_L t)] \mathbf{e}_y \}, \quad (5.6)$$

where I have assumed that both Raman fields have the same amplitude $E_A = E_B = E_0$.

The vector light shift from the Raman beams, which is proportional to $\mathbf{E}^* \times \mathbf{E}$, generates an effective Zeeman magnetic field along \mathbf{e}_x of the form

$$\mathbf{B}_{\text{eff}} \propto -E_0^2 \cos(2k_L x + \Delta\omega_L t) \mathbf{e}_x, \quad (5.7)$$

whose interaction with the effective magnetic moment of the atoms, $\mu = g_F m_F \hat{\mathbf{F}}$ [where $\hat{\mathbf{F}}$ is the $F=1$ angular momentum operator, (see Appendix A)], gives the interaction Hamiltonian $\hat{H}_R = -\mu \cdot \mathbf{B}_{\text{eff}}$.

In the frame rotating at $\Delta\omega_L$, making the rotating wave approximation (RWA), and expressing the coupling Hamiltonian in the basis of bare spin states $\{| -1 \rangle, | 0 \rangle, | +1 \rangle\}$, we obtain

$$\hat{H}_R/\hbar = \begin{pmatrix} 0 & (\Omega_R/2)e^{i2k_L x} & 0 \\ (\Omega_R/2)e^{-i2k_L x} & 0 & (\Omega_R/2)e^{i2k_L x} \\ 0 & (\Omega_R/2)e^{-i2k_L x} & 0 \end{pmatrix}, \quad (5.8)$$

where Ω_R is the Rabi frequency that characterizes the strength of the coupling field and $\delta = \Delta\omega_L - \omega_Z$ is the detuning from Raman resonance.

5.2.1.3 The Raman coupling Hamiltonian in momentum space. Energy and angular momentum selection rules dictate that spin-momentum states coupled by the Raman beams involve those states differing in spin by $\Delta m_F = \pm 1$ which also differ in momentum by $\hbar\Delta k_x = \pm 2\hbar k_L$.

The set of Raman coupled states $\{| -1, k_x+2k_L \rangle, | 0, k_x \rangle, | +1, k_x-2k_L \rangle\}$, where $\hbar k_x$ is referred to as the quasimomentum, constitutes a basis in which the \hat{H}_x term of the overall Hamiltonian given

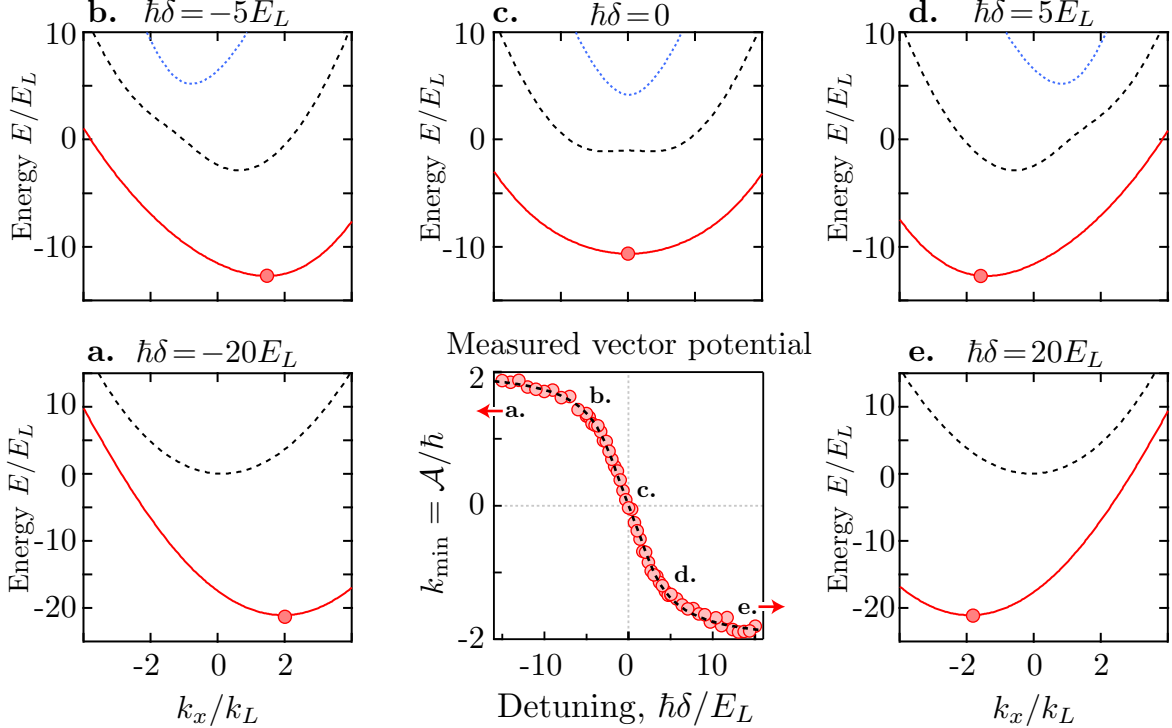


Figure 5.3: Panels **a.** to **e.** show the calculated energy bands of the Raman coupling Hamiltonian at $\hbar\Omega_R = 10E_L$ for selected values of the detuning; circles indicate the location of the minimum of the dispersion relation $E(k_x)$. In the central panel at the bottom we plot the measured (circles) and calculated (dashed curve) location $k_{\min} = \mathcal{A}/\hbar$ as a function of detuning at $\hbar\Omega_R = 10.5E_L$. (Data from Ref. [6].)

in Eq. (5.4) is given by

$$\hat{H}_x = \begin{pmatrix} \hbar^2(k_x + 2k_L)^2/2m - \hbar\delta & \hbar\Omega_R/2 & 0 \\ \hbar\Omega_R/2 & \hbar^2k_x^2/2m - \hbar\epsilon & \hbar\Omega_R/2 \\ 0 & \hbar\Omega_R/2 & \hbar^2(k_x - 2k_L)^2/2m + \hbar\delta \end{pmatrix}. \quad (5.9)$$

Due to the separability of the overall Hamiltonian, in our experiments we mainly focus on the effects introduced by \hat{H}_x ; since this Hamiltonian captures the physics of the whole Raman coupling scheme described in Fig. 5.1 we simply refer to it as the Raman coupling Hamiltonian. It should be also noted that our engineered vector potential has a single non-zero component $\mathcal{A} = (\mathcal{A}_x, 0, 0)$; from here on we simply refer to it as $\mathcal{A}_x = \mathcal{A}$.

We see from Eq. (5.9) that \hat{H}_x is reminiscent of the bandstructure in a periodic potential as studied in Sec. 7.2. The key features in the Raman coupling scheme are that we only have three energy bands, as well as two extra tuning parameters (namely the Zeeman energies δ and ϵ); the latter play an important role in defying the nature of the eigenstates.

5.2.2 Energy-momentum dispersion relation $E(k_x)$. We now focus on the Raman coupling Hamiltonian of Eq. (5.9) and the origin of an experimentally tunable vector potential \mathcal{A} .

Under no dressing (no illumination from the Raman beams), the Hamiltonian is diagonal and the energy of the spin-momentum states of the basis $\{| -1, k_x + 2k_L \rangle, | 0, k_x \rangle, | +1, k_x - 2k_L \rangle\}$ corresponds to the entries along the main diagonal, i.e. their dispersion is that of free-particles; this is illustrated in Fig. 5.2 as dotted parabolae (light grey).

When the Raman coupling is turned on, the crossings of the bare spectrum become gaps as shown in Fig. 5.2. The solid, dashed and dot-dashed curves correspond to the lowest, first excited and second excited energy bands, respectively; these were obtained by numerically diagonalizing \tilde{H}_x as a function of the quasimomentum k_x . When the Raman beams are adiabatically turned on and illuminate the atoms in a BEC, the atoms adiabatically follow the ground state of the system and the lowest energy band $E(k_x)$ becomes their new dispersion relation. For sufficiently strong Raman coupling $\hbar\Omega_R \gg 4E_L$ the new dispersion is free-particle like, namely $E(k_x) \approx \hbar^2(k_x - k_{\min})^2/2m^*$ or equivalently $E(k_x) \approx (\hbar k_x - \mathcal{A})^2/2m^*$, where $\mathcal{A} = \hbar k_{\min}$ corresponds to an experimentally artificial vector potential, and m^* is an effective mass which accounts for the fact that the curvature of $E(k_x)$ is not the same as that of the dispersion of the bare spin-momentum states. (The physics of the small Raman coupling limit $\hbar\Omega_R < 4E_L$ are discussed in Chapter 9, while a deeper study of effective mass is presented in Chapter 8.)

The most important feature of the Raman coupling scheme is that the dispersion relation $E(k_x)$ is tunable via the Raman coupling strength Ω_R and via the detuning δ ; and that both parameters are experimentally adjustable: via the Raman lasers intensity and through small changes to the amplitude B_0 of the external bias field, respectively. Figure 5.3 shows the calculated energy bands at $\hbar\Omega_R = 10E_L$ at different values of the detuning, together with a measurement demonstrating the experimental control on a light-induced vector potential \mathcal{A} [6].

Not only does the lowest band, but also the second excited band experiences a vector potential in the large Raman coupling limit [4]; this is most evident from Fig. 5.3. We observe the minima

Table 5.1: Physical effects of light-induced artificial gauge fields.

| Nature of \mathcal{A} | Physical effect on ultracold neutral atom systems | |
|-------------------------|--|--|
| Uniform | $\mathcal{A} = \hbar k_{\min}$ | Shift of the dispersion relation [5] |
| Spatially varying | $\mathcal{B} = \nabla \times \mathcal{A}$ | Synthetic magnetic field [7], Hall physics [8] |
| Time varying | $\mathbf{E}^* = \partial \mathcal{A} / \partial t$ | Artificial electric field [6] |
| Matrix valued | $\mathcal{A}_x = -\hbar k_L \sigma_y$ | Spin-orbit coupling [9] |
| Uniform in 1D lattice | $\mathcal{A} = (\phi/\pi)\hbar k_L$ | Complex tunneling matrix element [30] |

of both bands shift in opposite directions, this constitutes a feature of interest in experiments considering oppositely-charged particles in artificial gauge fields; however the measured 1/e lifetime for decay from such excited state [$\tau=12(1)$ ms [11]] limits its use.

5.3 PHYSICAL MANIFESTATION OF AN ARTIFICIAL VECTOR POTENTIAL

Having discussed the origin of a light-induced vector potential \mathcal{A} , I will briefly give an overview of its physical effects. As with conventional gauge fields, we study the effects of not only uniform light-induced vector potentials, but also focus on their temporal and spatial variations. This chapter focuses on spatially uniform artificial vector potentials in the large Raman coupling regime $\hbar\Omega_R \gg 4E_L$, and their time dependence; Chapter 6 discusses the case of spatially varying artificial gauge fields and the generation of synthetic magnetic fields; Chapter 9 describes matrix valued artificial gauge fields and the experimental realization of spin-orbit coupled BECs. Table 5.1 summarizes the topics to be covered in the rest of this thesis.

5.3.1 Uniform light-induced vector potential. Figure 5.3 illustrates the most obvious effect of a uniform light-induced artificial vector potential \mathcal{A} , this is the shift of the energy-momentum dispersion relation $E(k)$. This light induced vector potential is the basis for our experiments with artificial gauge fields; and can be directly measured from absorption images of atomic distributions as shown in Fig. 5.4a.

5.3.2 Time-dependent artificial vector potential. Temporal changes in a vector potential \mathbf{A} generate electric fields, which ultimately exert forces on charged particles; when expressed in the form of Newton's second law we obtain that the rate of change of the mechanical momentum $\Delta p = mv$, for a particle of mass m and velocity v , is directly proportional to the rate of change of the vector potential.

For our $F=1$ Raman-dressed system the mechanical momentum corresponds to the population-weighted average of the momentum in the three m_F states; and the canonical momentum p_{can} is the variable canonically conjugated to position. The mechanical and canonical momenta are related by $mv = p_{\text{can}} - \mathcal{A}$, where \mathcal{A} is an artificial vector potential. Atoms in a BEC have a narrow momentum distribution centered at zero; meaning that in equilibrium, their mechanical momentum is zero (Fig. 5.4a).

An artificial vector potential \mathcal{A} is expected to have the same effect on neutral atoms as a real vector potential has on charged particles; namely to change their mechanical momentum by $-\Delta p = \mathcal{A}_f - \mathcal{A}_i$, where $\mathcal{A}_{i(f)}$ is the initial (final) value of the artificial vector potential. By imposing a temporal dependence on a light-induced vector potential we generated a synthetic electric field force for ultracold neutral atoms, whose effects are directly measured from the atomic momentum distributions as shown in Fig. 5.4b,c.

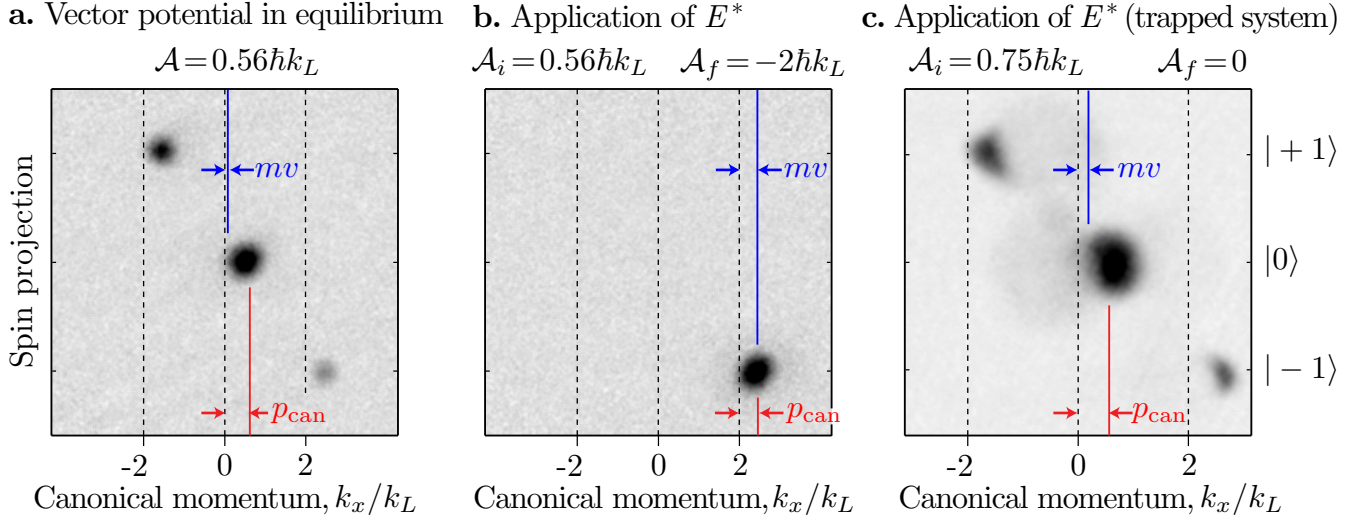


Figure 5.4: Detection of Raman dressed states after TOF. **a.** A Raman dressed state in equilibrium showing the canonical momentum $p_{\text{can}} = \mathcal{A}$, the experimental parameters are $\hbar\delta = -1.7E_L$. This is a measurement example of those in the lower central panel of Fig. 5.3. **b.** Starting in the configuration shown in **a.**, where $\mathcal{A}_i = 0.56 \hbar k_L$, we apply a synthetic electric field \mathbf{E}^* by changing the vector potential to the final value $\mathcal{A}_f = -2 \hbar k_L$; the mechanical momentum of the atoms changes by $\Delta p = 2.56 \hbar k_L$. **c.** A synthetic electric field is generated by changing the vector potential from $\mathcal{A}_i = 0.75 \hbar k_L$ to $\mathcal{A}_f = 0$, this is a picture of an out of equilibrium condition where the atoms oscillate in the trap after the application of \mathbf{E}^* .

5.4 EXPERIMENTAL CHARACTERIZATION

5.4.1 System preparation. All artificial gauge field experiments described in this thesis share similar experimental setups. Minor changes such as the direction, wavelength and polarization of the Raman lasers; the direction and amplitude of the bias fields; the geometry of the dipole trap; and other extensions are summarized in Fig. 5.8.

All our experiments in artificial gauge fields have a common starting point, namely they start with ^{87}Rb BECs in the $|F=1, m_F=-1\rangle$, and are loaded into the lowest Raman dressed state using an auxiliary rf-field.

5.4.1.1 rf-assisted loading into the lowest energy dressed state. The procedure to adiabatically load a BEC into the lowest Raman dressed state is described in Ref. [5], and we have adopted it as the standard method in all subsequent experiments; its experimental setup coincides with that of Fig. 5.1.

All experiments start with ^{87}Rb BECs in the $|F=1, m_F=-1\rangle$ state in a crossed optical dipole trap with frequencies (f_x, f_y, f_z) . A uniform bias field $B_0 \mathbf{e}_y$ sets the quantization axis and Zeeman splits the spin states by $\hbar\omega_Z$. We prepare spin mixtures using an auxiliary rf field $B_{\text{rf}} \mathbf{e}_x$, characterized by an oscillating frequency $\omega_{\text{rf}} = \omega_Z$ and a Rabi frequency $\hbar\Omega_{\text{rf}}$, to realize a partial

rapid passage to $\delta = 0$ by ramping the magnitude of $B_0 \mathbf{e}_y$ in 9 to 15 ms. The auxiliary rf field is useful to set initial energy gaps between the dressed states, which support faster adiabatic loading into the Raman dressed state [5].

A pair of λ Raman laser beams, counter-propagating along \mathbf{e}_x and differing in frequency by $\Delta\omega_L$, are turned on from zero to their final coupling strength Ω_R in 20-100 ms; and couple the internal degrees of freedom of the BEC with strength Ω_R . During the turn-on ramp of the Raman beams, the rf-field is removed, and the atoms are loaded into the lowest Raman dressed state with quasimomentum $\hbar k_x = 0$.

We load the system into lowest energy band at non-zero quasimomentum $\hbar k_x = \mathcal{A}$, by ramping the detuning from Raman resonance (the experimental control parameter being the electrical current generating the bias field); we keep the frequency difference of the Raman beams $\Delta\omega_L$ constant. The time scale for adiabaticity, such that the BEC always sits at the minimum of the new dispersion curve, is set by the effective trapping frequency along the direction of the Raman beams [5].

5.4.2 The Raman laser beams. A full characterization of the Raman laser properties is necessary to understand and properly engineer artificial gauge fields for cold atoms. We care about most properties of these beams: intensity, wavelength (frequency), mode, polarization.

5.4.2.1 The quantization axis and the polarization of the Raman beams. Once a quantization axis has been set by the external bias field \mathbf{B}_0 , the polarization of the laser beams has to be carefully chosen to allow Raman processes. Due to their origin as a vector light-shift ($\propto \mathbf{E}^* \times \mathbf{E}$) a rule to optimize the coupling strength is to make the cross product of their (linear) polarizations to be orthogonal to the quantization axis; this ensures optimal conditions for both π - and σ_{\pm} -transitions to occur.

It suffices to use a suitable polarizing beam splitter to determine the polarization of each Raman beam; by changing the angle of the $\lambda/2$ -waveplate, located at the output port of the optical fiber sending the laser to the main experiment, the polarization can be adjusted.

5.4.3 Resonance conditions and the Raman coupling strength. Our experiments on artificial gauge fields are based on the internal structure of ^{87}Rb , particularly on the $F=1$ ground state manifold; and an external bias field $B_0 \mathbf{e}_y$ sets the linear ω_Z and quadratic ϵ Zeeman shifts among the m_F sublevels.

5.4.3.1 Determining the resonance condition for the Raman coupling scheme. After setting up the experimental scheme for Raman coupling (having chosen the Zeeman splitting $\hbar\omega_Z$), we prepare nearly pure ^{87}Rb BECs in the $|F=1, m_F=-1\rangle$ state. We determine the amplitude of the magnetic field which produces such Zeeman splitting, by illuminating the atoms with an rf-field oscillating at $\nu_{\text{rf}} = \omega_Z/2\pi$ to perform a partial adiabatic rapid passage; partial here means that the atoms do not

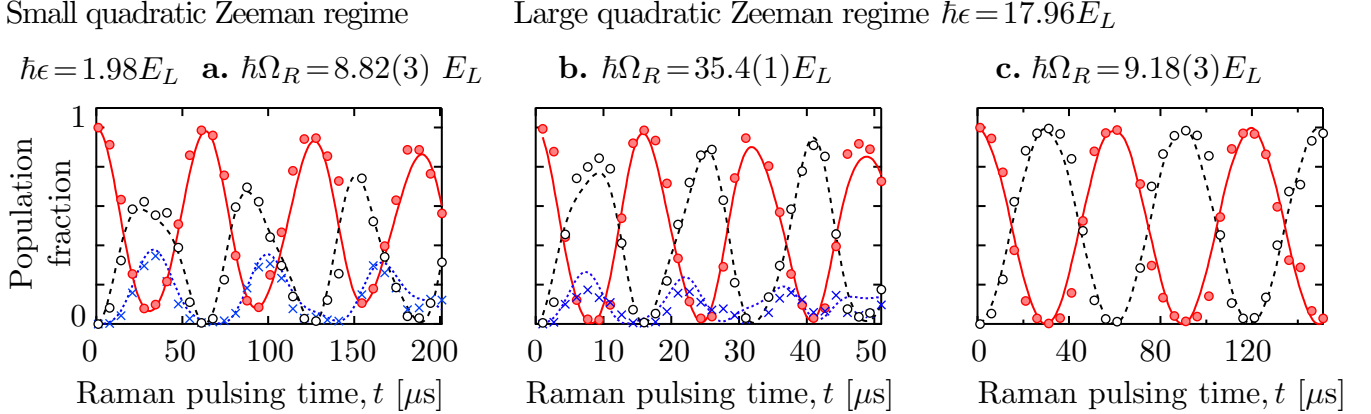


Figure 5.5: Calibration of Raman coupling strength by pulsing. We show the time evolution of an initially pure $|m_F = -1\rangle$ BEC in the presence of both Raman beams. To optimize the contrast in this measurement, the detuning was set to: **a.** $\hbar\delta \approx -2E_L$, and **b.-c.** $\hbar\delta \approx 14E_L$. The curves are simultaneous fits to the fractional populations in each data set: $|m_F = -1, k_x\rangle$ (closed symbols), $|m_F = 0, k_x - 2k_L\rangle$ (open symbols), $|m_F = +1, k_x - 4k_L\rangle$ (crosses), calculated from the unitary evolution of the Raman Hamiltonian. Three of the four fitting parameters were kept constant ($\lambda = 791.1$ nm, δ, ϵ), only the Raman coupling strength Ω_R was varied.

entirely end up in $|F=1, m_F=+1\rangle$, instead we put them in a spin superposition which on resonance exhibits balanced populations of $m_F=\pm 1$. Rapid passage is performed in 15 ms [5], starting below resonance by tens of kHz (see Sec. 6.2.1 for more details on time scales).

We monitor the individual spin populations after expansion in TOF: we suddenly turn off the confining potentials and the rf-field, thus projecting the rf-dressed state into its bare spin components; then we apply a Stern-Gerlach (SG) field during part of TOF to spatially separate the spin components and measure the population in each state; the resolution on the bias fields allows to determine resonance to within tens of kHz; this condition is subject to ambient field noise as described in Sec. 4.9.

5.4.3.2 Calibration of Ω_R from unitary evolution of the Raman coupled system. We measure the coupling strength of the Raman field by studying the unitary time evolution of an initially pure $|m_F = -1\rangle$ BEC in the presence of both Raman beams. Raman processes populate states of increasing spin and momentum which constitute a basis of the form $\{|m_F = -1, k_x\rangle, |m_F = 0, k_x - 2k_L\rangle, |m_F = +1, k_x - 4k_L\rangle\}$; the eigenstate of the system at any given time can be expressed as a superposition of these states.

Efficient transfer between the initial and the first Raman coupled state (here $|m_F = 0, k_x - 2k_L\rangle$) occurs when their energies differ by $4E_L$, this is readily achieved by adjusting the detuning to $\hbar\delta = \hbar\epsilon - 4E_L$; and can be understood in terms of energy conservation: the intermediate state has extra kinetic energy on the amount of $E_{\text{kinetic}} = (2\hbar k_L)^2/2m = 4E_L$, acquired by the two photon

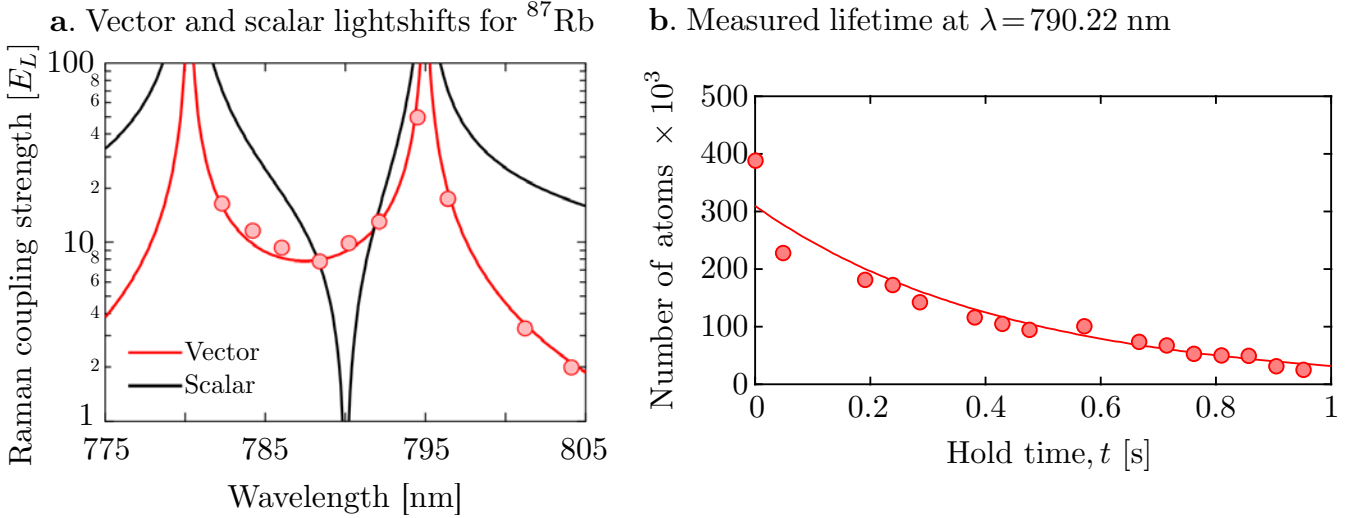


Figure 5.6: **a.** Measured vector light-shift for ^{87}Rb atoms as a function of wavelength. The continuous curves represent the calculated scalar (black) and vector (red) light-shift as a function of wavelength, for a pair of Gaussian laser beams with waists ($1/e^2$ radii) $w_0=150\ \mu\text{m}$ and a power of 200 mW. **b.** An exponential fit (curve) to the decaying number of atoms (circles) in a $\lambda=790.22\ \text{nm}$ Raman dressed state as a function of time gives a lifetime $\tau=0.44(4)\ \text{s}$.

Raman process. In the large quadratic Zeeman regime ($\hbar\epsilon\gg 4E_L$) not only do we have to overcome the $4E_L$ units of extra kinetic energy, but also the quadratic shift itself; efficient transfer is achieved at large detuning values, comparable to ϵ .

Having determined resonance at ω_Z as described in Sec. 5.4.3.1, our pulsing experiments are as follows: we prepare nearly pure ^{87}Rb BECs in the $|F=1, m_F=-1\rangle$ state and ramp the external bias field to the efficient transfer condition $\hbar\delta=\hbar\epsilon-4E_L$. A pair of Raman beams with nearly balanced intensities, wavelength λ and frequency difference $\Delta\omega_L=\omega_Z$ is suddenly switched on for a variable time t ranging from a few to hundreds of μs depending on the laser intensity.

Figure 5.5 shows typical data for the calibration of the Raman coupling strength; these data was measured with the Raman beams propagating along orthogonal directions $\mathbf{e}_x\pm\mathbf{e}_y$, for $\lambda=791.1\ \text{nm}$, where $1E_L\approx h\times 1.835\ \text{kHz}$. In the large quadratic Zeeman measurements, the power in each of the beams was about: (b) 95 mW and (c) 24 mW. Fig. 5.5c experimentally demonstrates that in the large quadratic Zeeman regime, at low coupling, the third spin state is effectively decoupled and our bosonic system can be described as an effective “spin-1/2” system (see Chapter 9).

5.4.3.3 The vector light-shift as a function of wavelength and the lifetime of Raman dressed states. The Raman beams produce both scalar and vector light-shifts whose strength depends on the resonance from the atomic transitions D₁ and D₂. By measuring the Raman coupling strength Ω_R as a function of wavelength, keeping the overall laser power constant at about 200 mW for each

laser, we obtained a measure of the amplitude of the vector light-shift giving rise to our Raman processes; Fig. 5.6a shows the experimental data and their excellent agreement with calculations.

Previous experiments were realized around 803 nm, well above resonance to minimize heating from spontaneous emissions, but with a significant scalar light-shift which ultimately contributes to the overall trapping potential. This is undesirable since the alignment of the Raman beams acquires significant importance, in particular for experiments which require extreme control on the detuning as a function of the location in the trap [7]. The resonance conditions for non-zero light-shift schemes, as described in Sec. 5.4.3.1, were actually determined in the presence of the Raman beams (whose frequency difference was set at $\Delta\omega_L = 2$ MHz to prevent Raman transitions) to include their scalar light-shift.

To overcome this issue, we opted to work at the magic wavelength 790 nm, where the scalar light-shift is mostly suppressed [82], while the coupling strength is increased by a factor of 5 (Fig. 5.6a). Being closer to resonance with respect to the D₁ transition, spontaneous emissions reduced the lifetime of our Raman dressed states to $\tau = 0.44(4)$ s (Fig. 5.6b), i.e. by 68% with respect to the reported value at 804 nm [7]; such reduced lifetime is still suitable for experiments with gauge fields.

5.4.4 Detection of dressed states after TOF. Raman dressed states are spin-momentum superpositions of the bare states of the basis

$$\{| -1, k_x + 2k_L \rangle, | 0, k_x \rangle, | +1, k_x - 2k_L \rangle\}; \quad (5.10)$$

whose relative composition is a function of the coupling strength Ω_R and the detuning from Raman resonance δ , as shown in Fig. 5.2b for typical experimental parameters: $\hbar(\Omega_R, \epsilon) = (10.5, 0.44)E_L$.

We experimentally measure the bare spin-momentum composition of a Raman dressed state (via absorption imaging after TOF) by either of two methods, detailed below: (i.) by suddenly turning off the dressing fields, *projecting* the dressed state into its free-particle bare spin-momentum components; or (ii.) by adiabatically turning off the dressing fields on resonance, and subsequently ramping the detuning, thus *deloading* the Raman dressed state into a single spin state.

5.4.4.1 Projecting to the bare spin-momentum basis. Figure 5.4 shows images the spin-momentum composition of Raman dressed states obtained by this technique; the atoms imaged in Fig. 5.4a, were adiabatically loaded in the lowest Raman dressed state and the bias field was adiabatically ramped to generate a detuning $\hbar\delta = -1.7E_L$ and an artificial vector potential $\mathcal{A} = 0.56\hbar k_L$; then the dressing and confining potentials were suddenly turned off, and a 20.1 ms TOF immediately followed. Had we allowed the atoms to freely expand, the bare spin-momentum components would have separate along \mathbf{e}_x due to the acquired momentum in the Raman processes; instead we applied

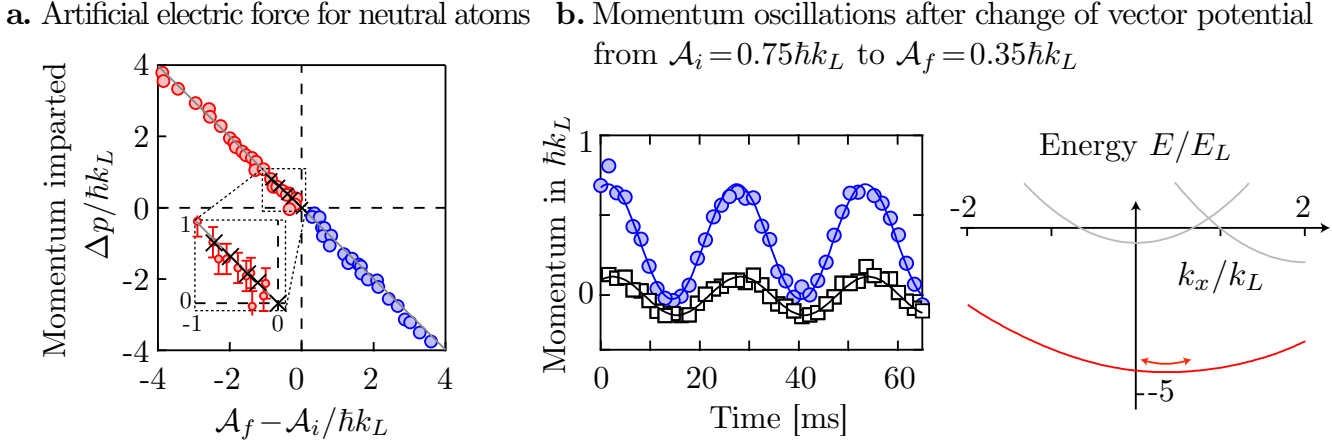


Figure 5.7: Testing the Lorentz force from a synthetic electric field E^* acting on neutral atoms. **a.** Mechanical momentum imparted as a consequence of a sudden change in the vector potential $\Delta\mathcal{A}$. The circles indicate the data from “free” neutral atoms, where the external trap was removed right before \mathcal{A} was changed, and where $\mathcal{A}_f = \pm 2\hbar k_L$ (“-” for red, “+” for blue). **b.** In trap oscillations induced by $\Delta\mathcal{A}$, where $\mathcal{A}_f = 0$; the closed symbols correspond to the canonical momentum, while the open squares represent the mechanical momentum; the dispersion at the extreme right illustrates the conditions for momentum oscillations.

an SG field during part of TOF to separate the spin-momentum distributions along \mathbf{e}_y based on their spin; which helps with the analysis of data.

Projecting into the spin-momentum components also provides a direct measurement of both: the canonical momentum p_{can} , defined as the relative momentum of the $|m_F=0\rangle$ state with respect to $k_x = 0$; and the mechanical momentum mv , which is the population-weighted average of the momentum in the three m_F states.

5.4.4.2 Adiabatic deloading. Band deloading is very similar to band mapping in optical lattices as described in Chapter 8. The deloading procedure depends on the particular experiment and involves a combination of changes in both δ and Ω_R to map the momentum of dressed atoms into the free-particle momentum. Chapter 8 describes a generalized example of band deloading in an engineered lattice with an artificial vector potential.

5.4.5 A uniform vector potential for ultracold neutral atoms. A uniform vector potential \mathcal{A} for ultracold neutral atoms is observable from the shift of the momentum distribution [5, 6] of Raman dressed states as shown in Fig. 5.3.

5.4.6 A synthetic electric force acting on neutral atoms. We studied the mechanical momentum imparted to a neutral atom system as a function of the change in an artificial vector potential $\Delta\mathcal{A} = \mathcal{A}_f - \mathcal{A}_i$. The measurements are summarized in Fig. 5.7a; and the data shows that

the imparted momentum Δp is proportional to ΔA with proportionality constant $-0.996(8)$, where the expected value is -1 [6]; this demonstrates a synthetic electric force acting on neutral atoms.

Figure 5.7 illustrates two important facts: (a, circles) untrapped neutral atoms respond to an effective electric field \mathbf{E}^* as charged particles do; (b) when the atoms are confined, the electric field induces oscillatory motion in the trap, and the mechanical momentum sloshes around the equilibrium value of zero; however, its amplitude (a, crosses) is proportional to ΔA as expected.

Furthermore, data in (b) highlights the contrasting difference between the mechanical and canonical momenta of a trapped BEC, namely the latter is allowed to oscillate around a non-zero value. This technique, based on an effective Lorentz force, is used in subsequent experiments to initiate sloshing and characterize effective mass (see Chapter 8).

5.5 CONCLUSIONS

Using ^{87}Rb BECs we have demonstrated light-induced artificial gauge field for ultracold neutral atoms; and have succeeded in simulating synthetic electric fields.

I have focused in this chapter on detailing relevant experimental techniques for the full characterization of the Raman interaction Hamiltonian, the core of all our experiments current experiments with artificial gauge fields.

The success on the experimental demonstration of such fields has triggered both theoretical and experimental efforts to find the best schemes to not only simulate challenging regimes like that of strong uniform magnetic fields (to gain a better understanding of the quantum Hall effect using ultracold atoms) but also to demonstrate phenomena beyond condensed matter models.

Experiments have already succeeded in realizing artificial gauge fields using fermions, the ultimate simulators of electronic systems [32, 33].

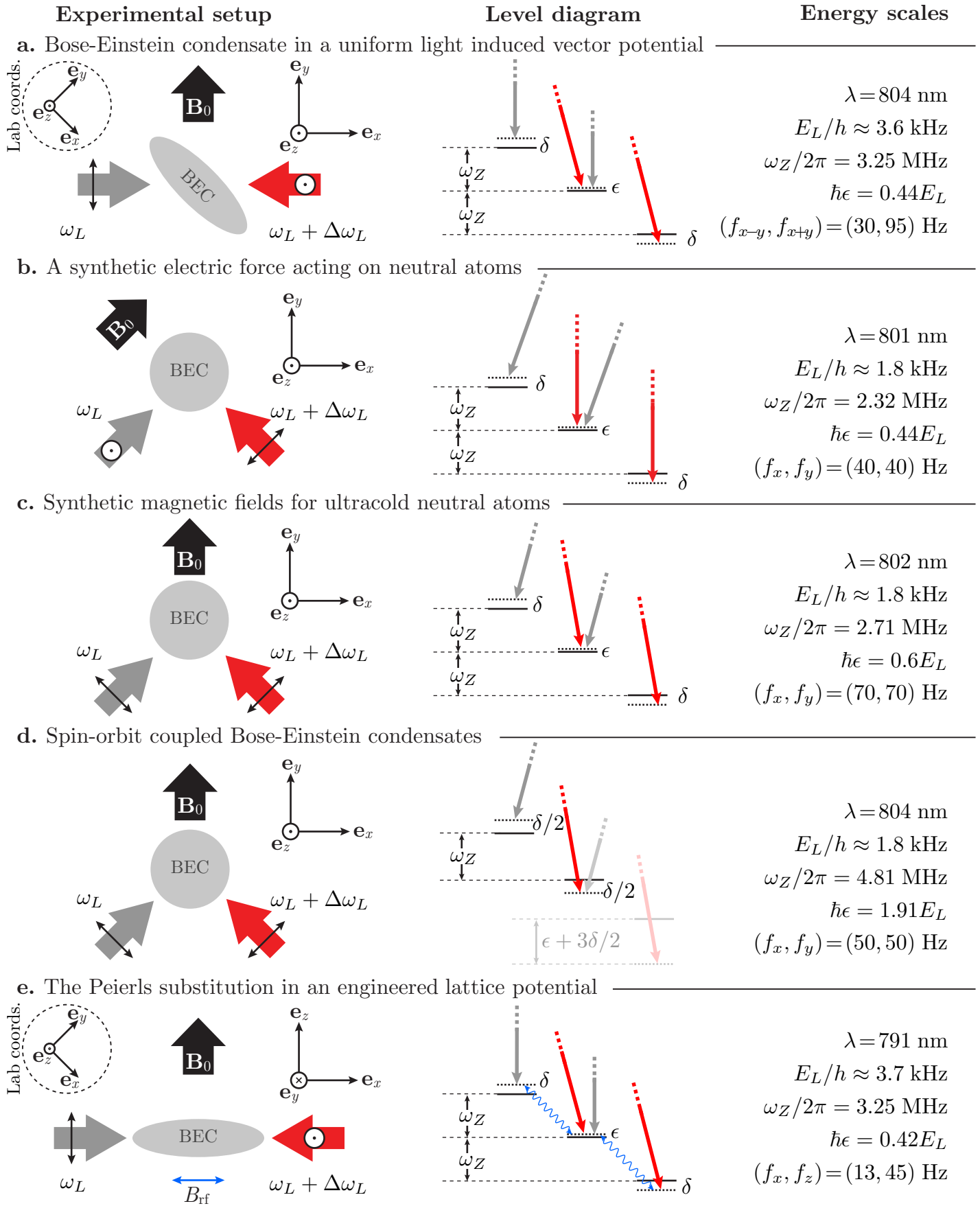


Figure 5.8: Summary of experimental setups for the realization of artificial gauge fields. The exper-

CHAPTER 6

SYNTHETIC MAGNETIC FIELDS FOR ULTRACOLD NEUTRAL ATOMS

This chapter discusses the experimental demonstration of a spatially dependent artificial vector potential \mathcal{A} giving rise to a synthetic magnetic field $\mathcal{B} = \nabla \times \mathcal{A}$ for ultracold neutral atoms. With the realization of such synthetic magnetic fields, an ever wider range of experiments can be explored with ultracold atoms; here we turn our attention to the physics of the Hall effect [83].

In the classical Hall effect an electric current flows perpendicular to a magnetic field; a voltage which is transverse to both the magnetic field and the current, develops as a consequence of the Lorentz force. The characterization of such Hall voltage unveils internal properties of the material in which it was prepared, in particular the properties of the current carriers (density and charge).

With this motivation, we designed an experiment to induce an atomic current in the presence of an synthetic magnetic field \mathcal{B} , to probe internal properties of a BEC. Our experiment is based on the study of *quadrupole*-like collective modes, discussed in Chapter 2, and their response to \mathcal{B} .

6.1 SIGNATURE OF A SYNTHETIC MAGNETIC FIELD

We first describe the physical effects of a synthetic magnetic field acting on ultracold neutral atoms. As discussed in Chapter 2, the local velocity \mathbf{v} of an interacting BEC is equal to the gradient of the phase of its wavefunction $\psi = f e^{i\phi}$; as a consequence, there exist irrotational flow ($\nabla \times \mathbf{v} = 0$) whenever the phase is not singular.

The circulation of a fluid is defined as the line integral $\kappa = \oint_{\mathcal{C}} d\mathbf{l} \cdot \mathbf{v}$ around a closed path \mathcal{C} ; by means of Stokes' theorem we deduce that the circulation is $\kappa = 0$, when ϕ is not singular. On the other hand regions of zero density can exhibit non-zero circulation, such regions constitute vortices in the system. The circulation around a vortex acquires quantized values, $\kappa = lh/m$ with $l \in \mathbb{Z}$, as a consequence of the single-valued nature of the BEC wavefunction.

Quantized vortices are distinguished as regions of zero density in the BEC and can be generated for a sufficiently strong synthetic magnetic field. Quantized vorticity was first proposed to exist in superfluid liquid He II [84, 85], and it is a signature not only of superfluids but also of superconductors in a magnetic field. In the field of ultracold atoms, quantized vortices were first demonstrated

a. Dressed state at $\Omega_R=8.20E_L$, $\delta'=0$ **b.** Dressed state at $\Omega_R=8.20E_L$, $\delta'=0.34 \text{ kHz}/\mu\text{m}$

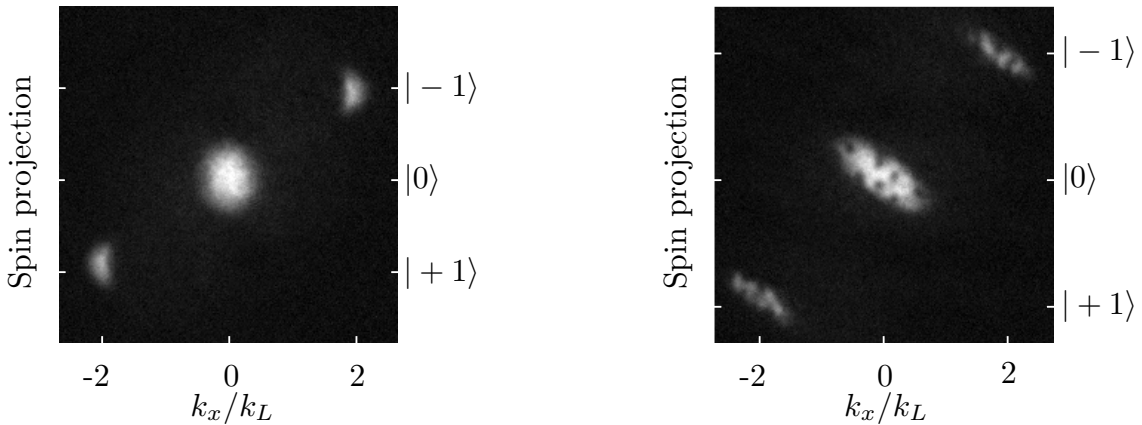


Figure 6.1: Signature of an effective magnetic field B^* acting on neutral atoms. Comparison between Raman dressed states imaged after a 25.1 ms TOF with and without a detuning gradient δ' . A Stern-Gerlach fields separates the spin components along \mathbf{e}_y .

in experiments with rotating ultracold atom systems [86, 87, 88, 89], and here with light-induced gauge fields [7].

Figure 6.1 shows a comparison between a BEC in the presence of a uniform light-induced artificial vector potential $\mathcal{A}=0$ (a Raman dressed state on resonance) and a BEC in a spatially dependent artificial vector potential $\mathcal{A}(y)$; the latter exhibits quantized vortices, the signature of a non-zero synthetic magnetic field $\mathcal{B}=\nabla\times\mathcal{A}$. The length scale of these vortices is given by the healing length ξ of the condensate, as discussed in Chapter 2; they are typically imaged after TOF, when their expanded size can be resolved by standard imaging methods, in particular via resonant absorption imaging.

6.1.1 Superfluid Hall effect in an ultracold atom system Below a critical value of the synthetic magnetic field, quantized vorticity is not energetically favored. The GP equation (Sec. 2.3.4) was developed to study superfluid hydrodynamics [44] with focus on quantized vorticity [45, 46]; it is a suitable equation for predicting the critical conditions for vorticity in trapped atom systems.

A cylindrically symmetric system in a synthetic magnetic field \mathcal{B} allows vortices to enter when $\mathcal{B} > \mathcal{B}_c$, where \mathcal{B}_c is a critical value given by [90]

$$\mathcal{B}_c = \frac{5h}{2\pi R_{\text{TF}}^2} \ln \left(0.67 \frac{R_{\text{TF}}}{\xi} \right);$$

R_{TF} is the TF radius of the system and ξ is the healing length. We take advantage of the fact that even when the system remains irrotational at $\mathcal{B} < \mathcal{B}_c$, it still experiences an effective Lorentz force [8].

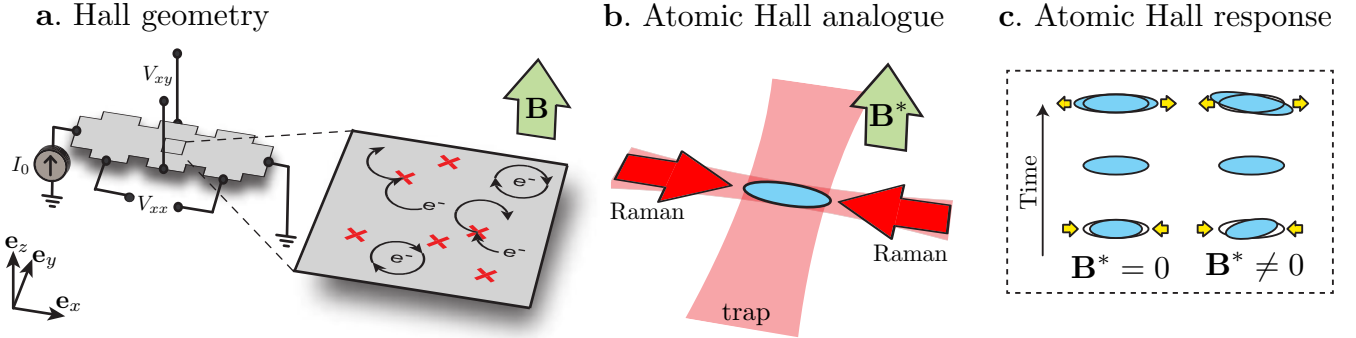


Figure 6.2: Geometry for the observation of the classical Hall effect and its analogue using ultracold atoms in synthetic magnetic fields. **a.** A sample of material carrying an electrical current in an external magnetic field develops a Hall voltage V_{xy} and internal properties of the material can be measured from the characterization of such signal. **b.** An atomic Hall analogue is realized with a BEC in an synthetic magnetic field \mathcal{B} . **c.** The response of an atomic current, generated via collective oscillations in the BEC, to \mathcal{B} reveals internal properties of the BEC.

Figure 6.2 illustrates the concept of the quantum simulation of the Hall effect with ultracold neutral atoms. We prepare BECs in an elongated optical trapping potential, resembling the typical geometry in condensed matter Hall experiments (Fig. 6.2a), and create a light-induced synthetic magnetic field \mathcal{B} (Fig. 6.2b) in the Raman scheme [4, 7]. We investigate mass transport, generated by driving *quadrupole*-like oscillations with the optical trap, in the presence the \mathcal{B} field (Fig. 6.2c).

6.2 EXPERIMENTAL CHARACTERIZATION

Our experiments with light-induced synthetic magnetic fields \mathcal{B} have two primary goals: (i.) to demonstrate the realization of \mathcal{B} from a spatially varying artificial gauge field; and (ii.) to realize the ultracold atom analog of the classical Hall effect.

All experiments start with ^{87}Rb BECs under uniform light-induced artificial gauge fields \mathcal{A} for ultracold neutral atoms, prepared by following the procedures described in Sec. 5.4.1. We create synthetic magnetic fields by imposing a spatial dependence on \mathcal{A} using our bias and quadrupole magnetic field sources (Sections 4.5.2 and 4.5.3, respectively), and firstly describe the characterization of such fields in Sec. 6.2.1. The demonstration of synthetic magnetic fields is addressed in Sec. 6.2.2, while the measurements for the SF Hall effect are discussed in Sec. 6.2.3.

6.2.1 Magnetic fields and the detuning from Raman resonance. The bias fields are at the core of our experiments with artificial gauge fields since they provide the main control the detuning from Raman resonance; additionally the quadrupole magnetic field is of particular importance since it allowed to impose the spatial dependence on the detuning and thus to realize an synthetic magnetic field. I describe here the methods for calibrating the resolution of the magnetic bias fields and the quadrupole magnetic field gradient.

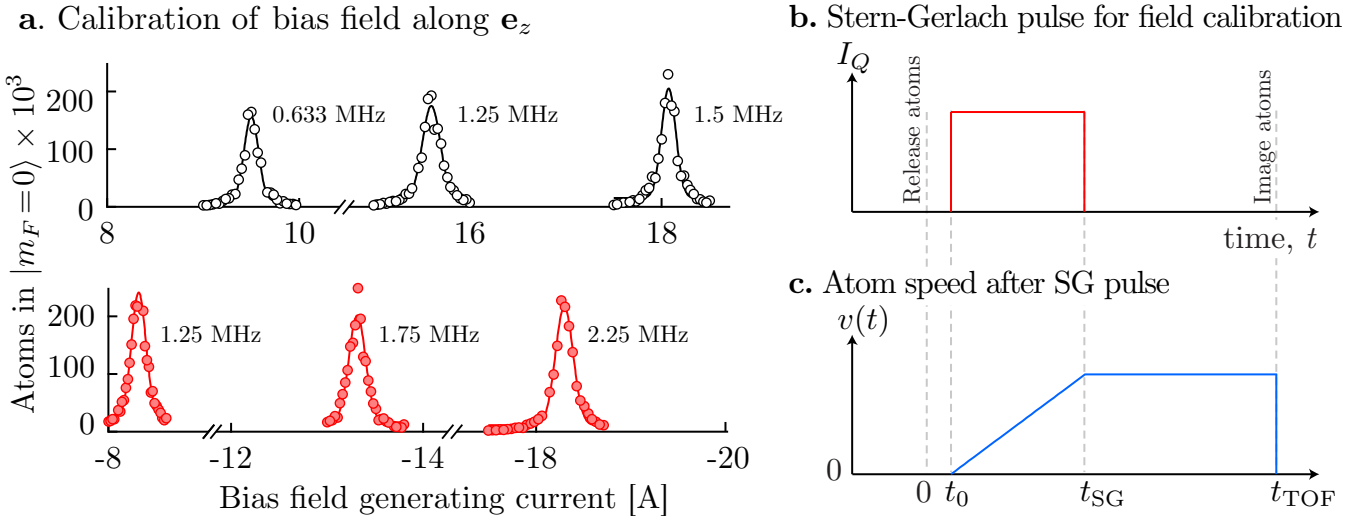


Figure 6.3: Calibration of the bias coils along \mathbf{e}_z via rf-spectroscopy. Population in the $|m_F = 0\rangle$ as a function of the bias current in adiabatic rapid passage sequences from $|m_F = -1\rangle$ to $|m_F = +1\rangle$. Shown are the measurements for the calibration of the bias field along \mathbf{e}_z at six different values of ν_{rf} , both for positive (open symbols) and negative (closed symbols) values of the bias current. b.-c. Field gradient calibration from TOF measured momentum.

6.2.1.1 Determining the frequency resolution of the bias fields via rf-spectroscopy. Our experimental apparatus has three nominally orthogonal pairs of Helmholtz coils as described in Chapter 4. We perform rf-spectroscopy on each independent pair of coils to calibrate the Zeeman splitting $\hbar\omega_Z$ as a function of the electrical current in the coils. Here I describe the calibration of the bias field along \mathbf{e}_z , the calibration method for the other pairs of coils is almost identical.

We prepare a ^{87}Rb BEC in the $|m_F = -1\rangle$ and illuminate it with an rf-field, whose frequency is set at ν_{rf} . To achieve adiabatic rapid passage to $|m_F = +1\rangle$, we ramp a uniform bias field $B_0\mathbf{e}_z$ in two steps: (i.) from zero to an initial value $B_z - \delta B$ (chosen to be below resonance); and (ii.) from $B_z - \delta B$ to a final value B_z . The first ramp is realized in a few ms, while the time scale for the second ramp (where the actual rapid passage takes place) is determined by the coupling strength of the rf-field; for a coupling strength $\Omega_{\text{rf}} = 15$ kHz, we use a 15 ms ramp.

Care should be taken when selecting the detuning range in the adiabatic passage ramp, if the window of detuning (set by $B_z - \delta B$) is too small we could observe confusing contributions to the spin populations. It is also important to take into account the effect of the quadratic Zeeman shift specially at large fields: when $\hbar\Omega_{\text{rf}} \gg \hbar\epsilon$ the population of the $|m_F = 0\rangle$ atoms is maximized on resonance; in contrast, when $\hbar\Omega_{\text{rf}} \ll \hbar\epsilon$ avoided crossings develop away from resonance where two of the three spin states are primarily coupled.

Keeping the initial detuning δB fixed, we scan the base value B_z and monitor the spin populations. Figure 6.3a shows typical measurements for the calibration of the bias field along \mathbf{e}_z at

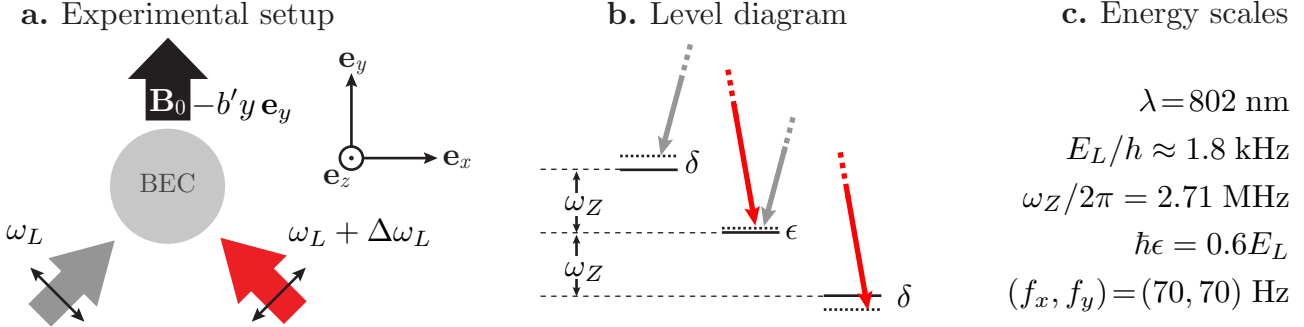


Figure 6.4: Setup and level diagram for pioneering synthetic magnetic field experiments. **a.** A uniform bias field \mathbf{B}_0 Zeeman splits the energy levels in the $F=1$ ^{87}Rb ground-state manifold (**b.**), while a pair of counter propagating Raman beams illuminate an $m_F = -1$ BEC, creating a light induced artificial gauge field \mathcal{A} . A magnetic field gradient b' along \mathbf{e}_y provides a spatial dependence to \mathcal{A} and generates a synthetic magnetic field $\mathcal{B} = \nabla \times \mathcal{A}$.

six different values of ν_{rf} . We fit each trace with a Lorentzian distribution to determine the resonant current and from a line fit to the data we obtain that the Zeeman splitting is $\omega_Z/2\pi = |I_z - 3.65 \text{ A}| \times 0.116 \text{ MHz/A}$, where I_z is the current in the bias coils along \mathbf{e}_z . Similar measurements were performed in the other directions and are reported in Table 4.7.

6.2.1.2 The quadrupole magnetic field gradient. We calibrate the magnetic field gradient from TOF measurements of the momentum imparted to the atoms of $|F = 1, m_F = \pm 1\rangle$ ^{87}Rb BECs by a SG force. The magnetic field gradient B'_y is typically along the direction orthogonal to the Raman momentum transfer, thus the SG force has a non-zero component along \mathbf{e}_y of the form $F_y = g_F \mu_B m_F B'_y$. An schematic of the experimental sequence for calibration is shown in Fig. 6.3b.

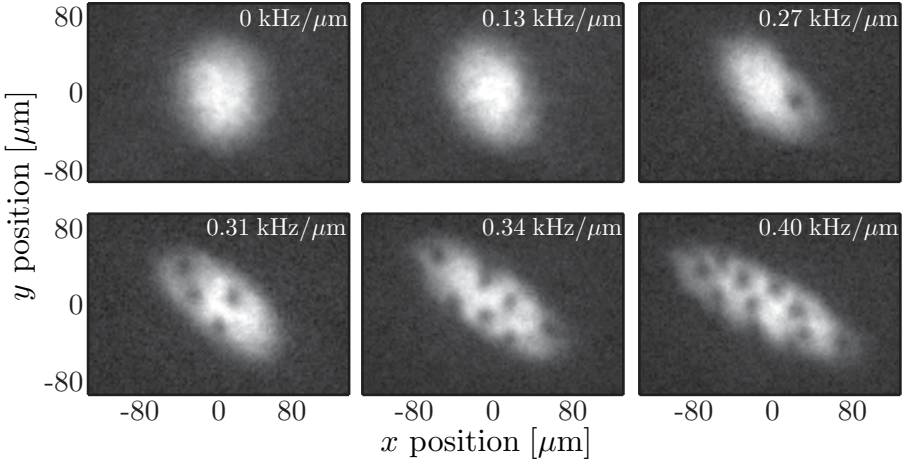
At $t=0$ we release the atoms for expansion in TOF, and align the bias field along \mathbf{e}_y ; then at $t=t_0=2$ ms we apply an SG pulse by turning on the quadrupole gradient. We turn off the gradient at $t=t_{\text{SG}}$ and the atoms freely expand in the remaining TOF. We realize such measurements with a spin species at a time, and monitor the final position of the atoms along \mathbf{e}_y via absorption imaging at $t=t_{\text{TOF}}$.

Under the effects of a uniform field gradient, the acceleration a of the atoms is constant and their velocity v along \mathbf{e}_y increases linearly as shown in Fig. 6.3c. After removing the gradient, the atoms continue to expand with a constant velocity. The total displacement of the atoms is given by

$$y = a \frac{(t_{\text{SG}} - t_0)^2}{2} + a(t_{\text{SG}} - t_0)(t_{\text{TOF}} - t_{\text{SG}}). \quad (6.1)$$

We get $B'_y = ma/g_F \mu_B m_F$ from above, and by repeating the measurement as a function of current I_Q in the quadrupole coils we obtain $B'_y/I_Q = 0.0172 \text{ kHz } \mu\text{m}^{-1}\text{A}^{-1}$.

a. Signature of an artificial magnetic field in ultracold neutral atoms



b. Vortex number

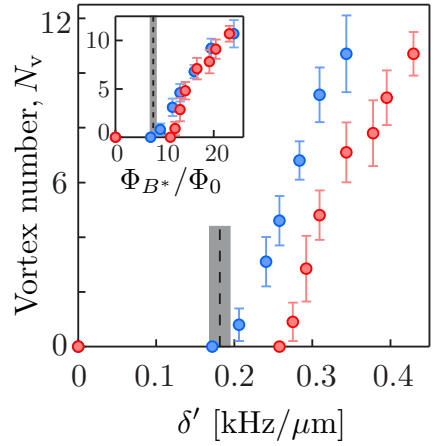


Figure 6.5: Vortices entering the condensate as a function of detuning gradient δ' . **a.** TOF images of Raman dressed BECs ($|m_F = 0\rangle$ component) in the presence of various detuning gradients. **b.** Number of vortices as a function of δ' for $\hbar\Omega_R = 5.85 E_L$ (blue) and $\hbar\Omega_R = 8.2 E_L$ (red). The vertical dashed lines (and bands) indicate the critical value of δ' above which vortices are expected.

6.2.2 A synthetic magnetic field for ultracold neutral atoms. We demonstrated the generation of a synthetic magnetic field by the observation of quantized vorticity on the wavefunction of ^{87}Rb BECs [7]. The synthetic magnetic field $\mathcal{B} = \nabla \times \mathcal{A}$ is a consequence of the spatial dependence of the detuning from Raman resonance δ , which leads to a spatially dependent vector potential $\mathcal{A}(y)$. The spatial dependence was achieved by imposing a real magnetic field gradient (thus a detuning gradient δ') to our Raman dressing scheme (see Sec. 6.2.1.2).

6.2.2.1 Introducing the detuning gradient δ' . The experimental setup for the first experiments with synthetic magnetic fields is shown in Fig. 6.4a. We start with a Raman dressed state at resonance $\delta=0$ in a uniform magnetic bias field $\mathbf{B}=B_0\mathbf{e}_y$, providing a Zeeman splitting of $\omega_Z/2\pi=2.71$ MHz.

We create a synthetic magnetic field \mathcal{B} by applying a magnetic field gradient b' , giving a total field $\mathbf{B}=(B_0-b'y)\mathbf{e}_y$. The magnetic field gradient is generated from the quadrupole coils and is introduced to the system in a 0.3 s ramp from $b'=0$ to a final variable value up to 0.55 mG/ μm .

In the presence of the magnetic field gradient the detuning from Raman resonance is $\delta'=g\mu_B b'/\hbar$; this imposes a spatial dependence on the artificial vector potential¹

$$\frac{\partial \mathcal{A}}{\partial y} = \frac{\partial \mathcal{A}}{\partial \delta} \frac{\partial \delta}{\partial y} = \frac{\partial \mathcal{A}}{\partial \delta} \delta'. \quad (6.2)$$

Given the spatial extent of the BEC and the range of magnetic field gradients used in this exper-

¹It is important to keep in mind that our artificial vector potential only has a non-zero component $\mathcal{A} = (\mathcal{A}_x, 0, 0)$ as discussed in Sec. 5.2.1.3.

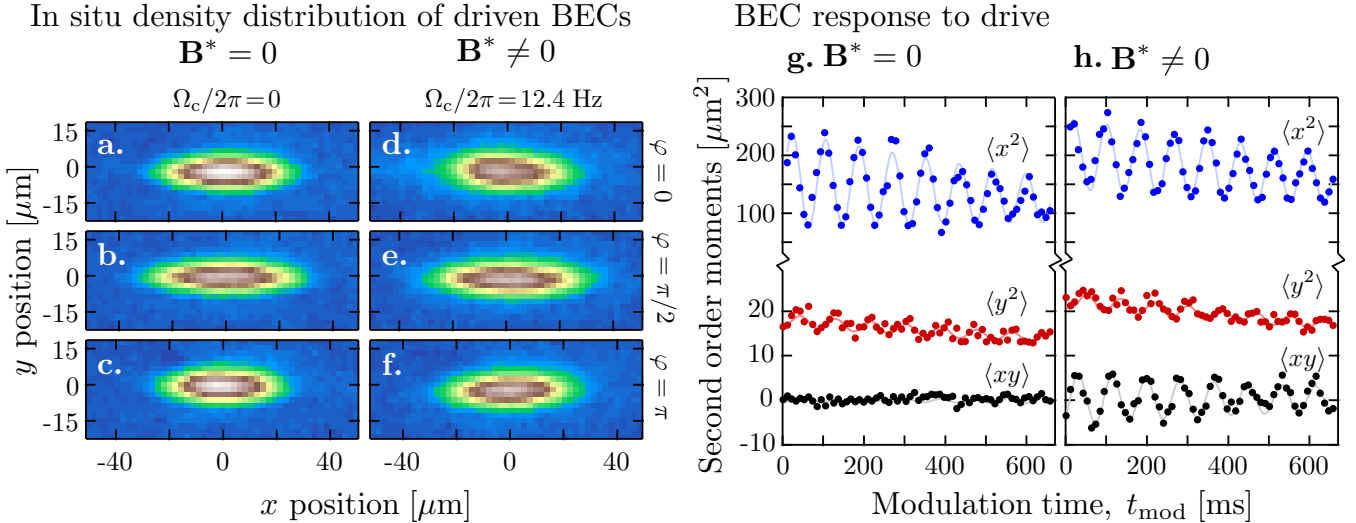


Figure 6.6: Superfluid Hall effect in ultracold atomic systems.

iment, the quantity $\partial\mathcal{A}/\partial\delta$ is nearly uniform (cf. the linear dependence of \mathcal{A} with δ in Fig. 5.3), resulting in an approximately uniform synthetic magnetic field

$$\mathcal{B} = \nabla \times \mathcal{A} = \left(0, 0, -\frac{\partial\mathcal{A}}{\partial y} \right) = \frac{\partial\mathcal{A}}{\partial\delta} \delta' \mathbf{e}_z. \quad (6.3)$$

6.2.2.2 Detection by resonant absorption imagining after TOF. Figure 6.1 shows resonant absorption images of Raman dressed systems with $\delta' = 0$ and $\delta' = 0.34$ kHz/ μm , at a coupling strength $\hbar\Omega_R = 8.20E_L$. Our detection scheme consists of suddenly releasing the system from all dressing and confining potentials in $t_{\text{off}} < 1$ μs , projecting the dressed state into its bare spin-momentum components. We subsequently let the system expand in TOF (lasting from 10.1 to 30.1 ms), during part of which a magnetic field gradient separates the spin components along \mathbf{e}_y due to the Stern-Gerlach effect.

In the presence of a detuning gradient the atomic distribution of the unconfined atoms present a skew (Fig. 6.1b); this is the result of the synthetic electric forces arising from the sudden turn off of the Raman dressing fields (see Sec. 5.4.6).

6.2.2.3 Dependence of vortex number on the amplitude of \mathcal{B} . The vortices are allowed in the system for a critical value of \mathcal{B} , we studied their dependence on the detuning gradient δ' . For synthetic magnetic field greater than a critical value vortices enter the condensate as shown in Fig. 6.5.

6.2.3 Observation of a superfluid Hall effect in an ultracold atom system. Even when quantized vorticity is a striking signature of a non-zero synthetic magnetic field $\mathcal{B} = \nabla \times \mathcal{A}$, is not

a necessary condition for the existence \mathcal{B} . By working at small amplitudes of the synthetic field we studied Hall physics in a BEC [8].

In analogy to the Hall effect [83], we induced an atomic current and studied its response to a synthetic magnetic field. The atomic current was generated by modulating the optical trap confining a BEC along \mathbf{e}_x . Figure 6.6 compares the behavior of the density distribution of driven BECs without (a-c) and with (d-f) an applied synthetic field \mathcal{B} (each panel corresponds to a different time in the modulation process). The time response is quantified via the second order moments of the density distribution, this give a measure of how the shape of the atomic cloud responds to the drive and in particular how it responds to a synthetic magnet field. Panel (h) shows the most distinctive signature of the effects of \mathcal{B} , namely a transverse signal both to the synthetic field and to the atomic current, thus demonstrating a superfluid Hall effect [8].

6.3 CONCLUSIONS

We introduced spatial dependence to an artificial vector potential \mathcal{A} for ultra cold atoms via the detuning parameter, using a magnetic field gradient, to demonstrate an artificial magnetic field $\mathcal{B} = \nabla \times \mathcal{A}$. We characterized \mathcal{B} as a function of the detuning gradient in terms of the number of quantized vortices that entered the system.

We measured the effects of such synthetic magnetic field \mathcal{B} on an atomic current, generated by driving *quadrupole*-like collective modes, to probe internal properties of BECs. This experiment constitutes the cold-atom analog to the Hall effect.

CHAPTER 7

ULTRACOLD BOSE GASES IN OPTICAL LATTICES

Optical lattices share a strong bond with condensed matter physics, since atoms in optical lattices resemble the electrons in the ionic lattice of a crystal. Optical lattices are a vast field of research on their own, and they have allowed the realization of an important number of experiments including: the observation of matter wave diffraction [91, 92, 93]; the control of the bandstructure using moving lattices [94] and driven lattices [95]; the realization of effects not previously observable in ordinary crystals such as Bloch oscillations [96]; the fermionization of a bosonic system in a deep 1D optical lattice, namely the Tonks-Girardeau gas [97]; the realization of the Bose-Hubbard model and the superfluid to Mott-insulator (SF-MI) quantum phase transition [20] together with the study of their quantum correlations [98, 99]; and the realization of optical lattice clocks [100, 82].

We focus in this chapter on the realization of the 2D Bose-Hubbard model using a harmonically trapped BEC. Previous efforts to reduce the uncertainty in the determination of the SF-MI transition, due to inhomogeneity of the system and the persistence of the phase coherence even beyond the transition point to MI [101], have been realized by characterizing the transport properties as a function of both lattice depth and quasimomentum in moving optical lattices [102]. Here, we investigate the transition from a SF to a MI with a magnetic resonance imaging (MRI) approach to eliminate the non-uniform ensemble averaging due to the harmonic confinement in an optical trap. Based on the work of Rigol *et al.* [103] we introduce a scaled dimensionless variable, the characteristic density, containing relevant information of the trapped system which leads to a universal diagram of the phases of a harmonically trapped 2D Bose gas.

First we introduce the optical lattice and discuss general properties of particles in a periodic potential. Later we focus on the physics of the Bose-Hubbard model and the SF-MI transition. Finally I present the experimental characterization of the system and relevant results.

7.1 OPTICAL LATTICE POTENTIALS

An optical lattice is a periodic potential created from the coherent combination of optical fields, whose origin is the interference between two or more traveling waves. The spatial intensity distri-

bution $I(\mathbf{r})$ of a superposition of laser beams provides a trapping potential $V \propto \alpha(\lambda)I(\mathbf{r})$, where $\alpha(\lambda)$ is the atomic polarizability at the laser wavelength λ [57].

One of the major advantages of optical lattices is the experimental control of the lattice properties: the strength of the lattice potential is directly tunable through the intensity of the laser beams, the lattice geometry can be tuned with the spatial configuration of the lasers, the frequency of the lasers can be detuned in order to modify the attractive or repulsive nature of the lattice with respect to the intensity maxima. In our experiments the lasers are red detuned enough to minimize heating by spontaneous emissions and provide conservative trapping potentials for our ^{87}Rb BECs.

A pair of laser beams with wave-vectors \mathbf{k}_1 and \mathbf{k}_2 and wavelength λ , both with linear polarization vector $\hat{\epsilon}$, create a 1D trapping potential

$$V_{\text{latt}}(x) = V_0 \sin^2 \left(\frac{\pi x}{d} \right), \quad (7.1)$$

where V_0 is the lattice depth, $d = \lambda/[2 \sin(\theta/2)]$ is the lattice period and θ is the angle between the wave-vectors¹. A single laser beam retro-reflected on itself suffices to create a 1D optical lattice with spatial period $\lambda/2$. The addition of more laser beams allows the realization of 2D and 3D lattices, but care has to be taken with the polarizations and phases. Deep optical lattices are typically used to decrease the dimensionality of a 3D atomic sample: a 1D standing wave can slice a BEC into a collection of 2D systems; while a square lattice (created by two orthogonal standing waves) creates a collection of tubes which can be considered 1D systems. An important feature of optical lattices is that they can be turned on and off any time, allowing access to the momentum distribution of Bloch states.

7.2 SINGLE PARTICLE IN A 1D PERIODIC POTENTIAL

The wavefunction $\psi(x)$ of a particle in a periodic potential $V(x) = V_0 \sin^2(kx)$, where $k = 2\pi/\lambda$, satisfies the Schrödinger equation

$$-\frac{\hbar^2}{2m} \frac{d^2}{dx^2} \psi_n(x) + V(x) \psi_n(x) = E_n \psi_n(x). \quad (7.2)$$

Bloch's theorem [104] states that the eigenfunction of a particle in a periodic potential can be written as $\psi_{nq}(x) = e^{iqx} u_{nq}(x)$, where q is a quantity with units of momentum called the quasi-momentum and $u_{nq}(x)$ is a periodic function whose periodicity is that of $V(x)$. After substituting

¹Long period lattices can be implemented by interfering laser beams at shallow angles, i.e. with the lasers almost co-propagating.

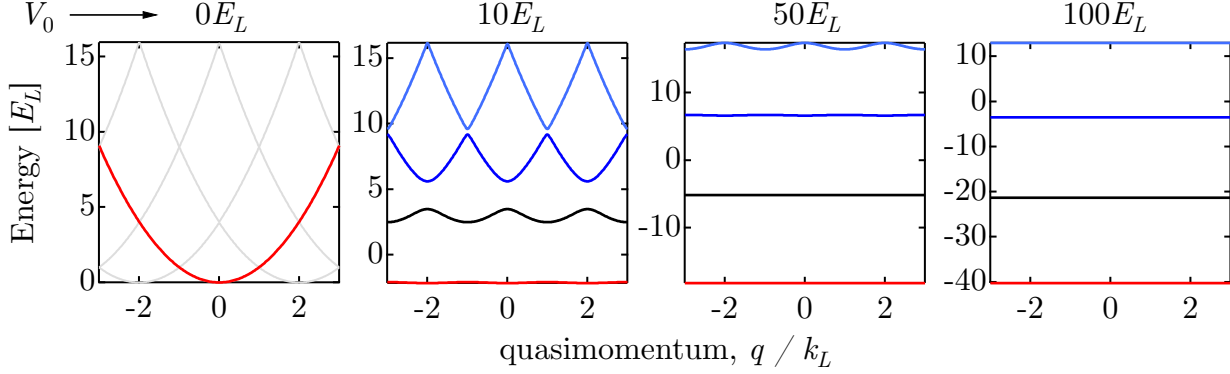


Figure 7.1: The bandstructure of a 1D lattice for different lattice depths was calculated by diagonalizing the matrix of Eq. (7.6) with $l=24$; here we show the energy bands $E_n(q)$ for $n=0, 1, 2, 3$. In the absence of a lattice, at $V_0=0$, we obtain the dispersion of a free particle $E \propto q^2$ (red curve). We found that $l=10$ is the minimum value for convergence of the calculated bandstructure. A noticeable feature is that for deeper lattices, the energy bands $E_n(q)$ flatten out, and the energy gaps between consecutive bands increase.

the Bloch wave $\psi_{nq}(x)$ into Eq. (7.2) we obtain

$$-\frac{\hbar^2}{2m} \left(\frac{d^2}{dx^2} + 2iq \frac{d}{dx} - q^2 \right) u_{nq}(x) + V(x)u_{nq}(x) = E_n u_{nq}(x).$$

We can express it as a Fourier series in the form $u_{nq}(x) = \sum_l a_l e^{2iklx}$ where a_l are constant coefficients and $-\infty < l < \infty$; substitution in the above equation yields

$$\frac{\hbar^2}{2m} \sum_l (q + 2kl)^2 a_l e^{i2klx} + \sum_l V(x) a_l e^{i2klx} = E_n \sum_l a_l e^{i2klx}. \quad (7.3)$$

The lattice potential only contains three Fourier components $V(x) = -V_0(e^{-2ikx} - 2 + e^{2ikx})/4$. We discard the constant term since it is just an energy offset, and upon insertion into Eq. (7.3) we get

$$\frac{\hbar^2}{2m} \sum_l (q + 2kl)^2 a_l e^{i2klx} - \frac{V_0}{4} \sum_l a_l [e^{2ik(l-1)x} + e^{2ik(l+1)x}] = E_n \sum_l a_l e^{i2klx}; \quad (7.4)$$

forcing the arguments of the exponentials to be degenerate we arrive to a system of equations for the Fourier coefficients

$$\frac{\hbar^2}{2m} (q + 2kl)^2 a_l - \frac{V_0}{4} (a_{l+1} + a_{l-1}) = E_n a_l, \quad (7.5)$$

which can be expressed in the form of an infinite square matrix, whose eigenvalues $E_n(q)$ are the eigenenergies of the particle as a function of quasimomentum q .

For practical calculations this matrix is truncated to get a $2l + 1$ square matrix of the form

$$\begin{pmatrix} \frac{\hbar^2}{2m}(q - 2kl)^2 & -V_0/4 & 0 & 0 & 0 & 0 & 0 \\ -V_0/4 & \ddots & -V_0/4 & 0 & 0 & 0 & 0 \\ 0 & -V_0/4 & \frac{\hbar^2}{2m}(q - 2k)^2 & -V_0/4 & 0 & 0 & 0 \\ 0 & 0 & -V_0/4 & \frac{\hbar^2}{2m}q^2 & -V_0/4 & 0 & 0 \\ 0 & 0 & 0 & -V_0/4 & \frac{\hbar^2}{2m}(q + 2k)^2 & -V_0/4 & 0 \\ 0 & 0 & 0 & 0 & -V_0/4 & \ddots & -V_0/4 \\ 0 & 0 & 0 & 0 & 0 & -V_0/4 & \frac{\hbar^2}{2m}(q + 2kl)^2 \end{pmatrix}. \quad (7.6)$$

Figure 7.1 shows the calculated bandstructure $E_n(q)$ for various lattice depths, where I have used the energy and momentum scales given by the single photon recoil momentum $\hbar k = 2\pi/\lambda$ and the single photon recoil energy $E_L = \hbar^2 k^2 / 2m$.

When atoms are tightly confined in the lattice sites [tight binding limit ($V_0 > 5E_L$)], the energy of the lowest band becomes sinusoidal as shown in Fig. 7.2a, and its amplitude $\Delta E = E_0(q = k_L) - E_0(q = 0)$ decreases with V_0 . Figure 7.2b displays three approximations for the bandwidth ΔE as a function of V_0 , namely: *numerical*, based on the diagonalization of Eq. (7.6); *tight-binding*, where the lattice potential is approximated as a harmonic-oscillator potential near its minima and the lowest energy bandwidth is [39, 105]

$$\Delta E/E_L \approx \frac{16}{\sqrt{\pi}} \left(\frac{V_0}{E_L} \right)^{3/4} \exp \left[-2 \left(\frac{V_0}{E_L} \right)^{1/2} \right]; \quad (7.7)$$

and *analytic*, where the tunneling matrix element $t \approx \Delta E/4$ is derived from a fit to calculated values from an analytic expression in terms of Mathieu functions [106]

$$t/E_L = \alpha \left(\frac{V_0}{E_L} \right)^\beta \exp \left[-\gamma \left(\frac{V_0}{E_L} \right)^{1/2} \right] \quad (7.8)$$

with fitting parameters $\alpha = 1.39666$, $\beta = 1.051$ and $\gamma = 2.12104$. The above expressions are consistent with each other to within 12% for depths $V_0 > 20E_L$, and we find agreement within 3% between our numerical calculation of ΔE and $\Delta E \approx 4t$ from Eq.(7.8) for $V_0 > 2E_L$. In our experiments, we rely on our numerical calculation to determine ΔE from measurements of V_0 .

7.2.1 The effective mass. The flattening of the energy bands can be interpreted in terms of an effective mass m^* associated with the particles in the lattice. If we consider a single particle occupying the lowest energy band of a lattice potential and make a Taylor expansion of the bandstructure around one of its minima (e.g. around $q = 0$ and for small displacements in q), we

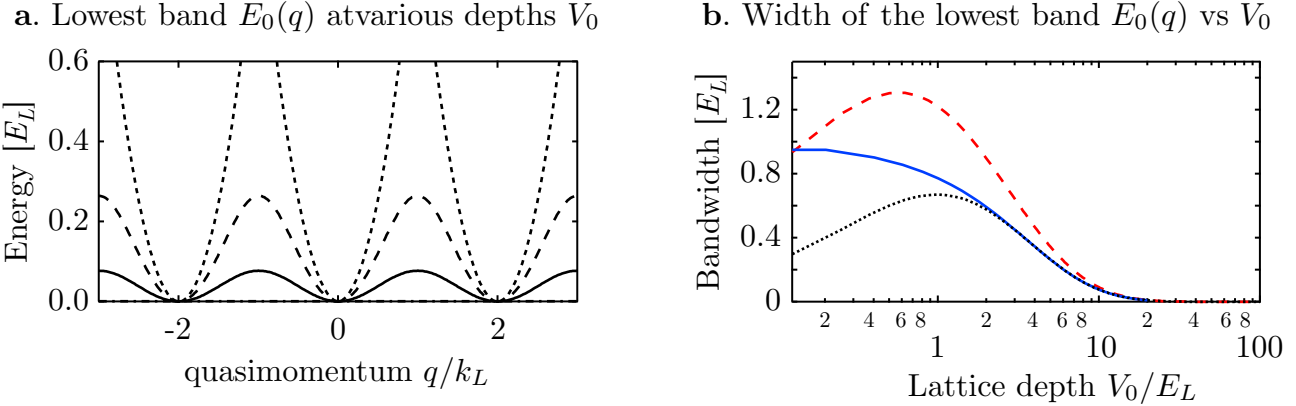


Figure 7.2: **a.** Lowest band $E_0(q)$ at various depths V_0
b. Width of the lowest band $E_0(q)$ vs V_0

obtain the dispersion relation of a free-particle $E_0(q) \approx \hbar^2 q^2 / 2m^*$ whose effective mass is defined as $m^* = \hbar^2 [d^2 E_0(q) / dq^2]^{-1}$. The effective mass geometrically represents the inverse of the curvature of the bandstructure; its physical interpretation is straightforward: in the shallow lattice regime $V_0/E_L \ll 1$ the dispersion relation is very close to that of a free particle, the effective mass tends to the actual mass m , and the particle is free to move all over the lattice. On the other hand, in the deep lattice limit $V_0/E_L \gg 1$ the energy bands are almost flat which corresponds to an increased effective mass; the particle is tightly confined to a lattice site since it is harder to make a massive object move. Depending on the quasimomentum around which the effective mass is calculated, it can acquire even negative values; this is physically related to dynamical instabilities [107, 108] in the system as discussed in Chapter 8.

7.3 THE BOSE-HUBBARD HAMILTONIAN

The Bose-Hubbard model describes a collection of atoms in a lattice potential, which can move in the lattice by tunneling to their nearest neighboring sites with tunneling matrix element t , and which repulsively interact with other atoms with an on-site interaction strength U . In the formalism of second-quatization and in the presence of an external potential, the Bose-Hubbard (BH) Hamiltonian is

$$\hat{H} = -\frac{t}{2} \sum_{\langle j,j' \rangle} \hat{b}_j^\dagger \hat{b}_{j'} + \sum_j (\epsilon_j - \mu) \hat{b}_j^\dagger \hat{b}_j + \frac{U}{2} \sum_j \hat{b}_j^\dagger \hat{b}_j^\dagger \hat{b}_j \hat{b}_j, \quad (7.9)$$

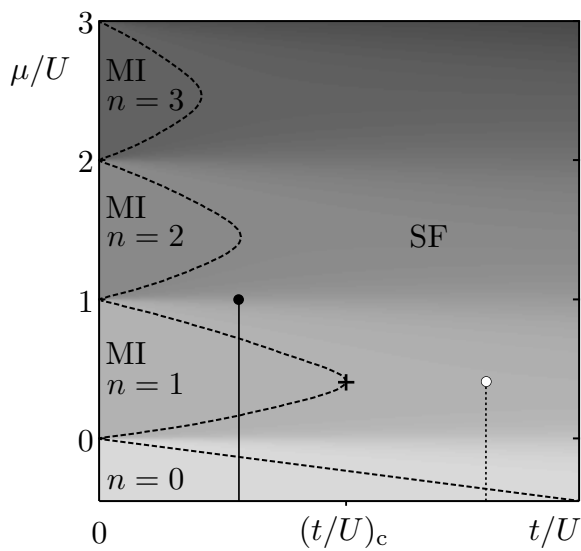
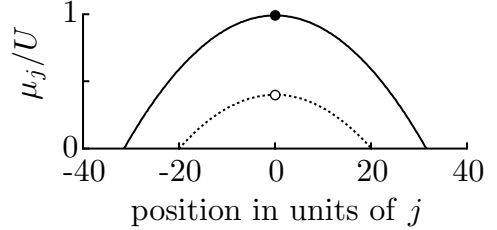
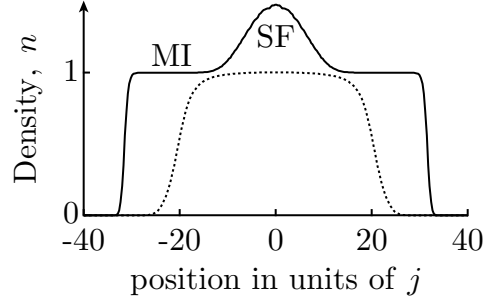
a. MF phase diagram for SF – MI transition**b.** LDA chemical potential in HO trap**c.** Spatial density n in HO trap

Figure 7.3: MF calculation of SF-MI transition. **a.** Mean number of atoms per site n as a function of t/U and μ/U in the ground state of a uniform system under the BH Hamiltonian. The ground state exhibits either of two phases: a Mott insulating (MI) phase where an integer number of atoms per lattice site; and a superfluid (SF) phase with non-integer fillings per site. The transition from SF to a $n = 1$ MI (cross symbol) occurs at the critical value of $(t/U)_c$. **b.-c.** In the local density approximation (LDA), we use the local chemical potential $\mu_j = \mu - \epsilon_j$ to compute the density profile in a HO trap. For a sufficiently large local chemical potential (closed symbols, continuous curves) the trapped system corresponds to alternating shells of SF and MI. For sufficiently large (t/U) (open symbols, dotted curves) the system is SF.

where \hat{b}_j^\dagger is the creation operator of a boson at site j , and $\langle j, j' \rangle$ constrains the first sum to nearest-neighboring tunneling. The external trapping potential is described by ϵ_j , and μ is the chemical potential at the center of the trap.

The bosonic creation and annihilation operators satisfy the commutation relations given by $[\hat{b}_j, \hat{b}_{j'}^\dagger] = \delta_{j,j'}$; $[\hat{b}_j, \hat{b}_{j'}] = 0$ and $[\hat{b}_j^\dagger, \hat{b}_{j'}^\dagger] = 0$; they are defined such that

$$\hat{b}_j^\dagger |n_j\rangle = \sqrt{n_j + 1} |n_j + 1\rangle \quad \text{and} \quad \hat{b}_j |n_j\rangle = \sqrt{n_j} |n_j - 1\rangle, \quad (7.10)$$

where n_j are the eigenvalues of the number operator $\hat{n}_j = \hat{b}_j^\dagger \hat{b}_j$, for the occupation number on each lattice site, and $|n_j\rangle$ represents a state in the occupation number basis. With the above definitions the BH Hamiltonian of Eq. (7.9) reduces to

$$\hat{H} = -\frac{t}{2} \sum_{\langle j, j' \rangle} \hat{b}_j^\dagger \hat{b}_{j'} + \sum_j (\epsilon_j - \mu) \hat{n}_j + \frac{U}{2} \sum_j \hat{n}_j (\hat{n}_j - 1). \quad (7.11)$$

7.3.1 The tight-binding limit. An important result from the BH Hamiltonian [Eq. (7.11)] is obtained in the absence of interactions ($U=0$) and for sufficiently deep lattices. Ultracold atoms in deep optical lattices typically occupy the lowest vibrational energy level of the harmonic-oscillator potential provided by the lattice site to which they are tightly confined.

If only the lattice potential is present, then we can assume that $\epsilon_j - \mu$ is a uniform energy offset which we define as zero. By working in the Heisenberg picture, we obtain the Heisenberg equation for the time dependence of the annihilation operator \hat{b}_j , namely $i\hbar d\hat{b}_j/dt = [\hat{b}_j, \hat{H}]$. Assuming periodic boundary conditions, the commutation relations between \hat{b}_j and \hat{b}_j^\dagger , and traveling wave solutions, we obtain

$$i\hbar \frac{d\hat{b}_j}{dt} \approx -2t \cos(qd) \hat{b}_j. \quad (7.12)$$

The energy of a single particle state in the lattice is $E(q) = -2t \cos(qd)$ [39], where d is the lattice period. The tight binding model is characterized by a single band whose width is $\Delta E = 4t$; 1D lattices as deep as $V_0=5 E_L$ already satisfy the above criteria for tight binding.

7.3.2 Ground state of the BH Hamiltonian. For a uniform system ($\epsilon_j=0$) the ground state of the Hamiltonian is entirely dictated by the dimensionless coefficients t/U and μ/U . The competition between the kinetic and interaction energies, characterized by t/U , defines the nature of the ground state. In the limit when $t/U \ll 1$, tunneling is suppressed and interactions dominate; the system is in a state known as the Mott insulator (MI) phase. In contrast, when $t/U \gg 1$, the kinetic energy dominates over interactions and the system minimizes energy by delocalizing over the lattice; in this regime, the system exhibits superfluid (SF) behavior.

We performed a mean-field (MF) calculation based on the approach presented by Sheshadri *et al.* [109] and calculated the SF-MI phase diagram for a uniform 2D system under the BH Hamiltonian, as discussed below. Figure 7.3a presents the number of atoms per lattice site as a function of t/U and μ/U ; the system can be driven between a SF phase at non-integer fillings, and a MI phase with integer fillings. Furthermore, we assume the local density approximation (LDA) and define a local chemical potential $\mu_j = \mu - \epsilon_j$ to compute the density profile in a HO trap.

7.3.3 MF site decoupled calculation of SF-MI phase diagram. We consider a uniform system $\epsilon_j=0$ and work with the dimensionless BH Hamiltonian $\hat{H}' = \hat{H}/U$

$$\hat{H}' = -\frac{tn_z}{2U} \sum_{\langle j,j' \rangle} \hat{b}_i^\dagger \hat{b}_{j'} - \frac{\mu}{U} \sum_j \hat{n}_j + \frac{1}{2} \sum_j \hat{n}_j (\hat{n}_j - 1), \quad (7.13)$$

where I have introduced the number of nearest neighbors n_z (for a 2D square lattice $n_z=4$, while for a cubic lattice $n_z=6$) [39]. We consider the mean field approximation

$$\hat{b}_j^\dagger \hat{b}_{j'} = \langle \hat{b}_j^\dagger \rangle b_{j'} + \langle \hat{b}_{j'}^\dagger \rangle b_j^\dagger - \langle \hat{b}_j^\dagger \rangle \langle \hat{b}_{j'}^\dagger \rangle; \quad (7.14)$$

where the order parameter is given by $\psi = \langle \hat{b}_j^\dagger \rangle = \langle \hat{b}_{j'}^\dagger \rangle$. The above approximation decouples the sites in the tunneling term of the BH Hamiltonian, which acquires the form $\hat{H}' = \sum_j \hat{H}'_j$, where

$$\hat{H}'_j = -\frac{tn_z}{2U}[(\hat{b}_j^\dagger + \hat{b}_j)\psi - \psi^2] - \frac{\mu}{U}\hat{n}_j + \frac{1}{2}\hat{n}_j(\hat{n}_j - 1). \quad (7.15)$$

We work in the occupation number basis $\{|n_j\rangle\}$ and set an upper bound in the maximum number of atoms n_{\max} . We diagonalize $\hat{H}'_j(\psi)$ to get the ground state ψ_0 , and compute $b_j = \langle \psi_0 | \hat{b}_j | \psi_0 \rangle$. We execute an iterative process to find ψ by defining as $\psi' = 0.9 \psi + 0.1 b_j$, and repeating the above process for $\hat{H}'_j(\psi')$.

It takes about 50 iterative steps for ψ to converge, for $n_{\max}=5$, and an initial value of $\psi=1$. Figure 7.3a shows the mean occupation number per lattice site $n = \langle \psi_0 | \hat{n}_j | \psi_0 \rangle$, where ψ_0 denotes the ground state of $\hat{H}'_j(\psi)$ at the convergence value of ψ . We find that the critical value for the transition from SF to a $n=1$ MI occurs at $(t/U)_c \approx 0.0796$, or equivalently $(U/t)_c \approx 12.56$, while homogeneous system quantum Monte Carlo (QMC) calculations [110] predict $(U/t)_c \approx 16.5$.

We use the local density approximation (LDA) to calculate the spatial profile of the mean occupation number n for a harmonically trapped system. We introduce the external potential as $\epsilon_j = \epsilon j^2$, where $\epsilon = m\omega^2 d^2 / 2$, d is the lattice spacing, and j is the lattice site label. By defining a local chemical potential $\mu_j = \mu - \epsilon j^2$ (Fig. 7.3b) we obtain the spatial profile shown in Fig. 7.3c; we conclude that both phases can coexist in a trapped system forming a shell structure of alternating SF and MI domains.

7.4 UNIVERSAL PHASE DIAGRAM FOR TRAPPED BOSONS IN A 2D LATTICE

Ultracold atoms in optical lattices can experimentally realize the 2D Bose-Hubbard model but they require external trapping potentials, thus spatial inhomogeneity is guaranteed. This system can be driven through a transition from SF to MI by tuning the dimensionless interaction strength U/t [19] or the chemical potential μ , both quantities representing experimentally tunable parameters. For U/t larger than a critical value $(U/t)_c$ the system can enter a MI domain as seen in Figure 7.3a and for $U/t \gg (U/t)_c$, the phases alternate between SF and MI, increasing in density as μ increases [111]. Due to the presence of a harmonic trap, both the SF and MI phases can coexist forming a shell structure of alternating phases (see Fig. 7.3c).

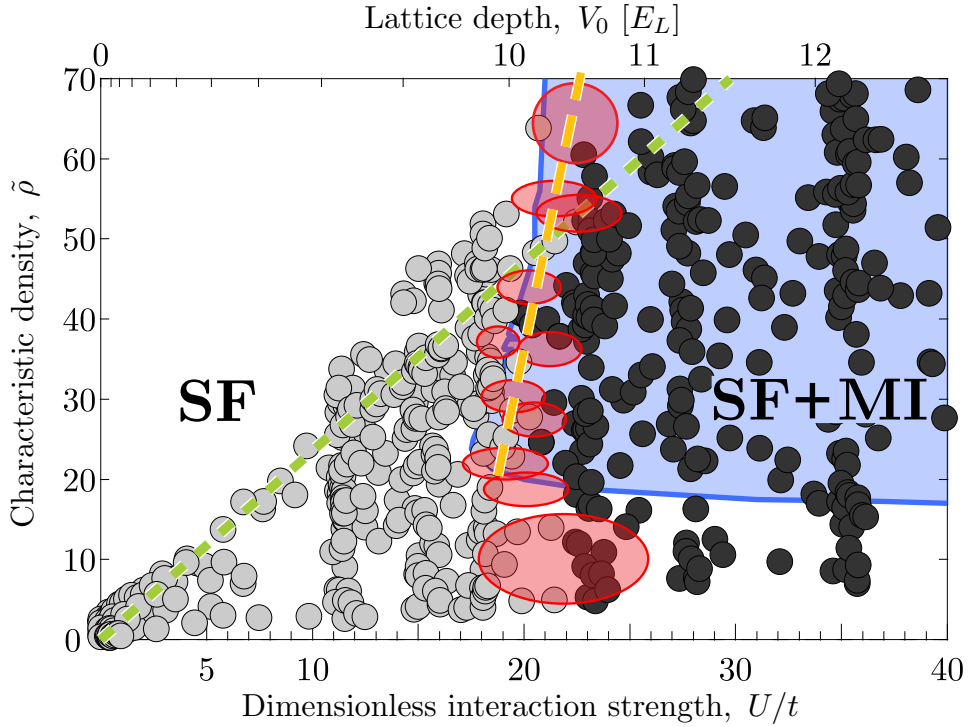


Figure 7.4: State diagram for a harmonically trapped 2D Bose gas. The blue line shows the QMC prediction [103] of the first appearance of MI. The transition was measured at various N_{2D} from $f(U/t)$ data (see Fig. 7.13). The ovals denote the measured transition boundary; their sizes represent the uncertainties in $\tilde{\rho}$ and $(U/t)_c$. The small circles indicate individual measurements, and are colored according to the side of the transition on which they are. The yellow dashed line is a fit to the measured boundary for $\tilde{\rho} > 20$; that it is non-vertical [$\theta_{\text{exp}} = 85.5(27)^\circ$ from horizontal] suggests a breakdown of the LDA close to the transition.

It is possible to introduce a universal state diagram for harmonically confined atoms in spite of the inhomogeneity of cold atom systems [103], by identifying the phases of the system (distinguishing between pure SF and coexisting SF and MI phases) and making use of a scaled dimensionless variable, the characteristic density.

The characteristic density is $\tilde{\rho} = N_\delta d^\delta (V/t)^{\delta/2}$, where N_δ is the total number of atoms, d is the lattice period, δ is the dimensionality, V the trap-curvature and t the tunneling matrix element. For systems with different trap-curvatures and different numbers of atoms, a plot of the identified phases (SF or coexisting SF and MI) as a function of dimensionless interaction U/t strength and $\tilde{\rho}$ reproduces the same transition boundary, giving a universal character to the SF-MI phase diagram in the context of trapped systems [103]. The solid curve shown in Fig. 7.4 corresponds to the QMC predicted boundary [103] between pure SF and coexisting SF and MI phases in a harmonically trapped system.

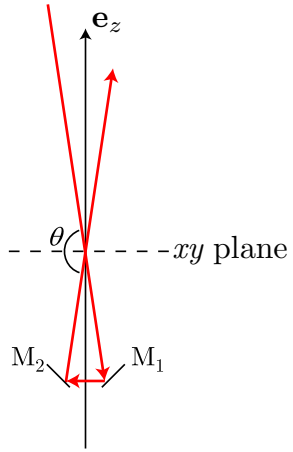
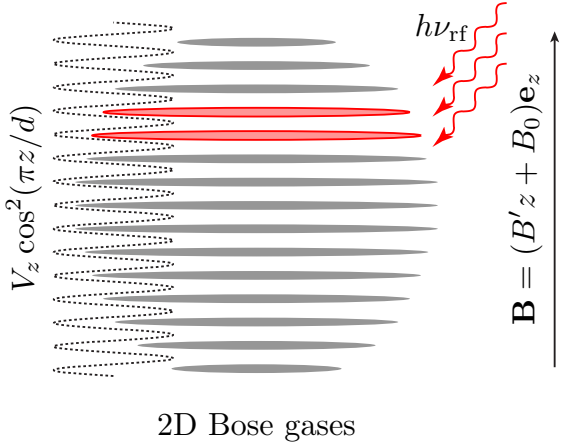
a. Vertical lattice setup**b.** MRI selection of 2D systems with rf

Figure 7.5: **a.** Schematic of vertical lattice to create a collection of 2D systems; the vertical lattice is created from a nearly counter-propagating [$\theta = 164(1)^\circ$] single laser beam with $\lambda = 810$ nm. M₁ and M₂ are protected silver mirrors. **b.** Our 3D BEC is divided into nearly 60 2D systems by a 24 E_L deep lattice (dotted curve). The system is in the presence of a linear magnetic field gradient B' along \mathbf{e}_z .

7.5 EXPERIMENTAL CHARACTERIZATION

I describe next the experimental methods followed to measure the SF-MI universal phase diagram of harmonically trapped 2D bosonic systems [29], here I have separated each of the techniques involved in the experiment for clarity.

7.5.1 System preparation. We realize the BH Hamiltonian in 2D systems of a single spin species of ^{87}Rb $F = 1$ ground state. Our atoms are prepared in an optical trap in the presence of magnetic field gradient along \mathbf{e}_z , with the spin state most appropriate for its response to magnetic trapping.

If working with the magnetically trappable state, thermal atoms generated either due to heating or from further evaporating in the optical trap, remained trapped due to the magnetic potential and represented an undesired background in our measurements. In contrast, the high-field seeking state experiences an anti-trapping potential in the xy -plane, which allows undesired thermal atoms to leave the trap, thus overcoming the background. Based on these considerations, we work in the $|F=1, m_F=+1\rangle$ spin state.

Our experiments begin with a ^{87}Rb BEC prepared in the $|F=1, m_F=-1\rangle$ spin state in an optical dipole trap located at the intersection of a pair of 1064 nm dipole beams with waists ($1/e^2$ radii) of 55 μm , propagating along $\mathbf{e}_x \pm \mathbf{e}_y$ in the laboratory frame. The BEC is in the presence of a uniform bias field $B_0\mathbf{e}_z$ generating a tunable Zeeman splitting² $\omega_Z/2\pi$. We realize adiabatic

²The tunable bias field sets an initial Zeeman splitting $\omega_Z/2\pi$ about 20 kHz below rf-resonance for the adiabatic

rapid passage (ARP) from $|m_F = -1\rangle$ to $|m_F = +1\rangle$ by illuminating the BEC with an rf-field at $\nu_{\text{rf}} = 1.35$ MHz, and ramping the bias field through rf-resonance in 500 ms.

Once all atoms are in $|m_F = +1\rangle$, we invert the bias field direction from \mathbf{e}_z to $-\mathbf{e}_z$ by ramping the current that generates this field in 2 ms, and suddenly turn on the quadrupole trap. The zero of the quadrupole magnetic field is located at 620 μm below the BEC. Evaporation continues during 3.6 s in the combined magnetic plus optical trap to reach a nearly pure BEC in the $|F = 1, m_F = +1\rangle$ spin state, with measured trap frequencies $\{f_{x-y}, f_{x+y}, f_z\} = \{23.2(5), 27.4(3), 42.8(9)\}$ Hz.

We calibrate our magnetic field gradient by removing the optical trap and magnetically levitating the atoms against gravity; we infer a gradient of $2.180(4)$ kHz/ μm along \mathbf{e}_z at a quadrupole current of 61.5 A. The gradient is nearly linear along \mathbf{e}_z , but it adds a quadratic anti-trapping potential in the xy -plane for the $|m_F = +1\rangle$ atoms, as desired.

7.5.2 Alignment of the laser beams with respect to the atoms. The initial step toward the realization of the BH Hamiltonian is to set up the laser beams that will generate the optical lattice potentials. In this section I review some methods to align the lattice beams to the BEC, which are general methods suitable for the alignment of any laser beam in our experiment. Also in this section I describe the procedure for the calibration of the lattice depth.

7.5.2.1 Geometrical alignment. The initial alignment of a laser beam is based purely on the geometry of the main experimental chamber, and on the assumption that the atoms are located at its center. Alignment can be particularly challenging if the input and output ports of the chamber have limited access, as is the case for the vertical ports. Figure 7.5a shows an schematic of the vertical lattice beams; these beams do not counter-propagate since that would require blocking the field of view of the xy -imaging system.

In general, it is worth spending a reasonable amount of time in making sure the beams go exactly through the center of the chamber to within a millimeter. I recommend using suitable targets made of milli-metric paper to better quantify the propagation of the beam; these targets would (ideally) be located at equidistant planes from the center of the chamber, which are parallel to the input and output ports. If available, it is useful to draw marks on the targets corresponding to laser beams already aligned to the atoms, e.g. the probe beams or the dipole trap beams.

7.5.2.2 Alignment with respect to a compressed MOT. If the geometrical alignment cannot be realized with the required accuracy, we can try a rough approach: to make the beams go through a MOT, whose typical diameter is about 1 cm. For any beam with tunable wavelength, we prepare a standard MOT (see Chapter 4) and independently aim each beam at it. The cooling mechanism is affected if the atoms are illuminated by light at $\lambda = 794.986$ nm (near the $^{87}\text{Rb D}_1$ transition), rapid passage sequence.

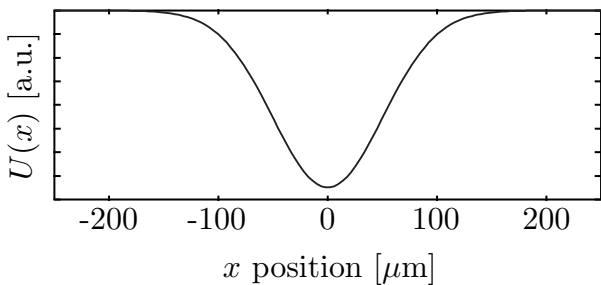
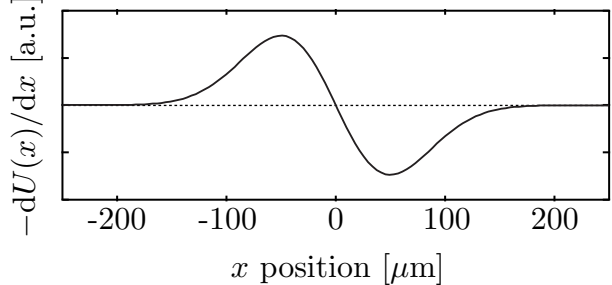
a. Trapping potential along x **b.** Dipole force along x 

Figure 7.6: Dipole force for alignment of laser beams to atoms. **a.** Trapping potential $U(x)$ for a Gaussian beam propagating along \mathbf{e}_y , with waist ($1/e^2$ radii) of $w_0 = 100 \mu\text{m}$. **b.** The dipole force along x is $-\frac{dU}{dx}$; it presents a linear dependence around the point of intensity maxima $x=0$. In our alignment procedure, x represents the relative position between the laser and the BEC; optimum alignment is thus achieved at $x=0$.

and the MOT is almost completely extinguished. We optimize the effect with a compressed MOT, achieved by increasing the quadrupole current, to improve alignment with a smaller target.

7.5.2.3 Optimizing alignment with magnetically trapped atoms. When properly done, the initial alignment should be close enough such that we can see an effect on cold atoms in a magnetic trap. An easy test of alignment is to prepare a thermal cloud in a weak magnetic trap, such that the atoms are barely confined in it. The presence of a nearby laser beam can be diagnosed by absorption imaging the atomic distribution and looking for a signature of laser trapping (dense regions of atoms along the beam of interest). In our experiment this approach works best by imaging in the xz -plane. Ramping the magnetic bias fields to move the quadrupole trap is a non-invasive approach to look for an increase in atom density.

7.5.2.4 Dipole force alignment. The dipole force alignment allows the independent alignment of each laser beam, and is primarily used in our experiments to align the lattice beams and the dipole trap, when required.

Dipole force alignment is achieved by measuring the effects of the dipole force from each beam on a BEC. Most of our laser beams are red detuned, exerting an attractive force and imparting momentum to the atomic distribution. Figure 7.6 shows the dipole potential and the dipole force generated by a red detuned Gaussian beam propagating along \mathbf{e}_y , as a function of the position along \mathbf{e}_x . Optimal alignment is achieved when the BEC and the laser beam overlap, and the dipole force is approximately linear with position.

We prepare a BEC and suddenly illuminate it with a single beam for a $1/4$ period of the relevant trapping frequency (from 40 ms to 0.3 s). Then we release the BEC from all its confining potentials and absorption image it after TOF to amplify the effect of the force. We measure the final position

Diffraction from 1D lattices with balanced populations in 0th and 1st orders.

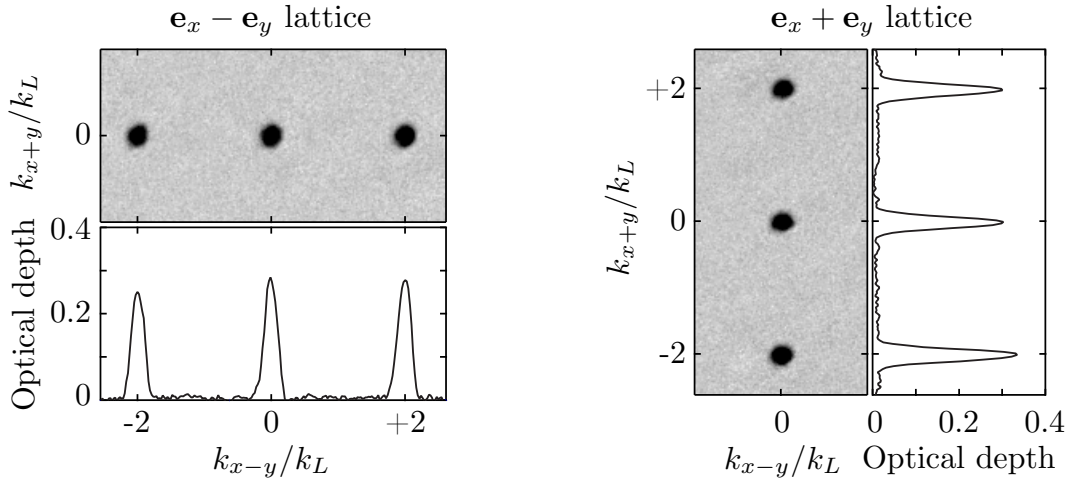


Figure 7.7: Lattice depth calibration. We calibrate the depth of 1D lattices by studying atomic diffraction. The time duration (t_{pulse}) of the lattice interaction with the atoms required to balance the populations of the 0th and 1st diffracted orders gives the lattice depth $V_0 = 2\gamma_0\hbar/t_{\text{pulse}}$, where $\gamma_0 = 1.4346$. The absorption images correspond to the isolated $|m_F = 0\rangle$ atomic distribution extracted from the ensemble using a $400 \mu\text{s}$ resonant rf-pulse; the atoms are imaged after a 18.1 ms TOF. The accompanying continuous curves represent the integrated optical depth along the direction orthogonal to the lattice. The pulse time $t_{\text{pulse}}=11 \mu\text{s}$ gives $V_0=11.9(2)E_L$.

of the atoms as a function of the laser alignment and observe a dependence such as that of Fig. 7.6b; the laser intensity can empirically be adjusted to scale the effect of the force. When the beam is properly aligned, it overlaps with the BEC and the dipole forces due to the spatial variation at the center of the Gaussian profile cause no net force; the final position of the BEC should be within $5 \mu\text{m}$ from the BEC's unperturbed position.

7.5.3 Calibration of the lattice depth. We use a total of three optical lattices, generated from the same Ti:Sapphire laser operated at $\lambda=810 \text{ nm}$. The vertical lattice is created using nearly counter-propagating beams as illustrated in Fig. 7.5a. We denote the xy -lattices as A and B, they propagate along $\mathbf{e}_x + \mathbf{e}_y$ (y_{rot} axis) and $\mathbf{e}_x - \mathbf{e}_y$ (x_{rot} axis), respectively.

We use the diffraction of atoms from the optical lattice in the Kapitza-Dirac regime [91] to calibrate the lattice depth to within 2%. Given that the population in each diffracted order is $P_n = J_n^2(\gamma)$; where $J_n(\gamma)$ are the Bessel functions of the first kind [93], n is the index of the diffracted order, and $\gamma = t_{\text{pulse}}V_0/2\hbar$; we adjust the time duration of the lattice interaction with the atoms t_{pulse} until the populations of the 0th and 1st diffracted orders balance. From the condition for balanced populations $J_0^2(\gamma) = J_1^2(\gamma)$, whose smallest root is $\gamma_0 = 1.4346$, we obtain the lattice depth $V_0 = 2\gamma_0\hbar/t_{\text{pulse}}$. Figure 7.7 shows absorption images of atomic diffraction by independent 1D optical lattices illustrating the conditions for calibrating lattice depth.

7.5.3.1 Measurement of the scalar light-shift for the ground state of ^{87}Rb vs λ . The lattice beams produce both scalar and vector light-shifts whose strength depends on the resonance from the atomic transitions D1 and D2. By measuring the lattice depth V_0 as a function of wavelength λ , keeping the overall laser power constant at about 200 mW for each laser in lattice A, we obtained a measure of the amplitude of the scalar light-shift; Fig. 3.5 shows the experimental data and their excellent agreement with calculations.

7.5.4 Contribution of lattices to overall trapping potential. The characteristic density for our 2D systems is given by $\tilde{\rho} = N_{2\text{D}}\epsilon/t$, where $\epsilon = m\omega^2 d^2/2$ is the overall curvature of the trap.

The presence of the optical lattice modifies the trapping potential due to their non-zero light-shift. It is important to quantify their contribution to the overall trap, since all trapping potentials shall be included in the trapping parameter ϵ defining the characteristic density $\tilde{\rho}$.

Since we are dealing with a 2D system we focus on the characterization of the contribution to the xy trapping frequencies. In this section I will describe how to include the effect of the lattice beams on ϵ .

A single Gaussian beam of waist w_0 propagating along \mathbf{e}_z produces a harmonic trapping potential of the form

$$U_{\text{dipole}} = -U_{\text{trap}} \left[1 - \frac{2(x^2 + y^2)}{w_0^2} - \frac{z^2}{z_R^2} \right]; \quad (7.16)$$

where the trap depth U_{trap} is proportional to the laser intensity I , $z_R = \pi w_0^2/\lambda$ is the Rayleigh range, λ is the laser wavelength and the trapping frequencies are

$$2\pi f_{x,y} = \sqrt{\frac{4U_{\text{trap}}}{mw_0^2}} \quad \text{and} \quad 2\pi f_z = \sqrt{\frac{2U_{\text{trap}}}{mz_R^2}}. \quad (7.17)$$

If we add a second Gaussian laser beam with associated trapping frequencies f'_j , where j labels the direction in the trap, the overall trapping frequencies f''_j are the result of their independent values combined in quadrature

$$f''_j{}^2 = f_j^2 + f'_j{}^2. \quad (7.18)$$

Extending this logic to the case of an optical dipole trap in the presence of a pair of lattice beams, we determine the contribution from the lattice beams to the dipole trap frequency as

$$f_j(\text{both beams})^2 = \alpha[f_j(\text{dipole trap} + \text{both beams})^2 - f_j(\text{dipole trap})^2]; \quad (7.19)$$

where $\alpha = V_{\text{lattice}}/V_0$ is a scaling factor to account for the dependence on the lasers intensity, V_0 is the lattice depth at which the measurement was done and V_{lattice} is the actual lattice depth. One

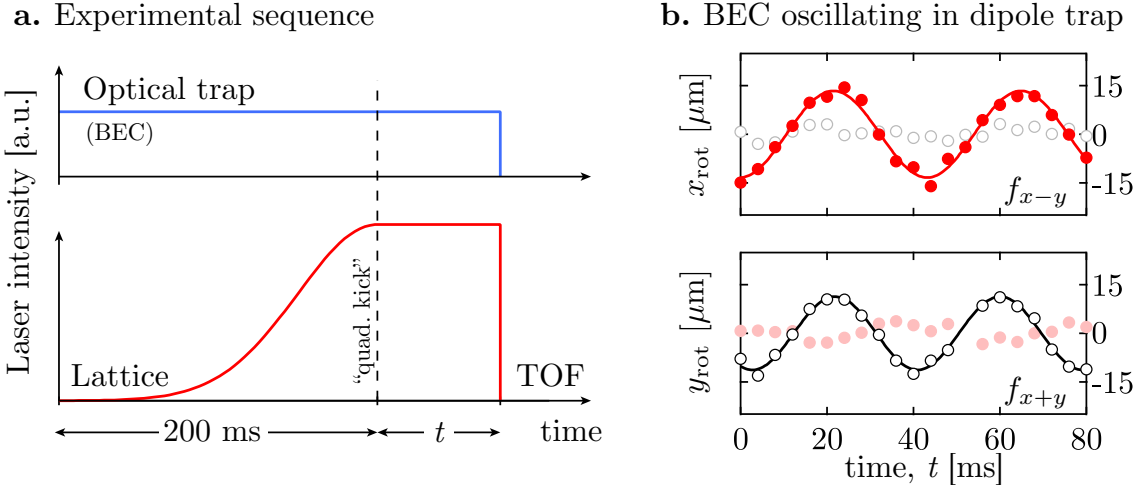


Figure 7.8: Contribution of lattices to overall trapping potential. **a.** We adiabatically load each optical lattice in 200 ms to its final depth, and apply a 2 ms directional “quadrupole kick” to initiate sloshing. **b.** Typical measurements of the BEC coordinates from absorption images after TOF as a function of hold time t , closed (open) symbols represent the rotated coordinate x_{rot} (y_{rot}).

should keep in mind that the lattices will mainly contribute to the trapping frequency along the direction orthogonal to their axis of propagation.

We infer the contributions from the each lattice (both beams) to the overall trap by measuring the frequency shift of the sloshing mode in the trap. Figure 7.8a shows the experimental sequence to measure the sloshing frequency. For a BEC in a pure optical trap, the sloshing motion is induced by suddenly turning on and off (2 ms) a magnetic field gradient along the desired direction. This exerts a sudden force on the atoms and initiates the motion; we absorption-image the atoms after TOF and measure their final location as a function of hold time t . To measure the effect of each lattice on the trapping potential, we adiabatically load the lattice in 200 ms from 0 to its final depth V_0 ; then we apply the 2 ms directional “quadrupole kick”, hold for a variable time t and measure the position as before; our measurements are summarized in Table 7.1. With this calibration we can properly account for the overall trap curvature in the definition of the characteristic density $\tilde{\rho}$.

Table 7.1: Contribution of optical lattices to overall trap frequency.

| Configuration | V_0/E_L | f_{x+y} [Hz] | f_{x-y} [Hz] |
|--|-----------|----------------|----------------|
| dipole trap + lattice A($\mathbf{e}_x + \mathbf{e}_y$) | 16 | - | 29.4(5) |
| dipole trap + lattice B($\mathbf{e}_x - \mathbf{e}_y$) | 16 | 33.0(3) | - |
| dipole trap + Vertical(\mathbf{e}_z) | 22 | 34.6(3) | 35.9(2) |
| dipole trap | - | 26.2(3) | 23.0(3) |

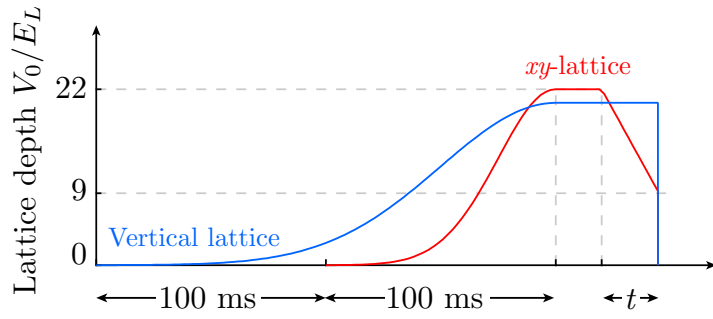
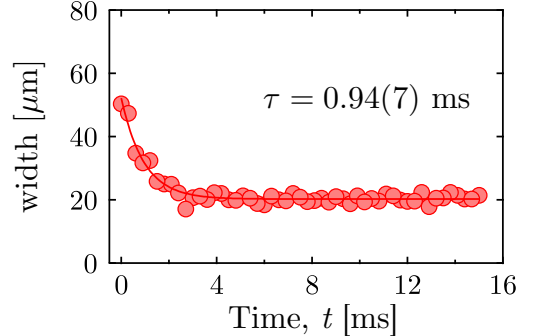
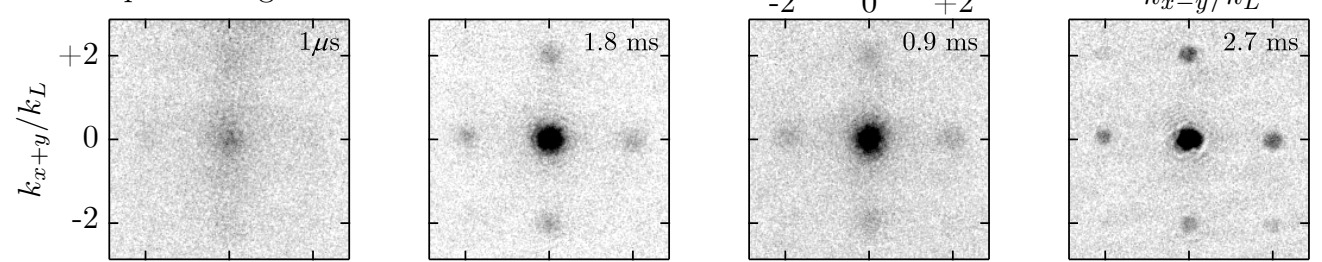
a. Time sequence for the restoration of coherence**b.** Width of the central atomic distribution**c.** Absorption images after 18.1 ms TOF

Figure 7.9: Restoring coherence. **a.** Time sequence for system preparation. After reaching the MI phase by ramping the xy -lattice to a depth of $22E_L$, we ramp the depth in a variable time t down to $9E_L$ to recover the SF phase. We apply a $400 \mu\text{s}$ rf-pulse to transfer a few 2D systems into $|m_F=0\rangle$. We suddenly release all 2D systems and apply a magnetic field gradient during part of the 18.1 ms TOF, to separate non $|m_F=0\rangle$ atoms from our sample. **b.** We perform 1D Gaussian fits to the central peak of the sampled distribution along $\mathbf{e}_x \pm \mathbf{e}_y$, shown is the average width as a function of ramp down time t . The exponential decay has a time constant $\tau = 0.94(7)$ ms. **c.** Absorption images showing the $|m_F=0\rangle$ atomic distribution for different ramp down times t .

7.5.5 Implementing the Bose-Hubbard Hamiltonian. The xy lattice beams nearly co-propagate with the dipole trap beams; each lattice beam is retro-reflected on itself to create an independent $\lambda/2$ lattice. To avoid cross talking between the xy -lattice beams they have linearly orthogonal polarization at the atoms and differ in frequency by 2.824 MHz; the vertical lattice beam is frequency shifted by about 160 MHz with respect to the xy beams.

We loaded the BEC into a $24 E_L$ deep 1D optical lattice along \mathbf{e}_z to produce an ensemble of 2D systems as illustrated in Fig. 7.5; additionally, two weaker 1D optical lattices in the xy - plane realized the Bose-Hubbard Hamiltonian in each 2D system. All lattices were adiabatically ramped from zero intensity to their final power in 100 ms with half-Gaussian intensity ramps. We control the interaction strength U/t by adjusting the laser intensity of the xy -lattice beams; the depth of the xy -lattice ranges 0 to 20 E_L .

7.5.6 Restoring coherence We study the time it takes a MI configuration to restore coherence after returning the system to a SF. Figure 7.9a shows the system preparation. We ramp the vertical

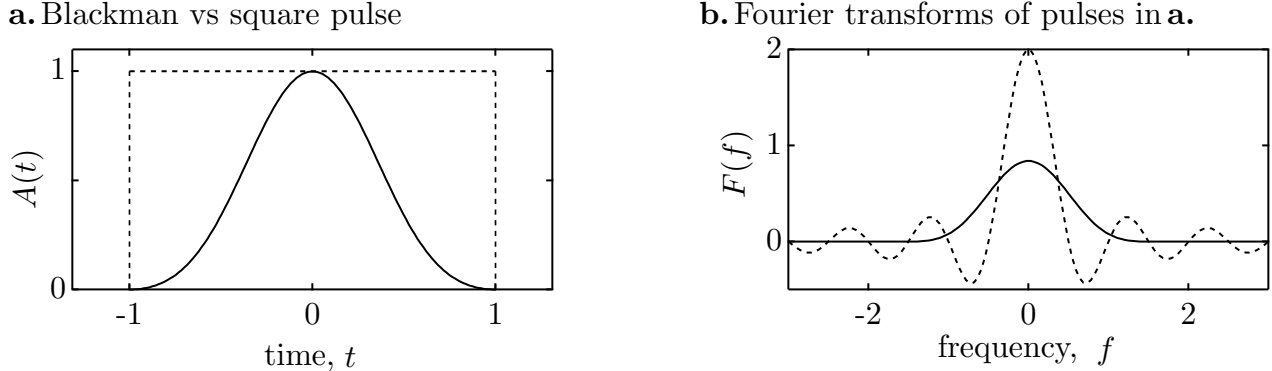


Figure 7.10: Comparison between a uniform (dashed) and a Blackman pulse (solid) and their Fourier transforms.

lattice to a final depth of $20.3 E_L$, with a half-Gaussian intensity ramp in 200 ms; the vertical lattice depth remains unchanged until the release of the atoms at the end of the experiment. Within the last 100 ms of vertical lattice ramp, we ramp the xy -lattice to a final depth of $22 E_L$ to bring the 2D systems into the MI regime, and hold for 20 ms. We then ramp the xy -lattice depth down to $9 E_L$ (SF regime) where the systems recover their phase coherence, in a variable time t .

We apply a $400 \mu\text{s}$ rf-pulse on resonance with the largest 2D systems ($\nu_{\text{rf}} = 1.33 \text{ MHz}$) to transfer a small fraction of the atoms into the $|m_F = 0\rangle$ state, after which the atoms are released from all confinement potentials.

The 2D systems are projected into their spin components, which separate in the presence of a magnetic field gradient within 18.1 ms TOF. We focus on the atomic distribution of $|m_F = 0\rangle$ atoms and measure the width of the central peak as a function of time t ; the average width along the $\mathbf{e}_x \pm \mathbf{e}_y$ directions is shown in Fig. 7.9b. These results are in excellent agreement with those reported by Greiner *et al.* [20].

7.5.7 MRI approach to control the size of the 2D systems. Experiments have been realized in the context of quantum microscopy of single 2D systems [112, 113] to overcome the issue of spatial inhomogeneity in trapped gases. Here, we implement a technique analogous to MRI to eliminate the ensemble averaging present in previous experiments and to control the system size $N_{2\text{D}}$.

We prepare a BEC in an optical trap and in the presence of a magnetic field gradient generated by our quadrupole trap to implement our MRI approach. Being in the presence of a magnetic field gradient $B'z\mathbf{e}_z$, the Zeeman splitting between the hyperfine sub-levels becomes a function of z position; this allows the selective coupling of small subsets of neighboring 2D systems via the illumination with a locally resonant rf-field as indicated in Fig. 7.5b. The rf-field is briefly pulsed to transfer two nearly identical 2D-systems from $|m_F = +1\rangle$ to $|m_F = 0\rangle$.

We select 2D systems of a particular size $N_{2\text{D}}$ by adjusting the center frequency ν_{rf} of the rf-pulse. To minimize accidental addressing from neighboring 2D systems, we avoided using a simple

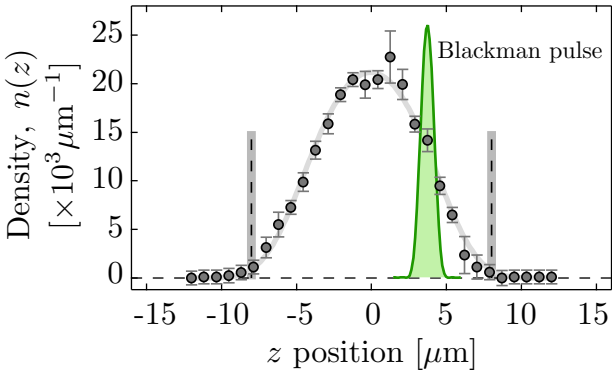
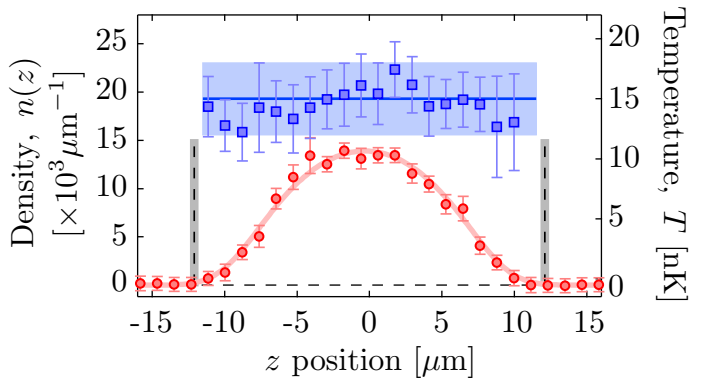
a. 3D BEC $N_{\text{int}} = 1.89(5) \times 10^5$ **b.** 2D systems $N_{\text{int}} = 1.84(5) \times 10^5$ 

Figure 7.11: Density profile $n(z)$ for: **a.** a 3D BEC and **b.** an ensemble of 2D systems. The atom number calculated from the *in situ* Thomas-Fermi radius $R_z = 8.2(2) \mu\text{m}$ is $N_{\text{TF}} = 1.8(4) \times 10^5$. The vertical dashed lines indicate the Thomas-Fermi radius from our fit. Continuous lines show a fit to the *in situ* 1D density profile $n(z)$. The temperature of the selected 2D systems (squares in **b.**) is displayed on the right axis, as a function of position along \mathbf{e}_z ; on average $T = 15(3) \text{ nK}$.

square pulse; instead we implemented a pulse whose profile is given by the Blackman function

$$A(t) = \frac{21}{50} + \frac{1}{2} \cos\left(\frac{\pi t}{a}\right) + \frac{2}{25} \cos\left(\frac{2\pi t}{a}\right). \quad (7.20)$$

An rf-pulse with a Blackman envelope has a reduced number of frequency components compared to a square pulse, as illustrated in Fig. 7.10.

A linearly polarized rf-field $B_{\text{rf}} \mathbf{e}_x$ transfers atoms from $|m_F = +1\rangle$ to $|m_F = 0\rangle$ and $|m_F = -1\rangle$. We fixed the pulse duration at $400 \mu\text{s}$ and adjusted the amplitude B_{rf} to maximize the transfer into $|m_F = 0\rangle$. The Blackman envelope was generated by a programmable SRS DS345 function generator, whose output was combined with that of the rf-synthesizer prior to being amplified and sent to the experiment (see Sec. 4.5.4). The 2 kHz rms spectral width of this pulse, combined with the magnetic field gradient along \mathbf{e}_x gives a $0.9 \mu\text{m}$ rms spatial resolution (≈ 2 lattice sites).

7.5.8 Number calibration. We carefully calibrated the atom number by measuring the *in situ* 1D density profile $n(z)$, of our 3D BEC using the MRI technique (see Fig. 7.11a). The Thomas-Fermi (TF) radius $R_z = 8.2(2) \mu\text{m}$ gives an atom number $N_{\text{TF}} = 1.8(4) \times 10^5$; direct integration of $n(z)$ gives $N_{\text{int}} = 1.89(5) \times 10^5$; measurement of absorption by all atoms after TOF gives $N_{\text{abs}} = 1.90(5) \times 10^5$. These measurements are consistent with a combination of shot-to-shot number fluctuations and number measurement uncertainty of $\sim 3\%$. We confirm this by loading the BEC into the 1D optical lattice along \hat{z} , and again measuring $n(z)$. We find that the density profile expands along \mathbf{e}_z (Fig. 7.11b, circles) but the integrated atom number $N_{\text{int}} = 1.84(5) \times 10^5$ remains constant. Figure

7.11b also shows the measured temperature T in a 1D optical lattice as a function of z (squares). $T = 15(3)$ nK is nearly uniform over all significantly occupied lattice sites, indicating that the 2D systems taken together are effectively in thermal equilibrium.

7.5.9 Band mapping and extraction of addressed 2D systems in TOF. The dynamic control offered by optical lattices allows the implementation of band mapping [105, 114], i.e. the adiabatic removal of the lattice potential in which quasimomentum is mapped to free particle momentum. The time scales for adiabaticity are dictated by the single particle energy scales in the optical lattice, specifically the process has to be slow compared to the associated band gap [115].

At the edges of the Brillouin zone the band gap is reduced during band mapping and the adiabaticity condition cannot be reached, band mapping approximately maps the occupied crystal momentum states in the lowest Brillouin zone (BZ) to free momentum states [115]. This is an issue only if the lowest band is fully occupied, i.e. up to the edge of the BZ.

We performed band mapping after the rf-pulse to improve the signal to noise ratio in our measurements. The lattice potentials were turned off with exponentially decreasing ramps ($400\ \mu\text{s}$ time constant), and at the same time we removed the optical dipole trap in $<1\ \mu\text{s}$; the atoms then expanded for 18.1 ms TOF.

During part of TOF, we switch the direction of the bias field to get a magnetic field gradient approximately along $\mathbf{e}_x + \mathbf{e}_y$ to separate the three $|m_F\rangle$ components. We detect the final spatial distribution of all three components using resonant absorption imaging, which gives the approximate momentum distribution of each spin component separately. The $|m_F=0\rangle$ distribution directly measures the momentum composition of the nearly identical 2D systems selected by the rf pulse, virtually eliminating the inhomogeneous averaging that is present in the $|m_F=+1\rangle$ distribution. Since $|m_F=0\rangle$ atoms are insensitive to gradients in magnetic fields, the momentum distribution experiences no distortions due to field gradients.

7.5.10 Matter wave focusing We used a matter-wave focusing technique –a temporal atom lens– that “focuses” the *in situ* momentum distribution at a finite TOF [116, 117]; this technique helps to better distinguish the sharp features in the momentum distribution.

The sudden increase on the dipole trap depth exerts a force on the atoms proportional to their distance to the trap center as illustrated in Fig. 7.12a, in analogy with an optical lens in the paraxial approximation [118]. The atoms that are further away from the center will be more strongly pushed inwards, while those atoms already at the center will remain unperturbed by the trap. As the strength of the trapping pulse increases, the system size will be reduced up to the point when interatomic interactions overcome the inward kick and the system starts expanding again as shown in Fig. 7.12c. This phenomenon is referred to as matter wave focusing [119, 116] and we use it to better distinguish between SF and non SF components in our experiments with 2D Bose gases.

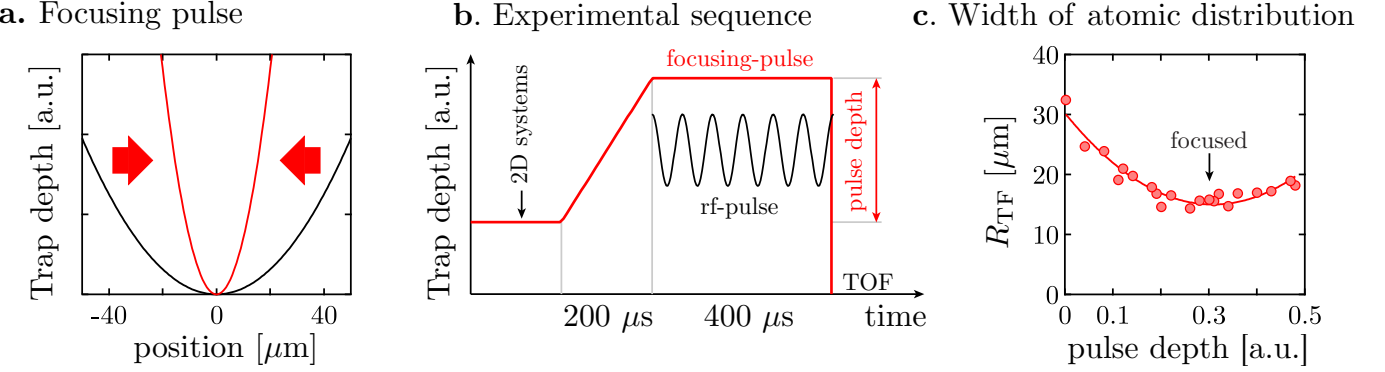


Figure 7.12: **a.** When the trap depth is suddenly increased, trapped atoms experience an inward force proportional to their location in the trap; this is analogously to an optical lens focusing a light beam. **b.** After loading a 1D optical lattice to create a set of 2D systems, along \mathbf{e}_z , we suddenly ramp the trap depth and hold it for $400\mu\text{s}$. In parallel, a $400\mu\text{s}$ rf-pulse at $\nu_{\text{rf}} = 1.33$ MHz transfers a small fraction of the largest 2D systems into the $m_F = 0$ state. We then suddenly remove all dressing and confining potentials and let the atoms expand during a 18.1 ms TOF. **c.** We monitor the TF radii of the $|m_F=0\rangle$ atomic distribution as a function of the pulse depth and identify the focus at the minimum of this curve.

Figure 7.12b shows the experimental sequence we followed to characterize our matter wave focusing pulse. Our experiment begins with a $|m_F=+1\rangle$ BEC in a pure optical trap, in the presence of a magnetic field gradient. We prepare a collection of 2D systems by adiabatically turning on the vertical lattice up to a depth of $22 E_L$. We ramp the dipole trap intensity to a final variable value in $200\mu\text{s}$, and hold it for $400\mu\text{s}$.

We additionally apply an rf-pulse on resonance with the largest 2D systems ($\nu_{\text{rf}} = 1.33$ MHz) to transfer a small fraction of the atoms into the $|m_F=0\rangle$ state, in those last $400\mu\text{s}$. We then suddenly release the 2D systems from all confining potentials, and a magnetic field gradient separates the spin components within a 18.1 ms TOF. We measure the size of the $|m_F=0\rangle$ atomic distribution to characterize the effect of the focusing-pulse. Figure 7.12c shows that as the strength of the pulse increases, the size of the atomic distribution is reduced; when interactions overcome the inward focusing pulse, we observe an increase [119] on the final size of the system. The optimum configuration for focusing used in our experiments required to tighten the dipole trap to increase the trapping frequency by a factor of about 3.

7.5.11 Location of the phase transition and universal phase diagram. We measure the condensate fraction f as an indicator of the SF component in the system. We experimentally define f as the fraction of atoms in the sharp, focused feature in the momentum distribution (insets in Fig. 7.13). We fit the broad background, present due to thermal effects and quantum depletion, including atoms in the MI phase, to the thermal distribution of non-interacting classical particles

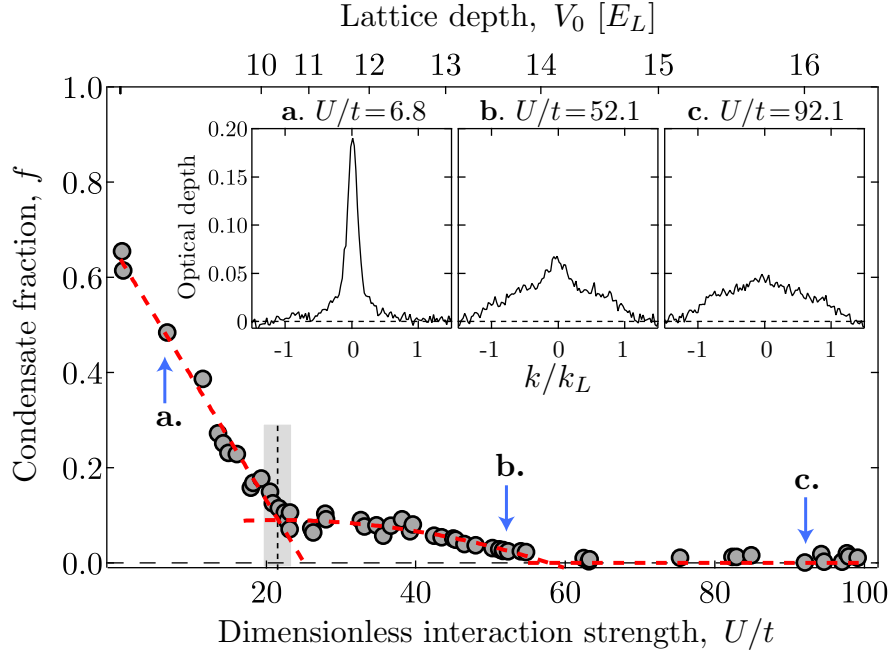


Figure 7.13: Condensate fraction of a 2D $N_{2D} \approx 3500$ atom Bose gas measured through the SF to MI transition. We identify the formation of the first MI region at $U/t = 21(2)$, where the slope of f changes markedly; we associate the subsequent decay in f with the spatial growth of the MI domains. For $U/t > 60$, f is indistinguishable from zero. The red dashed curves are fits described in the text. The insets (a.-c.) display the averaged momentum distribution $n(k) = [n_A(k) + n_B(k)]/2$ at different U/t , where $n_{A,B}(k)$ are the momentum distributions integrated over direction of the optical lattices.

in a 2D sinusoidal band; in the shallow lattice limit the width of this distribution is interpreted as temperature: $T = 0.9(2)t/k_B$ [120]. We smoothed the fit function in a region within $0.1 k_R$ of the edge of the Brillouin zone to account for non-adiabaticities in the lattice turn off near the band edge [115]. We exclude a disk with $0.16 k_R$ radius around the condensate feature from the fit and identify the condensate as the atoms that remain within the disk after subtracting the background fit. (We associate $f > 0$ with existence of SF regions as is conventional.)

Figure 7.13 shows f as a function of U/t for 2D systems with $N_{2D} \approx 3500$ and an initial temperature $T = 0.9(2)t/k_B$, a factor of two lower than that reported in Ref. [120] where $f \lesssim 0.4$ and $T \approx 2t$. We identify $(U/t)_c$ from the behavior of the condensate fraction: it decreases rapidly in the shallow lattice regime down to $f \approx 0.12$ and $(U/t)_c = 21(2)$ (Fig. 7.13, fit to a line); when it suddenly changes its decaying slope (Fig. 7.13, fit to a parabola) to finally be indistinguishable from zero in the deep lattice regime $U/t > 60$. We associate the value of $(U/t)_c = 21(2)$ as the onset of MI, and the subsequent decay in f for $(U/t)_c > 21$ with the spatial growth of the MI domains.

Our MRI approach allows the measurement of f for systems of different size N_{2D} , i.e. different characteristic densities $\tilde{\rho}$. We sampled about 1300 images with $\tilde{\rho}$ up to 100 and U/t up to 100 and

Table 7.2: Measured and QMC values of $(U/t)_c$.

| $\tilde{\rho}$ | $(U/t)_c$ | $\tilde{\rho}_{\text{QMC}}$ | $(U/t)_c$ QMC |
|----------------|-----------|-----------------------------|---------------|
| 64(5) | 22(2) | - | - |
| 55(2) | 21(2) | 56 | 21 |
| 53(2) | 23(2) | 53 | 21 |
| 44(2) | 20(2) | 44 | 20 |
| 37(2) | 19(1) | 38 | 19 |
| 36(2) | 21(2) | 36 | 19 |
| 30(2) | 19(2) | 30 | 18 |
| 27(2) | 20(2) | 27 | 18 |
| 22(2) | 19(2) | 22 | 18 |
| 19(2) | 20(2) | 19 | 23 |
| 10(6) | 22(4) | - | - |

for each image extracted f . Table 7.2 shows the measured values³ of $(U/t)_c$ at different values of $\tilde{\rho}$ and compares them with QMC calculated values from Ref. [103].

The data from Table 7.2 (shown in Fig. 7.4 as red ovals) constitute the measured boundary for the onset of MI; the width and height of each oval represent the associated uncertainties in the measurement. The green dashed line corresponds to a constant atom number ($N_{2D} \approx 3500$) path in the $U/t - \tilde{\rho}$ plane. The circles in Fig 7.4 are colored according to the side of the transition on which they are: light grey (dark grey) corresponds to SF (coexisting SF and MI).

Figure 7.4 also displays the QMC state diagram [103]; the deviation from vertical of the upper portion of this curve, reproduced by the data, differs from the LDA prediction. Linear fits for the measured (yellow dashed line in Fig. 7.4) and predicted transition boundaries, for $\tilde{\rho} > 20$, intersect the horizontal axis at angles $\theta_{\text{exp}} = 85.5(27)^\circ$ and $\theta_{\text{QMC}} = 83.7(3)^\circ$ respectively, suggesting the breakdown of LDA near the transition. Under the LDA, for $\mu/U > 0.5$ the first appearance of ($n=1$) MI is independent of $\tilde{\rho}$ as seen from Fig. 7.3a. The universal character of the state diagram is revealed when it is expressed in the $U/t - \tilde{\rho}$ plane: it is independent of N_{2D} or ϵ and of the validity of the LDA [103]. The discrepancy for $\tilde{\rho} < 15$ is expected due to increased sensitivity to thermal effects at low density where the SF transition temperature is extremely low.

7.6 CONCLUSIONS

Optical lattices have become a thriving field both for theoretical and experimental physics. They constitute a basic tool in ultracold atom experiments due to their ability to be dynamically mod-

³As a reference, a previous experiment reported $(U/t)_c = 15.8(20)$ [120], whereas homogeneous system QMC calculations [110, 121] give $(U/t)_c = 16.5$.

ified. In particular, they provide suitable conditions to study the Bose-Hubbard model and the SF-MI quantum phase transition.

With the use of optical lattice potentials, we created an ensemble of 2D harmonically trapped 2D Bose-Hubbard systems from a ^{87}Rb BEC and used an MRI approach to select a few 2D systems for study, eliminating ensemble averaging. Our identification of the transition from SF to MI, as a function of both atom density and lattice depth, is in excellent agreement with a QMC universal state diagram suitable for our trapped system [103]. Our measurements suggests a breakdown of the LDA near the transition region.

CHAPTER 8

UNIFORM ARTIFICIAL GAUGE FIELD IN A 1D LATTICE POTENTIAL

This chapter describes a method to synthesize both a lattice potential together with a uniform tunable vector potential, realizing the Peierls substitution in ultracold atomic gas. The Peierls substitution is the introduction of the effects of a vector potential \mathbf{A} on charged particles, to the Hamiltonian describing the physics of such particles in a lattice potential. As we will show below, an rf-Raman coupling scheme realizes a 1D lattice coexisting with a uniform artificial vector potential with which the Peierls phase ϕ is experimentally tunable by adjusting the detuning from Raman resonance.

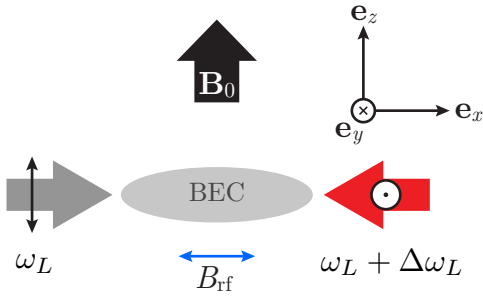
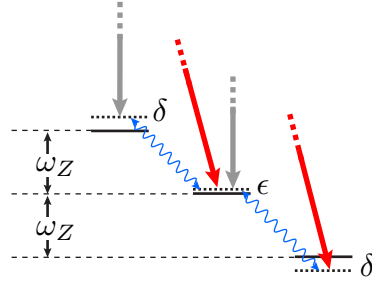
We use a combination of rf and Raman fields to couple the $F=1$ spins in the $5S_{1/2}$ ground state manifold of ^{87}Rb . This work constitutes a first step towards the realization of flux lattices [122], novel lattice structures that would help to reach the quantum Hall regime in ultracold atomic gases, by overcoming the limitations on magnetic field strength and restrictively low energy scales associated with such states [80, 123].

First we describe the mechanism to synthesize the combined lattice and vector potential, and introduce the Peierls substitution; then we discuss the experiments we performed to characterize this rf-Raman lattice; and finally we propose how to generate a flux lattice which is gauge equivalent to the 1/3 flux Hofstadter model.

8.1 RF-RAMAN LATTICE POTENTIAL

Let us consider the experimental setup as shown in Fig. 8.1a. As is standard in our experiments, a uniform bias field $\mathbf{B}_0 = B_0 \mathbf{e}_z$ Zeeman splits the $F = 1$ internal states of ^{87}Rb 's $5^2S_{1/2}$ ground state manifold; the linear and quadratic Zeeman shifts are $\omega_Z/2\pi = 3.25$ MHz and $\epsilon = 1.54$ kHz, respectively. We illuminate an $m_F = -1$ BEC both with a linearly polarized rf-field B_{rf} of frequency $\omega_{\text{rf}} = \omega_Z$; and with a pair of orthogonally polarized Raman beams, whose frequency difference we set to $\Delta\omega_L = \omega_{\text{rf}}$.

As discussed in Chapter 5, in the rotating wave approximation for the frame rotating at $\Delta\omega_L$, the combined vector light shift from the Raman beams and the interaction with the rf-field $E_{\text{rf}} e^{-i\omega_{\text{rf}} t} \mathbf{e}_x$

a. Experimental setup**b. Level diagram****c. Energy scales**

$$\lambda = 791 \text{ nm}$$

$$E_L/h \approx 3.7 \text{ kHz}$$

$$\omega_Z/2\pi = 3.25 \text{ MHz}$$

$$\hbar\epsilon = 0.42 E_L$$

$$(f_x, f_z) = (13, 45) \text{ Hz}$$

Figure 8.1: Setup and level diagram for rf-Raman lattice experiments. **a.** A uniform bias field \mathbf{B}_0 Zeeman splits the energy levels in the $F = 1$ ^{87}Rb ground-state manifold (**b.**), while a pair of counter propagating Raman beams and an rf field illuminate an $m_F = -1$ BEC.

give the coupling Hamiltonian, expressed in the basis of spin states $\{| -1\rangle, | 0\rangle, | +1\rangle\}$:

$$\hat{H}_{\text{rf+R}}(x)/\hbar = \begin{pmatrix} -\delta & \{\Omega_{\text{rf}} + \Omega_{\text{R}} e^{i2k_L x}\}/2 & 0 \\ \{\Omega_{\text{rf}} + \Omega_{\text{R}} e^{-i2k_L x}\}/2 & -\epsilon & \{\Omega_{\text{rf}} + \Omega_{\text{R}} e^{i2k_L x}\}/2 \\ 0 & \{\Omega_{\text{rf}} + \Omega_{\text{R}} e^{-i2k_L x}\}/2 & \delta \end{pmatrix} \quad (8.1)$$

where Ω_{rf} and Ω_{R} are the Rabi frequencies that characterize the strength of the coupling fields, and $\delta = \Delta\omega_L - \omega_Z$ is the detuning from Raman resonance.

When expressed in terms of the components of the $F=1$ angular momentum operator, $\hat{\mathbf{F}} = \{F_x, F_y, F_z\}$, the rf-Raman coupling Hamiltonian becomes

$$\hat{H}_{\text{rf+R}}(x) = \frac{1}{\sqrt{2}}[\Omega_{\text{rf}} + \Omega_{\text{R}} \cos(2k_L x)]\hat{F}_x - \frac{1}{\sqrt{2}}\Omega_{\text{R}} \sin(2k_L x)\hat{F}_y + \delta\hat{F}_z - \epsilon(\hbar^2\hat{1} - \hat{F}_z^2)/\hbar, \quad (8.2)$$

where $\hat{1}$ is the 3×3 identity matrix. The structure of the coupling Hamiltonian of Eq. (8.2), namely $\hat{H}_{\text{rf+R}}(x) = \boldsymbol{\Omega}(x) \cdot \hat{\mathbf{F}} - \hat{H}_Q$, is that of the interaction between the magnetic moment associated with the total angular momentum operator $\hat{\mathbf{F}}$ with a spatially dependent effective Zeeman field $\mathbf{B}_{\text{eff}}(x) = \hbar\boldsymbol{\Omega}(x)/g_F\mu_B$, where μ_B is the Bohr magneton, g_F is the Landé g -factor,

$$\boldsymbol{\Omega}(x) = \frac{1}{\sqrt{2}}[\Omega_{\text{rf}} + \Omega_{\text{R}} \cos(2k_L x), -\Omega_{\text{R}} \sin(2k_L x), \sqrt{2}\delta], \quad (8.3)$$

and $\hat{H}_Q = -\epsilon(\hbar^2\hat{1} - \hat{F}_z^2)/\hbar$ describes the quadratic Zeeman shift.

The eigenenergies $E(x)$ of the rf-Raman coupling Hamiltonian are solutions of the characteristic polynomial

$$E^3 + \epsilon E^2 - \{\delta + [\Omega_{\text{rf}}^2 + \Omega_{\text{R}}^2 + 2\Omega_{\text{rf}}\Omega_{\text{R}} \cos(2k_L x)]\}E - \epsilon\delta^2 = 0; \quad (8.4)$$

these eigenenergies are spatially periodic along \mathbf{e}_x with period $\lambda/2$, and correspond to effective

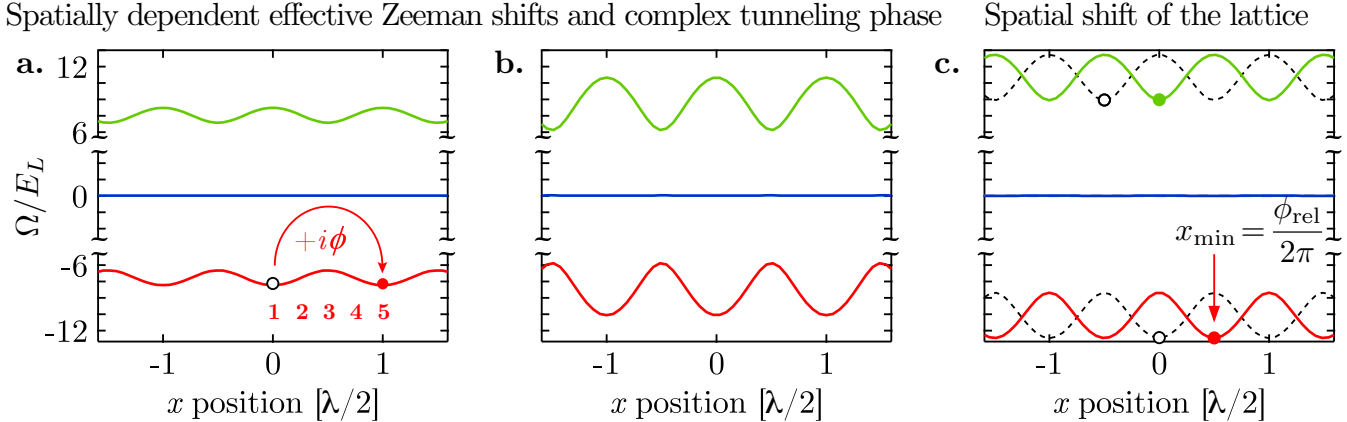


Figure 8.2: Effective Zeeman lattice potential. This figure shows the effective Zeeman shifts calculated by diagonalizing $\hat{H}_{\text{rf+R}}(x)$ at different coupling strengths: **a** $\hbar(\Omega_{\text{rf}}, \Omega_{\text{R}}, \Omega_z) = (1, 10, 2)E_L$; **b** $\hbar(\Omega_{\text{rf}}, \Omega_{\text{R}}, \Omega_z) = (3.5, 11.5, 2)E_L$; **c** $\hbar(\Omega_{\text{rf}}, \Omega_{\text{R}}, \Omega_z) = (3, 15, 2)E_L$ (dashed). **a.** The effective Zeeman field \mathbf{B}_{eff} precesses in space within a lattice period (points 1-5) as shown in Fig. 8.3. Neutral particles acquire a geometrical phase ϕ upon tunneling from site j (open symbol) to $j + 1$ (closed symbol). **c.** Conveyor-belt transport of particles [124] can be implemented by introducing a relative phase ϕ_{rel} between the rf and Raman coupling fields; the spatial displacement of the potential (solid) is proportional to ϕ_{rel} . The closed and open circles indicate the displacement from zero to x_{\min} .

Zeeman shifts produced by the spatially varying field $\mathbf{B}_{\text{eff}}(x)$ (Fig. 8.2). Our atoms are prepared in the lowest energy eigenstate of the rf-Raman coupling Hamiltonian.

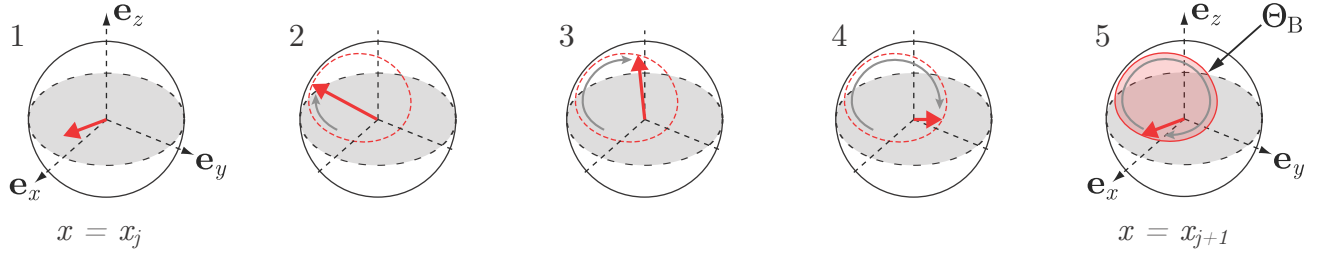
The most relevant characteristic of such engineered lattice arises from the spatial dependence of the effective Zeeman field; $\mathbf{B}_{\text{eff}}(x)$ precesses in space in proportion to the vector $\boldsymbol{\Omega}(x)$, as shown in Figure 8.3. This precession is responsible for the acquisition of a geometrical Berry's phase [125] by a slowly moving atom tunneling from site j to site $j + 1$. In the adiabatic approximation, where the atom moves slowly enough such that the precession rate of the effective field is small compared to the hyperfine splitting ω_Z , \mathbf{B}_{eff} defines a local quantization axis; after a full precession cycle the final state of the atom differs from the initial state by a geometric phase factor ϕ , the Peierls phase, proportional to the solid angle enclosed by \mathbf{B}_{eff} .

A closed expression can be determined for the Peierls phase in the limit of large Raman coupling ($\Omega_{\text{R}} \gg 4E_L, \Omega_{\text{rf}}, \epsilon$); it is given by $\phi = \Theta_B + 2\pi$, where $\Theta_B = 2\pi m_F(1 - \delta/\Omega)$ is Berry's phase, $m_F = -1$, and $\Omega = (\Omega_{\text{R}}^2/2 + \delta^2)^{1/2}$, independent of Ω_{rf} . In our experiment, Ω_{R} is not sufficiently large for this approximation to be valid, so we instead compare our results to the numerically computed bandstructure, as discussed below.

8.2 THE PEIERLS SUBSTITUTION

Particles with charge q moving along a 1D lattice in the presence of a vector potential \mathbf{A} acquire a geometrical phase $\phi_j = (q/\hbar) \int_{x_j}^{x_{j+1}} \mathbf{A} \cdot \mathbf{e}_x dx$ upon tunneling from site j to $j + 1$ (Fig. 8.2a). For

a. Spatial precession of $\mathbf{B}_{\text{eff}}(x)$ for comparable rf and Raman coupling strengths



b. Spatial precession of $\mathbf{B}_{\text{eff}}(x)$ in the large Raman coupling limit

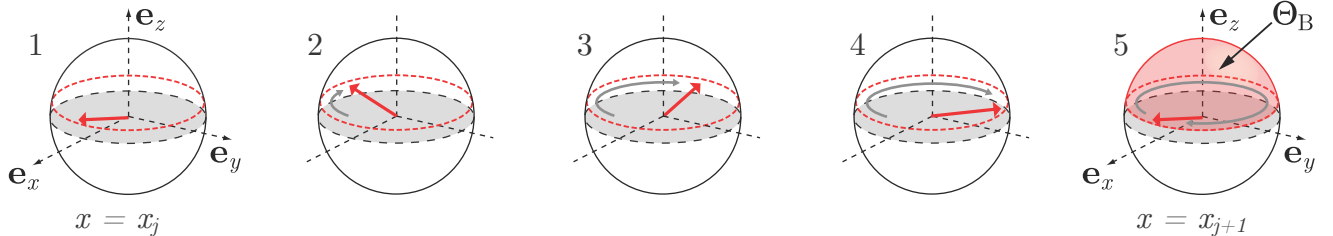


Figure 8.3: Spatial precession of $\mathbf{B}_{\text{eff}}(x)$ (radial vector) and the solid angle it subtends when an atom tunnels from site j to site $j+1$. Only when both dressing fields are illuminating the atoms does the lattice potential exist; therefore, the effective Zeeman field is in general not symmetric about \mathbf{e}_z . This behavior is emphasized when the coupling strengths are comparable in magnitude, **a.** shows the case for $\hbar(\Omega_{\text{rf}}, \Omega_R, \Omega_z) = (3, 3, 2)E_L$. In contrast, in the limit where $\Omega_R \gg \Omega_{\text{rf}}$, the effective Zeeman field spans the whole xy -plane; **b.** displays the case for $\hbar(\Omega_{\text{rf}}, \Omega_R, \Omega_z) = (10, 1, 2)E_L$. The geometrical Berry's phase Θ_B gives the Peierls phase ϕ .

sufficiently deep lattice potentials, where the atoms are tightly confined to the lattice sites, the second quantization form of the Hamiltonian for a particle in a lattice potential is

$$\hat{H} = - \sum_j [t \exp(i\phi_j) \hat{a}_{j+1}^\dagger \hat{a}_j + \text{h.c.}], \quad (8.5)$$

where \hat{a}_j^\dagger describes the creation of a particle at site j , and $t \exp(i\phi_j)$ is the complex matrix element for tunneling between neighboring sites. Using the phases ϕ_j to represent the effect of \mathbf{A} is known as the Peierls substitution [126], and for a uniform phase ϕ the energy of the lowest band is given by $E(k_x) = -2t \cos(\pi k_x/k_L - \phi)$, where k_x is the particle's crystal momentum. A key signature of the Peierls substitution is thus the shift of the structure of the lowest energy band (Fig. 8.4a). By tuning the experimental parameters: Ω_{rf} , Ω_R and Ω_z we can vary not only the amplitude of the tunneling matrix element t , but also the Peierls tunneling phase ϕ (Fig. 8.4b,c).

We numerically diagonalized the combined rf-Raman Hamiltonian $\hat{H}_{\text{rf+R}}$ given the experimental parameters: Ω_{rf} , Ω_R and Ω_z , in order to compute the properties of our lattice potential. For simplicity we work in the momentum space representation of $\hat{H}_{\text{rf+R}}$, described below. This representation offers an alternative understanding of the effective Zeeman lattice structure that arises from the

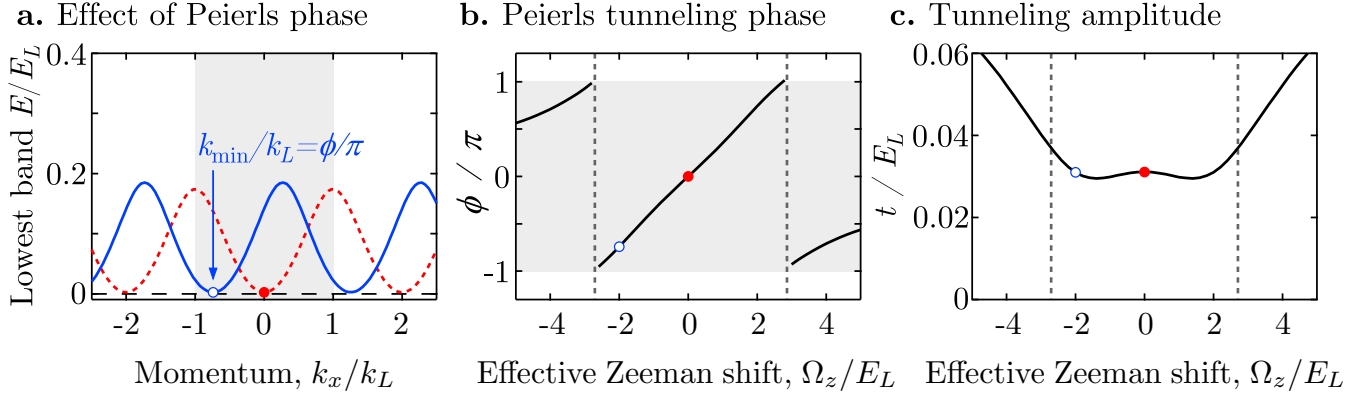


Figure 8.4: The Peierls substitution in a lattice potential. **a.** Calculated lowest band with minimum located at $k_{\min}/k_L = \phi/\pi$, defined within the first Brillouin zone (gray region). The curves correspond to: $\hbar(\Omega_{\text{rf}}, \Omega_R, \Omega_z) = (0.75, 10, 0)E_L$ (dashed) and $\hbar(\Omega_{\text{rf}}, \Omega_R, \Omega_z) = (0.75, 10, -2)E_L$ (continuous). **b.-c.** Peierls phase and tunneling amplitude as a function of the effective Zeeman shift $\hbar\Omega_z$ for the above coupling strengths. The open (closed) symbol corresponds to the shifted (unmodified) lowest band. The vertical dashed lines indicate the limits of the first Brillouin zone.

combination of rf and Raman coupling fields.

8.3 MOMENTUM REPRESENTATION OF $\hat{H}_{\text{rf+R}}$

Raman transitions couple together states with m_F differing by ± 1 , and momentum differing by $\pm 2\hbar k_L$, while rf-coupling processes only change m_F by ± 1 , leaving the momentum unchanged. The combination of both Raman and rf fields generates states with higher order momentum transfer. The available states under rf-Raman coupling constitute a set of spin-momentum states $\{|\Psi_n\rangle\} = \{|m_F, \hbar(k_x + 2nk_L)\rangle\}$ where $n \in \mathbb{Z}; m_F = 0, \pm 1$. As expected, this basis is that of a lattice. It is important to emphasize here as we did in previous chapters that given our experimental setup, with the Raman beams propagating along the \hat{x} direction, the momentum distribution is modified exclusively along \hat{x} (Fig. 8.1), while it remains unchanged in the other directions.

The Hamiltonian $\hat{H}_{\text{rf+R}}$ is a Hermitian block matrix of size $3(2N+1)$ in the basis $\{|\Psi_n\rangle\}$, where n is restricted to $n \leq N$. For our parameters, dimensions larger than $3(2N+1) = 81$ provided indistinguishable results. The dimension of this basis is appropriate for our calculations since we observed the population of states with up to $|n| = 4$. For clarity, we construct the Hamiltonian by arranging the spin-momentum states in the $\{\Psi_n\}$ basis with increasing momentum index $n = -N, -N+1, \dots, N$. Along the principal diagonal, we have 3×3 blocks

$$\mathbb{A}_{k_x}(n) = \frac{\hbar^2}{2m}(k_x + 2nk_L)^2 \hat{1} + \frac{\Omega_{\text{rf}}}{\sqrt{2}} F_x - [\Omega_z F_z + \frac{\epsilon}{\hbar} (\hbar^2 \hat{1} - F_z^2)];$$

these terms correspond to kinetic energy, rf coupling of spin states with equal momentum, and the

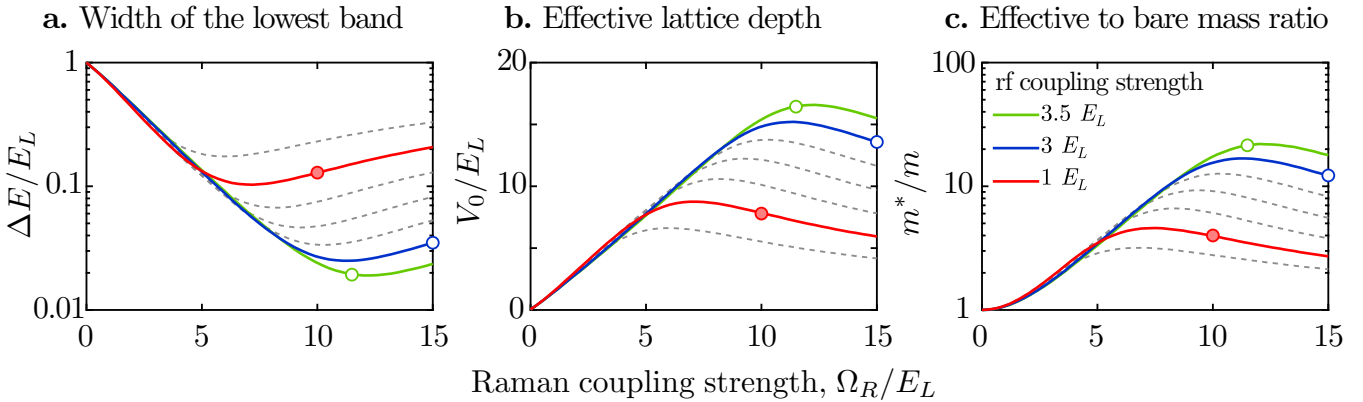


Figure 8.5: Effective Zeeman lattice properties. **a.** Calculated width of the lowest energy band ΔE , as a function of Ω_R , for $0.5 < \hbar\Omega_{\text{rf}}/E_L < 3.5$ and with $\Omega_z=0$. **b.** Effective depth of the engineered Zeeman lattice. **c.** Effective to bare mass ratio m^*/m . The symbols indicate the experimental regime in which we: (i) reported BEC diffraction from the effective Zeeman lattice (open symbols), and (ii) measured the Peierls tunneling phase (closed symbols) [30].

real Zeeman interaction, respectively. Above and below the $\mathbb{A}_{k_x}(n)$ blocks, we have 3×3 blocks $\mathbb{B} = \sqrt{2}\Omega_R(F_x - iF_y)/4$ describing the Raman coupling of spin-momentum states differing in momentum by $\Delta k_x = \pm 2k_L$.

The diagonalization of $\hat{H}_{\text{rf+R}}(n)$ as a function of k_x gives the bandstructure of the combined rf-Raman lattice potential, $E(k_x) = E(k_x, \Omega_{\text{rf}}, \Omega_R, \Omega_z)$. The structure of $E(k_x)$ captures all the relevant properties that characterize our lattice potential, i.e. the depth V_0 of the lattice, the effective mass m^* , the tunneling amplitude t and the Peierls tunneling phase ϕ . The next section describes how each quantity is determined.

8.3.1 Calculation of lattice properties. We extract the Zeeman lattice properties by fully characterizing the lowest energy band, which in the tight binding regime is of the form $E(k_x) = -2t \cos(\pi k_x/k_L - \phi)$, see Fig. 8.4a.

We obtained the Peierls phase ϕ by computing the shift of the lowest band [with minimum at $k_{\min} = (\phi/\pi)k_L$] as a function of the experimental parameters (Fig. 8.4b). For $\Omega_R \gg 50E_L$, our numerical calculation agrees with the exact result in the large Raman limit ($\Omega_R \gg 4E_L, \Omega_{\text{rf}}, \epsilon$) to better than 10%; however, in our experiment, Ω_R is not sufficiently large and we instead compare our results to the numerically computed bandstructure.

The effective mass is given by $m^* = \hbar^2 [d^2 E(k_x)/dk_x^2]^{-1}$, where the derivative is evaluated at the point of interest (this is at $k_x = k_{\min}$, unless otherwise indicated). In the tight-binding limit, the tunneling matrix element is $t = (m/m^*)/\pi^2$ (Fig. 8.4,c). However, the general relation between effective mass and tunneling amplitude is $m/m^*(k_x) = \pi^2 \cos(\pi k_x/k_L - \phi)t/E_L$.

Figure 8.5a presents the calculated width $\Delta E = E(k_x = 1) - E(k_x = 0)$ of the lowest energy

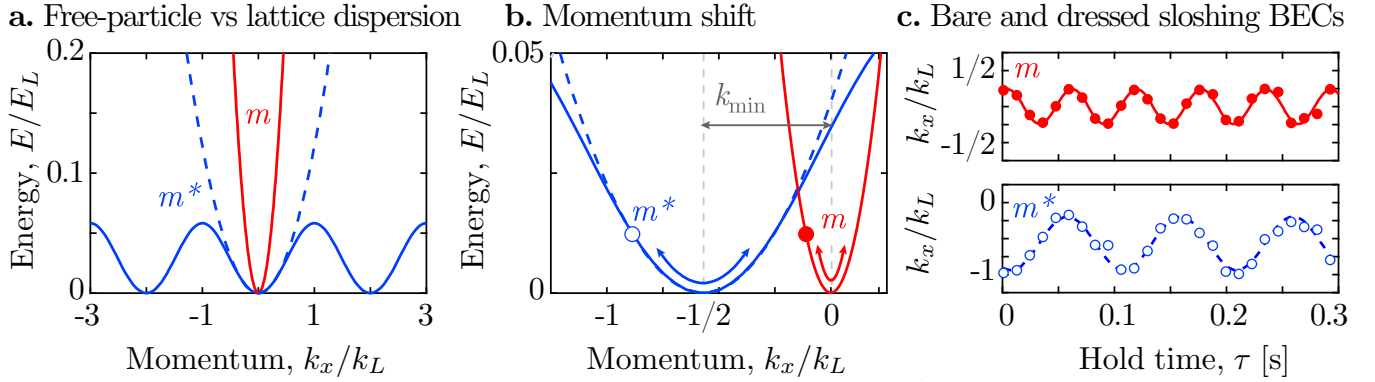


Figure 8.6: Effective mass and Peierls phase in the engineered lattice potential. **a.** Comparison between free-particle dispersion and the lowest band structure of a particle in an effective lattice potential where $\hbar(\Omega_{\text{rf}}, \Omega_R, \Omega_z) = (0.75, 10, 0)E_L$. For small displacements around the minimum, the dispersion in the lattice can be expressed as $E \approx \hbar^2(k_x - k_{\min})^2/2m^*$ (dashed curve), where m^* is the effective mass. **b.** Shift of the bandstructure to $k_{\min}/k_L = \phi/\pi$ due the introduction a Peierls phase ϕ . **c.** In the absence of the lattice (closed symbols), the oscillations were induced by suddenly applying and removing a Stern-Gerlach field gradient; the measured sloshing frequency is that of the optical trap $f_x = 17.3(8)$ Hz. When the lattice is on [open symbols, $\hbar(\Omega_{\text{rf}}, \Omega_R, \Omega_z) = (0.75, 10, -1.6)E_L$], the particles behave as heavier objects and the sloshing frequency is $f^* = 9.9(7)$ Hz; the measured parameters are: $\phi/\pi = -0.57(1)$; $m^*/m = 3.05(5)$, and $t/E_L = 0.033(1)$.

band for the effective lattice potential as a function of Ω_{rf} and Ω_R , with $\Omega_z = 0$. Using the relation between the depth V_0 of a lattice and the width of its lowest energy band ΔE (see Chap. 7), we computed the effective depth of the engineered Zeeman lattice, shown in Fig. 8.5b. Finally, we also investigated the dependence of m^*/m on the coupling strengths Ω_{rf} and Ω_R , at $\Omega_z = 0$. Figure 8.5 summarizes the fact that the deeper the lattice, the flatter the lowest band and the more massive the particles behave.

8.4 EXPERIMENTAL CHARACTERIZATION

We applied the engineered lattice to $m_F = -1$ ^{87}Rb BECs, and designed our experiments to measure: the effective mass m^* , the amplitude of their tunneling matrix element t , the acquired Peierls phase ϕ , and the short time dynamics under such periodic potential. These experiments can be categorized as follows: (a) we suddenly induce sloshing to extract m^* , t and ϕ ; (b) we adiabatically change the bandstructure to directly measure ϕ ; or (c) we abruptly turn-on the lattice to investigate BEC dynamics.

8.4.1 System preparation. All experiments start with ^{87}Rb BECs in the $|F=1, m_F=-1\rangle$ state in a crossed optical dipole trap with frequencies $(f_x, f_y, f_z) = (13, 45, 90)$ Hz¹. In the presence of a

¹Both the trap frequencies and λ were slightly different in some of the experiments: $(f_x, f_y, f_z) = (17.3, 41.4, 90)$ Hz, and $\lambda = 790.14$ nm

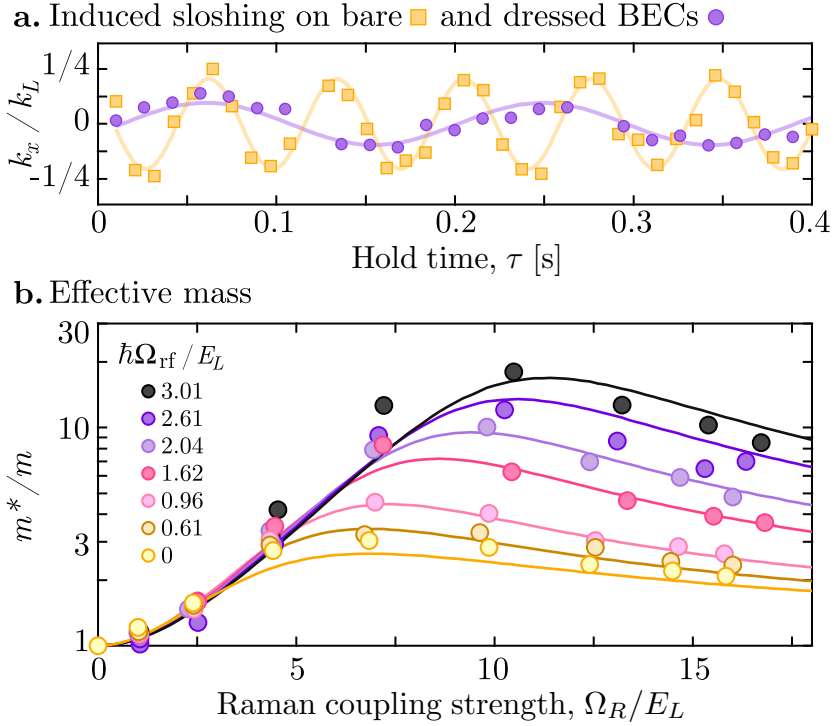


Figure 8.7: Measured effective mass at $\Omega_z = 0$. **a.** Comparison of the oscillations of a BEC in the $|m_F = -1\rangle$ state to those in an rf-Raman dressed BEC [$\hbar\Omega_R = 12.4(9)$ E_L and $\hbar\Omega_{rf} = 2.04(6)$ E_L]. The curves are fits to a sinusoid from which we obtain $f_x = 14.0(1)$ Hz and $f^* = 5.3(1)$ Hz, thus $m^*/m = 7.0(3)$ and $t = 0.015(1)$ E_L . **b.** Measurements of m^*/m as a function of Ω_R and Ω_{rf} . The curves depict the expected m^*/m ratio.

uniform bias field² $B_0 \mathbf{e}_y$, we apply an rf magnetic field with frequency $\Delta\omega/2\pi = g_F\mu_B B_0 = 3.25$ MHz and prepare the BEC in the lowest energy rf-dressed state [5]. Two $\lambda = 790.33$ nm Raman laser beams, counter-propagating along \mathbf{e}_x and differing in frequency by $\Delta\omega$, couple the BEC's internal degrees of freedom with strength Ω_R (Fig. 8.1a,b). The combination of rf and Raman coupling creates a 1D lattice potential along \mathbf{e}_x , the direction of momentum exchange defined by the Raman beams.

8.4.2 Sloshing experiments. Starting with the rf-dressed state described in above, we ramped the Raman beams from 0 to $\Omega_R > 4 E_L/\hbar$ in 70 ms. Then we ramped the rf coupling strength to an adjustable final value Ω_{rf} in 2 ms, such that an effective Zeeman lattice was created. We induce dipole oscillations [6, 127] by applying a synthetic electric field (see Sec. 5.4.6), achieved by ramping the z -component of the Zeeman field to $\hbar\Omega_z \approx 2E_L$ and then jumping it back to some final value³ in

²The long term drift of the Zeeman field defining the splitting of the hyperfine levels was about 0.2kHz=0.05 E_L over a data acquisition period of 1.7 hr.

³To study rf-Raman dressed states with small $\Omega_R < 4 E_R$, where the band structure has sharp features near the avoided crossings at $k_x = \pm 2k_L$, we followed the previously described procedure to prepare a dressed state with $\Omega_R > 4 E_R$, kick the atoms with the synthetic electric force and then ramped $\Omega_R > 4$ to its final small value in 200

2 ms. The atoms experience a net force equal to the rate at which the minimum of quasimomentum is changed (proportional to the rate at which their mechanical momentum changes), thus they initiate oscillatory motion in the dipole trap.

8.4.2.1 Dynamical instabilities. Figure 8.6 summarizes the ideas for the sloshing experiments. The energy-momentum dispersion relation of a free-particle is $\hbar^2 k_x^2 / 2m$; in the presence of a lattice we obtain bandstructure (Fig. 8.6a); the modification of the dispersion relation is characterized by a new effective mass m^* , and around a minimum of the lowest energy band we obtain $E \approx \hbar^2(k_x)^2 / 2m^*$. When $\Omega_z \neq 0$ we introduce a Peierls phase ϕ and shift the bandstructure to $k_{\min}/k_L = \phi/\pi$; the rate of change in the minimum of quasimomentum is felt by the atoms as a force, thus they begin oscillatory motion in the optical dipole trap (Fig. 8.6b). A comparison between free-particle and lattice sloshing is shown in Fig. 8.6c. We realized sloshing experiments in two regimes: (i) at a final $\Omega_z = 0$ to focus on m^*/m ; and (ii) at variable Ω_z to measure the Peierls phase ϕ .

i. Measurements at final $\Omega_z = 0$. We obtain the effective mass m^* by measuring shifts in the oscillation frequency as a function of the coupling strengths Ω_R and Ω_{rf} . The atoms slosh in the lattice for a variable time τ , after which we remove all coupling and confining potentials (thus projecting the final spin-momentum superposition into bare atomic states) and absorption image after a 28.2 ms time-of-flight (TOF). Figure 8.7 shows that the measured effective to bare mass ratio $m^*/m = (f_x/f^*)^2$, as a function of Ω_R and Ω_{rf} , is in good agreement with calculations. Those data provide the tunneling matrix element amplitude $t/E_L = (m/m^*)/\pi^2$ in the tight-binding regime.

ii. Measurements of the Peierls phase at variable Ω_z . We focus on the robustness of the Peierls phase by first adiabatically loading to $\phi = \pm\pi$ (the condensate sits at the edge of the Brillouin zone) and then suddenly changing both Ω_z and Ω_{rf} to new values (changing both ϕ and t). We modulated the rf coupling strength as $\Omega_{rf} = \Omega_{rf0} + \Delta\Omega_{rf} \cos(2\pi f_{rf}\Omega_z)$, where $\hbar\Omega_{rf0} = 0.75E_L$, $\hbar\Delta\Omega_{rf} = 0.23E_L$ and $f_{rf}/\hbar = 0.4E_L^{-1}$. The resulting momentum space oscillations are centered at k_{\min} . After a time τ we release the BEC, and subsequently deload all atoms into a single bare spin state to finally absorption image them after 13.1 ms TOF (see Sec. 8.4.3).

There are two main sources of dynamical instability in a BEC in a combined harmonic and periodic potential. The first one is related to the critical momentum ($k_x = |k_L/2|$) beyond which the system can evolve into a lower energy one by means of the emission of energy and momentum conserving phonon-excitations, depleting the original condensate. The second condition arises from the combination of interactions and the periodicity of the trapping potential.

We observed the first type of dynamical instability, namely the one that results in the depletion of the superfluid when its velocity is greater than a critical velocity, and in the strong damping of the oscillatory motion of the center of mass. We fit three oscillation cycles, 50 ms after the

ms.

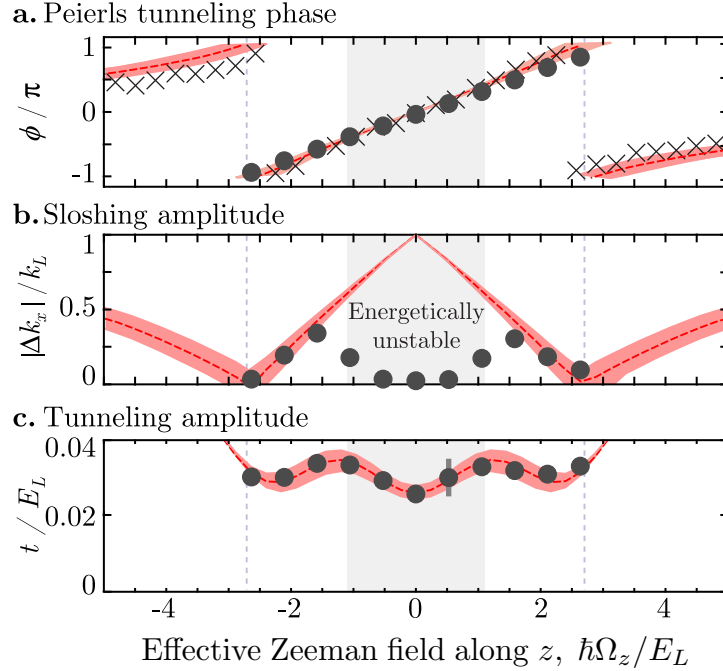


Figure 8.8: Measured Peierls tunneling amplitude and phase. **a.** Peierls phase ϕ measured using adiabatic (crosses) and sudden (circles) changes of Ω_z . Vertical lines denote the first Brillouin zone. **b.** Sloshing amplitude after suddenly changing Ω_z . We observed strong damping of oscillations in the region shaded in gray. **c.** Tunneling amplitude t measured from oscillation frequency. The rf coupling was modulated as a function of Ω_z to test the robustness of the Peierls phase ϕ . The Raman coupling was held at $\hbar\Omega_R = 10.0(8)E_L$. The dashed curves correspond to the expected behavior calculated from $\hat{H}_{\text{rf+R}}$, and the pink bands arise from the experimental uncertainty in Ω_R .

oscillatory motion started, with $k_x(\tau) = k_{\min} + \Delta k_x \cos(2\pi\tau f^* + \gamma)$, where Δk_x is the amplitude, and γ is an overall phase-shift whose average value is $0.9(1)\pi$. For the most strongly damped data the damping was nearly instantaneous; the system rapidly approached the equilibrium momentum ($k_{\min}/k_L = \phi/\pi$) and then oscillated with extremely small (but non-zero) amplitude about this value. The region of strong damping shown in Fig. 8.8 coincides with the expected range $\Delta k_x > 0.5k_L$ (shaded gray region) for this dynamical instability [107].

8.4.3 Deloading into a single spin state. The deloading process consists on rapidly ramping Ω_z to 0, and taking $\hbar\Omega_R \rightarrow 0$ to zero in $500 \mu\text{s}$ while increasing $\hbar\Omega_{\text{rf}} \rightarrow 3E_L$; this maps the occupied crystal momentum k_x to free-particle momentum. We then ramped $\hbar\Omega_z \rightarrow -140E_L$ transferring all atoms into $|m_F=+1\rangle$ (see Fig. 8.9).

8.4.4 Adiabatic measurement of the Peierls phase. In the adiabatic method, we load a BEC at $k_x = 0$ and adiabatically change Ω_z , such that the BEC always sits at the minimum of $E(k_x)$ located at k_{\min} . The time scale for adiabaticity is set by the modified trapping frequency f^* along the direction of the Raman beams. Once Ω_z reaches its final value, we remove the trapping

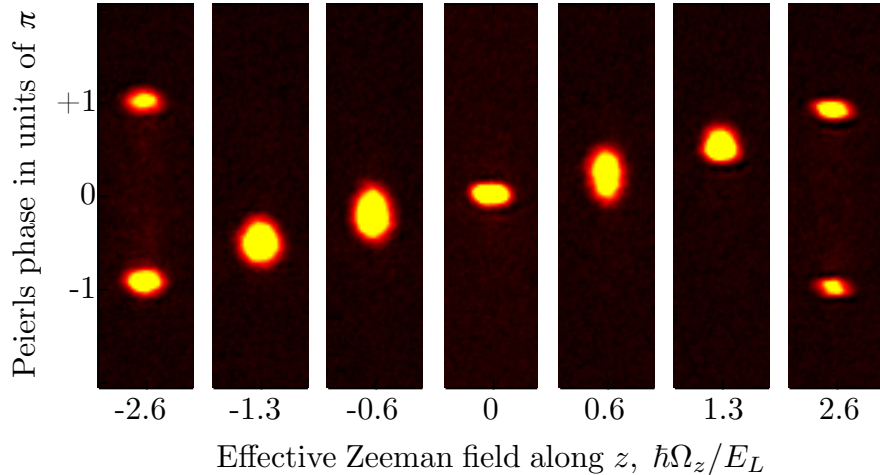


Figure 8.9: Adiabatic measurement of the Peierls phase. Shown is a collection of absorption images (13.1 ms TOF) of the momentum distribution of rf-Raman dressed states, after adiabatically ramping Ω_z (the z component of the effective Zeeman field), band-mapped the rf-Raman dressed state to reveal the occupied momentum states, and deloaded it into the single spin state $|+1\rangle$. The shift in the momentum distribution is a direct measure of the Peierls phase (Fig. 8.8a, circles); the effective mass (or equivalently the tunneling amplitude in tight binding) changes as a function of detuning (Fig. 8.8c, circles), this is observed as a change in the aspect ratio of the atomic distributions.

potential and deload as described above. We image the atomic distribution after a 13.1 ms TOF, revealing k_{\min} (Fig. 8.9).

Measurements from the adiabatic and sudden methods are in good agreement with each other and their expected values [30], highlighting the precise experimental control offered by our rf-Raman induced effective Zeeman lattice. This agreement also demonstrates the robustness of our engineered Hamiltonian to deliberate variations in Ω_{rf} of up to $0.25E_L$, as was anticipated by the absence of Ω_{rf} in the large Ω_R expression for ϕ . We find that the hopping phase is unaltered by small changes in Ω_{rf} even when t changes significantly.

8.4.5 Short time BEC dynamics. Having discussed the behavior of atoms in the lowest band of the lattice, we now explore the full lattice by suddenly turning it on, diabatically projecting a ground state BEC into higher bands. At the beginning of such a pulse, an ordinary periodic potential would first spatially modulate the BEC's phase before the atoms begin to move [93]; our effective Zeeman lattice induces such a modulation but in a spin-dependent manner. We focus on the $\Omega_R \gg \Omega_{\text{rf}}$ and $\Omega_R \ll \Omega_{\text{rf}}$ tight-binding regimes and investigate the spin and spatial structure of our lattice. Our data extends well beyond the short-time phase modulation regime.

There exists no lattice in the absence of either Raman or rf coupling. As indicated in Fig. 8.10a, we use two different methods to introduce our lattice on an initial spatially uniform state: (*i*) starting with an rf-dressed state (with $k_x = 0$), we suddenly ($t_{\text{on}} < 1 \mu\text{s}$) turn on the Raman beams;

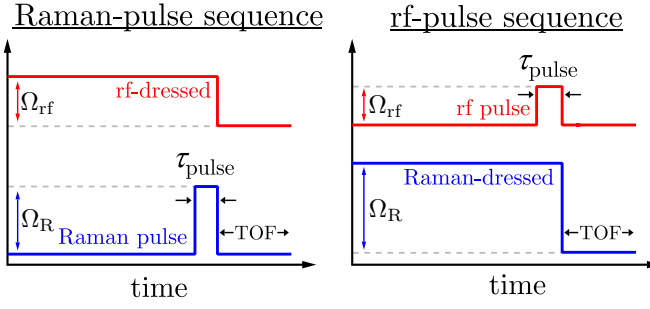
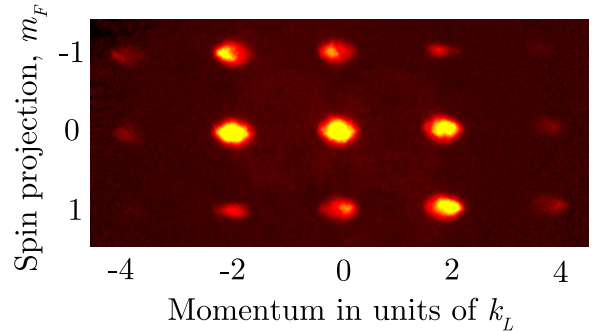
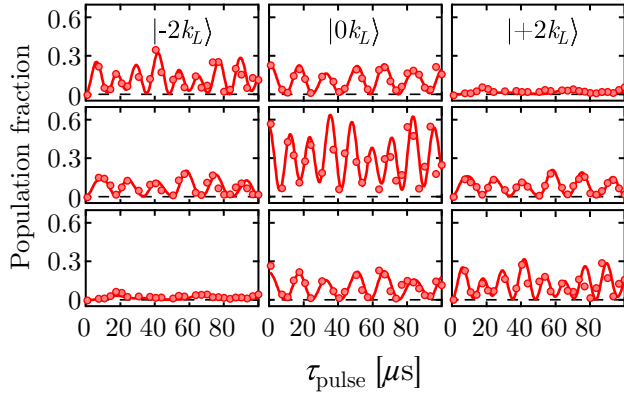
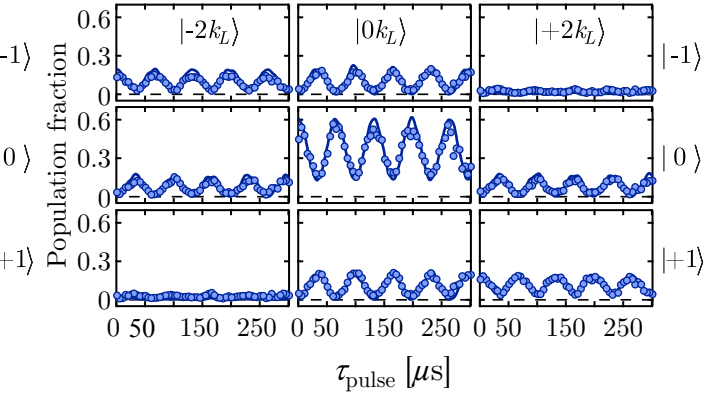
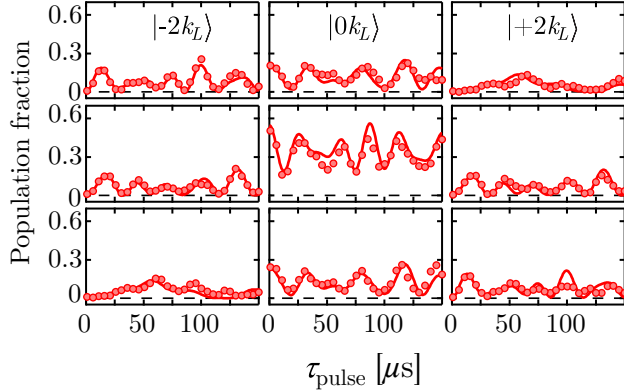
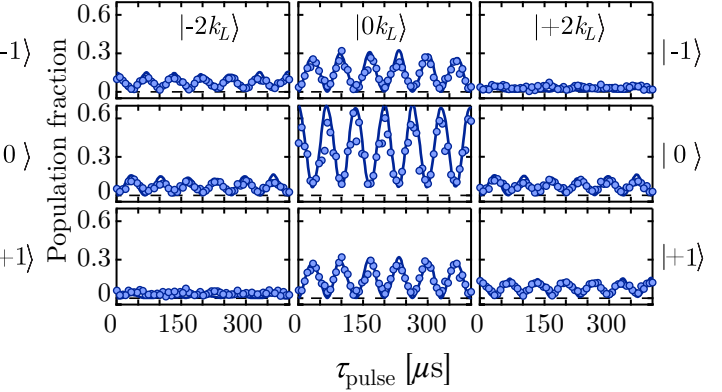
a. Pulse sequences**b. Typical TOF data****c. rf-dressed $3.37 E_L$ + Raman pulse $15.05 E_L$** **d. Raman-dressed $14.15 E_L$ + rf-pulse $3.08 E_L$** **e. rf-dressed $3.12 E_L$ + Raman pulse $6.12 E_L$** **f. Raman-dressed $7.05 E_L$ + rf-pulse $3.13 E_L$** 

Figure 8.10: BEC diffraction from the effective Zeeman lattice. **a.** Starting with an rf-dressed (Raman-dressed) state, we suddenly turn-on the Raman (rf) field for a variable time τ_{pulse} . **b.** Using TOF absorption images of the projected spin-momentum distributions, we count the number of atoms in each diffracted order and determine its fractional population. Panels **c-f** depict time evolution of these fractions. The curves are fits to the data, calculated from \hat{H}_{rf+R} . The fit parameters indicated in the figure are all within 12% from our calibrated values.

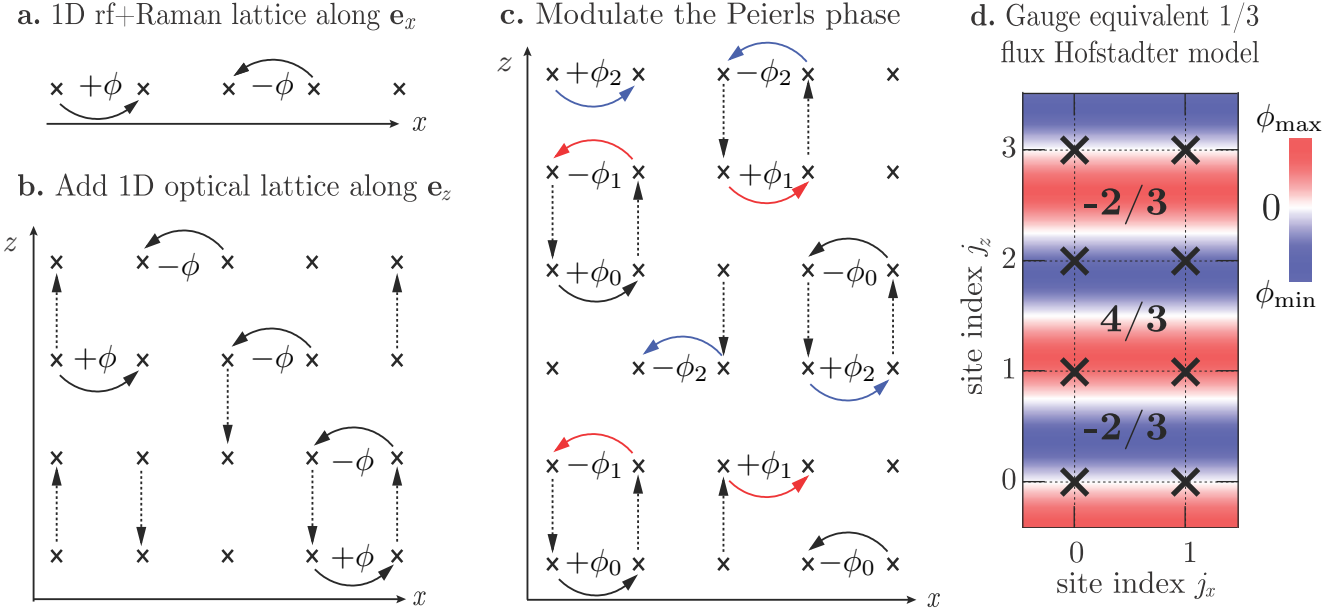


Figure 8.11: Generation of the 1/3 flux Hofstadter model. **a.** Atoms tunneling along our engineered 1D lattice acquire but do not accumulate phase. **b.** A 1D optical lattice along \mathbf{e}_z allows motion in 2D, still without accumulation of phase. **c.** When the Peierls phase is spatially dependent along \mathbf{e}_z , atoms are able to acquire a net phase. **d.** Schematic showing effective 1/3 flux per plaquette modulo 1. The color scale indicates the effective phase gradient induced by the vector lattice. Atoms acquire phase as they hop along \mathbf{e}_x , in contrast, no phase is acquired by hopping along \mathbf{e}_z . In **c.-d.** the phase ϕ_{j_z} at sites with index j_z is $\phi_0=0$, $\phi_1=2/3$ and $\phi_2=-2/3$.

or (ii) starting with a Raman-dressed state [5] (a superposition of $|m_F = 0, k_x = 0\rangle$ and $|m_F = \pm 1, k_x \mp 2k_L\rangle$), we suddenly turn on the rf-field.

After holding the lattice on for a time τ_{pulse} , we suddenly turn off the rf and Raman fields, together with the confining potential. The atoms are projected onto the bare spin-momentum basis and separate in TOF in the presence of a magnetic field gradient (along \mathbf{e}_z), allowing us to resolve their spin and momentum components.

We observe detectable population in states with momenta up to $|k_x| \leq 4k_L$ (Fig. 8.10b). We perform such experiments for $\Omega_R/\Omega_{\text{rf}} \approx 3$ and 5. We minimize the effects of interactions by working with small BECs ($\approx 9 \times 10^4$ atoms). Figures 8.10c-f show the fraction of atoms in each diffracted order evolving with time. We observe multiple revivals of the initial spin-momentum state and find symmetry in the population dynamics of spin-momentum states with opposite momentum *and* opposite spin. The curves represent fits to the populations in all spin-momentum components. The parameters from the fits are all within 10% for our calibrated values, demonstrating that the spin-momentum dynamics are well described by the unitary evolution of the initial states under $\hat{H}_{\text{rf+R}}$.

8.4.6 Spontaneous emission limited lifetime. We measured a spontaneous emission limited lifetime of $0.50(8)$ s for the dressed rf-Raman dressed system with $\Omega_{\text{rf}}=0.75E_L$ and $\Omega_{\text{R}}=10E_L$. The lifetime of the dressed systems can be simply increased by a factor of 4, by going to a configuration where the Raman beams are orthogonal to each other, such that E_L is decreased by a factor of 2, and by working at a reduced Raman coupling strength (our technique works well down to about $\Omega_{\text{R}}=5E_L$) [7].

8.4.7 1/3-Flux gauge equivalent Hofstadter model. Having demonstrated the experimental control on the Peierls tunneling phase in a 1D lattice potential, we propose to extend our results into 2D to create a flux lattice [1, 122] that is *topologically* equivalent to the Hofstadter model with flux density $n_\Phi=1/3$ per plaquette.

Particles moving in our engineered 1D lattice cannot accumulate phase (Fig. 8.11a) as is required to simulate the physics of materials in extreme magnetic fields. By adding a 1D optical lattice along \mathbf{e}_z , we allow the atoms to move in the xy -plane, still without accumulation of phase (Fig. 8.11b). It is by associating a spatial dependence to the Peierls phase along \mathbf{e}_z [7], that atoms moving in the lattice would acquire a non-zero phase. In particular we propose to modulate the Peierls phase (via Ω_z) using a spin dependent lattice with a period $3a/2$ (e.g., from an additional 790 nm laser, nearly counter-propagating). By exploiting the fact that the phase is defined modulo 2π , in a similar way of the flux rectification mechanism proposed in Ref. [128], atoms in this lattice would realize the physics of a 2D electron gas in a uniform strong magnetic field. It can be demonstrated that this scheme has non-trivial Chern numbers [129] as those of the $n_\Phi=1/3$ Hofstadter model: $(1, -2, 1)$.

8.5 CONCLUSIONS

We realized a 1D lattice potential for ultracold atoms using only rf and Raman transitions, in which the tunneling matrix element is in general complex. This work constitutes a first step towards realizing flux lattices [122], in which the physics of charged particles in strong magnetic fields can be simulated. The tunability of the Peierls phase achieved with our rf-Raman lattice would allow the observation of nonlinear effects of ultracold atoms in 1D periodic potentials, such as atomic density modulations with periodicity larger than the lattice spacing [130].

CHAPTER 9

MATRIX VALUED GAUGE FIELDS: SPIN-ORBIT COUPLING IN BECs

Light-induced artificial gauge fields allow experimentalists to overcome the limitations imposed by the neutrality of charge in ultracold atom systems, and have succeeded in the realization of artificial electric [6] and magnetic fields [7]. Taking advantage of the extraordinary control offered by the manipulation of both light fields and ultracold atom internal degrees of freedom our experiments have now turned to the simulation of matrix valued artificial gauge fields, in particular of spin-orbit coupling [9]. This chapter describes our experimental realization of spin-orbit coupling (SOC) not only in ultracold atomic gases, but in a bosonic system of any kind.

Spin-orbit coupling is at the core of the spin-Hall effect [74, 75]. The spin-Hall effect refers to the generation of a pure spin current transverse to an applied electric field in the absence of applied magnetic fields, where spin accumulation is expected at the edges of the sample. The spin-Hall effect has important potential use in the field of spintronics where the control of the spin degree of freedom, in this case in the form of spin currents, is essential. Evidence of the spin-Hall effect has been observed in thin films of semiconductors [24], metals [131] and other condensed matter systems [132, 133, 134].

The quantum spin-Hall phase can be a macroscopic signature of time reversal invariant topological insulators [12], i.e. electronic materials that have a bulk band gap like an ordinary insulator but allow protected charge and spin conducting states on their edge (2D) or surface (3D). Exciting new states can occur at the surface of a topological insulator [25, 135]; in particular they would lead to states supporting Majorana fermions [13] and are potential ingredients for the realization of topological quantum computation [27].

Ultracold atom systems, with their extreme purity and tunable experimental control, are ideal candidates to investigate spin-orbit coupling phenomena, including generalized $s > 1/2$ coupling schemes [28] which do not have a condensed matter analog, as is the case for the “spin-1/2” bosonic-SOC described here.

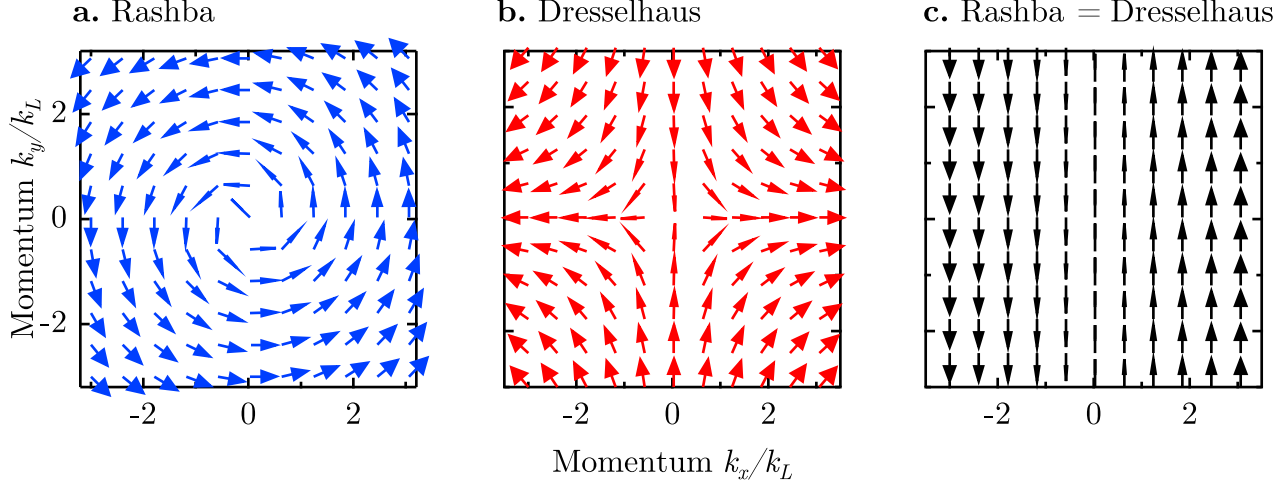


Figure 9.1: Spin-Orbit coupling as a momentum dependent vectorial Zeeman field. The thickness of the vectors (arrows) indicates the strength of the SOC. **a.** Rashba SOC shows circulation. **b.** The linear Dresselhaus type SOC resembles a quadrupole field. **c.** We engineered an equal sum of Rashba and Dresselhaus SOC. It has a single non-zero vectorial component whose magnitude depends on k_x .

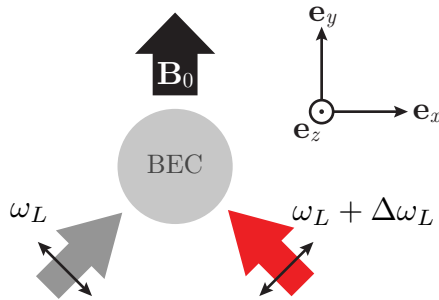
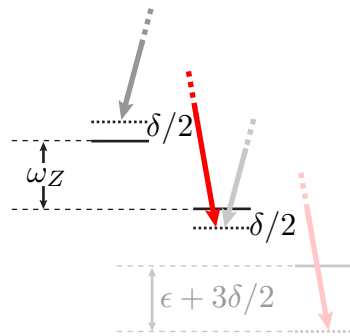
9.1 SPIN-ORBIT COUPLING

SOC can most simply be understood for particles moving in the presence of a static electric field \mathbf{E}_0 . Under a Lorentz transformation to the moving frame of a particle with momentum $\hbar\mathbf{k}$, the electric field gives rise to a momentum dependent magnetic field [51] $\mathbf{B}'(k) = (-k_y, k_x, 0)\hbar E_0/mc^2$. The SO interaction is the Zeeman interaction of the spin of the particle and the magnetic field $\mathbf{B}'(\mathbf{k})$, namely $-\mu \cdot \mathbf{B}'(\mathbf{k}) \propto k_y \hat{\sigma}_x - k_x \hat{\sigma}_y$; this particular combination of spin-momentum terms is known as the Rashba SO interaction and $\hat{\sigma}_j$ stand for the Pauli matrices, where $j \in \{x, y, z\}$. The breakdown of inversion symmetry is responsible for the linear Dresselhaus type of spin-orbit coupling, which is proportional to $-\sigma_x k_y - \sigma_y k_x$. These two types describe SOC in solids to linear order in 2D.

A general expression for linear spin-orbit coupling in 2D spin-1/2 systems is

$$H = \frac{\hbar^2 \mathbf{k}^2}{2m} \hat{1} + \frac{\Omega}{2} \hat{\sigma}_z - \alpha(k_y \hat{\sigma}_x - k_x \hat{\sigma}_y) - \beta(-k_y \hat{\sigma}_x - k_x \hat{\sigma}_y), \quad (9.1)$$

where α and β correspond to the Rashba and Dresselhaus SOC strengths, respectively. Figure 9.1 displays the nature of the momentum-dependent Zeeman field associated with each of the above SO interactions [(a) and (b)] and their equal sum (c), i.e. when $\alpha=\beta$ the spin-orbit coupling term is $2\alpha k_x \hat{\sigma}_y$.

a. Experimental setup**b. Level diagram****c. Energy scales**

$$\lambda = 804 \text{ nm}$$

$$E_L/h \approx 1.8 \text{ kHz}$$

$$\omega_Z/2\pi = 4.81 \text{ MHz}$$

$$\hbar\epsilon = 1.91 E_L$$

$$(f_x, f_y) = (50, 50) \text{ Hz}$$

Figure 9.2: Setup and level diagram for SO coupling experiments. **a.** A uniform bias field $\mathbf{B}_0 \mathbf{e}_y$ Zeeman splits the hyperfine sublevels of an $F = 1$ ^{87}Rb BEC, and a pair of Raman beams illuminate the atoms. **b.** The field strength B_0 generates a large quadratic Zeeman shift $\hbar\epsilon/E_L \gg 1$ which effectively decouples the third spin state. By adjusting the detuning δ we select the states $| -1 \rangle = |\downarrow\rangle$ and $| 0 \rangle = |\uparrow\rangle$ to form an effective two-level system.

9.2 THE RAMAN COUPLING SCHEME FOR AN EFFECTIVE SPIN-1/2 SYSTEM

We work with a BEC of ^{87}Rb atoms in the $F = 1$ ground state manifold, prepared in an optical dipole trap with frequencies $(f_x, f_y, f_z) = (50, 50, 140)$ Hz formed at the intersection of a pair of 1064 nm laser beams. A bias field $B_0 \mathbf{e}_y$ Zeeman shifts the $|m_F = \pm 1\rangle$ spin states by $\omega_Z/2\pi \approx 4.81$ MHz, and introduces a quadratic Zeeman shift $\epsilon/h \approx 3.39$ kHz.

Figure 9.2 shows the schematic of the experimental setup with which we realize SOC [9]. We optically dress a BEC with a pair of Raman lasers [5] with $\lambda = 804.1$ nm and propagating along $(\mathbf{e}_y \pm \mathbf{e}_x)/\sqrt{2}$, whose frequency difference was kept constant at $\Delta\omega_L/2\pi = 4.81$ MHz. The detuning from Raman resonance is defined as $\delta = \Delta\omega_L - \omega_Z$, and in experiment was controlled by small changes to B_0 . The Raman field is characterized by a coupling strength $\hbar\Omega_R$, which is experimentally controlled by the intensity of the lasers.

As discussed in Chapter 5, when expressed in the basis of states coupled by the Raman field $\{| -1, k_x + 2k_L \rangle, | 0, k_x \rangle, | +1, k_x - 2k_L \rangle\}$, in the frame rotating at $\Delta\omega_L$ and making the RWA, the combined kinetic energy and Raman interaction Hamiltonian becomes

$$\hat{H}_R = \begin{pmatrix} \frac{\hbar^2}{2m}(k_x + 2k_L)^2 + \hbar\delta & \hbar\Omega_R/2 & 0 \\ \hbar\Omega_R/2 & \frac{\hbar^2 k_x^2}{2m} - \hbar\epsilon & \hbar\Omega_R/2 \\ 0 & \hbar\Omega_R/2 & \frac{\hbar^2}{2m}(k_x - 2k_L)^2 - \hbar\delta \end{pmatrix}. \quad (9.2)$$

Figure 9.3 shows the eigenenergies of \hat{H}_R as a function of the quasimomentum k_x in different experimental regimes. The continuous, dashed and dot-dashed curves indicate the ground, first- and second-excited dressed energy levels: $E_0(k_x)$, $E_1(k_x)$ and $E_2(k_x)$ as a function of the quasimomen-

tum k_x . Absent the Raman dressing $\Omega_R = 0$, the Hamiltonian is diagonal in the bare spin-momentum states with eigenenergies lying on the principal diagonal of Eq. (9.2); these eigenenergies correspond to free spin- m_F particles with dispersions $\propto (k_x - 2m_F k_L)^2$ shifted by the Zeeman effect (dotted curves in Fig. 9.3).

9.3 SOC IN AN EFFECTIVE TWO-LEVEL SYSTEM

Under typical experimental conditions, where $\epsilon \ll \Omega_R$, the bare spin-momentum states are almost degenerate as shown in Fig. 9.3a. As the bias field is increased and ϵ is comparable to Ω_R , the energy of the bare state $|0, k_x\rangle$ significantly decreases as indicated in Fig. 9.3b. By making the detuning $|\delta| = \epsilon$, we can achieve the degeneracy for a pair of bare states; Fig. 9.3c shows the particular choice $\delta = -\epsilon$, where we create the degenerate pair $\{|-1, k_x + 2k_L\rangle, |0, k_x\rangle\}$. In contrast, the spin-momentum state $|+1, k_x - 2k_L\rangle$ becomes less energetically favorable, being away from the degenerate system by $\Delta E = +2\hbar\epsilon$. Figure 9.3d shows the small Raman coupling regime, where $\epsilon \gg \Omega_R$, for the degenerate pair at $\delta = -\epsilon$. [Note that as Ω_R increases one must tune δ to keep the minima degenerate (Fig. 9.4a).]

We prepare the atoms in the ground Raman dressed state, where they experience an effective energy-momentum dispersion relation given by $E_0(k_x)$. At the minima of the dispersion curves (open symbols in Figure 9.3), the group velocity $v_g = \partial E / \hbar \partial k_x$ is zero; a wave packet would be static and well behaved in such points. The dispersion relation $E_0(k_x)$ exhibits a single minimum in the large coupling limit, $\hbar\Omega_R \geq 4E_L$, but bifurcates in the small Raman coupling regime $\hbar\Omega_R < 4E_L$. This defines two important limits: the double well – or spin-orbit – limit in which the physics is best understood in terms of an effective “spin-1/2” system, where each dressed spin lives at a minimum with zero group velocity; and the single minimum – or vector potential – limit where we have “spinless bosons” with which have demonstrated artificial electric and magnetic fields for ultracold neutral atoms (see Chapter 5).

Summing up, to achieve an effective two-level system under SOC we require: a large quadratic Zeeman shift $\epsilon > 4E_L$; a detuning of comparable magnitude; and small Raman coupling strengths $\Omega_R < 4E_L$ for the lowest band $E_0(k_x)$ to exhibit double minima. I want to emphasize that we are exploring the same experimental configuration as in Chapter 5, with the same lasers but in a different Raman coupling regime, in a different basis of states.

Figure 9.4 shows the calculated eigenenergies of the coupling Hamiltonian, Eq. (9.2), in the limit where $\hbar\epsilon \gg 1E_L$. The lowest energy band $E(k_x)$ was calculated for various Raman coupling strengths, at $\epsilon = 3.8 E_R$, and the detuning δ was adjusted for the dressed spins $|\downarrow'\rangle$ and $|\uparrow'\rangle$ to be energetically degenerate.

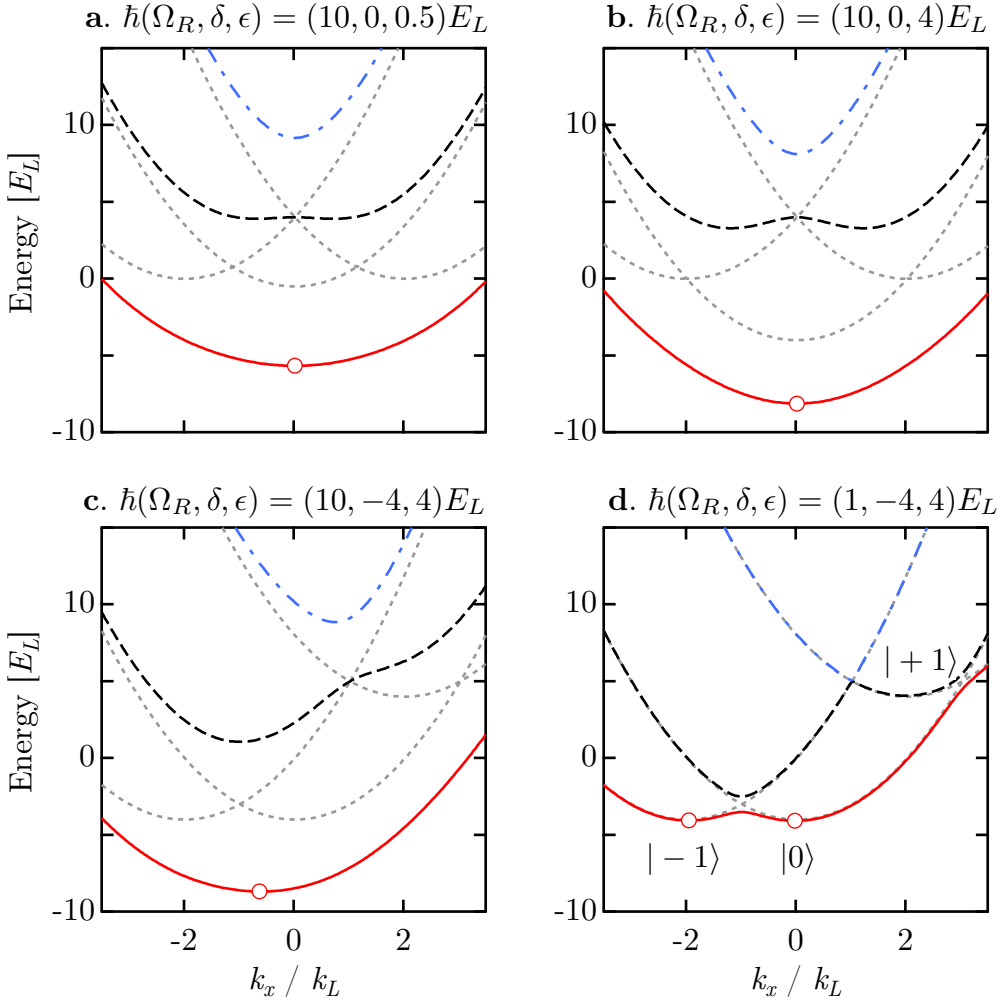


Figure 9.3: Dispersion relations in a Raman dressed system. Free particle spin-momentum states (dotted parabolae), coupled under Raman dressing [Eq. (9.2)], become new dispersion relations for dressed atoms. Our ultracold atomic sample is prepared at the energy minima (open symbols) of the lowest dressed state $E_0(k_x)$ (continuous curve), where the group velocity is $v_g = 0$. Panels a.-c. show the large coupling limit, $\hbar\Omega_R \geq 4E_L$, where $E_0(k_x)$ has a single minimum and the physics is described in terms of “spinless bosons”. Panel d. shows the regime where $E_0(k_x)$ develops two minima, which are populated by the spin states of an effective “spin-1/2” system, and SOC is most evident.

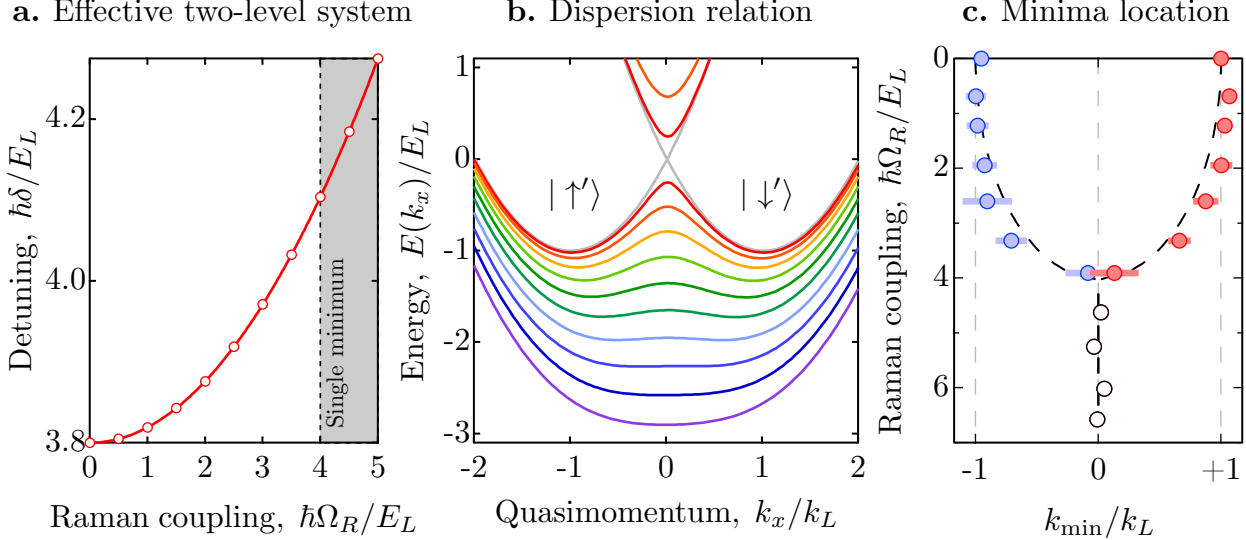


Figure 9.4: SOC Dispersion relation. **a.** For the dressed spins $|\uparrow'\rangle$ and $|\downarrow'\rangle$ to form a degenerate spin-1/2 SOC system, the detuning δ is adjusted quadratically with the Raman coupling strength Ω_R . **b.** Calculated eigenenergies of the SOC Hamiltonian Eq. (9.2) for the detuning indicated in **a**, $\hbar\epsilon = 3.8 E_L$ and $\Omega_R = 0$ (grey) to $5E_L$ (purple) in $0.5E_L$ steps. **c.** Measured minima locations as a function of Ω_R ; the dashed curves indicate the expected behavior. For $\Omega_R > 4 E_L$, the single-minimum dispersions correspond to those of spinless particles.

9.3.1 Two-level spin-orbit coupling Hamiltonian Having intuitively justified the effective decoupling of the highest energy bare state, we can restate the Raman coupling Hamiltonian in the reduced basis of pseudo-spin-1/2 states $\{|-1, k_x + k_L\rangle, |0, k_x - k_L\rangle\}$. Notice that the bare states in the reduced basis still differ in momentum by $2\hbar k_L$ but are centered symmetrically with respect to $k_x = 0$. I define an effective detuning $\delta' = \delta + \epsilon$ such that

$$\hat{H}_R = \begin{pmatrix} \frac{\hbar^2}{2m}(k_x + k_L)^2 + \hbar\delta'/2 & \hbar\Omega_R/2 \\ \hbar\Omega_R/2 & \frac{\hbar^2}{2m}(k_x - k_L)^2 - \hbar\delta'/2 \end{pmatrix}. \quad (9.3)$$

If expressed in terms of the 2×2 Pauli matrices $(\hat{\sigma}_x, \hat{\sigma}_y, \hat{\sigma}_z)$ and the 2×2 identity matrix $\hat{1}$, the effective two-level coupling Hamiltonian is

$$\hat{H}_R = \left(\frac{\hbar^2 k_x^2}{2m} + E_L \right) \hat{1} + \frac{\hbar\Omega_R}{2} \hat{\sigma}_x + \frac{\hbar\delta'}{2} \hat{\sigma}_z + 2 \frac{E_L}{k_L} k_x \hat{\sigma}_z, \quad (9.4)$$

where the last term corresponds to an equal mixture of Rashba and Dresselhaus SO coupling terms. Two pseudo-spin rotations¹ suffice to demonstrate the equivalence between the SOC term in

¹The explicit transformation is $\hat{\sigma}'_j = \hat{U}_z(\theta)\hat{U}_y(\theta)\hat{\sigma}_j\hat{U}_y^\dagger(\theta)\hat{U}_z^\dagger(\theta)$; where $\hat{U}_j(\theta)$ are the rotation operators for a spin-1/2 system, $\theta = \pi/2$ and $j = x, y, z$. These rotations give: $\hat{\sigma}'_x = \hat{\sigma}_z$, $\hat{\sigma}'_y = \hat{\sigma}_x$ and $\hat{\sigma}'_z = \hat{\sigma}_y$.

Eq. (9.4) and that in Eq. (9.1) with $\alpha = \beta$. The rotated Hamiltonian is

$$\hat{H}'_R = \left(\frac{\hbar^2 k_x^2}{2m} + E_L \right) \hat{1} + \frac{\hbar \Omega_R}{2} \hat{\sigma}_z + \frac{\hbar \delta'}{2} \hat{\sigma}_y + 2 \frac{E_L}{k_L} k_x \hat{\sigma}_y. \quad (9.5)$$

The spin-orbit coupling strength $\alpha = E_L/k_L \propto k_L$ is independent of the experimental parameters other than the geometry of the Raman beams, and reaches its maximum when the beams counter-propagate. Another method for tuning the SOC strength is by means of the modulation of Ω_R via intensity of the lasers [31], and will be discussed in Sec. 9.4.

The full Hamiltonian \hat{H} of the system includes the kinetic energy terms along the directions unaffected by the Raman beams, i.e. $[\hbar^2(k_y^2 + k_z^2)/2m]\hat{1}$; by adding this term and rearranging the resulting expression, we find that the gauge field we created $[\hat{\mathbf{A}} = (-k_L \hat{\sigma}_y, 0, 0)]$ is Abelian with trivially commuting components and

$$\hat{H} = \frac{\hbar^2(\mathbf{k} - \hat{\mathbf{A}})^2}{2m} + \frac{\hbar \Omega_R}{2} \hat{\sigma}_z + \frac{\hbar \delta'}{2} \hat{\sigma}_y. \quad (9.6)$$

9.4 TUNABLE SPIN-ORBIT COUPLING STRENGTH

Our experimental setup realizes SOC with uniform coupling strength $\alpha = E_L/k_L \propto k_L$, set by the spatial orientation of the Raman beams; α reaches its maximum value when the beams counter-propagate. Another method for tuning α is by temporally modulating Ω_R via the intensity of the lasers [31].

The SOC Hamiltonian in an $F = 1$ system can be expressed in the unmodulated case as:

$$\hat{H}_{\text{soc}} = \frac{\Omega_R}{\sqrt{2}} \hat{F}_x - \left(\delta - \frac{\hbar k_L}{m} k_x \right) \hat{F}_z + \left(\frac{\epsilon}{\hbar} + \frac{4E_L}{\hbar} \right) \hat{F}_z^2 + E_0 \hat{1}; \quad (9.7)$$

where $\hat{\mathbf{F}} = (\hat{F}_x, \hat{F}_y, \hat{F}_z)$ is the $F = 1$ angular momentum operator, whose entries are proportional to the spin-1 Pauli matrices; E_0 is a uniform energy offset and $\hat{1}$ is the 3×3 identity matrix.

Assuming that the Raman coupling strength is modulated in time as $\Omega_R = \Omega_0 + \Omega \cos(\omega t)$, the above expression is approximately

$$\hat{H}_{\text{soc}} \approx \frac{\Omega_0}{\sqrt{2}} \hat{F}_x - \left(\delta - \frac{\hbar k_L}{m} k_x \right) J_0(\Omega/\omega) \hat{F}_z + \left(\frac{\epsilon}{\hbar} + \frac{4E_L}{\hbar} \right) \left\{ J_0(2\Omega/\omega) \hat{F}_z^2 + (\hat{F}_x^2 - \hat{\mathbf{F}}^2) \left[\frac{J_0(2\Omega/\omega) - 1}{2} \right] \right\},$$

where we identify that the SOC strength varies as the zeroth order Bessel function² $J_0(\Omega/\omega)$. For a fixed modulation frequency ω , an increase in the Raman coupling strength Ω is reflected as a

²In this treatment it useful to keep in mind the Bessel identities: $f[\Omega \sin(\omega t)/\omega] = \sum_n J_n(\Omega/\omega) f(n\omega t)$; where f is either of the circular functions $f(x) = \sin(x), \cos(x)$; and the limits of the sum are $-\infty < n < +\infty$.

reduction of the SOC strength.

9.5 EXPERIMENTAL CHARACTERIZATION

The experiments described below consist of the demonstration of spin-orbit coupling in an effective “spin-1/2” bosonic system in the presence of Raman dressing; and the demonstration of the dynamical control on the SOC strength. All these projects share a common system preparation (described below), and each will be described within this section.

9.5.1 System preparation Our experiments start with a nearly pure ^{87}Rb BEC in the $|F=1, m_F=-1\rangle$ state in a crossed optical dipole trap³ with frequencies $(f_x, f_y, f_z) = (50, 50, 140)$ Hz. We prepare spin mixtures using an auxiliary rf field $B_{\text{rf}}\mathbf{e}_x$, characterized by an oscillating frequency $\omega_{\text{rf}}/2\pi = 4.81$ MHz and a Rabi frequency $\hbar\Omega_{\text{rf}} \approx 5E_L$, to realize a partial rapid passage to $\delta' = 0$ by ramping the magnitude of $B_0\mathbf{e}_y$ in 15 ms [5]. On resonance, the Zeeman splitting is $\omega_Z/2\pi = 4.81$ MHz and the quadratic Zeeman shift is $\hbar\epsilon = 1.91E_L$. We reduced $\hbar\Omega_{\text{rf}}$ to about $0.085E_L \ll \hbar\epsilon$ in 6 ms and suddenly turned off Ω_{rf} to project the system into a balanced spin superposition of $|\uparrow\rangle$ and $|\downarrow\rangle$. Finally, the Raman laser beams (Fig. 9.2a) were adiabatically turned on to their final coupling strength Ω_R in 70 ms, and we let the system equilibrate by holding this configuration during $t_h = 70$ ms.

9.5.2 Spin-orbit coupled BECs To measure the quasimomentum of the dressed spins $|\uparrow'\rangle$ and $|\downarrow'\rangle$, we relied on the preparation of balanced spin superpositions and on the precise control of the detuning δ to achieve double wells with degenerate energy minima.

We measured the location of the momentum minima as a function of the Raman coupling strength. We start with a BEC with equal population in each of the bare spins, and then adiabatically increased Ω_R . We ramped the detuning δ within the expected values (Fig. 9.4a) to achieve balanced populations in each well and then we made various measurements in the nominally balanced configuration. For detection we projected the dressed state into its bare spin-momentum components by suddenly turning off the Raman lasers and the dipole trap, then we absorption imaged the atoms after 30.1 ms time of flight (TOF). For $\hbar\Omega_R < 4E_L$, we observed two momentum components in each spin state, which correspond to the regime where the dispersion relation is a double well in momentum space. In contrast, for $\hbar\Omega_R \geq 4E_L$ both spin states were part of the same momentum family, i.e. they were located at the single minimum of the dispersion relation.

The data in Fig. 9.4c is the result of averaging over at least 10 realizations; the fact that we observe a correlation between spin and momentum, demonstrates the existence of SOC in an effective “spin-1/2” system under Raman dressing; furthermore we observe good agreement with

³For these experiments the 0th order dipole beam had 1/e²-radii of $w_0 \approx 65$ μm; while the 1st order dipole beam had an elliptical profile with 1/e² radii of $w_1 \approx 120$ μm and $w_{1z} \approx 50$ μm.

the expected behavior (dashed curves). The deviation from the expected behavior is both due to interactions between the effective spins (Sec. 10.1.1) and magnetic field noise (Sec. 10.3.2).

A complementary approach to realize the above measurement is ramping the Raman coupling strength from $\hbar\Omega_R > 4E_L$ to zero by maintaining balanced populations once we reached the double well regime. This method is particularly challenging since we need to guarantee that the detuning δ at each point in the decreasing ramp of the Raman coupling is properly matched to achieve the balanced condition. Similar results were measured, but the population balance was not maintained.

9.5.3 Tunable spin-orbit coupling strength The experimental setup for the tunable SOC experiments is slightly different from the one shown in Fig. 9.2a. The Raman lasers still propagate along $\mathbf{e}_y \pm \mathbf{e}_x$, but their wavelength is set at $\lambda = 790.1$ nm ($1E_L/h = 1.835$ kHz). Since the nature of the coils generating the fields in the xy plane limited the amplitude of the field to $B_0 \approx 7.2$ G, we switched to a larger field this time along \mathbf{e}_z to reach a Zeeman splitting $\omega_Z = 2\pi \times 15$ MHz ($B_0 = 21.42$ G), and a quadratic Zeeman shift $\hbar\epsilon = 17.96E_L$. In this regime, the presence of the third hyperfine state $|m_F = +1\rangle$ is negligible. The frequency difference between the Raman lasers was kept constant at $\Delta\omega_L/2\pi = 15$ MHz.

Our experimental procedure is very similar to that described in Sec. 9.5.1. We start with a BEC in the $F = 1$ ground state manifold, prepared in a pure optical dipole trap with frequencies⁴ $(f_x, f_y) = (31.6, 37)$ Hz formed at the intersection of a pair of 1064 nm laser beams. Prior to dressing the atoms with the Raman field, our initial state was either a balanced spin mixture or a single spin component:

Spin mixture: We prepare spin mixtures using an auxiliary rf field $B_{\text{rf}}\mathbf{e}_x$, with oscillating frequency $\omega_{\text{rf}}/2\pi = 15$ MHz and a Rabi frequency⁵ $\hbar\Omega_{\text{rf}} \approx 2.5 E_L$, to realize a adiabatic rapid passage to $\delta' = 0$ by ramping the magnitude of $B_0\mathbf{e}_y$ in 15 ms [5]. We reduced Ω_{rf} to about $0.04E_L \ll \hbar\epsilon$ in 6 ms and suddenly turned off the rf-field to project the system into a balanced spin superposition of $|\uparrow\rangle$ and $|\downarrow\rangle$.

Single spin state: Because our BEC starts in the $|\downarrow\rangle$ spin state, we ramp the Zeeman field to 1 kHz below resonance ($\omega_Z/2\pi = 15$ MHz) and start the modulation. We observe unwanted population of the $|\uparrow\rangle$ state, probably due to magnetic-field-noise-induced coupling to the $|\uparrow\rangle$ state, since the double well's barrier is so small. To start in $|\uparrow\rangle$, a rapid passage with starting with the rf frequency ν_{rf} ($0 < \delta < \epsilon$) should suffice.

⁴Our dipole trap was modified from $(f_x, f_y) = (73.2, 28.4)$ Hz to $(f_x, f_y) = (31.6, 37)$ Hz to avoid having trap frequencies close to the 60 Hz frequency of the power line (under Raman dressing the effective mass along \mathbf{e}_x is such that the oscillating frequency in the trap is close to 60 Hz).

⁵The rf-coupling strength at this higher frequency was slightly attenuated due to the bandwidth of the rf-amplifier and the antenna design.

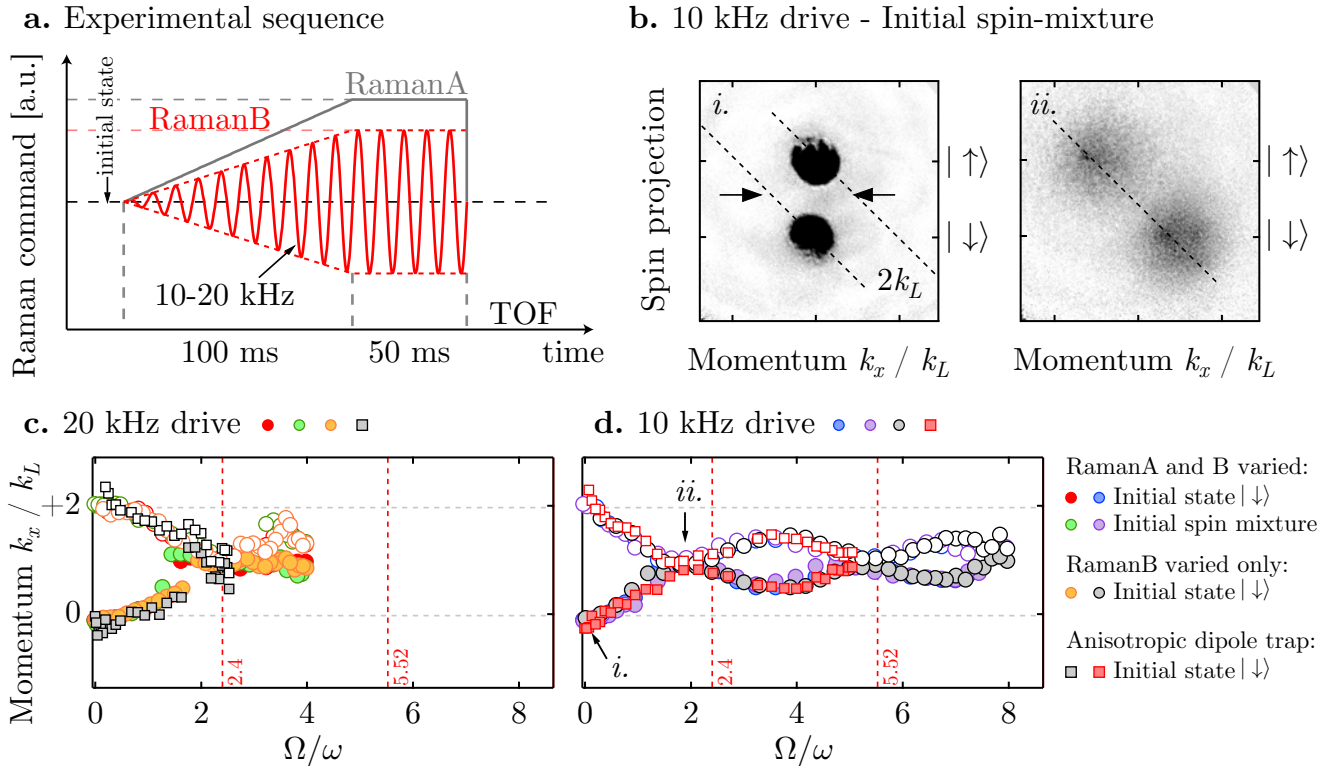


Figure 9.5: Tunable spin-orbit coupling. **a.** Experimental sequence for modulating the intensity of RamanB. **b.** Density distribution after TOF for a $\omega/2\pi = 10$ kHz drive at different coupling strengths. **c.-d.** Quasimomentum as a function of Raman coupling strength measured from TOF images. The open (closed) symbols represent $|\uparrow\rangle$ ($|\downarrow\rangle$) atoms. We observe the suppression of SOC in agreement with the first and second roots of $J_0(\Omega/\omega)$ (indicated by vertical dashed lines). This behavior was reproduced with different initial states, loading schemes and in different dipole traps.

We label the Raman lasers as RamanA and RamanB; each was ramped from zero to its final coupling strength as indicated in Fig. 9.5a. Only the intensity of RamanB is modulated, using a sinusoidal ramp with zero offset, turned on under a linear ramp envelope in 100 ms. The atoms are held in the Raman-dressed configuration for 50ms, after which all potentials are snapped-off and the atomic distributions are allowed to expand for 34.45 ms TOF, during part of which a Stern-Gerlach field separates the spin components along \mathbf{e}_y (Fig. 9.5b).

Our cold atom systems were driven at $\omega/2\pi = 10$ and 20 kHz. Fig. 9.5b shows the spin momentum distributions at $\Omega_R = 0$ and $\hbar\Omega_R \approx 10E_L$ driven at 10 kHz. Figure 9.5c,d summarizes our measurements and shows the excellent agreement among various data sets whose preparation is either:

- a. Initial state: $|\downarrow\rangle$ in isotropic trap ($f_x, f_y) = (31.6, 37)$ Hz. We scanned the final intensities of both Raman beams simultaneously to set Ω (red and blue circles). RamanA was ramped to a fixed final value, and we scanned the final intensity of RamanB to vary Ω (yellow and gray circles);
- b. Initial state: balanced spin mixture in isotropic trap. Both final intensities varied together (purple and green circles); and
- c. Initial state: $|\downarrow\rangle$ in anisotropic trap ($f_x, f_y) = (73.2, 28.4)$ Hz. Both final intensities varied together (red and gray squares).

Figure 9.5c,d demonstrates tunable SOC as a function of Ω_R . For systems driven at 20 kHz, the SOC strength is fully tunable within $0 < \hbar\Omega_R < 20E_L$; we observed the scaled interval $0 < \hbar\Omega_R < 10E_L$ when the system was driven at 10 kHz, as expected from the $J_0(\Omega/\omega)$ dependence on the SOC term of the Hamiltonian. As seen by the creation of a large thermal component (Fig. 9.5b-ii), a large amount of heating was present in the driven system; this did not prevent the observation of tunable SOC, but should be further investigated.

9.6 CONCLUSIONS

Being an essential ingredient of the spin Hall effect and topological insulators, SOC is an important phenomenon to be investigated in ultracold atom systems; current experimental efforts in our group have recently demonstrated the spin-Hall effect [10] in a similar scheme as discussed in this chapter. If experimentally controlled, SOC could trigger the development of spintronics devices. Here we exploited extreme experimental control on ultracold atoms, and simulated spin-orbit coupling in a “spin-1/2” bosonic system, a physical system with no analog in condensed matter.

Spin-orbit coupled Fermi gases have successfully been demonstrated [32, 33], and promise to realize important physics phenomena such as topological insulators in fermionic neutral atom systems. The course of action of this experiment is not only to move on to fermionic systems, but also to further investigate the possibility of engineering a lattice potential to study the physics of spin-1/2 bosons in spin-orbit-coupled flat bands [136].

CHAPTER 10

CONTROL OF INTERACTIONS WITH ARTIFICIAL GAUGE FIELDS

The control of interactions between atoms is a remarkable feature in ultracold quantum gases. The interacting term in the Hamiltonian of ultracold atoms can be engineered either by the inclusion of lattice potentials, or by the use of Feshbach resonances (both magnetic and optical) [43]. This chapter describes the modification of interactions in ^{87}Rb BECs as a consequence of Raman dressing.

Firstly, we focus on the SOC limit introduced in Chapter 9, with Raman coupling strengths $\hbar\Omega_R < 4E_L$, and demonstrate that the SOC interaction drives a quantum phase transition in our spinor system from a spatially miscible spin superposition to a spatially phase-separated state as a function of the Raman coupling strength.

Secondly, we study colliding BECs under Raman dressing and characterize their scattering products in the limit where $\hbar\Omega_R > 4E_L$. We observe not only s - but also d - and g -wave contributions, and study their dependence on Ω_R . The analogous effect in fermionic systems would be to reach p -wave contributions, essential to the observation of Majorana fermions as proposed in Refs. [76, 137].

10.1 A NOVEL TOOL FOR TUNING SPINOR INTERACTIONS WITH LIGHT

Spinor condensates were first experimentally realized in a magnetic trap, by mixing two low-field seeking spin states of ^{87}Rb [138]. It was not until spin-independent optical traps were implemented [139] that the spin degree of freedom could truly be considered a free parameter of the system [140].

Here I consider low energy, spin preserving, contact interactions in a mixture of two spin components of the $F = 1$ ground state manifold of ^{87}Rb . The interaction potential between two spin-1 atoms is given by [140]

$$V_S = c_0 + c_2 \mathbf{F}_1 \cdot \mathbf{F}_2 \hbar^{-2}; \quad (10.1)$$

where $c_0 = (g_0 + 2g_2)/3$ is the spin-independent term and $c_2 = (g_2 - g_0)/3$ characterizes spin-spin interactions; these coefficients are defined in terms of the interaction strengths $g_F = 4\pi\hbar^2a_F/m$, which in turn depend on the s -wave scattering length a_F . The nature of the spin mixture ground state depends mostly on c_2 , the spin-spin interaction coefficient. If $c_2 > 0$, the interaction energy is

minimized by having the spins aligned anti-parallel to each other, which corresponds to the anti-ferromagnetic or polar configuration. If $c_2 < 0$, the energy is minimized when the spins are aligned parallel and the system is in ferromagnetic state.

The interaction Hamiltonian \hat{H}_{int} can be expressed in terms of the Clebsch-Gordan coefficients as [140]

$$\hat{H}_{\text{int}} = \frac{1}{2} \int d^3r \sum_{F=0}^{2f} g_F \sum_{m_F=-F}^F \hat{O}_{F,m_F}^\dagger \hat{O}_{F,m_F}; \quad (10.2)$$

where

$$\hat{O}_{F,m_F} = \sum_{m_1, m_2} \langle F, m_F | F_1 m_1; F_2 m_2 \rangle \hat{\psi}_{m_1} \hat{\psi}_{m_2}; \quad (10.3)$$

and $\hat{\psi}_{m_F}(\mathbf{r})$ is the field operator for the annihilation of an atom in the state $|F_{1,2} = 1, m_{1,2}\rangle$ at the position \mathbf{r} . Here we restrict ourselves not only to the $F = 1$ manifold¹, but to the effective two-level system composed by the states $|\downarrow\rangle = |m_F = -1\rangle$ and $|\uparrow\rangle = |m_F = 0\rangle$ (see Chapter 9); the effective Hamiltonian is reduced to

$$\hat{H}_{\text{int}} = \frac{1}{2} \int d^3r \left[c_0 \hat{\psi}_\uparrow^\dagger \hat{\psi}_\uparrow^\dagger \hat{\psi}_\uparrow \hat{\psi}_\uparrow + (c_0 + c_2) \hat{\psi}_\downarrow^\dagger \hat{\psi}_\downarrow^\dagger \hat{\psi}_\downarrow \hat{\psi}_\downarrow + 2(c_0 + c_2) \hat{\psi}_\downarrow^\dagger \hat{\psi}_\uparrow^\dagger \hat{\psi}_\uparrow \hat{\psi}_\downarrow \right]. \quad (10.4)$$

Using normal order and introducing the density of each spinor component as $\hat{\psi}_{m_F}^\dagger \hat{\psi}_{m_F} = \hat{\rho}_{m_F}$, we obtain

$$\begin{aligned} \hat{H}_{\text{int}} &= \frac{1}{2} : \int d^3r \left[c_0 \hat{\rho}_\uparrow^2 + (c_0 + c_2) \hat{\rho}_\downarrow^2 + 2(c_0 + c_2) \hat{\rho}_\downarrow \hat{\rho}_\uparrow \right] :, \\ \hat{H}_{\text{int}} &= \frac{1}{2} : \int d^3r \left[\left(c_0 + \frac{c_2}{2} \right) (\hat{\rho}_\downarrow + \hat{\rho}_\uparrow)^2 + \frac{c_2}{2} (\hat{\rho}_\downarrow^2 - \hat{\rho}_\uparrow^2) + c_2 \hat{\rho}_\downarrow \hat{\rho}_\uparrow \right] :. \end{aligned} \quad (10.5)$$

The first term indicates that the spin independent interaction described by $(c_0 + c_2/2)$, depends on the total density of the system. In contrast, the spin-dependent interaction described by c_2 depends on which state the system is prepared, see e.g. the last term. For ^{87}Rb atoms in $F=1$, the interaction coefficients are $c_0/\hbar = 7.79 \times 10^{-12}$ Hz cm³ and $c_2/\hbar = -3.61 \times 10^{-14}$ Hz cm³; thus for the two-component mixture, the energy is minimized when both distributions spatially overlap: the ground state is miscible [72].

10.1.1 Interaction between the optically dressed spins Under the SO interaction introduced in Chapter 9, the effective interaction between the dressed spin states $|\downarrow'\rangle$ and $|\uparrow'\rangle$ is modified. When the interaction Hamiltonian is expressed in the basis of dressed states, a new spin-dependent interaction term emerges whose strength is proportional to the Raman lasers intensity

¹Refer to Appendix A for the specific values of the Clebsch-Gordan coefficients for the addition identical $F = 1$ angular momentum operators.

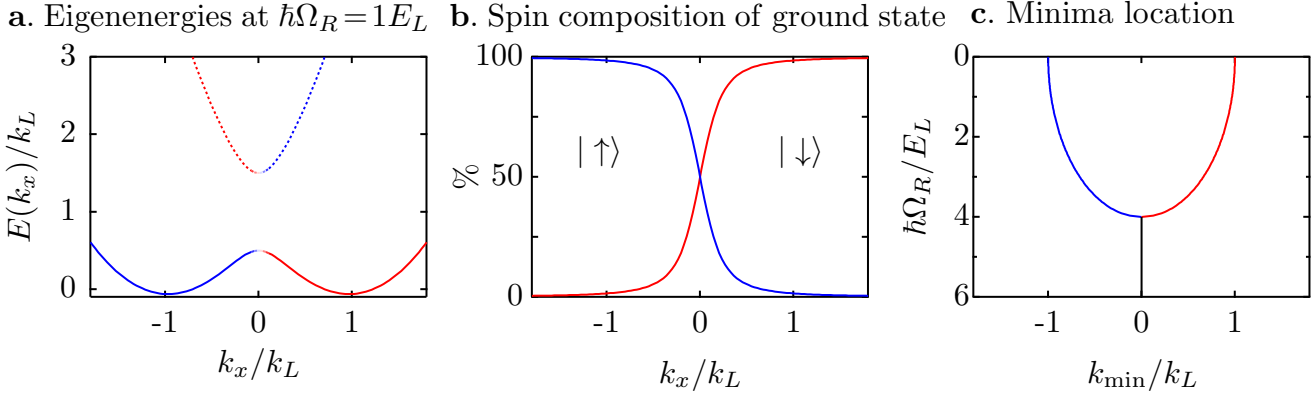


Figure 10.1: Calculated spin composition of effective two-level system under SOC. **a.** Eigenenergies of the Raman coupling Hamiltonian in the SOC limit at $\hbar\Omega_R = 1E_L$. The lowest energy states (continuous curve) and the excited states (dotted curve) are colored according to their spin composition: blue (red) indicates bare spin $|\uparrow\rangle$ ($|\downarrow\rangle$). **b.** Spin composition of the ground state at $\hbar\Omega_R=1E_L$. **c.** Calculated minima location as a function of Raman coupling strength Ω_R .

squared. By adjusting the strength of the Raman induced interaction term, we drive a quantum phase transition from a spatially mixed to a spatially separated state in a ^{87}Rb spin mixture.

The eigenvalues and eigenvectors of the spin-orbit Hamiltonian \hat{H}_R given by Eq. (9.3) are²

$$E_{\pm}(k_x) = 1 + k_x^2 \pm \frac{1}{2} \sqrt{(\delta' + 4k_x)^2 + \Omega_R^2}; \quad (10.6)$$

$$|\psi_{\pm}(k_x)\rangle = \frac{1}{\sqrt{2} [(4k_x + \delta')^2 + \Omega_R^2]^{1/4}} \begin{pmatrix} \pm\{(4k_x + \delta')^2 + \Omega_R^2\}^{1/2} \pm (4k_x + \delta') \}^{1/2} \\ \Omega_R \{(4k_x + \delta')^2 + \Omega_R^2\}^{1/2} \pm (4k_x + \delta') \}^{-1/2} \end{pmatrix}. \quad (10.7)$$

I will focus on the interaction between the particles occupying the minima of the lowest energy dispersion relation $E_-(k_x)$, shown in Fig. 10.1a. The eigenstates at these points are composed mostly of a single spin species, but have a small admixture of their Raman coupled counterpart (Fig. 10.1b). To obtain the minima locations of the lowest band, we compute $\partial E_-(k_x)/\partial k_x = 0$, which gives

$$k_x = \frac{\delta' + 4k_x}{\sqrt{(\delta' + 4k_x)^2 + \Omega_R^2}}. \quad (10.8)$$

For energetically degenerate double wells ($\delta' = 0$) the minima are located at $k_{\uparrow,\downarrow} = \mp\sqrt{4^2 - \Omega_R^2}/4$, this behavior is indicated in Fig. 10.1c. For Raman coupling strengths $\Omega_R \leq 4$ the dispersion relation presents a single minimum, and the system is described in terms of spinless particles. We are interested in studying the behavior in the small Raman coupling limit $\Omega_R < 4$, where SOC is the most suitable description.

²In this section, to obtain a simplified expression of the eigenenergies and eigenvalues, I have redefined all the parameters in the Hamiltonian to be dimensionless; i.e. $k_x/k_L \rightarrow k_x$, $\hbar\delta'/E_L \rightarrow \delta'$ and $\hbar\Omega_R/E_L \rightarrow \Omega_R$.

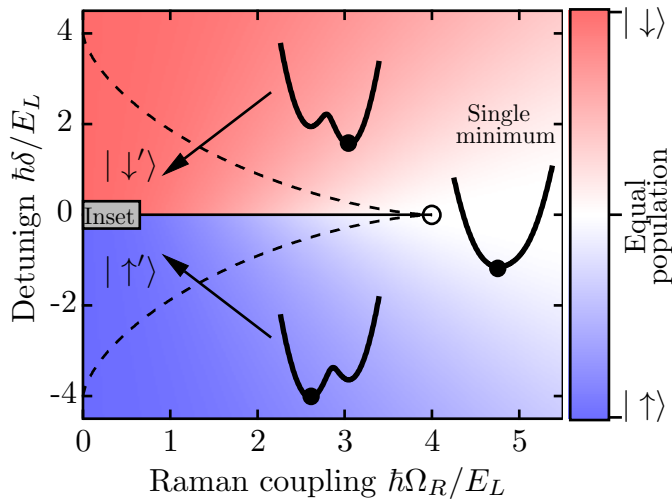
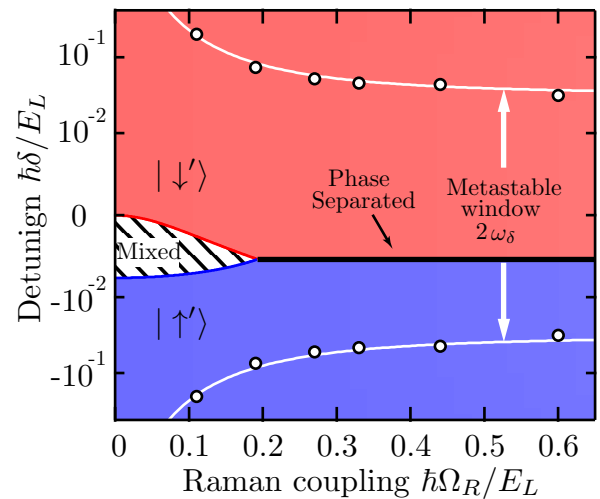
a. Mean field phase diagram**b.** Phase diagram, inset

Figure 10.2: Quantum phase transition from mixed to phase separated. **a.** Calculated mean-field phase diagram for an infinite and homogeneous system as a function of the experimental parameters Ω and δ . The dashed curves delimit the regions where the dispersion relation has two minima. **b.** Zoom-in to the inset indicated in (a.). For a metastable window of detuning both spin components coexisted in the double well.

The eigenstates of the lowest band which occupy the minima of the effective dispersion [located at $k_{\uparrow\downarrow} = \mp 1$, in the limit of weak Raman coupling ($\Omega_R \ll 4$)] are given by

$$|\uparrow'\rangle \approx \begin{pmatrix} 1 - \Omega_R^2/128 \\ -\Omega_R/8 \end{pmatrix} \quad \text{and} \quad |\downarrow'\rangle \approx \begin{pmatrix} -\Omega_R/8 \\ 1 - \Omega_R^2/128 \end{pmatrix}; \quad (10.9)$$

this is, they have a large component from one bare spin, and a small contribution with amplitude $\gamma = \Omega_R/8$. In the basis of bare spin-momentum states coupled by the Raman field, this mixture can be expressed as

$$|\uparrow', k\rangle = |\uparrow, k\rangle - \gamma |\downarrow, k+2\rangle \quad \text{and} \quad |\downarrow', k\rangle = |\downarrow, k\rangle - \gamma |\uparrow, k-2\rangle. \quad (10.10)$$

Inverting the unitary transformation between the dressed and the bare basis, allows to re-express the eigenstates in second quantization form, with creation and annihilation operators including the appropriate phases corresponding to the momentum transfer in real space

$$\hat{\psi}_\uparrow(r) = \hat{\psi}_{\uparrow'}(r) + \gamma e^{2ik_L x} \hat{\psi}_{\downarrow'}(r) \quad \text{and} \quad \hat{\psi}_\downarrow(r) = \hat{\psi}_{\downarrow'}(r) + \gamma e^{-2ik_L x} \hat{\psi}_{\uparrow'}(r). \quad (10.11)$$

Starting from the above field operators we obtain the modified interaction Hamiltonian

$$H_{\text{int}} = \frac{1}{2} \int d^3\mathbf{r} \left[\left(c_0 + \frac{c_2}{2} \right) (\hat{\rho}'_{-1} + \hat{\rho}'_0)^2 + \frac{c_2}{2} (\hat{\rho}'_{-1}^2 - \hat{\rho}'_0^2) + (c_2 + c'_{-1,0}) \hat{\rho}'_{-1} \hat{\rho}'_0 \right]; \quad (10.12)$$

where $c'_{-1,0} \approx 8c_0\gamma^2$. In the presence of Raman coupling, the induced interaction term modifies the nature of the ground state, and drives a phase transition from miscible ($\Omega_R = 0$) to phase separated for a Raman coupling strength above a critical value $\Omega_c = \sqrt{-8c_2/c_0}E_L \approx 0.19E_L$ [9].

10.1.2 Mean-field phase diagram The phase diagram of the Raman coupled system (Fig. 10.2) shows the configurations that minimize the energy of the system in different parameter regimes.

Single component phase. In the SOC limit ($\hbar\Omega_R < 4E_L$) the dispersion relation is a double-well, whose energy minima are energetically degenerate when carefully balanced by the detuning (Fig. 9.4). For non-zero detuning, the double well is unbalanced; the particles tend to condense in the well with lowest energy unless there is a competing spin-dependent interaction energy which can overcome δ , thus the system is mostly composed of a single dressed spin. This behavior is indicated in the regions labeled as $|\downarrow'\rangle$ and $|\uparrow'\rangle$ in Fig. 10.2a,b.

Two component phase. Still considering the SOC regime ($\hbar\Omega_R < 4E_L$), the system can be a mixture of the two dressed spins only for a small window of detuning (see Fig. 10.4). In the absence of Raman dressing, the ground state is miscible; the interaction term characterized by $c'_{-1,0}$ in Eq. (10.12) modifies the state of minimum energy such that beyond the critical coupling strength Ω_c , the mixture of spins avoids being spatially overlapping and the ground state is phase separated. In the large Raman coupling limit ($\hbar\Omega_R \geq 4E_L$), the atoms condense into the single minimum of the lowest energy eigenstate and the system is a superposition of dressed spins whose dispersion relation is that of a free particle with effective mass $m^* = \hbar^2[d^2E_-(k_x)/dk_x^2]^{-1}$.

10.2 SYNTHETIC PARTIAL WAVES IN ULTRACOLD ATOMIC COLLISIONS

An interesting signature of Raman dressing in the vector potential limit $\hbar\Omega_R > 4E_L$, is the modification of the effective interaction between colliding BECs. The theory of scattering is well understood by treating the wavefunction of the scattered particle in the formalism of partial waves; in particular, ultracold collisions are characterized by the lowest energy and angular momentum scattering partial wave, namely they experience short-range *s*-wave collisions (see Chapter 2).

Collisions between Raman dressed BECs can be understood in terms of higher order partial waves when expressed in terms of the dressed basis (a similar treatment to the spinor case described in Sec. 10.1.1); where part of the *s*-wave interactions redistributes in the form of higher order partial waves. It is important to highlight that for the bosonic wavefunction to remain symmetric under

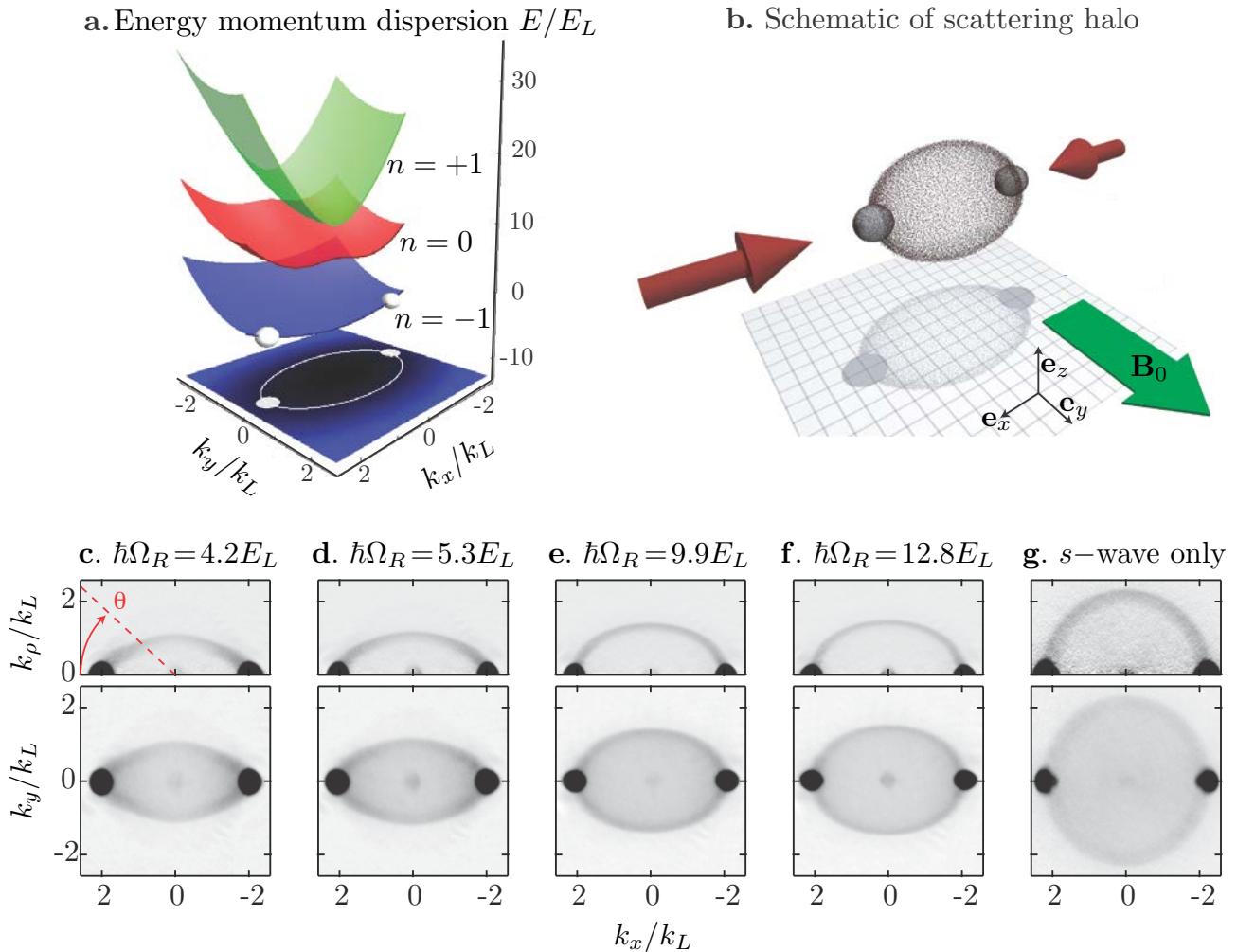


Figure 10.3: Synthetic higher order partial waves in ultracold atomic collisions. **a.** Schematic of the collisional scheme, where dressed BECs in the lowest energy band are set to collide. **b.** Schematic of the formation of the scattering shell after the collision and its projection in the imaging plane. **c.-f.** (bottom panels) Scattering halos imaged after TOF. The inhomogeneity of the distribution of the scattering products in the scattering “shells” (top panels) is a signature of beyond s -wave collisions for Raman dressed BECs. **g.** Bare BECs display homogenous s wave scattering as expected.

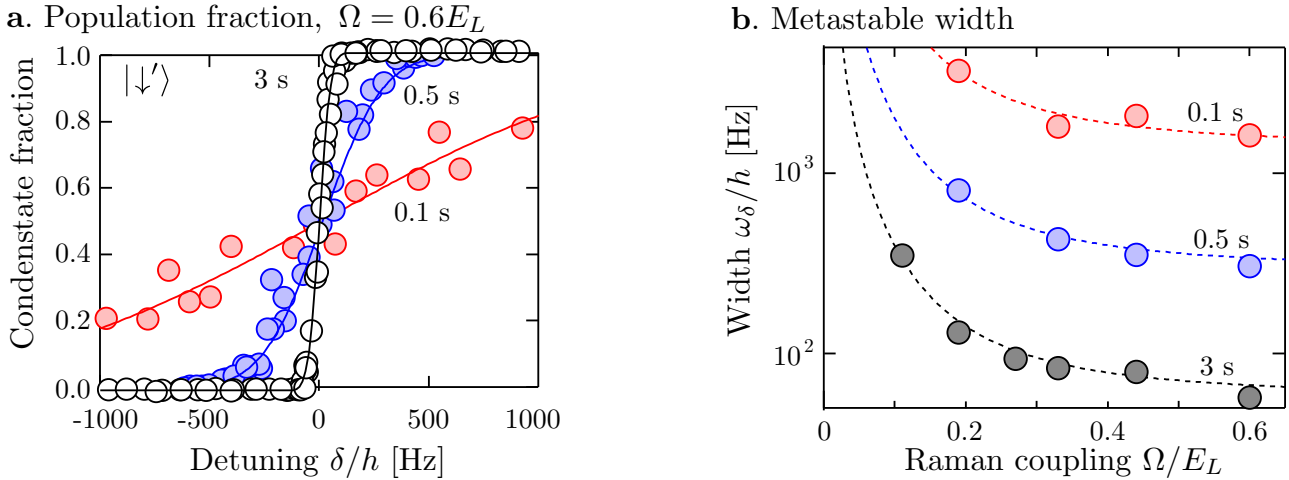


Figure 10.4: Metastable detuning width for two component phase. **a.** Measured condensate fraction in the dressed spin state $|\downarrow'\rangle$ as a function of detuning for different hold times t_h . We fit $f_{\downarrow'}$ vs δ using the error function (solid curves) to obtain the detuning width ω_δ , plotted in (b.) as a function of the coupling strength Ω . The width in detuning ω_δ within which both dressed spins coexist decreases as the system is allowed to equilibrate for longer times.

particle exchange, only higher order partial waves with even parity are observed, namely d - and g -wave scattering are expected.

The range of the effective interaction is screened beyond that of van der Waals interactions (see Chapter 2). The nature of the interactions is unchanged, but rather the structure of the collisional products exhibits higher order partial waves.

10.3 EXPERIMENTAL CHARACTERIZATION

The experiments described below consist of the observation of modified interactions between Raman-dressed atoms in the $F=1$ ground state manifold of ^{87}Rb as a function of the Raman coupling strength. We measured a miscible-immiscible phase transition and characterized the scattering products of colliding BECs under Raman dressing.

10.3.1 Phase transition from miscible to phase separated The preparation of BECs for the miscible-immiscible phase transition phase transition experiments is identical to that described in Sec. 9.5.1; the experimental setup and energy scales are indicated in Fig. 9.2.

We measured the location of the transition from spatially mixed to spatially separated as a function of the Raman coupling strength Ω , by quantifying the amount of spatial separation s of the dressed-spin density distributions.

We prepared a balanced spin-momentum superposition as described above, and held the final configuration for t_h up to 3 s. To determine the detuning window within which both spin states coexisted, we ramped the final detuning and monitored the fraction of the condensed atoms in just

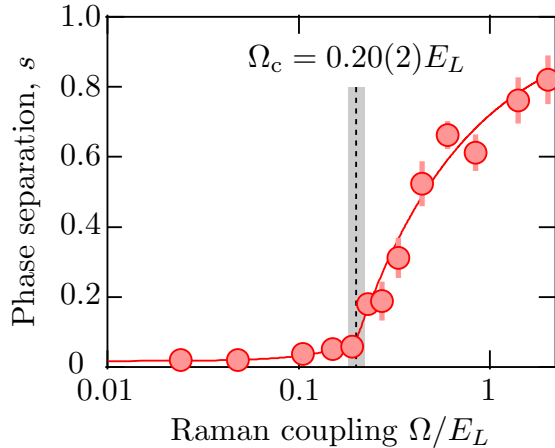
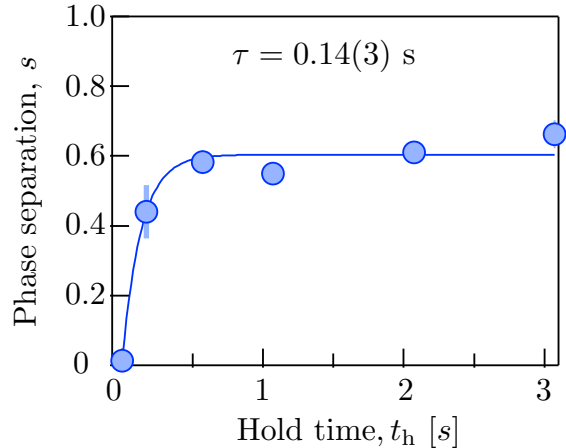
a. Miscibility after 3 s hold**b.** Dynamics at $\Omega = 0.6E_L$ 

Figure 10.5: Measuring the quantum phase transition. **a.** Measured degree of phase separation s as a function of Ω across the phase transition from miscible to phase separated. We identify the transition point by fitting the data to a slowly increasing function below Ω_c , and the power law $1 - (\Omega/\Omega_c)^{-a}$; where $a=0.75(5)$.

$| \downarrow \rangle$ (Fig. 10.4a). These measurements define a metastable window where the transition from phase mixed to phase separated is investigated (Fig. 10.4b).

For the longest hold time $t_h = 3$ s, we measured the miscibility of the dressed system from their spatial density profiles $n_{\uparrow',\downarrow'}$ after TOF. The detuning was kept nominally on resonance by maintaining an equal atom number in each well. We define the degree of phase separation to be proportional to the product of the density distributions

$$s = 1 - \frac{\langle n_{\uparrow'} n_{\downarrow'} \rangle}{\sqrt{\langle n_{\uparrow'}^2 \rangle \langle n_{\downarrow'}^2 \rangle}}; \quad (10.13)$$

where $\langle \dots \rangle$ indicates the spatial average over a single image. A miscible ground state corresponds to $n_{\uparrow'} = n_{\downarrow'}$, i.e. $s = 0$; for a phase-separated state $n_{\uparrow'} n_{\downarrow'} = 0$ and we obtain $s = 1$.

Figure 10.5 shows the measured phase separation s as a function of Ω . The sudden increase in the signal indicates a quantum phase transition at the critical coupling strength $\Omega_c = 0.02(2)E_L$, driven by the Raman induced effective interaction.

Due to finite size effects, the transition is not sharp, as it would be in the case of an infinite and homogeneous system. Our system can be considered as homogeneous as long as its size vastly exceeds the spin-healing length³[141] $\xi_s = \sqrt{\hbar^2/2m|c_2 + c'_{\uparrow',\downarrow'}|n}$, where n is the local density. The spin healing length sets the spatial extent of the boundary between the phase-separated spins; since

³The spin-healing length is the length scale of spatial variations in the density distribution by the spin-dependent interactions.

a. Miscible to immiscible transition

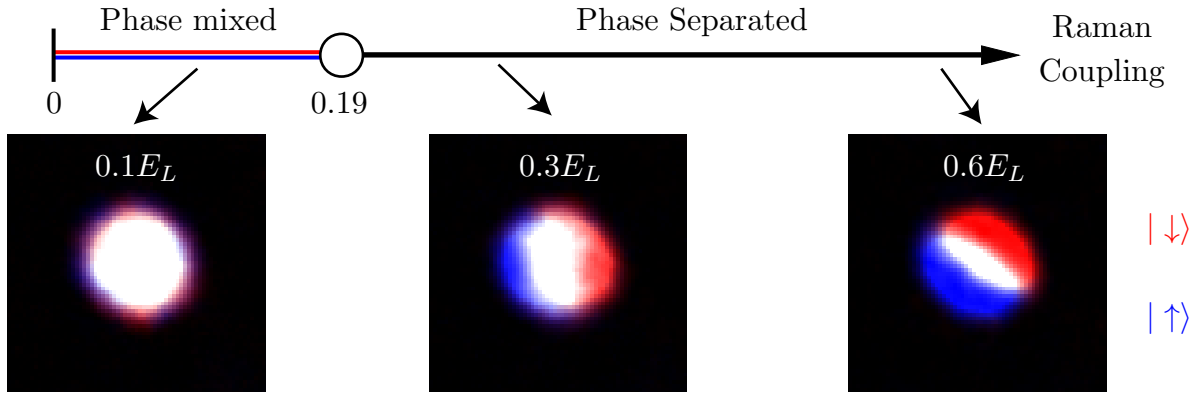


Figure 10.6: Spatial density profiles across the phase transition. **a.** Spatial density profiles, mapped from the dressed into the base spin states, indicating the degree of phase separation as a function of the coupling strength. The spin populations in all images are nominally balanced within the metastable region of detuning. The spatial overlapping of the spin distributions is colored white.

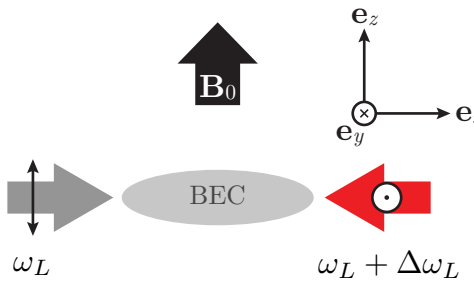
$c'_{\uparrow',\downarrow'} \propto \Omega_R^2$ the spin healing length is reduced for increasing $\Omega_R > \Omega_c$, and there is an enhancement in the phase separation parameter s as shown in Figure 10.5a.

The time scale associated with the phase separation is determined by measuring s as a function of hold time t_h above the phase transition, and fitting the data to an exponential as shown in Fig. 10.5b. The fit's time constant $\tau = 0.14(3)$ s indicates that the system had reached equilibrium at $t_h = 3$ s hold time. (Although the domain pattern did change with time, the degree of separation saturated).

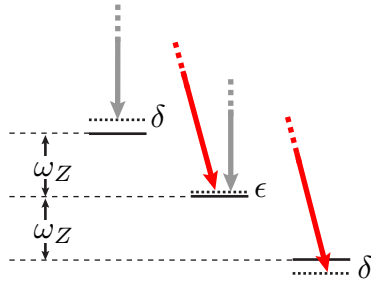
10.3.2 Canceling magnetic field noise. To get a sense of the resolution and the tolerance on magnetic field noise required for this task, let us revisit Fig. 9.4. The energy scale that imposes the lower bound to magnetic field variations is the height of the barrier ΔE between the double wells, whose dependence on Ω_R is approximately $\Delta E = 0.062(1)[(\Omega_R/E_L) - 4]^2$ from a fit to the calculated values. At a coupling strength 10% below the transition to single minimum, the barrier height is only $0.1E_L \approx h \times 17.7$ Hz.

Our experiment is mostly sensitive to 60 Hz noise from the power line, but due to the small energy scales associated with our SOC experiments, stray magnetic field gradients are also an issue. We characterize ambient noise as described in section 4.9, and mostly minimize it by identifying and reducing (or if possible eliminating) the noise sources. Typical noise levels are observed as changes in the detuning with standard deviation $\hbar\Delta\delta/2\pi \approx 110$ Hz; thus measuring the minima location of the double well close to the transition to single minimum exhibits a larger uncertainty (Fig. 9.4c). Additionally, we cancelled stray gradients in the xy plane with two pairs of anti-Helmholtz coils, aligned along $\mathbf{e}_x + \mathbf{e}_y$ and $\mathbf{e}_x - \mathbf{e}_y$ to 0.7 Hz/ μm .

a. Experimental setup



b. Level diagram



c. Energy scales

$$\begin{aligned} \lambda &= 791 \text{ nm} \\ E_L/h &\approx 3.7 \text{ kHz} \\ \omega_Z/2\pi &= 3.25 \text{ MHz} \\ \hbar\epsilon &= 0.42 E_L \\ (f_x, f_z) &= (13, 45) \text{ Hz} \end{aligned}$$

Figure 10.7: Setup and level diagram for collision experiments. **a.** A uniform bias field \mathbf{B}_0 Zeeman splits the energy levels in ^{87}Rb 's $F=1$ manifold, while a pair of counter propagating Raman beams and illuminate an $m_F=-1$ BEC.

10.3.3 Synthetic partial waves in ultracold atomic collisions. The experimental setup and energy scales for the collision experiments are shown in Fig. 10.7.

The collision experiments started with a nearly pure ^{87}Rb BEC of around 5×10^5 atoms in a crossed optical-dipole trap with frequencies of $(f_x, f_y, f_z) = (13, 45, 90)$ Hz. The BEC was then illuminated with a pair of Raman beams with wavelength $\lambda = 790.1$ nm and coupling strength Ω_R ; the BEC was loaded in the lowest dressed band and split into two (initially spatially overlapping) condensates with momenta $\hbar k_x = \pm 2\hbar k_L$ per atom [11]. The dipole trap was immediately turned off ($t_{\text{off}} < 1$ ms) after this preparation, allowing the collision between dressed condensates in the absence of any confining potential.

The Raman coupling strength Ω_R was held constant during 2 ms while the scattering halos formed, and the colliding BECs separated and expanded. After this initial 2 ms stage, we mapped the occupied momentum states by transferring the atoms from the ground dressed state into the bare $|F=1, m_F=+1\rangle$ spin state [6, 11] and imaged the atomic distribution after a 36.2 ms TOF.

In the presence of the Raman dressing, we investigated scattering between identical BECs and studied their collisional products. The main observable in this experiment are images of the scattering halos formed as a consequence of the collisional process; the structure of these halos obeys energy-momentum conservation laws, and is dictated by the shape of the lowest energy band of the Raman dressed system. Figure 10.3 illustrates the scheme in which such BECs were set to interact.

The bottom panels in Fig. 10.3 show both: the scattering halos resulting from Ramman dressed (c-f, bottom) and bare (g, bottom) colliding BECs; and their corresponding structure in cylindrical coordinates (c-g, top) calculated using an inverse Abel transform.

Ultracold collisions are characterized by isotropic s -wave scattering halos as shown in Fig. 10.3g. The distribution of the scattering products is uniform over the entire “shell” (g, top). In contrast, we observe a significant inhomogeneity in the distribution of the scattering products (most noticeably in c, top at $\theta=\pi/2$); and similar inhomogeneities can be quantified from the remaining images.

An analysis considering higher order partial waves [11] of the scattering products, reveals the presence of d - and g -wave components, typically energetically inaccessible in the regime of ultracold atoms.

10.4 CONCLUSIONS

We observed modified interactions between ultracold atoms in the presence of Raman dressing in two different regimes. In the limit when the Raman coupling strength is $\hbar\Omega_R > 4E_L$, we studied ultralow-energy colliding BECs; we measured d - and g -wave contributions to the scattering products, in addition to the expected s -wave. In the limit when $\hbar\Omega_R < 4E_L$, we measured the effective interaction between the dressed spin states and determined a quantum phase transition from phase mixed to phase separated.

The illumination of BECs with a pair of Raman beams has demonstrated to be a reliable mechanism to control effective interatomic interactions with light.

CONCLUSIONS AND OUTLOOK

This thesis introduced experimental techniques to realize light-induced artificial gauge fields for ultracold neutral atoms which allowed the demonstration of physical phenomena so far exclusive of electronic systems. Taking advantage of the richness and the high degree of experimental control of the atomic internal degrees of freedom, not only did we realize scalar valued but also matrix valued artificial gauge fields. We also investigated the physics of ultracold bosonic systems in lattice potentials without and with artificial gauge fields. Finally, we studied the effects of Raman dressing on the effective interatomic interactions of ultracold atom systems.

The main results of this thesis and potential directions for further research are summarized below.

Artificial gauge fields for ultracold neutral atoms. We discussed the “Raman” scheme to introduce an experimentally controllable light-induced vector potential \mathcal{A} for ultracold neutral atoms; and independently studied the effects of time- and spatially-dependent artificial vector potentials \mathcal{A} .

We generate an artificial electric field $\mathbf{E}^* = -\partial \mathcal{A}/\partial t$ and characterized the mechanical motion it imparted on the atoms; our technique allows a direct and unambiguous identification of the canonical and mechanical momenta, and has become a standard mechanism to excite collective oscillations to characterize the dispersion relation of the atoms.

We use a spatially dependent vector potential to demonstrate an artificial magnetic field $\mathbf{B}^* = \nabla \times \mathcal{A}$, which we further use to probe internal properties of BEC via the observation of a SF Hall effect.

To reach very strong artificial gauge fields and enter the quantum Hall regime, theoretical proposals [78, 80, 123] and experiments [79, 81, 30] are turning to the engineering of geometric phases in lattice potentials.

Artificial gauge fields and lattice potentials. We studied the physics of ultracold bosons not only in optical lattices but also in a lattice potential arising from the illumination of the atoms using rf and Raman fields. Such engineered lattices offer dynamical and fully controllable potential energy landscapes for ultracold atoms.

We first focused on the identification of the SF-MI transition in trapped 2D systems as a function of both atom density and lattice depth, to map a universal state diagram for 2D Bose gases in optical lattices. We developed an MRI technique to eliminate the ensemble average of the trapped system and found excellent agreement with QMC predictions [103].

Our second project combined rf and Raman fields to simultaneously realize a uniform vector potential in a 1D lattice, and to demonstrate the Peierls substitution. By extending our 1D rf-Raman lattice into the 2D regime (using a spatially modulated artificial vector potential) a uniform magnetic field gauge-equivalent to the Hofstadter model with a flux of 1/3 can be simulated [30]. Furthermore such extended 2D rf-Raman lattice could be used to measure the SF-MI phase transition in the presence of a synthetic magnetic field [142].

Matrix valued gauge fields and spin-orbit coupling. We generated bosonic spin-orbit coupling in an effective “spin-1/2” system, realizing a matrix valued artificial gauge field. We also demonstrated SOC with tunable coupling strength, by time-modulating the intensity of the Raman beams; a further study of this approach is required to understand and mitigate undesired heating (see Fig. 9.5).

Matrix valued gauge fields can be engineered to display non-abelian properties, useful to realize both quantum computation schemes [27] and generalized Hamiltonians which go beyond condensed matter systems.

An rf-Raman lattice can readily be implemented in an effective “spin-1/2” system to realize spin-orbit coupled lattice potentials [136], to investigate the stability of BECs in flat bands and their potential use in engineering fractional topological insulators [25].

Modified interactions in Raman dressed systems. We observed modified interactions between ultracold atoms in the presence of Raman dressing in two different regimes.

In the vector potential limit, where the Raman coupling strength is $\hbar\Omega_R > 4E_L$, we studied ultralow-energy colliding BECs; the partial wave composition of the scattering products not only included *s*-wave, but also *d*- and *g*-wave contributions. In the SOC limit, $\hbar\Omega_R < 4E_L$ we measured the effective interaction between the dressed spin states and determined a quantum phase transition from phase mixed to phase separated.

The illumination of BECs with a pair of Raman beams has demonstrated to be a reliable mechanism to control effective interatomic interactions with light. Ultracold fermions might be able to realize systems whose elementary excitations are Majorana fermions, by using light-induced *p*-wave interactions [76, 137].

Ultracold neutral atoms are excellent systems to study the physics of a wealth of quantum phenomena in their purest and most controllable way. We characterized ultracold bosonic systems subject to different quantum simulation schemes using novel light-induced artificial gauge fields.

Artificial gauge fields for ultracold neutral atoms has become a thriving field of research both theoretically and experimentally. We engineered such Hamiltonians for ultracold neutral bosons by optically dressing these systems with suitable rf and laser fields.

A general direction for these experiments is to move on to fermionic systems. Our experimental apparatus is already loaded with a potassium source, and progress is being done toward implementing light-induced artificial gauge fields on fermionic ^{40}K .

APPENDIX A

APPENDIX A

A.1 QUANTUM MECHANICAL MODEL OF THE ATOMIC POLARIZABILITY

I will describe in this appendix the interaction between an atom and the oscillating electric field from electromagnetic radiation, e.g. from a laser, and will directly derive the atomic polarizability; for the purpose of this calculations I followed the treatment described in [39]. The Hamiltonian for the system is given by

$$H = H_0 + H' \quad (\text{A.1})$$

where H_0 stands for the atomic Hamiltonian without perturbations, and H' is the time-dependent dipole interaction with an oscillatory electric field. We look for the solutions to the time-dependent Schrödinger equation

$$i\hbar \frac{\partial \Psi(t)}{\partial t} = H\Psi(t) = (H_0 + H')\Psi(t). \quad (\text{A.2})$$

Given that the eigenfunctions of the time-independent atomic Hamiltonian H_0 form a complete basis $\{\psi_n\}_n$ and that they satisfy

$$i\hbar \frac{\partial \psi_n}{\partial t} = H_0 \psi_n = E_n \psi_n, \quad (\text{A.3})$$

where E_n are the corresponding eigenenergies, any wavefunction associated with the atomic system can be expressed as a linear superposition. The solutions to eqn. (A.2) have the form

$$\Psi(t) = \sum_n c_n \psi_n e^{-iE_n t/\hbar}, \quad (\text{A.4})$$

where c_n is a time-dependent coefficient. Substituting eqn. (A.4) in the left hand side of eqn. (A.2) we get

$$\begin{aligned} i\hbar \frac{\partial \Psi(t)}{\partial t} &= i\hbar \sum_n \left(-\frac{i}{\hbar} E_n c_n + \dot{c}_n \right) \psi_n e^{-iE_n t/\hbar}, \\ &= \sum_n c_n E_n \psi_n e^{-iE_n t/\hbar} + \sum_n i\hbar \dot{c}_n \psi_n e^{-iE_n t/\hbar}; \end{aligned}$$

while the evaluation of the right-hand side of eqn. (A.2) gives

$$\begin{aligned} (H_0 + H')\Psi(t) &= \sum_n c_n H_0 \psi_n e^{-iE_n t/\hbar} + \sum_n c_n H' \psi_n e^{-iE_n t/\hbar}, \\ &= \sum_n c_n E_n \psi_n e^{-iE_n t/\hbar} + \sum_n c_n H' \psi_n e^{-iE_n t/\hbar}; \end{aligned}$$

and Schrödinger's equation reduces to

$$\sum_n i\hbar \dot{c}_n \psi_n e^{-iE_n t/\hbar} = \sum_n c_n H' \psi_n e^{-iE_n t/\hbar}. \quad (\text{A.5})$$

The basis of stationary states $\{\psi_n\}_n$, is orthogonal under the inner product defined by

$$\langle m|n\rangle = \int \psi_m^*(\mathbf{r}) \psi_n(\mathbf{r}) d^3\mathbf{r} = \delta_{mn}; \quad (\text{A.6})$$

from eqn. (A.5) we obtain the differential equation for the m -th time-dependent coefficient

$$\dot{c}_m = -\frac{i}{\hbar} \sum_n c_n \langle m|H'|n\rangle e^{i\omega_{mn}t}, \quad (\text{A.7})$$

where I have used the notation $\hbar\omega_{mn} = E_m - E_n$. We assume that at time $t = 0$ the atom is in state $\Psi(t = 0) = \psi_k$, with $c_n(t = 0) = \delta_{nk}$ in eqn. (A.4). Given this initial condition, we can compute the time-dependent coefficients of the wavefunction for $t > 0$. To do this, we substitute $c_n(t = 0) = \delta_{nk}$ in eqn. (A.7)

$$\begin{aligned} \dot{c}_m &= -\frac{i}{\hbar} \sum_n \delta_{nk} \langle m|H'|n\rangle e^{i\omega_{mn}t}, \\ &= -\frac{i}{\hbar} \langle m|H'|k\rangle e^{i\omega_{mk}t}, \\ &= \frac{i}{2\hbar} \langle m|\mathbf{d} \cdot \mathbf{E}|k\rangle [e^{i(\omega_{mk}+\omega)t} + e^{i(\omega_{mk}-\omega)t}]; \end{aligned}$$

then we integrate to obtain the time-dependent coefficients $c_m(t) = \int_0^t \dot{c}_m dt'$:

$$\begin{aligned} c_m(t) &= \frac{i}{2\hbar} \langle m | \mathbf{d} \cdot \mathbf{E} | k \rangle \int_0^t [e^{i(\omega_{mk} + \omega)t'} + e^{i(\omega_{mk} - \omega)t'}], \\ &= \frac{1}{2\hbar} \langle m | \mathbf{d} \cdot \mathbf{E} | k \rangle \left[\frac{e^{i(\omega_{mk} + \omega)t} - 1}{\omega_{mk} + \omega} + \frac{e^{i(\omega_{mk} - \omega)t} - 1}{\omega_{mk} - \omega} \right]. \end{aligned}$$

We use eqn. (A.7) to fully determine the time-dependent wavefunction; we break the sum into $n = k$ and $n \neq k$ terms, and substitute the above coefficients in the $n \neq k$ term. In this approximation we use $c_k = \delta_{nk}$ in the first term and get

$$\begin{aligned} \dot{c}_k &= -\frac{i}{\hbar} \langle k | H' | k \rangle - \frac{i}{\hbar} \sum_{n \neq k} c_n \langle k | H' | n \rangle e^{i\omega_{kn} t}, \\ &= -\frac{i}{\hbar} \langle k | \mathbf{d} \cdot \mathbf{E} \cos(\omega t) | k \rangle + \\ &\quad - \frac{i}{\hbar} \sum_{n \neq k} \frac{1}{2\hbar} \langle n | \mathbf{d} \cdot \mathbf{E} | k \rangle \left[\frac{e^{i(\omega_{nk} + \omega)t} - 1}{\omega_{nk} + \omega} + \frac{e^{i(\omega_{nk} - \omega)t} - 1}{\omega_{nk} - \omega} \right] \langle k | -\mathbf{d} \cdot \mathbf{E} \cos(\omega t) | n \rangle e^{i\omega_{kn} t}, \\ &= -\frac{i}{\hbar} \langle k | \mathbf{d} \cdot \mathbf{E} \cos(\omega t) | k \rangle + \\ &\quad - \frac{i}{2\hbar^2} \sum_{n \neq k} |\langle n | \mathbf{d} \cdot \mathbf{E} | k \rangle|^2 \left[\frac{e^{i(\omega_{nk} + \omega)t} - 1}{\omega_{nk} + \omega} + \frac{e^{i(\omega_{nk} - \omega)t} - 1}{\omega_{nk} - \omega} \right] e^{-i\omega_{nk} t} \cos(\omega t). \end{aligned}$$

Here, we further assume that $c_k(t) = \exp[i\phi_k(t)]$, thus $\dot{\phi}_k = -i\dot{c}_k \exp[-i\phi_k(t)]$, and average over a period of oscillation of the electric field $T = 2\pi/\omega$. The first term vanishes since $\cos(\omega t)$ averages to zero; but if in addition ψ_k is an eigenstate of the parity operator, $\langle k | H' | k \rangle = 0$ since a change in parity is required for a electric dipole transition. The remaining non-zero term is

$$\begin{aligned} \langle \dot{\phi}_k \rangle_t &= \frac{1}{T} \int_0^T \dot{\phi}_k(t') dt', \\ &= \frac{1}{2\hbar^2} \sum_{n \neq k} |\langle n | \mathbf{d} \cdot \mathbf{E} | k \rangle|^2 \frac{1}{T} \int_0^T \left[\frac{e^{i(\omega_{nk} + \omega)t'} - 1}{\omega_{nk} + \omega} + \frac{e^{i(\omega_{nk} - \omega)t'} - 1}{\omega_{nk} - \omega} \right] e^{-i\omega_{nk} t'} \cos(\omega t') dt', \\ &= \frac{1}{2\hbar^2} \sum_{n \neq k} |\langle n | \mathbf{d} \cdot \mathbf{E} | k \rangle|^2 \frac{1}{T} \int_0^T \left[\frac{e^{i\omega t'} - e^{-i\omega_{nk} t'}}{\omega_{nk} + \omega} + \frac{e^{-i\omega t'} - e^{-i\omega_{nk} t'}}{\omega_{nk} - \omega} \right] \cos(\omega t') dt'. \end{aligned}$$

Expressing $\cos(\omega t')$ in exponentials and continuing with the integration

$$\begin{aligned}\langle \dot{\phi}_k \rangle_t &= \frac{1}{4\hbar^2} \sum_{n \neq k} |\langle n | \mathbf{d} \cdot \mathbf{E} | k \rangle|^2 \frac{1}{T} \int_0^T \left[\frac{e^{i\omega t'} - e^{-i\omega_{nk} t'}}{\omega_{nk} + \omega} + \frac{e^{-i\omega t'} - e^{-i\omega_{nk} t'}}{\omega_{nk} - \omega} \right] [e^{i\omega t'} + e^{-i\omega t'}] dt', \\ &= \frac{1}{4\hbar^2} \sum_{n \neq k} |\langle n | \mathbf{d} \cdot \mathbf{E} | k \rangle|^2 \frac{1}{T} \int_0^T \left[\frac{e^{i2\omega t'} + 1 - e^{i(\omega - \omega_{nk})t'} - e^{-i(\omega + \omega_{nk})t'}}{\omega_{nk} + \omega} + \right. \\ &\quad \left. + \frac{1 + e^{-i2\omega t'} - e^{i(\omega - \omega_{nk})t'} - e^{-i(\omega + \omega_{nk})t'}}{\omega_{nk} - \omega} \right] dt'.\end{aligned}$$

Since the terms oscillating at twice the frequency of the electric field average to zero, the result is

$$\begin{aligned}\langle \dot{\phi}_k \rangle_t &= \frac{1}{4\hbar^2} \sum_{n \neq k} |\langle n | \mathbf{d} \cdot \mathbf{E} | k \rangle|^2 \frac{1}{T} [t' + i \frac{e^{i(\omega - \omega_{nk})t'}}{\omega - \omega_{nk}} + i \frac{e^{-i(\omega + \omega_{nk})t'}}{\omega + \omega_{nk}}] \Big|_0^T \left[\frac{1}{\omega_{nk} + \omega} + \frac{1}{\omega_{nk} - \omega} \right], \quad (\text{A.8}) \\ &= \frac{1}{4\hbar^2} \sum_{n \neq k} |\langle n | \mathbf{d} \cdot \mathbf{E} | k \rangle|^2 \frac{1}{T} \left\{ t' + i \frac{e^{-i\omega_{nk}} [2\omega \cos(\omega t') + 2i\omega_{nk} \sin(\omega t')]}{\omega^2 - \omega_{nk}^2} \right\} \Big|_0^T \left[\frac{1}{\omega_{nk} + \omega} + \frac{1}{\omega_{nk} - \omega} \right], \\ &= \frac{1}{4\hbar^2} \sum_{n \neq k} |\langle n | \mathbf{d} \cdot \mathbf{E} | k \rangle|^2 \left(\frac{1}{\omega_{nk} + \omega} + \frac{1}{\omega_{nk} - \omega} \right).\end{aligned}$$

The above is a real valued expression which corresponds to an energy shift $U = -\hbar \langle \dot{\phi}_k \rangle_t$ for the state ϕ_k . In the following we consider the general case where the electric field has an arbitrary polarization $\hat{\epsilon}$, and by making the dipole approximation we can take its magnitude \mathcal{E}_0 out of the spatial integral $\langle n | \mathbf{d} \cdot \mathbf{E} | k \rangle$.

A change in the electric field $d\mathbf{E}$ modifies the perturbation energy by $dU = -\langle \mathbf{d} \rangle \cdot d\mathbf{E}$, where the expectation value of the induced electric dipole moment in the atom relates to the electric field via the atomic polarizability $\alpha(\omega)$ by $\langle \mathbf{d} \rangle = \alpha(\omega) \mathbf{E}$; the integrated contribution to the change on the interaction energy yields

$$U = \int dU = \int -\alpha \mathbf{E} \cdot d\mathbf{E} = -\frac{1}{2} \alpha |\mathbf{E}|^2, \quad (\text{A.9})$$

where the factor of 1/2 in the above equation is a consequence of the dipole moment being induced as opposed to being permanent. Assuming that $\mathbf{E}(t) = \mathcal{E}_0 \hat{\epsilon} \cos(\omega t)$, and expressing the energy shift induced by a time-averaged electric field $U = -\alpha(\omega) \langle \mathcal{E}_0^2 \cos^2(\omega t) \rangle_t / 2$, we identify from Eq. (A.8) the frequency-dependent atomic polarizability for the $k = 0$ ground state as

$$\alpha(\omega) = \frac{1}{\hbar} \sum_{n \neq 0} |\langle n | \mathbf{d} \cdot \hat{\epsilon} | 0 \rangle|^2 \left(\frac{1}{\omega_{n0} + \omega} + \frac{1}{\omega_{n0} - \omega} \right),$$

or equivalently in terms of the eigenenergies

$$\alpha(\omega) = \sum_{n \neq 0} \frac{2(E_n - E_0)|\langle n | \mathbf{d} \cdot \hat{\epsilon} | 0 \rangle|^2}{(E_n - E_0)^2 - (\hbar\omega)^2}. \quad (\text{A.10})$$

A.2 CLASSICAL MODEL TO DESCRIBE THE ATOMIC POLARIZABILITY

The atomic polarizability is a frequency dependent quantity which can be classically modeled by studying the dynamics of the electron (in a particular orbital, usually the valence one) of the atom in the presence of a time-varying electric field $\mathbf{E}(t) = \mathbf{E}_0 \cos(\omega t)$. We assume that the valence electron is attached to the atom by a restoring force $-m_e \omega_0^2 \mathbf{r}$, and that its position \mathbf{r} varies as $e^{i\omega t}$. Before setting up the equation of motion, let us recall that an accelerated charge loses energy by emitting radiation and that the radiative power is given by $P = e^2 \dot{\mathbf{r}}^2 \omega^2 / 6\pi\epsilon_0 c^3 = m_e \dot{\mathbf{r}}^2 \Gamma_\omega$, where Γ_ω is the damping rate. Due to such energy loss, the motion will be damped in proportion to Γ_ω and we obtain

$$\begin{aligned} m_e \ddot{\mathbf{r}} + m_e \Gamma_\omega \dot{\mathbf{r}} + m_e \omega_0^2 \mathbf{r} &= -e \mathbf{E}_0 e^{i\omega t}, \\ \ddot{\mathbf{r}} + \Gamma_\omega \dot{\mathbf{r}} + \omega_0^2 \mathbf{r} &= -\frac{e \mathbf{E}_0}{m_e} e^{i\omega t}. \end{aligned}$$

The above equations lead to the frequency dependent atomic polarizability

$$\alpha = \frac{e^2}{m_e} \frac{1}{\omega_0^2 - \omega^2 + i\omega\Gamma_\omega}. \quad (\text{A.11})$$

A.3 ROTATION OPERATORS

I will derive the explicit form of the rotation operators total angular momentum $F = 1$ and spin $s = 1/2$. This serves as a reference specially for Chapter 9, where a couple rotation transformations were indicated.

As the linear momentum operator is the generator of spatial translations, the angular momentum operators are generators of spatial rotations. A rotation by an angle θ around the axis defined by the unit vector $\hat{\mathbf{n}}$ is generated by the operator $\hat{U} = \exp(i\theta \hat{\mathbf{n}} \cdot \hat{\mathbf{L}}/\hbar)$, where $\hat{\mathbf{L}}$ is an angular momentum operator. It worthwhile noting that an operator $\hat{\mathbf{A}}$ under such unitary operation \hat{U} transforms as $\hat{\mathbf{A}}' = \hat{U} \hat{\mathbf{A}} \hat{U}^\dagger$.

A.3.1 Rotation operators for total angular momentum $F = 1$. The matrix representation of the components of the $F = 1$ total angular momentum operator $\hat{\mathbf{F}}$ are

$$\hat{F}_x/\hbar = \frac{1}{\sqrt{2}} \begin{pmatrix} 0 & 1 & 0 \\ 1 & 0 & 1 \\ 0 & 1 & 0 \end{pmatrix}, \quad \hat{F}_y/\hbar = \frac{1}{\sqrt{2}} \begin{pmatrix} 0 & -i & 0 \\ i & 0 & -i \\ 0 & i & 0 \end{pmatrix}, \quad \hat{F}_z/\hbar = \begin{pmatrix} 1 & 0 & 0 \\ 0 & 0 & 0 \\ 0 & 0 & -1 \end{pmatrix}; \quad (\text{A.12})$$

and satisfy $(\hat{F}_j/\hbar)^{2l+1} = (\hat{F}_j/\hbar)$ and $(\hat{F}_j/\hbar)^{2l} = (\hat{F}_j/\hbar)^2$, where $j = x, y, z$. The operator associated with a rotation by an angle θ around \mathbf{e}_j is given by

$$\hat{U}_j(\theta) = \hat{1} + (\cos \theta - 1) \left(\frac{\hat{F}_j}{\hbar} \right)^2 + i \sin \theta \left(\frac{\hat{F}_j}{\hbar} \right); \quad (\text{A.13})$$

which for each of the orthogonal directions \mathbf{e}_j becomes:

$$\hat{U}_x(\theta) = \begin{pmatrix} (\cos \theta + 1)/2 & i \sin \theta / \sqrt{2} & (\cos \theta - 1)/2 \\ i \sin \theta / \sqrt{2} & \cos \theta & i \sin \theta / \sqrt{2} \\ (\cos \theta - 1)/2 & i \sin \theta / \sqrt{2} & (\cos \theta + 1)/2 \end{pmatrix}; \quad (\text{A.14})$$

$$\hat{U}_y(\theta) = \begin{pmatrix} (1 + \cos \theta)/2 & \sin \theta / \sqrt{2} & (1 - \cos \theta)/2 \\ -\sin \theta / \sqrt{2} & \cos \theta & \sin \theta / \sqrt{2} \\ (1 - \cos \theta)/2 & -\sin \theta / \sqrt{2} & (1 + \cos \theta)/2 \end{pmatrix}; \quad (\text{A.15})$$

$$\hat{U}_z(\theta) = \begin{pmatrix} \exp(i\theta) & 0 & 0 \\ 0 & 1 & 0 \\ 0 & 0 & \exp(-i\theta) \end{pmatrix}. \quad (\text{A.16})$$

A.3.2 Rotation operators for spin angular momentum $s = 1/2$. In the case of spin $s = 1/2$, the matrix representation of components of the spin operator $\hat{\mathbf{S}}$ are the 2×2 Pauli matrices

$$\hat{\sigma}_x/\hbar = \begin{pmatrix} 0 & 1 \\ 1 & 0 \end{pmatrix}, \quad \hat{\sigma}_y/\hbar = \begin{pmatrix} 0 & -i \\ i & 0 \end{pmatrix}, \quad \hat{\sigma}_z/\hbar = \begin{pmatrix} 1 & 0 \\ 0 & -1 \end{pmatrix}; \quad (\text{A.17})$$

whose associated operators for rotation by an angle θ around \mathbf{e}_j are

$$\hat{U}_x = \begin{pmatrix} \cos(\theta/2) & i \sin(\theta/2) \\ i \sin(\theta/2) & \cos(\theta/2) \end{pmatrix}, \quad \hat{U}_y = \begin{pmatrix} \cos(\theta/2) & \sin(\theta/2) \\ -\sin(\theta/2) & \cos(\theta/2) \end{pmatrix}, \quad \hat{U}_z = \begin{pmatrix} e^{i\theta/2} & 0 \\ 0 & e^{-i\theta/2} \end{pmatrix}. \quad (\text{A.18})$$

A.4 ADDITION OF ANGULAR MOMENTUM

The addition of two angular momenta \mathbf{j}_1 and \mathbf{j}_2 , gives a total angular momentum $\mathbf{j} = \mathbf{j}_1 + \mathbf{j}_2$ which acquires the values $|j_1 - j_2| \leq j \leq j_1 + j_2$, and has spin projections $m = -j, -j+1, \dots, j$. The uncoupled basis $|j_1 j_2 m_1 m_2\rangle$ can be related to the basis of eigenstates of the angular momentum operator \mathbf{j}^2 , the basis of coupled states $|j, m\rangle$, by means of a unitary transformation of the form

$$|j, m\rangle = \sum_{m_1, m_2} \langle j_1 j_2; m_1 m_2 | j, m \rangle |j_1 j_2; m_1 m_2\rangle; \quad (\text{A.19})$$

where $\langle j_1 j_2; m_1 m_2 | j, m \rangle$ are known as the Clebsch-Gordan coefficients for the addition of angular momentum. By convention the Clebsch-Gordan coefficients are real and the one associated with the coupled state of maximum angular momentum and maximum spin projection, i.e. $|j_1 + j_2, j_1 + j_2\rangle$, is taken to be 1.

The Clebsch-Gordan coefficients are readily obtained by the application of the ladder operators

$$J_{\pm}|j, m\rangle = \hbar \sqrt{j(j+1) - m(m \pm 1)} |j_1 j_2; j, m \pm 1\rangle, \quad (\text{A.20})$$

particularly noting that $J_{\pm} = J_{1\pm} + J_{2\pm}$, and that similar expressions hold for the uncoupled states:

$$\begin{aligned} J_{1\pm}|j_1, m_1\rangle |j_2, m_2\rangle &= \hbar \sqrt{j_1(j_1+1) - m_1(m_1 \pm 1)} |j_1, m_1 \pm 1\rangle |j_2, m_2\rangle, \\ J_{2\pm}|j_1, m_1\rangle |j_2, m_2\rangle &= \hbar \sqrt{j_2(j_2+1) - m_2(m_2 \pm 1)} |j_1, m_1\rangle |j_2, m_2 \pm 1\rangle. \end{aligned}$$

A.4.1 Clebsch-Gordan coefficients for the addition of $j_1 = 1$ and $j_2 = 1$. The coupled states obtained from the addition of two spin-1 systems correspond to states with $j = 0, 1, 2$. Expressed in matrix form, the transformation between the coupled and uncoupled bases is

$$\left(\begin{array}{c} |2, +2\rangle \\ |2, +1\rangle \\ |1, +1\rangle \\ |2, 0\rangle \\ |1, 0\rangle \\ |0, 0\rangle \\ |1, -1\rangle \\ |2, -1\rangle \\ |2, -2\rangle \end{array} \right) = \left(\begin{array}{ccccccc} 1 & 0 & 0 & 0 & 0 & 0 & 0 & 0 \\ 0 & 1/\sqrt{2} & 0 & 1/\sqrt{2} & 0 & 0 & 0 & 0 \\ 0 & 1/\sqrt{2} & 0 & -1/\sqrt{2} & 0 & 0 & 0 & 0 \\ 0 & 0 & 1/\sqrt{6} & 0 & \sqrt{2/3} & 0 & 1/\sqrt{6} & 0 \\ 0 & 0 & 1/\sqrt{2} & 0 & 0 & 0 & -1/\sqrt{2} & 0 \\ 0 & 0 & 1/\sqrt{3} & 0 & -1/\sqrt{3} & 0 & 1/\sqrt{3} & 0 \\ 0 & 0 & 0 & 0 & 0 & 1/\sqrt{2} & 0 & -/\sqrt{2} \\ 0 & 0 & 0 & 0 & 0 & 1/\sqrt{2} & 0 & 1/\sqrt{2} \\ 0 & 0 & 0 & 0 & 0 & 0 & 0 & 1 \end{array} \right) \left(\begin{array}{c} |1, +1\rangle |1, +1\rangle \\ |1, +1\rangle |1, 0\rangle \\ |1, +1\rangle |1, -1\rangle \\ |1, 0\rangle |1, +1\rangle \\ |1, 0\rangle |1, 0\rangle \\ |1, 0\rangle |1, -1\rangle \\ |1, -1\rangle |1, +1\rangle \\ |1, -1\rangle |1, 0\rangle \\ |1, -1\rangle |1, -1\rangle \end{array} \right)$$

BIBLIOGRAPHY

- [1] J. Dalibard, F. Gerbier, G. Juzeliūnas, and P. Öhberg. *Colloquium: Artificial gauge potentials for neutral atoms.* *Rev. Mod. Phys.*, 83:1523–1543, 2011. [v, vi, 2, 96, 156]
- [2] G. Juzeliūnas, J. Ruseckas, P. Öhberg, and M. Fleischhauer. Light-induced effective magnetic fields for ultracold atoms in planar geometries. *Physical Review A*, 73:025602, 2006. [v, vi]
- [3] J. Ruseckas, G. Juzeliūnas, P. Öhberg, and M. Fleischhauer. Non-abelian gauge potentials for ultracold atoms with degenerate dark states. *Phys. Rev. Lett.*, 95:010404, 2005. [v, vi]
- [4] I. B. Spielman. Raman processes and effective gauge potentials. *Phys. Rev. A*, 79:063613, 2009. [v, vi, 97, 102, 114]
- [5] Y.-J. Lin, R. L. Compton, A. R. Perry, W. D. Phillips, J. V. Porto, and I. B. Spielman. Bose-Einstein condensate in a uniform light-induced vector potential. *Phys. Rev. Lett.*, 102:130401, 2009. [v, vi, 2, 57, 102, 104, 105, 106, 109, 150, 155, 159, 164, 165]
- [6] Y.-J. Lin, R. L. Compton, K. Jiménez-García, W. D. Phillips, J. V. Porto, and I. B. Spielman. A synthetic electric force acting on neutral atoms. *Nature Physics*, 7:531–534, 2011. [v, vi, 2, 101, 102, 109, 110, 150, 157, 177]
- [7] Y.-J. Lin, R. L. Compton, K. Jiménez-García, J. V. Porto, and I. B. Spielman. Synthetic magnetic fields for ultracold neutral atoms. *Nature*, 462:628–638, 2009. [v, vi, 2, 102, 108, 113, 114, 117, 156, 157]
- [8] L. J. LeBlanc, K. Jiménez-García, R. A. Williams, M. C. Beeler, A. R. Perry, W. D. Phillips, and I. B. Spielman. Observation of a superfluid Hall effect. *Proceedings of the National Academy of Sciences*, 109(27), 2012. [v, vi, 2, 20, 102, 113, 119]
- [9] Y.-J. Lin, K. Jiménez-García, and I. B. Spielman. Spin-orbit-coupled Bose-Einstein condensates. *Nature*, 471:83–86, 2011. [v, vi, 3, 102, 157, 159, 172]
- [10] M. C. Beeler, L. J. LeBlanc, R. A. Williams, K. Jiménez-García, A. R. Perry, and I. B. Spielman. A spin Hall effect in ultracold atoms. *The 23rd International Conference on Atomic Physics*, page 92, 2012. [v, vi, 167]

- [11] R. A. Williams, L. J. LeBlanc, K. Jiménez-García, M. C. Beeler, A. R. Perry, W. D. Phillips, and I. B. Spielman. Synthetic partial waves in ultracold atomic collisions. *Science*, 335(6066):314–317, 2012. [v, vi, 3, 103, 177, 178]
- [12] C. L. Kane and E. J. Mele. Z_2 Topological order and the quantum spin Hall effect. *Phys. Rev. Lett.*, 95:146802, 2005. [v, vi, 1, 96, 157]
- [13] F. Wilczek. Majorana returns. *Nature Phys.*, 5:614–618, 2009. [v, vi, 96, 157]
- [14] M. H. Anderson, J. R. Ensher, M. R. Matthews, C. E. Wieman, and E. A. Cornell. Observation of Bose-Einstein condensation in a dilute atomic vapor. *Science*, 269:198–201, 1995. [1, 9]
- [15] K. B. Davis, M.-O. Mewes, M. R. Andrews, N. J. van Druten, D. S. Durfee, D. M. Kurn, and W. Ketterle. Bose-Einstein condensation in a gas of sodium atoms. *Phys. Rev. Lett.*, 75(22):3969–3973, 1995. [1]
- [16] H. K. Onnes. The resistance of pure mercury at helium temperatures. *Commun. Phys. Lab. Univ. Leiden*, 12:120, 1911. [1]
- [17] P. Kapitza. Viscosity of liquid Helium below the λ -point. *Nature*, 141:74, 1938. [1]
- [18] J. F. Allen and A. D. Misener. Flow of Liquid Helium II. *Nature*, 141:75, 1938. [1]
- [19] D. Jaksch, C. Bruder, J. I. Cirac, C. W. Gardiner, and P. Zoller. Cold bosonic atoms in optical lattices. *Phys. Rev. Lett.*, 81:3108–3111, 1998. [1, 127]
- [20] M. Greiner, O. Mandel, T. Esslinger, T.W. Hänsch, and I. Bloch. Quantum phase transition from a superfluid to a mott insulator in a gas of ultracold atoms. *Nature*, 415:39–44, 2002. [1, 120, 136]
- [21] J. E. Hirsch. Attractive interaction and pairing in fermion systems with strong on-site repulsion. *Phys. Rev. Lett.*, 54:1317–1320, 1985. [1]
- [22] R. H. Parmenter. Superconductivity from antiferromagnetic exchange interactions. *Phys. Rev. Lett.*, 59:923–925, 1987. [1]
- [23] K. von Klitzing, G. Dorda, and M. Pepper. New method for high-accuracy determination of the fine-structure constant based on quantized Hall resistance. *Phys. Rev. Lett.*, 45:494–497, 1980. [1, 96]
- [24] Y. K. Kato, R. C. Myers, A. C. Gossard, and D. D. Awschalom. Observation of the Spin-Hall effect in Semiconductors. *Science*, 306(5703):1910–1913, 2004. [1, 157]

- [25] M. Z. Hasan and C. L. Kane. *Colloquium: Topological insulators.* *Rev. Mod. Phys.*, 82:3045–3067, 2010. [1, 157, 180]
- [26] B. A. Bernevig, T. L. Hughes, and S.-C. Zhang. Quantum spin-Hall effect and topological phase transition in HgTe quantum wells. *Science*, 314(5806):1757–1761, 2006. [1]
- [27] C. Nayak, S. H. Simon, A. Stern, M. Freedman, and S. Das Sarma. Non-abelian anyons and quantum computation. *Rev. Mod. Phys.*, 80:1083, 2008. [1, 157, 180]
- [28] G. Juzeliūnas, J. Ruseckas, and J. Dalibard. Generalized Rashba-Dresselhaus spin-orbit coupling for cold atoms. *Phys. Rev. A*, 81:053403, 2010. [2, 157]
- [29] K. Jiménez-García, R. Compton, Y.-J. Lin, W. D. Phillips, J. V. Porto, and I. B. Spielman. Phases of a two-dimensional Bose gas in an optical lattice. *Phys. Rev. Lett.*, 105:110401, 2010. [2, 129]
- [30] K. Jiménez-García, L. J. LeBlanc, R. A. Williams, M. C. Beeler, A. R. Perry, and I. B. Spielman. The peierls substitution in and engineered lattice potential. *Phys. Rev. Lett.*, 108:225303, 2012. [2, 102, 148, 153, 179, 180]
- [31] Y. Zhang, G. Chen, and C. Zhang. Tunable spin-orbit coupling and quantum phase transition in a trapped Bose-Einstein condensate. *arXiv*, 1111.4778v1, 2011. [3, 163]
- [32] P. Wang, Z.-Q. Yu, Z. Fu, J. Miao, L. Huang, S. Chai, H. Zhai, and J. Zhang. Spin-orbit coupled degenerate Fermi gases. *arXiv*, 1204.1887v1, 2012. [3, 110, 167]
- [33] L. W. Cheuk, A. T. Sommer, Z. Hadzibabic, T. Yefsah, W. S. Bakr, and M. Zwierlein. Spin-injection spectroscopy of a spin-orbit coupled Fermi gas. *arXiv*, 1205.3483, 2012. [3, 110, 167]
- [34] A. Einstein. Quantentheorie des einatomigen idealen gases. *Sitzungsberg. Kgl. Preuss. Akad. Wiss.*, 1924:261, 1924. [4]
- [35] F. Dalfovo, S. Giorgini, L. P. Pitaevskii, and S. Stringari. Theory of Bose-Einstein condensation in trapped gases. *Rev. Mod. Phys.*, 71:463–512, 1999. [4, 7]
- [36] W. Ketterle, D. S. Durfee, and D. M. Stamper-Kurn. Making, probing and understanding Bose-Einstein condensates. In *Proceedings of the International School of Physics “Enrico Fermi”*, volume 140, pages 67–176, Amsterdam, 1999. IOS Press. edited by Inguscio, M. and Stringari, S. and Wieman, C.E. [4]

- [37] P. C. Hohenberg. Existence of long-range order in one and two dimensions. *Phys. Rev.*, 158:383–386, 1967. [7]
- [38] H.-J. Miesner, D. M. Stamper-Kurn, M. R. Andrews, D. S. Durfee, S. Inouye, and W. Ketterle. Bosonic stimulation in the formation of a Bose-Einstein condensate. *Science*, 279(5353):1005–1007, 1998. [8]
- [39] C. J. Pethick and H. Smith. *Bose-Einstein Condensation in Dilute Gases*. Cambridge University Press, New York, second edition, 2008. [11, 31, 57, 123, 126, 127, 182]
- [40] M. R. Andrews, C. G. Townsend, H.-J. Miesner, D. M. Kurn, and W. Ketterle. Observation of interference between two Bose-Einstein condensates. *Science*, 275:637–641, 1997. [11]
- [41] Wolfgang Ketterle and Hans-Joachim Miesner. Coherence properties of Bose-Einstein condensates and atom lasers. *Phys. Rev. A*, 56:3291–3293, 1997. [11]
- [42] E. A. Burt, R. W. Ghrist, C. J. Myatt, M. J. Holland, E. A. Cornell, and C. E. Wieman. Coherence, correlations, and collisions: What one learns about Bose-Einstein condensates from their decay. *Phys. Rev. Lett.*, 79:337–340, 1997. [11]
- [43] C. Chin, R. Grimm, P. Julienne, and E. Tiesinga. Feshbach resonances in ultracold gases. *Rev. Mod. Phys.*, 82:1225–1286, 2010. [14, 168]
- [44] E. P. Gross. Hydrodynamics of a superfluid condensate. *J. Math. Phys.*, 4:195–207, 1963. [14, 15, 113]
- [45] E. Gross. Structure of a quantized vortex in boson systems. *Il Nuovo Cimento*, 20:454–477, 1961. [14, 113]
- [46] L. P. Pitaevskii. Vortex lines in an imperfect Bose gas. *Sov. Phys. JETP*, 13(2), 1961. [14, 113]
- [47] W. Bao, D. Jaksch, and P. A. Markowich. Numerical solution of the Gross-Pitaevskii equation for Bose-Einstein condensation. *J. of Comp. Phys.*, 187:318–342, 2003. [15, 16]
- [48] S. Stringari. Collective excitations of a trapped Bose-condensed gas. *Phys. Rev. Lett.*, 77:2360–2363, 1996. [19, 20]
- [49] W. Konh. Cyclotron resonance and de Haas-van Alphen oscillations of an interacting electron gas. *Phys. Rev.*, 123:1242–1244, 1961. [20]

- [50] M.-O. Mewes, M. R. Andrews, N. J. van Druten, D. M. Kurn, D. S. Durfee, C. G. Townsend, and W. Ketterle. Collective excitations of a Bose-Einstein condensate in a magnetic trap. *Phys. Rev. Lett.*, 77:988–991, 1996. [20]
- [51] J. D. Jackson. *Classical Electrodynamics*. Wiley, USA, third edition, 1998. [23, 97, 158]
- [52] B. H. Bransden and C. J. Joachain. *Introduction to Quantum-Mechanics*. Longman Scientific and Technical, New York, 1989. [28]
- [53] H. J. Metcalf and P. van der Straten. *Laser cooling and trapping*. Springer, New York, 1999. [31]
- [54] C. J. Foot. *Atomic Physics*. Oxford University Press, Great Britain, 2005. [31, 63]
- [55] D. Budker, D. F. Kimball, and D. P. DeMille. *Atomic Physics*. Oxford University Press, United Kingdom, second edition, 2008. [31]
- [56] R. Loudon. *The quantum theory of light*. Oxford University Press, United Kingdom, 2003. [32]
- [57] R. Grimm, M. Weidemüller, and Y. B. Ovchinnikov. Optical dipole traps for neutral atoms. *Adv. At. Mol. Opt. Phys.*, 42:95–70, 2000. [32, 34, 121]
- [58] P.J. Mohr, B. N. Taylor, and D. B. Newell. The 2012 CODATA Recommended Values of the Fundamental Physical Constants. *Web Version 6.0*, 2011. [38, 49, 86]
- [59] J. V. Prodan, W. D. Phillips, and H. Metcalf. Laser production of a very slow mono energetic atomic beam. *Phys. Rev. Lett.*, 49:1149–1153, 1982. [39]
- [60] J. Dalibard and C. Cohen-Tannoudji. Laser cooling below the Doppler limit by polarization gradients: simple theoretical models. *J. Opt.Soc. Am. B*, 6(11):2023–2045, 1989. [42]
- [61] P. D. Lett, R. N. Watts, C. I. Westbrook, and W. D. Phillips. Observation of atoms laser cooled below the Doppler limit. *Phys. Rev. Lett.*, 61:169–172, 1988. [42]
- [62] T. Yefsah, R. Desbuquois, L. Chomaz, K. J. Günter, and J. Dalibard. Exploring the thermodynamics of a two-dimensional Bose gas. *Phys. Rev. Lett.*, 107:130401, 2011. [43]
- [63] L. Allen and J. H. Eberly. *Optical resonance and two-level atoms*. Dover, New York, 1987. [44]
- [64] G. D. Sprouse and L. A. Orozco. Laser trapping of radioactive atoms. *Ann. Rev. Nucl. Part. Sci.*, 47:429–461, 1997. [45]

- [65] W. H. Wing. On neutral particle trapping in quasistatic electromagnetic fields. *Progress in Quantum Electronics*, 8:181–199, 1984. [48]
- [66] W. Petrich, M. H. Anderson, J. R. Ensher, and E. A. Cornell. Stable, tightly confining magnetic trap for evaporative cooling of neutral atoms. *Phys. Rev. Lett.*, 74:3352–3355, 1995. [49]
- [67] Y.-J. Lin, A. R. Perry, R. L. Compton, I. B. Spielman, and J. V. Porto. Rapid production of ^{87}Rb Bose-Einstein Condensates in a combined magnetic and optical potential. *Phys. Rev. A*, 79:063631, 2009. [49]
- [68] J.F. O'Hanlon. *A user's guide to vacuum technology*. Wiley, USA, second edition, 1989. [62]
- [69] W. D. Phillips and H. Metcalf. Laser deceleration of an atomic beam. *Phys. Rev. Lett.*, 48:596–599, 1982. [73]
- [70] A. Witte, Th. Kisters, F. Riehle, and J. Helmcke. Laser cooling and deflection of a calcium atomic beam. *J. Opt. Soc. Am. B*, 9:1030–1037, 1992. [73]
- [71] *Advanced Measurement Laboratory Facility Guidelines*. National Institute of Standards and Technology, Maryland, 2005. [88]
- [72] A. Widera, F. Gerbier, S. Fölling, T. Gericke, O. Mandel, and I. Bloch. Precision measurement of spin-dependent interaction strengths for spin-1 and spin-2 ^{87}Rb atoms. *N. J. Phys.*, 8:152, 2006. [88, 169]
- [73] M.-S. Chang, C. D. Hamley, M. D. Barret, J. A. Sauer, K. M. Fortier, W. Zhang, L. You, and M. S. Chapman. Observation of spinor dynamics in optically trapped ^{87}Rb Bose-Einstein condensates. *Phys. Rev. Lett.*, 92:140403, 2004. [88]
- [74] M. I. D'yakonov and V. I. Perel. Possibility of orienting electron spins with current. *JETP Lett.*, 13(11):657–660, 1971. [96, 157]
- [75] J. Sinova, D. Culcer, Q. Niu, N. A. Sinitsyn, T. Jungwirth, and A. H. MacDonald. Universal intrinsic spin Hall effect. *Phys. Rev. Lett.*, 92:126603, 2004. [96, 157]
- [76] C. Zhang, S. Tewari, R. M. Lutchyn, and S. Das Sarma. $p_x + ip_y$ superfluid from s -wave interactions of fermionic cold atoms. *Phys. Rev. Lett.*, 101:160401, 2008. [96, 168, 180]
- [77] A. L. Fetter. Rotating trapped Bose-Einstein condensates. *Rev. Mod. Phys.*, 81:647–491, 2009. [96]

- [78] D. Jaksch and P. Zoller. Creation of effective magnetic fields in optical lattices: the Hofstadter butterfly for cold neutral atoms. *N. J. Phys.*, 5:56, 2003. [96, 179]
- [79] M. Aidelsburger et al. Experimental realization of strong effective magnetic fields in an optical lattice. *Phys. Rev. Lett.*, 107:255301, 2011. [96, 179]
- [80] A. Sørensen, E. Demler, and M. Lukin. Fractional quantum Hall states of atoms in optical lattices. *Phys. Rev. Lett.*, 94:086803, 2005. [96, 143, 179]
- [81] J. Struck, C. Ölschläger, M. Weinberg, P. Hauke, J. Simonet, A. Eckardt, M. Lewenstein, K. Sengstock, and P. Windpassinger. Tunable gauge potential for neutral and spinless particles in driven optical lattices. *Phys. Rev. Lett.*, 108:225304, 2012. [96, 179]
- [82] A. Derevianko and H. Katori. *Colloquium: Physics of optical lattice clocks*. *Rev. Mod. Phys.*, 83:331–347, 2011. [108, 120]
- [83] E. H. Hall. On a new action of the magnet on electric currents. *Am. J. Math.*, 2(3):287–292, 1879. [112, 119]
- [84] L. Onsager. Statistical hydrodynamics. *Il Nuovo Cimento*, 6:279–287, 1949. [112]
- [85] R. P. Feynman. *Prog. Low. Temp. Phys.*, 1:17, 1955. [112]
- [86] K.W: Madison, F. Chevy, W. Wohlleben, and J. Dalibard. Vortex formation in a stirred Bose-Einstein condensate. *Phys. Rev. Lett.*, 84:806–809, 2000. [113]
- [87] J. R. Abo-Shaeer, C. Raman, J. M. Vogels, and W. Ketterle. Observation of vortex lattices in Bose-Einstein condensates. *Science*, 292:476–479, 2001. [113]
- [88] V. Schweikhard, I. Coddington, P. Engels, V. P. Mogendorff, and E. A. Cornell. Rapidly rotating Bose-Einstein condensates in and near the lowest Landau level. *Phys. Rev. Lett.*, 92:040404, 2004. [113]
- [89] M. Zwierlein, J. R. Abo-Shaeer, A. Schirotzek, C. H. Schunck, and W. Ketterle. Vortices and superfluidity in a strongly interacting Fermi gas. *Nature*, 435:1047–1051, 2005. [113]
- [90] Emil Lundh, C. J. Pethick, and H. Smith. Zero-temperature properties of a trapped bose-condensed gas: Beyond the thomas-fermi approximation. *Phys. Rev. A*, 55:2126–2131, 1997. [113]
- [91] P. L. Gould, G. A. Ruff, and D. E. Pritchard. Diffraction of atoms by light: the near-resonant Kapitza-Dirac effect. *Phys. Rev. Lett.*, 56:827–830, 1986. [120, 132]

- [92] P. J. Martin, B. G. Oldaker, A. H. Miklich, and D. E. Pritchard. Bragg scattering of atoms from a sanding light wave. *Phys. Rev. Lett.*, 60:515–518, 1988. [120]
- [93] Yu. B. Ovchinnikov et al. Diffraction of a released Bose-Einstein condensate by a pulsed standing light wave. *Phys. Rev. Lett.*, 83:284–287, 1999. [120, 132, 153]
- [94] J. H. Denschlag, J. E. Simsarian, H. Häffner, C. McKenzie, A. Browaeys, D. Cho, K. Helmerson, R. L. Rolston, and W. D. Phillips. A Bose-Einstein condensate in an optical lattice. *J. Phys. B.*, 35:3095, 2002. [120]
- [95] H. Lignier, C. Sias, D. Ciampini, Y. Singh, A. Zenesini, O. Morsch, and E. Arimondo. Dynamical control of matter-wave tunneling in periodic potentials. *Phys. Rev. Lett.*, 99:220403, 2007. [120]
- [96] M. Ben Dahan, E. Peik, J. Reichel, Y. Castin, and C. Salomon. Bloch oscillations of atoms in an optical potential. *Phys. Rev. Lett.*, 76:4508–4511, 1996. [120]
- [97] B. Paredes, A. Widera, V. Murg, O. Mandel, S. Fölling, I. Cirac, G. V. Shlyapnikov, T. W. Hänsch, and I. Bloch. Tonks-Girardeau gas of ultracold atoms in an optical lattice. *Nature*, 429:277–281, 2004. [120]
- [98] S. Fölling, F. Gerbier, A. Widera, O. Mandel, T. Gericke, and I. Bloch. Spatial quantum noise interferometry in expanding ultracold atom clouds. *Nature*, 434:481–484, 2005. [120]
- [99] I. B. Spielman, W. D. Phillips, and J. V. Porto. Mott-Insulator transition in a two dimensional Bose gas. *Phys. Rev. Lett.*, 98:080404, 2007. [120]
- [100] G. K. Campbell, A. D. Ludlow, S. Blatt, J. W. Thomsen, M. J. Martin, M. H. G. de Miranda, T. Zelevinsky, M. M. Boyd, J. Ye, S. A. Diddams, T. P. Heavner, T. E. Parker, and F. R. Jefferts. The absolute frequency of the ^{87}Sr optical clock transition. *Metrologia*, 45:539, 2008. [120]
- [101] F. Gerbier, A. Widera, S. Fölling, O. Mandel, T. Gericke, and I. Bloch. Phase coherence of an atomic Mott insulator. *Phys. Rev. Lett.*, 95:050404, 2005. [120]
- [102] J. Mun, P. Medley, G. K. Campbell, L. G. Marcassa, D. E. Pritchard, and W. Ketterle. Phase diagram for a Bose-Einstein condensate moving in an optical lattice. *Phys. Rev. Lett.*, 99:150604, 2007. [120]
- [103] M. Rigol, G. G. Batrouni, V. G. Rousseau, and R. T. Scalettar. State diagrams for harmonically trapped bosons in optical lattices. *Phys. Rev. A.*, 79:053605, 2009. [120, 128, 141, 142, 180]

- [104] N. W. Ashcroft and N. D. Mermin. *Solid State Physics*. Harcourt Brace College Publishers, 1976. [121]
- [105] I. Bloch, J. Dalibard, and W. Zwerger. Many-body physics with ultracold gases. *Rev. Mod. Phys.*, 80:885–964, 2008. [123, 138]
- [106] A. M. Rey. *Ultracold bosonic atoms in optical lattices*. PhD thesis, University of Maryland, 2004. [123]
- [107] S. Burger, F. S. Cataliotti, C. Fort, F. Minardi, M. Inguscio, M. L. Chiofalo, and M. P. Tosi. Superfluid and dissipative dynamics of a Bose-Einstein condensate in a periodic optical potential. *Phys. Rev. Lett.*, 86:4447–4450, 2001. [124, 152]
- [108] L. Fallani, L. De Sarlo, J. E. Lye, M. Modugno, R. Saers, C. Fort, , and M. Inguscio. Observation of dynamical instability for a Bose-Einstein condensate in a 1d moving optical lattice. *Phys. Rev. Lett.*, 93:140406, 2004. [124]
- [109] K. Sheshadri, H. R. Krishnamurthy, R. Pandit, and T.V. Ramakrishnan. Superfluid and insulating phases of an interacting-boson model: mean field theory and the RPA. *Euro. Phys. Lett.*, 22:257, 1993. [126]
- [110] W. Krauth and N. Trivedi. Mott and superfluid transitions in a strongly interacting lattice boson system. *Euro. Phys. Lett.*, 14:627, 1991. [127, 141]
- [111] M. P. A. Fisher, P. B. Weichman, G. Grinstein, and D. S. Fisher. Boson localization and the superfluid-insulator transition. *Phys. Rev. B.*, 40:546–570, 1989. [127]
- [112] W. S. Bakr, J. I. Gillen, A. Peng, S. Fölling, and M. Greiner. A quantum gas microscope for detecting single atoms in a hubbard-regime optical lattice. *Nature*, 462:74–77, 2009. [136]
- [113] N. Gemelke, X. Zhang, C.-L. Hung, and C. Chin. In situ observation of incompressible Mott-insulating domains in ultracold atomic gases. *Nature*, 460:995–998, 2009. [136]
- [114] M. Greiner, I. Bloch, O. Mandel, T. Hänsch, and T. Esslinger. Exploring phase coherence in a 2d lattice of Bose-Einstein condensates. *Phys. Rev. Lett.*, 87:160405, 2001. [138]
- [115] D. McKay, M. White, and B. DeMarco. Lattice thermodynamics for ultracold atoms. *Phys. Rev. A*, 79:063605, 2009. [138, 140]
- [116] A. H. van Amerongen, J. J. P. van Es, P. Wicke, K. V. Kheruntsyan, and N. J. van Druten. Yang-Yang thermodynamics on an atom-chip. *Phys. Rev. Lett.*, 100:090402, 2008. [138]

- [117] S. Tung, G. Lamporesi, D. Lobser, L. Xia, and E. A. Cornell. Observation of the presuperfluid regimen a two-dimensional Bose gas. *Phys. Rev. Lett.*, 105:230408, 2010. [138]
- [118] G. Brooker. *Modern classical optics*. Oxford University Press, Great Britain, 2002. [138]
- [119] I. Shvarchuck, Ch. Buggle, D. S. Petrov, K. Dieckmann, M. Zielonkowski, M. Kemmann, T. G. Tiecke, W. von Klitzing, G. V. Shlyapnikov, and J. T. M. Walraven. Bose-Einstein condensation into nonequilibrium states studied by condensate focusing. *Phys. Rev. Lett.*, 89:270404, 2002. [138, 139]
- [120] I. B. Spielman, W. D. Phillips, and J. V. Porto. Condensate fraction in a 2d Bose gas measured across the Mott-Insulator transition. *Phys. Rev. Lett.*, 100:120402, 2008. [140, 141]
- [121] N. Elstner and H. Monien. A numerical exact solution of the Bose-Hubbard model. *arXiv*: 9905367v1, 1999. [141]
- [122] N. R. Cooper. Optical flux lattices for ultracold atomic gases. *Phys. Rev. Lett.*, 106:175301, 2011. [143, 156]
- [123] M. Hafezi, A. Sørensen, E. Demler, and M. Lukin. Fractional quantum Hall effect in optical lattices. *Phys. Rev. A*, 76:023613, 2007. [143, 179]
- [124] A. Browaeys, H. Häffner, C. McKenzie, S.L. Rolston, K. Helmerson, and W.D. Phillips. Transport of atoms in a quantum conveyor belt. *Phys. Rev. A*, 72:053605, 2005. [145]
- [125] M. V. Berry. Quantal phase factors accompanying adiabatic changes. *Proceedings of the Royal Society of London. A. Mathematical and Physical Sciences*, 392(1802):45–57, 1984. [145]
- [126] Douglas R. Hofstadter. Energy levels and wave functions of bloch electrons in rational and irrational magnetic fields. *Phys. Rev. B*, 14:2239–2249, 1976. [146]
- [127] S. Chen et al. Revealing uncnventional properties of a Spin-Orbit coupled Bose-Einstein condensate from collective dipole oscillation. *arXiv*: 1201.6018v1, 2012. [150]
- [128] F. Gerbier and J. Dalibard. Gauge field for ultracold atoms in optical superlattices. *N. J. Phys.*, 12:033007, 2010. [156]
- [129] T. Fukui, Y. Hatsugai, and H. Suzuki. Chern numbers in discretized Brillouin zone: Efficient method of computing (spin) Hall conductances. *J. Phys. Soc. Jpn.*, 84:1674–1677, 2005. [156]
- [130] M. Machholm, A. Nicolin, C. J. Pethick, and H. Smith. Spatial period doubling in Bose-Einstein condensates in an optical lattice. *Phys. Rev. A*, 69:043604, 2004. [156]

- [131] E. Saitoh and G. Miyajima, H. Tatara. Conversion of spin current into charge current at room temperature: Inverse spin-Hall effect. *Appl. Phys. Lett.*, 88:182509, 2006. [157]
- [132] J. Wunderlich, B. Kaestner, J. Sinova, and T. Jungwirth. Experimental observation of the spin-Hall effect in a two-dimensional spin-orbit coupled semiconductor system. *Phys. Rev. Lett.*, 94:047204, 2005. [157]
- [133] O. T. Valenzuela and M. Tinkham. Direct electronic measurements of the spin Hall effect. *Nature*, 442:176–179, 2006. [157]
- [134] T. Kimura, Y. Otani, T. Sato, S. Takahashi, and S. Maekawa. Room-temperature reversible spin Hall effect. *Phys. Rev. Lett.*, 98:156601, 2007. [157]
- [135] X.-L. Qi and S.-C. Zhang. Topological insulators and superconductors. *Rev. Mod. Phys.*, 83:1057–1110, 2011. [157]
- [136] Y. Zhang and C. Zhang. BEC in spin-orbit coupled optical lattices: flat bands and superfluidity. *arXiv*, 1203.2389, 2012. [167, 180]
- [137] L. Jiang, T. Kitagawa, J. Alicea, A. R. Akhmerov, D. Pekker, G. Refael, J. I. Cirac, E. Demler, M. D. Lukin, and P. Zoller. Majorana fermions in equilibrium and in driven cold-atom quantum wires. *Phys. Rev. Lett.*, 106:220402, 2011. [168, 180]
- [138] C. J. Myatt, E. A. Burt, R. W. Ghrist, E. A. Cornell, and C. E. Wieman. Production of two overlapping Bose-Einstein condensates by sympathetic cooling. *Phys. Rev. Lett.*, 78:586–589, 1997. [168]
- [139] D. M. Stamper-Kurn, M. R. Andrews, A. P. Chikkatur, S. Inouye, H.-J. Miesner, J. Stenger, and W. Ketterle. Optical confinement of a Bose-Einstein condensate. *Phys. Rev. Lett.*, 80:2027–2030, 1998. [168]
- [140] T.-L. Ho. Spinor Bose condensates in optical traps. *Phys. Rev. Lett.*, 81:742–745, 1998. [168, 169]
- [141] M. Matuszewski. Ground states of trapped spin-1 condensates in magnetic field. *Phys. Rev. A*, 82:053630, 2012. [175]
- [142] O. Boada, A. Celi, and J. I. Latorre. Gauge-away effect in cold gases on optical lattices. *arXiv*, 0909.3937v2, 2009. [180]